Fluid-kinetic models for space plasma thrusters

by

Jesús Perales Díaz

A dissertation submitted by in partial fulfillment of the requirements for the degree of Doctor of Philosophy in

Ingeniería Aeroespacial

Universidad Carlos III de Madrid

Advisors:

Eduardo Ahedo Galilea

Adrián Domínguez Vázquez

Tutor:

Eduardo Ahedo Galilea

June 10, 2024

This thesis is distributed under license “Creative Commons Attribution – Non Commercial – Non Derivatives”.

Acknowledgements

La realización de esta tesis doctoral no hubiese sido posible sin la ayuda y las contribuciones inestimables de muchas personas, con las cuales estoy, y estaré siempre, sumamente agradecido. La sencillez y brevedad de estas líneas no es, ni mucho menos, proporcional a la gratitud que siento. Me gustaría dar las gracias, en primer lugar, a mis supervisores doctorales, por su continuo apoyo y guía durante estos años. En particular, quiero expresar mi gratitud con el Prof. Eduardo Ahedo, por aceptarme generosamente en el grupo EP2, y por darme la oportunidad de investigar junto a él en el fascinante campo de la propulsión por plasma; y con el Prof. Adrián Domínguez Vázquez, por su disponibilidad a compartir siempre sus conocimientos y a trabajar conmigo mano a mano. Aun sin ser mi supervisor, le debo al Prof. Filippo Cichocki el haberme iniciado en los mundos de la física de plasmas y la física computacional, y el conocimiento de los fundamentos sobre los que se ha basado mi trabajo diario. Quisiera mencionar también al Prof. Mario Merino y al Prof. Pablo Fajardo, por sus valiosas aportaciones a mi investigación, plasmadas en las publicaciones que forman parte de este documento. Aunque no he tenido la oportunidad de trabajar directamente con él, las conversaciones con el Prof. Jaume Navarro Cavallé han sido siempre enriquecedoras. Finalmente, quiero dar las gracias al Prof. Aaron Knoll por acogerme y guiar mi investigación durante mi estancia internacional.

En estos largos años he tenido la suerte de compartir fatigas junto a excelentes compañeros, de los cuales he aprendido tanto que no bastaría la extensión de esta tesis para resumirlo. Aunque solo mencione a algunos: Enrique, Albertos, Pedro, Xin, Scherezade, Tatiana, Simone, Marco, Jiewei, Alejandro, Borja, Álvaro ..., a todos les tengo en gran estima. Quiero recordar especialmente a Jesús Muñoz Tejeda, con quien, además de compartir nombre y amistad, distruté mi estancia internacional y tuve la oportunidad de aprender los rudimentos de la experimentación con motores de plasma, bajo el siempre encapotado cielo londinense.

En el plano personal, quiero recordar en primer lugar a mis amigos: han sido todos ellos un descanso para mí durante estos años. También lo ha sido mi familia. Me siento enormemente afortunado de haberlos tenido siempre cerca; mis abuelos, mis tios, mis primos... son un regalo inmerecido. Gracias a mis padres, Julia y Jesús. De ellos he recibido gran parte de lo que tengo: de lo tangible y, sobre todo, de lo intangible. Siempre se han esforzado, de miles de formas, para que yo pudiese dedicarme a mis estudios y a construir mi futuro. La cotidianeidad de su esfuerzo no hace decrecer mi admiración por ellos, sino todo lo contrario. No puedo olvidarme de mi hermano, Adrián, con quien he tenido la suerte de crecer y descubrir el mundo. Habría sido imposible sobrellevar la tesis durante el confinamiento de no haber sido por el tiempo compartido junto a él. Me alegro mucho de que haya encontrado en Alejandra a su compañera para el viaje de la vida. Yo también encontré durante este tiempo a la mía: Marta. Nuestro camino juntos hasta ahora es, entre otras muchas cosas increíbles, la historia de dos vidas cruzadas y dos tesis paralelas. Quiero agradecerle su disponibilidad para ayudarme siempre que lo he necesitado, su sentir junto al mío tanto en lo bueno como en lo malo, y su infinita paciencia y comprensión: nadie me entiende mejor. Este será un gran año para los dos. Doy gracias a Dios por todos ellos y por haber podido llevar adelante este proyecto.

The research presented in the different chapters of this thesis has been supported by the following projects: ESPEOS, funded by Agencia Estatal de Investigación, under grant agreement number PID2019-108034RBI00/AEI/10.13039/501100011033; EDDA, funded by the European Union's Horizon 2020 Research and Innovation Programme, under grant agreement number 870470; and ASPIRE, funded by the European Union's Horizon 2020 Research and Innovation Programme, under grant agreement number 101004366. Additionally, the research stay at IPPL has been funded by Universidad Carlos III de Madrid through the Programa Propio de Investigación, with project number 2022/00268/001.

Published and submitted content

The following list includes the journal articles published within the framework of the thesis:

- J. Perales-Díaz, F. Cichocki, M. Merino, E. Ahedo, "Formation and neutralization of electric charge and current of an ion thruster plume," *Plasma Sources Science and Technology,* 30(10):105023, 2021. https://doi.org/10.1088/1361-6595/ac2a19

  Contributions by authors: *Conceptualization*: EA, FC, MM; *Methodology*: EA, FC, **JPD**; *Software*: FC, **JPD**; *Formal Analysis*: **JPD**; *Writing-original draft*: **JPD**; *Writing-review & editing*: EA, FC, MM; *Supervision*: EA, FC.

  Chapter 2 is an exact reproduction of the contents of this article. The material from this source included in this Thesis is not singled out with typographic means and references.

- J. Perales-Díaz, A. Domínguez-Vázquez, P. Fajardo, E. Ahedo, F. Faraji, M. Reza and T. Andreussi, "Hybrid plasma simulations of a magnetically shielded Hall thruster," *Journal of Applied Physics,* 131(10):103302, 2022. https://doi.org/10.1063/5.0065220

  Contributions by authors: *Conceptualization*: ADV, EA, **JPD**, PF; *Methodology*: ADV, EA, **JPD**; *Software*: ADV, **JPD**; *Experimental investigation*: FF, MR, TA; *Formal Analysis*: **JPD**; *Writing-original draft*: **JPD**; *Writing-review & editing*: ADV, EA, PF; *Supervision*: ADV, EA.

  Chapter 3 is an exact reproduction of the contents of this article. The material from this source included in this Thesis is not singled out with typographic means and references.

- J. Perales-Díaz, A. Domínguez-Vázquez, P. Fajardo, E. Ahedo, "Simulations of driven breathing modes of a magnetically shielded Hall thruster," *Plasma Sources Science and Technology,* 32(7):075011, 2023. https://doi.org/10.1088/1361-6595/ace651

Contributions by authors: *Conceptualization*: ADV, EA, **JPD**; *Methodology*: ADV, EA, **JPD**; *Software*: ADV, **JPD**; *Formal Analysis*: **JPD**; *Writing-original draft*: **JPD**; *Writing-review & editing*: ADV, EA, PF; *Supervision*: ADV, EA.

Chapter 4 is an exact reproduction of the contents of this article. The material from this source included in this Thesis is not singled out with typographic means and references.

Acronyms correspond to:

JPD	Jesús Perales-Díaz, Universidad Carlos III de Madrid, *PhD candidate*.
ADV	Adrián Domínguez-Vázquez, Universidad de Málaga, *Advisor*.
EA	Eduardo Ahedo, Universidad Carlos III de Madrid, *Advisor and Tutor*.
FC	Filippo Cichocki, ENEA-Frascati Research Center.
FF	Farbod Faraji, Imperial College London.
MM	Mario Merino, Universidad Carlos III de Madrid.
MR	Maryam Reza, Imperial College London.
PF	Pablo Fajardo, Universidad Carlos III de Madrid.
TA	Tommaso Andreussi, Scuola Superiore Sant'Anna.

Other research merits

The next list includes the contributions made to conference proceedings and oral presentations:

- J. Perales-Díaz, F. Cichocki, M. Merino, E. Ahedo, "Studying the formation and neutralization of an ion thruster plume with EP2PLUS," in *36th International Electric Propulsion Conference,* 15-20 September, 2019.
- J. Perales-Díaz, A. Domínguez-Vázquez, P. Fajardo, E. Ahedo, F. Faraji, M. Reza and T. Andreussi, "Characterization of a 5kW-class Hall thruster via 2D hybrid simulations," in *7th Space Propulsion Conference*, Estoril, Portugal, 17-19 March, 2021.
- J. Perales-Díaz, A. Domínguez-Vázquez, P. Fajardo, E. Ahedo, F. Faraji, M. Reza and T. Andreussi, "Hybrid plasma simulations of the HT5k thruster," in *ExB plasma workshop (poster session)*, Madrid, Spain, 16-18 February, 2022.
- G. Bouhours, B. Spitaels , A. Piragino, S. Weis , J.Perales-Díaz, A. Domínguez-Vázquez, "Test results of H2020 european direct drive architecture study," in *8th Space Propulsion Conference*, Estoril, Portugal, 9-13 May, 2022.
- J. Perales-Díaz, A. Domínguez-Vázquez, P. Fajardo, E. Ahedo, T. Andreussi, A. Piragino, "Hybrid 2D plasma simulations of a 20kW-class magnetically shielded Hall effect thruster," in *37th International Electric Propulsion Conference*, Boston, MA, 19-23 June, 2022.
- A. Domínguez-Vázquez, J. Perales-Díaz, P. Fajardo and E. Ahedo, "Analysis of anode voltage modulation in Hall thruster operation and design with HYPHEN for project EDDA," in *EPIC Workshop 2023*, Naples, Italy, 9-12 May, 2023.

Abstract

Numerical studies of the discharge of plasma thrusters are deemed essential for the growing electric propulsion industry. On the one hand, the design and optimization processes of new or existing thrusters benefit from a significant reduction of time and monetary costs, thanks to a decrease in the needed experimental effort achieved through numerical modeling. On the other hand, the amount of details and information from numerical simulations allows the analysis of complex physical phenomena, relevant for the thruster performance, which cannot be analyzed experimentally. This Thesis is devoted to the study, by means of fluid-kinetic or fully-kinetic codes, of the discharge of plasma propulsion engines, especially the Hall effect thruster. This overall objective has involved, firstly, the improvement of some existing numerical tools; and, secondly, the simulation of different discharge scenarios and the subsequent analysis of the results.

The first task of the Thesis has consisted on the upgrade of the hybrid 3D code EP2PLUS, developed within the EP2 group, to enable the modeling of the plasma discharge through the grid optics of ion thrusters. A realistic scenario has been simulated by means of 2D and 3D models, and the outputs have been satisfactorily compared with analytical and experimental results, for a partial validation of the tool. The second and central task of the Thesis has been the numerical study of two high power Hall effect thrusters designed by SITAEL, the HT5k and the HT20k, characterized by the magnetic shielding of their chamber walls and the use of a central cathode. The hybrid 2D (axial-radial) code HYPHEN, developed within EP2, has been adapted and used for the modeling of both thrusters. A first study of the HT5k has fully characterized its time-averaged discharge as well as its performance, demonstrating the effectiveness of magnetic shielding. A similar analysis, extended to alternative propellants and other relevant studies, has been carried out on the HT20k thruster. A second study of the HT5k has analyzed the effect, on local plasma properties and efficiency, of the sinusoidal modulation of the discharge voltage. Finally, the third task, performed during the stay at the Imperial Plasma Propulsion Laboratory, has led to the improvement of its in-house full-PIC quasi-2D code PlasmaSim in its axial-radial version, for the simulation of a water-fuelled Hall effect thruster, called WET-HET.

Resumen

El estudio numérico de las descargas de motores de plasma resulta esencial para el creciente sector de la propulsión eléctrica. Por un lado, los procesos de diseño y optimización de prototipos nuevos o existentes se benefician de una considerable reducción de tiempos y de costes, gracias a la disminución de la carga experimental por medio del modelado numérico. Por otro lado, el nivel de detalle e información obtenido de las simulaciones numéricas permite el análisis de complejos fenómenos físicos del plasma, relevantes para el rendimiento de los motores, que no pueden ser estudiados por medios experimentales. Esta Tesis está dedicada al estudio, por medio de códigos fluido-cinéticos y puramente cinéticos, de la descarga de propulsores de plasma, especialmente de efecto Hall. Este objetivo general ha supuesto, en primer lugar, la mejora de herramientas numéricas ya existentes; y, en segundo lugar, la simulación de distintos escenarios de descarga, y el posterior análisis de los resultados.

La primera tarea ha consistido en la adaptación del código híbrido 3D EP2PLUS, desarrollado por el grupo EP2, al modelado de descargas a través de rejillas de motores iónicos. Un escenario realista ha sido simulado por medio de modelos 2D y 3D, y los resultados comparados satisfactoriamente con otros analíticos y experimentales, para una validación parcial de la herramienta. La segunda y principal tarea de la Tesis ha sido el estudio numérico de dos motores de efecto Hall de alta potencia diseñados por SITAEL, el HT5k y el HT20k, caracterizados por el apantallamiento magnético de sus paredes y el uso de un cátodo central. El código híbrido 2D HYPHEN, desarrollado en EP2, ha sido adaptado y utilizado para la modelización de ambos motores. Un primer estudio del HT5k ha caracterizado completamente su descarga promediada en el tiempo, así como su rendimiento, demostrando la efectividad del apantallamiento magnético. Un análisis similar, extendido a propulsantes alternativos y otros estudios de interés, se ha llevado a cabo con el motor HT20k. Un segundo estudio del HT5k ha analizado el efecto, sobre las propiedades locales del plasma y la eficiencia, de la modulación sinusoidal del voltaje de descarga. La tercera y última tarea, en el marco de la estancia junto al grupo "Imperial Plasma Propulsion Laboratory", ha permitido la mejora de su código full-PIC cuasi-2D PlasmaSim, en su versión axial-radial, para la simulación del motor de efecto Hall WET-HET, operado con agua.

List of Symbols

$\alpha, \alpha_{\mathrm{div}}$	Beam divergence angle
α_{t}	Momentum turbulent coefficient
γ	Electron polytropic cooling coefficient
Δt	Timestep
$\Delta\phi$	Electric potential difference
δ_{r}	Elastic reflection yield
δ_{SEE}	Secondary electron emission yield
ϵ_0	Vacuum permittivity
η	Thrust efficiency
η_{A}	Anodic efficiency
η_{ch}	Charge efficiency
η_{cur}	Current efficiency
η_{disp}	Dispersion efficiency
$\eta_{\mathrm{disp}'}$	Alternative definition of dispersion efficiency (used only in Chap. 4)
η_{div}	Divergence efficiency
η_{ene}	Energy efficiency
η_{u}	Propellant utilization efficiency
η_{vol}	Voltage (utilization) efficiency
λ_{D}	Debye length
ν	Collision frequency
Π	Normalized perveance per hole
ρ	Electric charge density
$\bar{\bar{\sigma}}$	Electric conductivity tensor
σ_{rp}	Electron VDF replenishment fraction

Φ	Thermalized potential function
ϕ	Electric potential function
φ	Phase shift between two signals
χ	Hall parameter
χ_{t}	Reduced Hall parameter
ω_{ce}	Electron cyclotron frequency
$\mathcal{E}_{s,\mathrm{wall}}$	Average energy per net collected particle of the s^{th} species
$\mathcal{F}_{\mathrm{z}}$	Axial flux-VDF of single ion species
$\boldsymbol{B}$	Magnetic field vector
B_{max}	Magnetic field peak intensity
d_{a}	Acceleration grid hole length
d_{hc}	Distance between hole centers
d_{s}	Screen grid hole length
$\boldsymbol{E}$	Electric field vector
$\boldsymbol{F}$	Thrust vector
f	Frequency
H	Width
I_{d}	Discharge current
i_{b}	Ion current extracted per hole in the ion optics scenario
I_{sp}	Specific impulse
$\boldsymbol{j}$	Current density vector
$\bar{\bar{K}}$	Thermal conductivity tensor
$\dot{m}_{\mathrm{A}}$	Anode mass flow
L	Length
l_{g}	Gap between the screen and the acceleration grid
m	Elementary particle mass of a species
n	Particle density
P	Total power deposited to the plasma
P_{d}	Discharge power
p	Pressure
Q_{A}	Anode volumetric flow

$\boldsymbol{q}$	Heat flux vector
R	Random number, or radius of beam cross-section
R_κ	Ionization rate of the κ ionization process
S	Particle source term in the continuity equation
T	Temperature
t_a	Thickness of the acceleration grid
t_s	Thickness of the screen grid
$\boldsymbol{u}$	Fluid velocity vector
$\boldsymbol{v}$	Macroparticle velocity vector
V_d	Discharge voltage
V_s	Source voltage
V_E	Potential of the discharge chamber plasma bulk with respect to the accelerator grid
V_N	Potential of the discharge chamber plasma bulk with respect to the neutralizer
V_S	Potential of the discharge chamber plasma bulk with respect to the screen grid
Z	Charge number
$(1_\mathrm{z}, 1_\mathrm{r}, 1_\theta)$	Cylindrical vector basis
(z, r, θ)	Cylindrical coordinates
$(1_\lambda, 1_\sigma, 1_\theta)$	MFAM vector basis
$(\lambda, \sigma, \theta)$	MFAM coordinates

Subscripts

A	Referring to the anode
C	Referring to the cathode
c	Referring to collisions
cc	Referring to cathode coupling
D	Referring to dielectric walls
d	Referring to the plasma discharge
e	Referring to electron species
el	Referring to elastic collisions
elec	Referring to the electric field
ex	Referring to excitation collisions
i	Referring to ion species
inel	Referring to inelastic collisions
iner	Referring to inertia
inj	Referring to injection
ion	Referring to ionization collisions
n	Referring to neutral species or "normal" with respect to a surface
prod	Referring to the plasma production
Q	Referring to the sheath edge
r	Referring to the electron reflection
res	Referring to resistive force
s	Referring to the sth plasma species
s, SEE	Referring to secondary electron emission
sh	Referring to the plasma sheaths
t	Referring to turbulent or anomalous effects
th	Thermal
W, wall	Referring to the thruster walls
∞	Referring to the downstream plume boundaries
$\perp$	Referring to the direction perpendicular to the B lines
$\parallel$	Referring to the direction parallel to the B lines

Accents

$\overline{\zeta}$	Time-averaged value of a given property ζ
$\tilde{\zeta}$	Axial-radial average value of property ζ
$\tilde{\boldsymbol{\zeta}}$	Projection of a vector magnitude $\boldsymbol{\zeta}$ onto an axial-radial plane
$\hat{\zeta}$	Radially-averaged value of the property ζ
ζ^*	Reference value of the property ζ

List of Abbreviations

AC	Alternating Current
ASPIRE	Advanced Space Propulsion for Innovative Realization of space Exploration
BM	Breathing Mode
BP	Background Pressure
CEX	Charge EXchange Collisions
CFL	Courant-Friedrichs-Lewy
CHT	Cylindrical Hall Thruster
CHEOPS	Consortium for Hall Effect Orbit Propulsion System
DC	Direct Current
DD	Direct-Drive
DM	Development Model
DMD	Direct Mode Decomposition
ECRT	Electron Cyclotron Resonance Thruster
EDDA	European Direct-Drive
EM	Engineering Model
EMI	ElectroMagnetic Interference
EP2	Plasma and Space Propulsion Team
EP2PLUS	Extensible Parallel Plasma PLUme Simulator
EP	Electric Propulsion
ESA	European Space Agency
FEEP	Field Emission Electric Propulsion
FFT	Fast Fourier Transform
GIT	Gridded Ion Thruster
GDML	Global Downstream Matching Layer

HET	Hall Effect Thruster
HDF5	Hierarchical Data Format (version 5)
HODMD	Higher Order Dynamic Mode Decomposition
HPT	Helicon Plasma Thruster
HYPHEN	HYbrid Plasma-thruster Holistic-simulation ENvironment
IBS	Ion Beam Shepherd
ICL	Imperial College London
IFE	Immersed Finite Elements
IPPL	Imperial Plasma Propulsion Laboratory
LAPACK	Linear ALgebra PACKage
LEOSWEEP	Low Earth Orbit Security With Enhanced Electric Propulsion
LIF	Laser-Induced Fluorescence
MCC	Monte Carlo Collision
MFAM	Magnetic Field Aligned Mesh
MPDT	Magneto-PlasmaDynamic Thruster
MS	Magnetic Shielding
NASA	National Aeronautics and Space Administration
OpenMP	Open Multi-Processing
PIC	Particle-In-Cell
PPT	Pulsed Plasma Thruster
PPU	Power Processing Unit
SEE	Secondary Electron Emission
SPT	Stationary Plasma Thruster
RLC	Resistor-Inductor-Capacitor
RMS	Root Mean Square
TAL	Thruster with Anode Layer
UC3M	Universidad Carlos III de Madrid
UE	Unreal Engine
US	UnShielded
VDF	Velocity Distribution Function

WET-HET	Water ElecTrolysis Hall Effect Thruster

Contents

List of Figures

List of Tables

Chapter 1

General introduction

1.1 In-space electric propulsion

The development of space-related technologies has shaped and shapes the world in which we live. The wide variety of daily-life applications for which in-space systems are indispensable reveals the paramount importance of these technologies. Just to mention a few of these applications, one could speak about GPS, communications, surveillance or meteorology. And the catalogue for this civil applications keeps on increasing day after day. This fact, together with the bursting on the scene of the private sector, leaving behind the space era under the sole control of national governments, is leading to an outstanding increase in the number of human-made satellites in space [1].

This trend is necessarily linked to the development and research on propulsive systems that allow space vehicles to steer themselves to target orbits or perform station-keeping maneuvers, all this with lower mission costs and increasing spacefraft (S/P) useful lifetimes. At the same time, scientific-related space missions, with more ambitious objectives every day, are also drivers for the development of efficient propulsion systems. As a response to these demands, the energy and mass limitations inherent to chemical propulsion can be overcome with electric propulsion (EP) technologies [2–5]. With conventional chemical propulsion, the achievable propellant exhaust velocities are limited by the internal energy of the propellant itself. In EP, instead, very high specific impulses can be obtained through the electromagnetic acceleration of charged particles, which leads to significant mass savings; and energy availability is practically unlimited since it does not depend on the propellant, but on other sources, like solar electric energy. For these reasons, the importance of EP in the space propulsion sector is boundlessly growing [6], being already the preferred choice among the latest space missions, like: Airbus' telecommunication satellites [7, 8], Boeing's all electric propulsion platforms [9], OneWeb and Starlink constellations [10], or scientific missions like SMART-1 [11], Hayabusa-1 and Hayabusa-2 [12], BepiColombo [13], the projected Lunar Gateway [14], etc.

A wide variety of electric thrusters exists featuring different operational powers, geometries and plasma-electromagnetic field interaction mechanisms for thrust generation. Some of the most important EP systems, arranged in terms of their common operational power, are: (*i*) in the range beyond 100 kW (very high power), the magnetoplasmadynamic thruster (MPDT) [15–17]; (*ii*) from 0.1's to 10's of kW, the gridded ion thruster (GIT) [18–21], the Hall effect thruster (HET) [22–25] and the arcjet/resistojet [2,26,27]; (*iii*) from units of W to units of kW, the helicon plasma thruster (HPT) [28–33] and the electron cyclotron resonance thruster (ECRT) [34–36], which are electrodeless; (*iv*) below 10's of W (micropropulsion), electrospray thrusters [37–39] and field emission electric propulsion (FEEP) thrusters [40, 41]. Pulsed plasma thrusters (PPT) [42–45], which operate in a pulsated regime, can work over a very wide range of operational power levels.

The different types of electric thrusters can be also classified, according to the mechanism for plasma-engine thrust transmission, into: electrothermal, electrostatic and electromagnetic [4]. An electrostatic thruster type, the GIT, and an electromagnetic one, the HET, constitute the most mature and performant technologies of the field, having flown extensively and exhibiting a reliable and highly efficient operation [11,46,47]. Electrothermal thrusters, like the arcjet and the resistojet, and some electromagnetic ones, like the MPDT and the PPT, posses a long heritage and a considerable degree of maturity [5], but they are in general less performant and reliable than GITs and HETs. The MPDT technology, in particular, can achieve the largest thrust densities within the EP field and is suitable for high-thrust missions, but its development is hindered by the lack of vacuum chambers with the adequate pumping capacity [2] and extensive research is needed to overcome current lifetime and efficiency issues. In the area of micropropulsion, due to the unfavourable downscaling of GITs and HETs, electrospray and FEEP thrusters are quickly evolving. These kind of devices, which electrostatically extract and accelerate ions or charged droplets from liquid propellants, have their niche in the fast-growing market of cubesats and nanosatellites [48], as well as in precise satellite pointing [49]. The electrodeless HPT and ECRT rely on plasma-wave coupling for ion production, and can render enhanced lifetimes thanks to the absence of the critical degradation mechanism of electrode erosion, inherent to most of the other plasma thruster types [50]. However, further research is needed to improve the plasma-wave coupling and other design characteristics, specially on the HPT side, to make electrodeless thrusters more efficient and viable alternatives to GITs and HETs [5].

Although the GIT and the HET are well-established technologies, there currently exist significant ongoing efforts for their further development, motivated by the growing space industry demands. These efforts include: (*i*) the low and high power scalability of the thrusters [51–54]; (*ii*) the development of direct-drive (DD) architectures for mass and cost savings in power processing units [55, 56]; (*iii*) erosion mitigation strategies for lifetime improvement [57,58], among which magnetic shielding in HETs is the most notable example [59]; (*iv*) the search for alternatives to the conventional propellant (xenon) [60–68]; (*v*) design strategies for optimal thermal management [69]; etc. Advances in these research lines require intensive experimental campaigns, which are costly and time-consuming.

1.2 Plasma simulations tools

In order to reduce the high cost associated to the development of GITs and HETs, and also to overcome current limitations in diagnostics capabilities, the realization of experimental campaigns and analysis of test data needs to be combined with the numerical modeling of the physically-complex plasma discharge of electric thrusters. For this reason, numerical simulations have become an essential tool for the development of GITs and HETs, and other EP devices. There exist strong efforts within the EP community to achieve reliable plasma simulation codes. The main obstacle preventing this achievement is the coexistence within plasma discharges of numerous multi-scale and coupled physical phenomena [70].

The three main types of computational techniques for the modelling of plasmas are the following [70–72]: fluid, kinetic (particle-based and grid-based) and hybrid approaches. During the last decades, a significant number of codes of all kinds have been developed and implemented for the numerical solution of the plasma discharge of EP thrusters. These codes leverage the main advantages of the different formulations, while dealing with their inherent limitations.

In first place, fluid methods solve different integral moments of the kinetic Boltzmann equation of the plasma species, assuming Maxwellian distributions for the closures. These approaches are attractive because of their short run times and low demand of computational resources [73–77]. However, they have a limited capability to model EP plasmas under the low collisionallity regime, in which the velocity distribution of the different species may significantly deviate from the Maxwellian function. One of the most important approximations in the modeling of the electron fluid is the so-called *drift-diffusion* approximation, in which time-dependent and inertial terms are neglected in the momentum conservation equation [78]. This allows obtaining a generalized Ohm's law, which does not exhibit non-linearities in terms of the electron fluid velocity. With the additional assumptions that magnetic and collisional forces are relatively small, as well as isothermal and electrostatic conditions, the simple Boltzmann relation can be applied. This relation has been used to model the electron transport parallel to the magnetic field lines in pseudo-2D formulations [79].

In second place, particle-based kinetic approaches, also known as full Particle-in-Cell (PIC), discretize the species velocity distribution functions (VDFs) with particle clusters called macroparticles, whose trajectories are obtained through the integration of kinematic equations and the self-consistent resolution of electromagnetic fields [80, 81]. PIC (full-PIC) methods are widely used since they can numerically model non-Maxwellian distributions and the algorithms associated with the particles motion are relatively simple [82–87]. Yet, these numerical approaches need to solve for very small scales (Debye length) relative to the characteristic length of the thruster, and very high frequencies (plasma frequency) relative to the characteristic frequencies of ion and neutral-related processes in the plasma discharge; which significantly increase the computational cost, as compared to fluid approaches [70]. To partially mitigate this limitation and accelerate the simulations, the Debye length or the time step can be augmented by artificially increasing, respectively, the permittivity of vacuum or the electron mass [88, 89]. The way in which these numerical artifacts modify the physics of the problem is not fully understood. Moreover, PIC methods also exhibit an inherent statistical noise, which can only be damped at the cost of more computationally-demanding simulations.

Grid-based direct kinetic methods solve directly the kinetic Boltzmann equation, coupled with Maxwell equations, by discretizing the six-dimensional phase-space in which the species VDFs are defined [90–92]. Grid-based direct kinetic codes, as PIC ones, are able to deal with non-Maxwellian VDFs. Yet, unlike PIC methods, they do not suffer from the statistical noise of particle methods [91]. The advantages of this approach are accompanied by many challenges such as the treatment of collisions due to the computational cost of modelling the Boltzmann integral for elastic collisions [90], or the numerical error associated to the discretization of the velocity space. These problems frequently restrict the application of these methods to simplified low dimensional studies.

In third place, an intermediate solution between fluid and kinetic approaches is found in the so-called hybrid PIC-fluid methods [93–99]. They are often regarded as an optimal alternative for many EP plasma scenarios. They combine the advantages of both full-PIC (i.e., kinetic description of the species modelled as macroparticles) and fluid models (i.e., low computational cost), the latter typically applied only to electrons. Nevertheless, the closure of the fluid equations for electrons still limits the capacity of hybrid codes to model particular scenarios in EP plasmas where deviations from the Maxwellian distribution are relatively important.

1.2.1 Simulation tools used in the Thesis

Most of the work developed within the framework of this Thesis has been carried out with three plasma simulation codes: EP2PLUS, HYPHEN and PlasmaSim. The first two have been developed at the Plasma and Space Propulsion Team (EP2), while PlasmaSim at the Imperial Plasma Propulsion Laboratory (IPPL). It follows a brief description of each of the codes.

EP2PLUS

EP2PLUS is a three-dimensional hybrid (PIC-fluid), OpenMP parallelized code developed in the framework of the LEOSWEEP project, for the numerical modeling of the plasma plume-object interaction in an ion beam shepherd (IBS) scenario, as part of the doctoral thesis of Filippo Cichocki [98, 100].

The PIC formulation (within its corresponding module) is applied to the heavy species (i.e. ions and neutrals), which are moved in a 3D space. The electron fluid model consists on a set of conservation equations coupled with Poisson's equation for the electric potential, which allows EP2PLUS to consistently model non-neutral plasmas, including plasma sheaths around objects. The code features an automatic division of the simulation domain into quasineutral and non-neutral regions based on the local relative charge density. Both PIC and electron modules operate in structured meshes of the simulation domain. The first version of EP2PLUS could only simulate non-magnetized plumes, like the ones from GITs [100, 101], and considered simplified electron thermodynamics with a polytropic energy closure. The most recent version of EP2PLUS, instead, incorporates the energy equation for the electron fluid [102] and allows modelling weakly magnetized plasma plumes from electromagnetic thrusters [103, 104]. It must be pointed that scenarios with high magnetization in the plume are still problematic and lead to large numerical diffusion.

In Chap. 2, the most relevant features of the code for the present work are presented in detail. A complete description of the whole simulation tool can be found in Ref. [98].

HYPHEN

HYPHEN is a two-dimensional axisymmetric (axial-radial), hybrid (PIC-fluid), OpenMP parallelized multi-thruster simulation code built modularly [105]. The development of HYPHEN, which mainly occurs in the framework of the H2020 CHEOPS project, benefits from the inherited knowledge from previous simulations codes, namely HPHall [93], HPHall-2 [96] or HallMA [97]. The main developers of HYPHEN are Adrián Domínguez Vázquez [99], Daniel Pérez Grande [106] and Jiewei Zhou [107].

The PIC formulation is similar to the one of EP2PLUS, in a 2D domain with cyclindrical coordinates; while a quasineutral and magnetized drift-diffusion fluid formulation (including the energy equation) is considered for the electron population, with a phenomenological experimentally-informed model for the anomalous transport [93, 96]. A planar sheath model provides the proper coupling between the quasineutral plasma and the wall conditions, and therefore, sheaths are treated as surface discontinuities by the code. The PIC formulation and its algorithms are implemented on a structured Cartesian mesh, while the electron-fluid ones on a complex unstructured magnetic field-aligned mesh (MFAM) [108]. The use of a MFAM enables the simulation of strongly-magnetized plasmas, like the one within a HET discharge chamber, which is the main simulation target of HYPHEN. Recently, the code has been upgraded to simulate electrodeless plasma thrusters [109–112]. HYPHEN and EP2PLUS codes have been compared in Ref. [104], in terms of the modeling of the near plume of a HET.

A detailed description of the code features relevant for the present work can be found in Chaps. 3 and 4. For a complete description of the whole simulation tool, the reader is referred to Refs. [99, 100, 105, 107, 113–115].

PlasmaSim

PlasmaSim is an electrostatic full-PIC code written in `C++` and `Julia`, developed by Aaron Knoll for the simulation of HETs. There exist 0D, 1D and quasi-2D versions of the code [67, 116, 117]. The denomination “quasi-2D” refers to the fact that the code features a reduced order scheme for the solution of the 2D Poisson’s equation, which is explained in Sec. 6. The present work is only related to the quasi-2D version, of which, at the same time, there exist two versions: (a) the axial (or radial)-azimuthal version written in `Julia` [118], which is mainly used for the study of high-frequency azimuthal plasma oscillations [117, 119]; and (b) the axial-radial one written in `C++` [67] (and Unreal Engine [120]), which is devoted to the modeling of large scale phenomena and performance analysis. The axial-radial version of the code is the one used and upgraded during the research stay. So, hereafter, “PlasmaSim” must be understood as the “quasi-2D axial-radial version of PlasmaSim”.

A brief description of the relevant characteristics of the code is provided in Chap. 6. A complete description of PlasmaSim can be found in Ref. [67].

1.3 Main objectives and structure of the Thesis

The overall objective of the Thesis is to adapt, improve, and apply the three simulation codes introduced in Sec. 1.2.1 to numerically study the physics and performances of GITs and HETs. Chapters 2 to 6 represent the core of the Thesis, each one with its own specific objectives. Chapter 2 presents a numerical study of the ion optics of a GIT. Then, Chapters 3-5 are devoted to the modeling of MS HETs. Finally, Chapter 6 is about the simulations of a conventional HET operated with water as propellant. It follows a brief description of the main contents of each of the Chapters:

- In Chapter 2, we take advantage of the 3D geometry of EP2PLUS and its capability to deal simultaneously with electrically non-neutral and quasineutral regions to simulate the plasma discharge across the ion optics of a GIT and the process of neutralization of the electric charge and electric current, coupling the electron emission of the external neutralizer and the ion beam extracted from the GIT discharge chamber. Two different setups are considered for the grids modelling: one with an infinite number of apertures, and another one with a finite number; with different computational costs associated to them. Both models are compared with each other and with a new 1D semi-analytical model for the plume. Moreover, numerical simulations are benchmarked against experimental data, in terms of the plume divergence angle. This Chapter is the exact reproduction of a first article, published in *Plasma Sources Science and Technology* [121].

- In Chapter 3, we improve and adapt HYPHEN to simulate the new family of HET prototypes featuring magnetic shielding (MS) topologies and centrally mounted hollow cathodes, in contrast to conventional magnetic lens topologies and external hollow cathodes. This research is framed mainly within the H2020 EDDA project, and the simulations are performed on the 5 kW-class HT5k thruster by SITAEL. A full 2D description of the discharge at different operational points is obtained and partially validated against experiments. The main characteristics of a MS HET discharge are identified and the capability of the code for its modeling demonstrated. This Chapter is the exact reproduction of a second article, published in *Journal of Applied Physics* [122].

- In Chapter 4, we continue extending HYPHEN capabilities, by imposing a time-modulated discharge voltage and analysing its effects on the HT5k discharge performance and local plasma properties. This study is motivated by previous works that have suggested increments in performance thanks to modulation. Simulations are performed again in the framework of the EDDA project, and their results are compared with data from previous experiments on different thrusters. Performance gains with modulation are studied and related to local plasma 2D dynamics. Two additional key contributions of this Chapter are: first, the analysis of the effects of voltage modulation in the discharge current oscillations, controlled through the electron temperature, and the transition from natural to driven breathing modes; and second, the isolation and identification with data-driven techniques of the most relevant spatio-temporal mode of the modulated discharge and its comparison to the unmodulated one. This Chapter is the exact reproduction of a third article, published in *Journal of Applied Physics* [123].

- In Chapter 5, we extend the analysis of Chapter 3 from the HT5k to the HT20k, a magnetically shielded 20 kW-class HET by SITAEL. The research is carried out in the context of the H2020 ASPIRE project. As a first step of this study, performances of the two thrusters with xenon are compared. Besides that, the main objectives of the analysis are: first, to simulate the discharge of the HT20k with xenon and krypton as propellants for different operation points, and to compare the different cases in terms of local plasma properties and performances; and second, to analyse the sensitivity of the simulations to different input parameters, related to the plasma-wall interaction and the plume modeling.

- In Chapter 6, we present the work developed during the international research stay at Imperial College, on the numerical modelling of the WET-HET, a Hall-effect thruster operated with water (or water electrolysis products) as propellant. The numerical tool used is the full-PIC code PlasmaSim, which is briefly described in this Chapter. The code upgrades accomplished during the research stay, whose main aim is to enable the simulation of a HET discharge with water, are also presented. Finally, some simulation results of the WET-HET discharge are shown and discussed.

- Chapter 7 gathers the main conclusions, including a list of the main contributions of the Thesis. In addition, future lines of work are suggested.

Therefore, this monograph combines a compendium of three peer-reviewed articles with two unpublished chapters which, after some refinement, we expect to submit independently for publication. We acknowledge that the hybrid nature of this document, partially breaks its harmony and may imply some repetitions, mainly in the introductory sections of Chapters 2 to 4. Yet, we believe that the exact reproduction of the published articles: emphasizes that each of them has been already peer-reviewed by at least two referees, protects better the text against plagiarism claims, and keeps the due recognition to coauthors beyond Thesis' advisors.

Chapter 2

Formation and neutralization of electric charge and current of an ion thruster plume

This Chapter integrally reproduces the contents of the article "Formation and neutralization of electric charge and current of an ion thruster plume", Plasma Sources Science and Technology, 30 (2021) [121]. The style has been adapted to the one of this document and the references have been unified in a single bibliography at the end of the document.

Abstract

A 3D hybrid model is introduced and applied to the simulation of the plasma plume extraction, formation, and neutralization in a gridded ion thruster. While ions and neutrals are treated with a particle-in-cell formulation, electrons are modeled as two independent isothermal populations: one inside the discharge chamber and one in the plume. The definition of a thermalized potential allows to solve the electron currents in the high-conductivity limit of the Ohm's law. The space charge neutralization distance is observed to be short and thus essentially independent of the cathode position. However, this position strongly affects the electric current neutralization paths in the near plume for each ion beamlet. Electron inertial forces are shown to be comparable to collisional forces in certain plasma regions. A semi-analytical 1D fluid model of the plume, matched to the hybrid model, allows to complete the far plume expansion down to infinity. Grids with an infinite and finite number of apertures are simulated and compared with each other and with the 1D model. The numerically obtained divergence angle of the ion plume is compared with experimental measurements, showing good agreement.

2.1 Introduction

Electric propulsion is an essential mission-enabling technology in space engineering. The large specific impulse of plasma thrusters permits a significant extension of the spacecraft lifetime and the development of more ambitious missions. Among the different existing technologies, the Gridded Ion Thruster (GIT) can be considered a consolidated one, having flown in numerous space missions since 1964 [46]. The GIT is characterized by a particular ion extraction-acceleration mechanism, which is carried out by a grid assembly. This confines the electrons inside the chamber, while extracting, accelerating and focusing an ion beam. Afterwards, the ion current is neutralized by the electrons emitted by an external hollow cathode [26], thus avoiding charge build-up inside the thruster, which would otherwise lead to beam stalling.

The design and optimization of this type of thrusters leans on the already existent flight experience and *ad hoc* experiments or tests. Yet, the iterative design process cannot uniquely rely on expensive experiments, in terms of both time and money. Instead, computer simulations, providing a mean to understand the underlying plasma physics, appear as a must in the design and characterization process. The design and operation parameters that plasma simulations must be capable of reproducing correctly are several: perveance, beam divergence angle, electron backstreaming voltage, beam flatness, efficiencies, etcetera [124]. This paper is focused on the first two, and also on the important phenomena of charge and current density neutralization in the very near-plume region.

The flight heritage and success of GITs has led to the development of numerous and miscellaneous tools for their ion optics and plume simulation. Among the different existing models to simulate the ion beam extraction, formation and neutralization, the most successful are hybrid models [125–127], based on particle-in-cell (PIC) modeling of the ions, and fluid modeling of the electrons. Yet, there exist also full-PIC codes attempting to overcome the inherent limitations of the electrons fluid modeling, with the corresponding computational burden [128, 129]. While simulations featuring a whole grid assembly [130] are relatively uncommon, most full-PIC codes normally consider a small, and yet significant, portion of the ion optics. Moreover, both 2D and 3D codes exist; while the former feature a reduced computational cost [131], the study of some important phenomena, such as the grids erosion with certain non axi-symmetric patterns, requires the use of 3D codes [127, 132]. Regarding the numerical schemes and meshing strategies, they vary from finite differences in a Cartesian mesh or in a octree mesh [133], to the IFE (Immersed Finite Elements) method [125]. Finally, diverse strategies are also observed in the treatment of neutrals, since their low speed does importantly delay reaching a stationary state, when modeled as macro-particles of the PIC model. Existing alternative approaches in the literature feature the use of a constant density background [134], the neutral density correction with Clausing factors [126], and also optical methods, based on view factors [135, 136].

In this paper, a 3D hybrid code named EP2PLUS (Extensible Parallel Plasma PLume Simulator) [100], is adapted to perform simulations on the formation and neutralization of an ion thruster beam. The code is capable of solving the non-linear Poisson's equation for the electric potential, as well as the electric current continuity and electron momentum balance equations, which enables the computation of the electric and electron current densities. Collisional and inertial effects on the electrons are retained in the model. A GIT grid with an infinite number of apertures, and a small GIT grid with a small number of apertures, are simulated and compared. Different aspects of the formation and neutralization of a GIT are explored with the simulations and contrasted with existing data: (i) the relation between perveance and divergence angle, (ii) the effect of the ion beamlet coalescence on near-plume properties and beam divergence, (*iii*) the comparison between infinite-apertures and finite-apertures simulations, (*iv*) the influence of electron inertia on the electron current, and (*v*) the influence of the neutralizer position on the electric current and charge neutralization phenomena. The 3D hybrid model is completed with a 1D semi-analytical model of the plasma plume allowing to characterize the far-plume expansion.

Regarding the structure of the paper, firstly both the PIC and the electron fluid models are presented in Sec. 2.2; the boundary conditions for the PIC and electron models are introduced respectively in Sec. 2.2.1 and 2.2.1, while the relevant model parameters are shown in Sec. 2.2.1. Infinite and finite-apertures simulations are presented in respectively Secs. 2.3 and 2.4. Electron inertial effects are specifically treated in Sec. 2.3.1. The semi-analytical 1D model is described in Sec. 2.5. Then, both numerical approaches and the 1D model are compared, and a comparison of the simulation results to experimental data, in terms of the divergence angle, is presented in Sec. 2.6. Finally, the main conclusions are summarized in Sec. 2.7.

2.2 3D hybrid model

EP2PLUS is a 3D hybrid code, in which ions and neutrals (heavy species) are treated as macro-particles within a PIC formulation and electrons are treated with a fluid model. So called I- and E-modules take care, respectively of these models. The physical domain is discretized based on a single structured mesh.

Regarding the PIC formulation, the reader is referred to Ref. [100] for a detailed description of the algorithms used. Here, only two heavy populations are considered: singly-charged Xe ions and Xe neutrals, and collisions between heavy species are neglected, since grid erosion is out of the scope of this work [134]. Finally, the heavy species bulk properties, like density and fluid velocities, are obtained at the structured mesh nodes, through a standard first-order weighting algorithm.

The E-module incorporates the electron fluid model and the Gauss law, and solves for the electron density (n_e), temperature (T_e), current density ($\boldsymbol{j}_\mathrm{e} = -en_\mathrm{e}\boldsymbol{u}_\mathrm{e}$), and the electric potential field (ϕ); the electric field $\boldsymbol{E} = -\nabla\phi$ is necessary to move the ion macro-particles. In fact, as shown in Fig. 2.1 (a), the E-module distinguishes between two electron populations: one inside the discharge chamber ($j = 1$), and one in the plume ($j = 2$), effectively separated by the large electric potential well (compared to the electron temperature) that forms around the acceleration grid and prevents most electrons from traversing the inter-grid region.

The system of equations for electrons is [100]:

$$0 = \nabla \cdot (\boldsymbol{j}_\mathrm{e} + \boldsymbol{j}_\mathrm{i})\,, \tag{2.1}$$

$$0 = -\nabla(n_\mathrm{e}T_e) + en_\mathrm{e}\nabla\phi + \frac{m_\mathrm{e}\nu_\mathrm{e}}{e}(\boldsymbol{j}_\mathrm{e} + \boldsymbol{j}_\mathrm{c}) - m_\mathrm{e}\nabla\cdot(n_\mathrm{e}\boldsymbol{u}_\mathrm{e}\boldsymbol{u}_\mathrm{e}) \tag{2.2}$$

$$T_e/n_e^{(\gamma-1)} = \mathrm{const} \tag{2.3}$$

$$\nabla^2\phi = \frac{e}{\epsilon_0}(n_\mathrm{e} - n_i)\,, \tag{2.4}$$

Here most of the symbols are conventional. All heavy-species magnitudes, such as densities and fluid velocities (n_s and $\boldsymbol{u}_s$) are provided by the I-module. In the electron momentum equation (2.2): $m_\mathrm{e}\nu_\mathrm{e}\left(\boldsymbol{j}_e + \boldsymbol{j}_c\right)/e$ is the resistive force between electrons and heavy species, with $\nu_e = \sum_{s\neq e}\nu_{\mathrm{e}s}$ the total electron collision frequency, $\nu_{\mathrm{e}s}$ the collision frequency between electrons and the s^{th} heavy species (neutrals or ions), and $\boldsymbol{j}_\mathrm{c} = en_\mathrm{e}\sum_{s\neq\mathrm{e}}(\nu_{\mathrm{e}s}/\nu_\mathrm{e})\boldsymbol{u}_s$ a collision-based current density from heavy species. The last term of Eq. (2.2) is the electron inertia, which, as shown in Sec. 2.3.1, is generally non-negligible and will be treated in an iterative way.

Equation 2.3 is a polytropic closure of the electron fluid model with the constant polytropic index γ equal or larger than 1. This closure allows us to introduce a barotropic function h_e, whose gradient $\nabla h_\mathrm{e} = \nabla(n_\mathrm{e}T_\mathrm{e})/n_e$ is an exact differential that can be integrated yielding [73]

$$h_\mathrm{e}(n_\mathrm{e}) = \begin{cases} h_{\mathrm{e}j} + T_{\mathrm{e}j}\ln\dfrac{n_\mathrm{e}}{n_{\mathrm{e}j}}, & \text{for } \gamma = 1 \\ h_{\mathrm{e}j} - \dfrac{\gamma T_{\mathrm{e}j}}{\gamma-1}\left[1 - \left(\dfrac{n_\mathrm{e}}{n_{\mathrm{e}j}}\right)^{\gamma-1}\right], & \text{for } \gamma > 1 \end{cases} \tag{2.5}$$

where, for each j^{th} electron population, the constant $h_{\mathrm{e}j}/e$ represents the electric potential at the reference point of that population, where the electron density and temperature are respectively $n_{\mathrm{e}j}$ and $T_{\mathrm{e}j}$. Numerically, at the separation plane between populations, both the electron density and temperature are discontinuous and this produces a small discontinuity in the barotropic function h_e, which however has no significant physical consequences, given the vanishing value of the electron density there.

As the plasma is weakly collisional, the two dominant terms in the electron momentum equation are the electric force and the pressure gradient. If the small resistive and inertial forces were both dropped in that equation, a Boltzmann relation between n_e and ϕ would be obtained, but the resulting model would not allow to compute $\boldsymbol{j}_\mathrm{e}$ from the electric current continuity equation alone. Ref. [103] defined the so-called thermalized potential Φ, whose gradient is $\nabla\Phi = \nabla\phi - \nabla h_\mathrm{e}/e$, so that:

$$\Phi = \Phi_j + \phi - h_e/e \tag{2.6}$$

where Φ_j is the thermalized potential value at the reference node of the j^{th} electron population. In terms of Φ, Eqs. 2.1 and 2.2 become:

$$\sigma_\mathrm{e}\nabla^2\Phi + \nabla\Phi\cdot\nabla\sigma_\mathrm{e} = \nabla\cdot(\boldsymbol{j}_\mathrm{i} - \boldsymbol{j}_\mathrm{c} + \boldsymbol{j}_{\mathrm{iner}}), \tag{2.7}$$

$$\boldsymbol{j}_\mathrm{e} = -\sigma_\mathrm{e}\nabla\Phi - \boldsymbol{j}_\mathrm{c} + \boldsymbol{j}_{\mathrm{iner}}, \tag{2.8}$$

where $\sigma_\mathrm{e} = e^2 n_\mathrm{e}/m_\mathrm{e}\nu_\mathrm{e}$ is the electron conductivity, and

$$\boldsymbol{j}_{\mathrm{iner}} = (e\nu_\mathrm{e})^{-1}\nabla\cdot(\boldsymbol{j}_\mathrm{e}\boldsymbol{j}_\mathrm{e}/n_\mathrm{e}) \equiv (e\nu_\mathrm{e})^{-1}\nabla\cdot(n_\mathrm{e}\boldsymbol{u}_\mathrm{e}\boldsymbol{u}_\mathrm{e}) \tag{2.9}$$

is an equivalent current accounting for inertia effects. Neglecting collisional effects yields $\sigma_\mathrm{e}\to\infty$ and $\nabla\Phi\to 0$ and, as anticipated, $\boldsymbol{j}_\mathrm{e}$ cannot be solved for. Eqs. 2.4, 2.6, 2.7, and 2.8 complete the mathematical model for ϕ, n_e, Φ, and $\boldsymbol{j}_\mathrm{e}$ to be solved here. Notice that

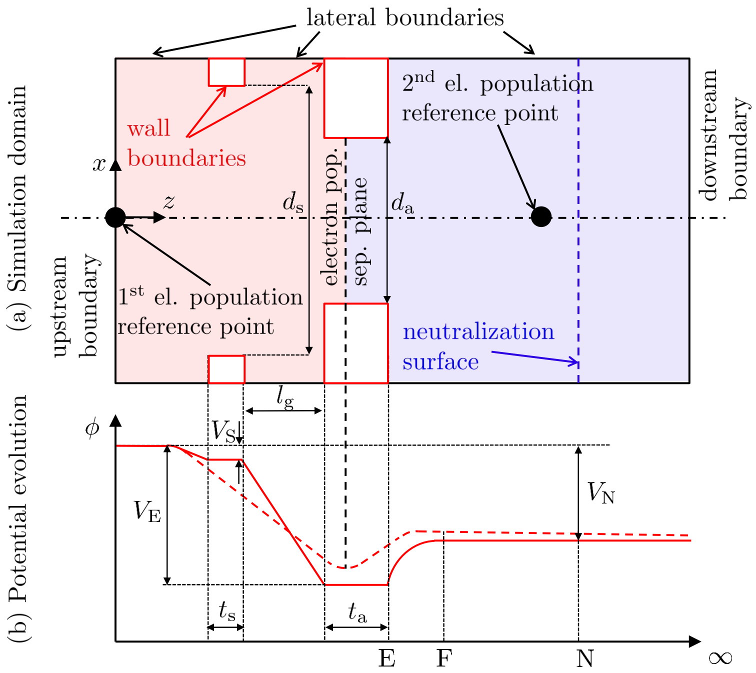

Figure 2.1: (a) 2D schematic view of the simulation setup and (b) expected evolution of the electric potential along the beamlet centerline (dashed line) and across the grids (solid line). In subplot (a), the two electron populations domains are highlighted in different shaded colors. The geometric magnitude of the grids used in the 2D simulations are $d_s = 2$mm, $t_s = 0.4$mm, $d_a = 1.2$mm, $t_a = 0.8$mm, $l_g = 2$mm, and the distance between hole centers, d_{hc}, is 2.8mm. In subplot (b), point F is the sheath edge defined in the 1D semi-analytical model.

the plasma is considered to be non-neutral and that the electron density is a function of the electric potential through Eq. 2.6, thus making Eq. 2.4 a non-linear Poisson's equation. For the isothermal case ($\gamma = 1$) considered here (except in the 1D model of Sec. 2.5), one has

$$n_{\mathrm{e}}(\phi, \Phi) = \hat{n}_{\mathrm{e}j} \exp\left(\frac{e(\phi - \Phi)}{T_{\mathrm{e}j}}\right), \tag{2.10}$$

where $\hat{n}_{\mathrm{e}j} = n_{\mathrm{e}j} \exp[(e\Phi_j - h_{\mathrm{e}j})/T_{\mathrm{e}j}]$. Although by keeping $\nu_{\mathrm{e}} \neq 0$ the electron current density can be determined, still $\nabla\Phi \ll \nabla\phi$, and the correction provided by $\nabla\Phi$ to the Boltzmann relation is rather marginal.

The two elliptic equations 2.4 and 2.7 for ϕ and Φ are coupled through the electron density $n_{\mathrm{e}}(\phi, \Phi)$, while Eq. 2.8 is used to determine the electron current density. Nonetheless, for numerical simplicity, these two equations are not solved simultaneously: Eq. 2.7 is solved first to obtain Φ, assuming the electron density of the previous time step, and then, after updating Φ, Eq. 2.4 is solved to update the values of ϕ and $n_{\mathrm{e}}(\phi, \Phi)$. We underline that this numerical approach does not affect the stationary solution.

Both elliptic equations are solved by discretizing the differential operators in a structured mesh with second order schemes, and with the boundary conditions for ϕ and Φ

described in Sec. 2.2.1. Ref. [100] describes in detail the iterative approach followed to solve the non-linear Poisson's equation. The only difference here is that the position of the separation plane between the two electron populations is actively controlled to be always at the electric potential minimum found along the beamlet centerline, as also shown in Fig. 2.1 (b). This enhances the solver convergence, without the need of linearizing the exponential dependence of the electron density on the electric potential for $\phi > h_{\mathrm{e}j}/e$, as done by several codes in the literature [126, 128].

The equation for Φ, Eq. 2.7, is also solved iteratively, given its non-linearity due to the inertial term on its right-hand side, which is a function of Φ (through $\boldsymbol{j}_{\mathrm{e}}$). In particular, the following steps are followed. In the first iteration, the inertia term is neglected and a first solution for $\boldsymbol{j}_{\mathrm{e}}$ is computed, whence a first guess for $\boldsymbol{j}_{\mathrm{iner}}$. In the following steps, a growing percentage of the inertia current density $\boldsymbol{j}_{\mathrm{iner}}$ (from 0 to 100%) is applied as an additional right hand side in both Eqs. 2.7 and 2.8. The inertial current density is always computed from the solutions for Φ and $\boldsymbol{j}_{\mathrm{e}}$ of the latest iteration. The progressive inclusion of the inertial current density is necessary to achieve a good convergence of the solver, since the inertial term can be the dominant term in Eq. 2.2 in certain regions of the simulation domain, especially where the radius of curvature of the electron streamlines happens to be very small.

2.2.1 Boundary conditions and model parameters

PIC model boundary conditions

The boundary conditions for the ion and neutral macro-particles are shown in Fig. 2.1 (a). From the upstream boundary, located inside the discharge chamber, ions and neutrals are injected thermally, thus simulating the incoming particle flux from the inner ionization chamber (many simulation codes assume a sonic ion injection here, thus missing the pre-sheath formation [128, 137]). At the material wall boundaries of the screen and acceleration grids, neutral macro-particles are reflected diffusely and ions are recombined into neutrals, and re-injected into the domain following a Lambertian emission law [138] with full energy accommodation with the wall. Then, when neutrals or ions reach the lateral external boundaries, they are either specularly reflected (in infinite-apertures simulations) or simply removed (in finite multi-apertures simulations). In the former case, the specular reflection simulates the symmetric interaction of the simulated beamlet with the surrounding ones of the grid, while in the latter case, the lateral boundary is an open free loss surface, transparent to macro-particles. Finally, macro-particles are always removed from the domain when they cross the downstream boundary.

Electron model boundary conditions

In order to solve the differential equations 2.4 and 2.7, appropriate boundary conditions for both ϕ and Φ must be implemented. Referring to Fig. 2.1, the following boundary conditions are applied on ϕ to solve Poisson's equation:

- Reference points of the electron populations. At the 1$^{\text{st}}$ population reference point, ϕ is set to 0. At the 2$^{\text{nd}}$ population reference point, ϕ is set equal to $-V_{\mathrm{N}}$, which is the net acceleration voltage of the beam. At these two points, the local electron density is also specified assuming quasineutrality: $n_\mathrm{e} = n_\mathrm{e}^* = n_\mathrm{i}$, with n_i given by the I-module.

- Material grid boundaries. The value of ϕ is set equal to the electric potential of either the screen or acceleration grid, respectively. Therefore, referring to Fig. 2.1 (b), the screen grid walls are at the potential $\phi = -V_\mathrm{S}$, while at the acceleration grid $\phi = -V_\mathrm{E}$.

- Upstream, downstream and lateral boundaries. A zero normal electric field is applied.

Introducing a normal unit vector $\mathbf{1}_\mathrm{n}$ at the simulation boundaries directed towards the plasma, the boundary conditions for Φ are then the following:

- Neutralization surface plane. A Dirichlet condition $\Phi = \mathrm{const}$ is applied, which means that the electron current density in the direction normal to the neutralizer is left free.

- Material grids boundaries. A thermal electron flux is imposed, that is: $\boldsymbol{j}_\mathrm{e} \cdot \mathbf{1}_\mathrm{n} = j_\mathrm{e,th} = e n_\mathrm{e}\sqrt{T_\mathrm{e}/(2\pi m_\mathrm{e})}$, which is equivalent to the non-homogeneous Neumann condition
$$\frac{\partial \Phi}{\partial \mathbf{1}_\mathrm{n}} = -\frac{(\boldsymbol{j}_\mathrm{c} - \boldsymbol{j}_\mathrm{iner}) \cdot \mathbf{1}_\mathrm{n} + j_\mathrm{e,th}}{\sigma_e}. \tag{2.11}$$

- Upstream, downstream and lateral boundaries. A zero normal electric current density is assumed: $(\boldsymbol{j}_\mathrm{e} + \boldsymbol{j}_\mathrm{i}) \cdot \mathbf{1}_\mathrm{n} = 0$, which means
$$\frac{\partial \Phi}{\partial \mathbf{1}_\mathrm{n}} = \frac{\boldsymbol{j}_\mathrm{i} - \boldsymbol{j}_\mathrm{c} + \boldsymbol{j}_\mathrm{iner}}{\sigma_e} \cdot \mathbf{1}_\mathrm{n}. \tag{2.12}$$

Model parameters

The presented 3D model features a certain number of parameters, which belong to two categories: fixed parameters that are not varied in the study, and variable parameters that are modified in certain simulations to investigate their effect (parametric analysis).

Referring to Fig. 2.1 (a), the grids geometry is defined by specifying the diameter $d_\mathrm{s} = 2$ mm of the screen grid holes, the diameter $d_\mathrm{a} = 1.2$ mm of the acceleration grid holes, the distance $d_\mathrm{h} = 2.8$ mm between the centers of two neighbouring holes at the screen grid (which is uniform, given the hexagonal holes distribution), the thickness $t_\mathrm{s} = 0.4$ mm and $t_\mathrm{a} = 0.8$ mm of respectively the screen and acceleration grids, and the distance $l_\mathrm{g} = 2$ mm between the screen and acceleration grids. These geometric parameters are kept constant in all simulations. Moreover, the problem geometry is completely specified by providing the position of the neutralizer surface and its size. In particular, this either occupies the full cross-section (at a constant axial coordinate z) of the simulation domain, like in the case of infinite apertures simulations, or just represents a small emission surface on the lateral boundary of the simulation domain, like in the case of the finite-apertures simulations. Two different axial positions of the neutralizer are considered in both infinite (15, 30 mm) and finite-apertures (15, 20 mm) setups.

Still referring to Fig. 2.1 (b), the applied voltages are V_{E} (electric potential difference between the discharge chamber plasma and the acceleration grid), V_{S} (potential difference between the discharge chamber plasma and the screen grid), and V_{N}, which fixes the total potential drop between the discharge chamber and the external cathode. These voltages are kept fixed in all simulations.

Regarding the electrons, the only parameters required by the model are the electron temperatures T_{e1} and T_{e2} of respectively the discharge chamber and plume populations. The Xe neutrals, which affect only the electron collision frequency, are injected with a constant thermal flux and temperature from the discharge chamber, and, for finite-apertures simulations, also from the neutralizer surface. For what concerns the ions, they are injected from the discharge chamber by providing the value of their injection temperatures and fluxes. While the former are kept constant, the latter are varied between simulations: an increase of the injected ion mass flow per hole produces a larger beamlet current i_{b}. A relevant parameter that is related to this, is the normalized perveance per hole, Π, which is defined as [139]:

$$\Pi = \frac{i_{\mathrm{b}}}{V_{\mathrm{E}}^{3/2}} \left[\left(\frac{l_{\mathrm{g}}}{d_{\mathrm{s}}} \right)^2 + \frac{1}{4} \right] \frac{V_{\mathrm{E},0}^{3/2}}{i_{\mathrm{b},0}} \tag{2.13}$$

where $V_{\mathrm{E},0} = 1000$ V, $i_{\mathrm{b},0} = 10^{-4}$ A are the reference voltage and current values. The normalized perveance per hole (herefater, the perveance) permits us to assess the influence of space charge effects, relative to the influence of the grid assembly electrical properties, on the extraction process. A relatively large value of Π leads to an under-focused beam, whereas a small value creates an over-focused beam with ion crossover trajectories [124]. The variation of the ion mass flow per hole commented above results in a variation of Π across different simulations.

Finally, the interaction between ions/neutrals and the material walls of the ion grid optics requires the definition of two additional parameters that are the accommodation coefficient α_{W} for both neutral reflection and ion recombination (refer to Ref. [100] for a detailed description of the model), and the walls temperature T_{W}. Both parameters are kept constant in all considered simulations.

2.3 2D case: grid with infinite apertures

The main simulation and geometric parameters considered for this case are shown in Tab. 2.2.1. As mentioned in Sec. 2.2.1, several simulations are performed by varying the value of the ion flux injected upstream, and hence the perveance. The simulation setup, depicted in Fig. 2.1 (a), consists of a single aperture with specular reflection conditions for the heavy species at the lateral boundaries, which reproduce the interaction with an infinite number of surrounding beamlets. The net acceleration voltage is set to 770 V, while the acceleration grid potential with respect to the ionization chamber plasma is -1100 V. Ions and neutrals are injected thermally from the upstream boundary, with a

Parameters	**Units**	**Infinite apertures**	**Finite apertures**
Number of apertures simulated	(-)	1	19
Domain physical size (x, y, z)	mm	[2.8,2.8,30]	[20,24.4,30]
Neutralizer center position (x, y, z)	mm	[0,0,14.8-30]	[0,14,14.8-20]
Chamber electron temperature, T_{e1}	eV	3.5	
Plume electron temperature, T_{e2}	eV	2.0	
Acceleration grid voltage, V_{E}	V	1100	
Cathode voltage, V_{N}	V	770	
Screen grid voltage, V_{S}	V	15	
Inflow Xe^+ temperature	eV	0.04	
Inflow Xe^+ mass flow per hole	μg/s	[0.07-0.34]	[0.18-0.92]
Inflow Xe mass flow per hole	μg/s	[0.007-0.034]	[0.018-0.092]
Neutralizer Xe mass flow	μg/s	0.0	0.001
Normalized perveance Π per hole	(-)	[0.28-0.94]	
Upstream plasma density, n_{e1}	m^{-3}	[26.0-124.3]$\cdot 10^{15}$	
Downstream plasma density, at neutralizer center, n_{e2}	m^{-3}	[1.1-2.4]$\cdot 10^{15}$	$6.5\cdot 10^{14}$
Grids material temperature, T_{W}	K	500	
Accommodation coefficient, α_{W}	(-)	1.0	

Table 2.1: Simulation parameters for both infinite and finite-apertures simulations. The upstream and downstream plasma densities represent the electron number densities at the reference points of the upstream and downstream electron populations. Voltage values represent the electric potential drop from the upstream chamber plasma.

temperature of 0.04 eV [140], and no gas is injected from the neutralizer surface downstream. The electron temperature of the source electrons is 3.5 eV, while the neutralizer electron temperature is 2 eV [140, 141].

Figs. 2.2 (a) to (c) show the contour map of the ion density at $x = 0$ for three different values of Π. As expected, the focusing of the ion beamlet decreases when the perveance grows. Indeed, when the perveance is the highest, Fig. 2.2 (c), meaning that space charge effects dominate over the grids electric influence, peripheral density peaks can be spotted, because the beam is under-focused. On the contrary, when the perveance is the lowest, Fig. 2.2 (a), the beamlet features a centered density peak in the inter-grid region, which is due to crossover trajectories: the beamlet is over-focused. These considerations are confirmed in Figs. 2.2 (d) to (f), showing the individual ion trajectories: in the lower perveance cases (d) and (e), some cross-over trajectories can be spotted, while in the highest perveance case, there is a non-negligible number of ions that hit the acceleration grid. The reason behind the under-focusing and over-focusing can be better appreciated

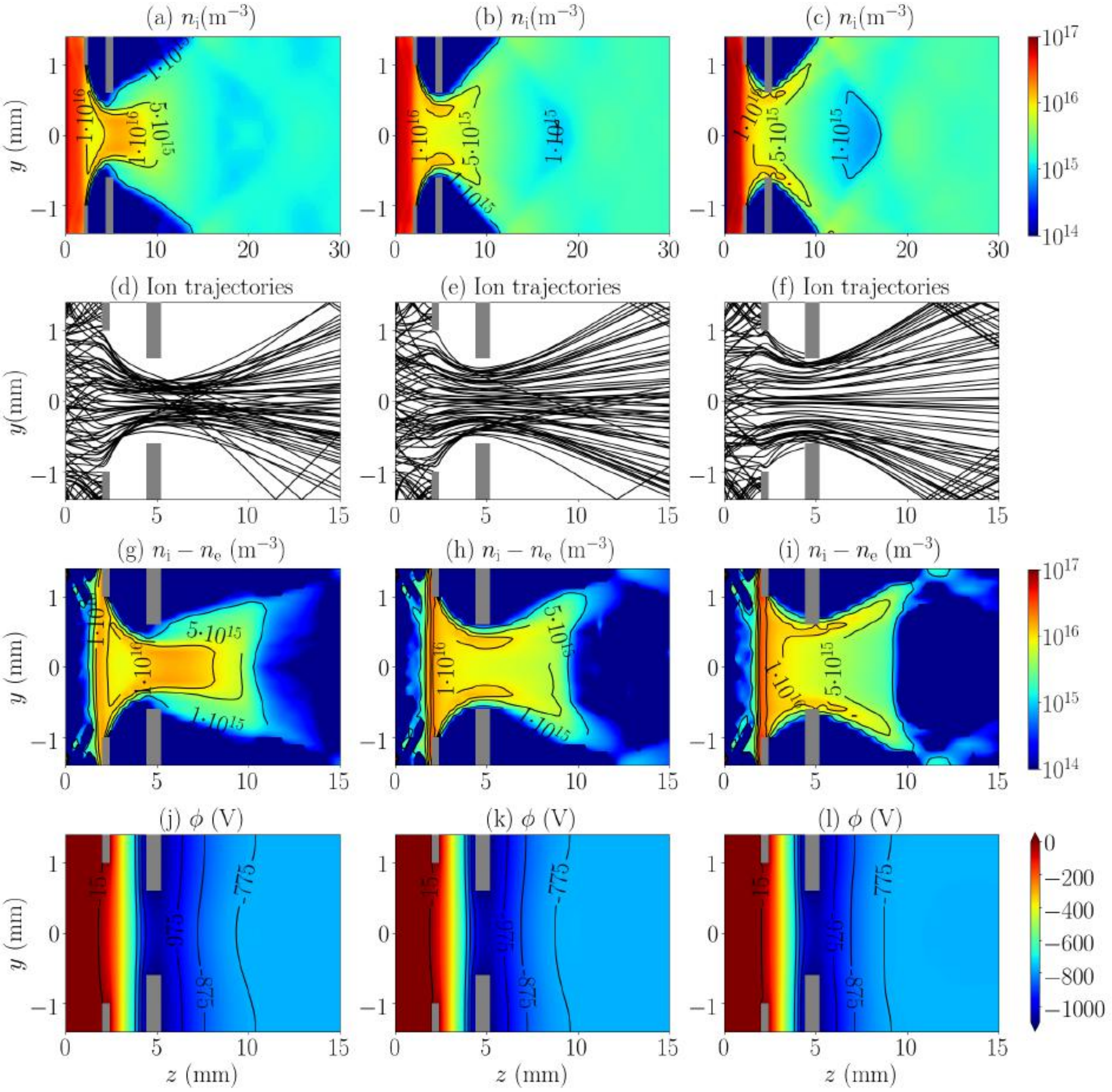

Figure 2.2: (a,b,c) Ion density n_i, (d,e,f) ion macroparticle trajectories, (g,h,i) $n_\mathrm{i}-n_\mathrm{e}$ and (j,k,l) electric potential ϕ (zoomed in, around the grid assembly), at $x=0$, for different values of the normalized perveance per hole: $\Pi = 0.60$ (a, d, g, j), 0.83 (b, e, h, k), and 0.94 (c, f, i, l).

in Figs. 2.2 (g) to (i), and (j) to (l), showing respectively the difference between ion and electron density (thus proportional to the charge density), and the electric potential, in a region close to the grids assembly. Although ϕ eventually tends to the imposed value of $-V_\mathrm{N}$, the curvature of its iso-lines and hence the radial electric field is strongly affected by the perveance. Indeed, both the upstream and downstream isolines are more curved when Π is lower, because plasma space charge effects are less relevant. The curvature of the electric potential iso-lines or, equivalently of the extraction sheath, is directly related to the beamlet divergence. When the curvature is excessive/too low, the beamlet becomes over-focused/under-focused and an increase in divergence is always observed. The intermediate perveance case of Fig. 2.2 represents an optimal one, minimizing the divergence angle. This behavior can be appreciated in Fig. 2.16, showing the evolution of the divergence angle with the normalized perveance (square markers line), and it agrees well with the results found in literature [125, 126].

The ion, electron, and electric current density and streamlines are then displayed in Fig. 2.3 for $\Pi = 0.83$. As expected, the ion current density is largest at the acceleration

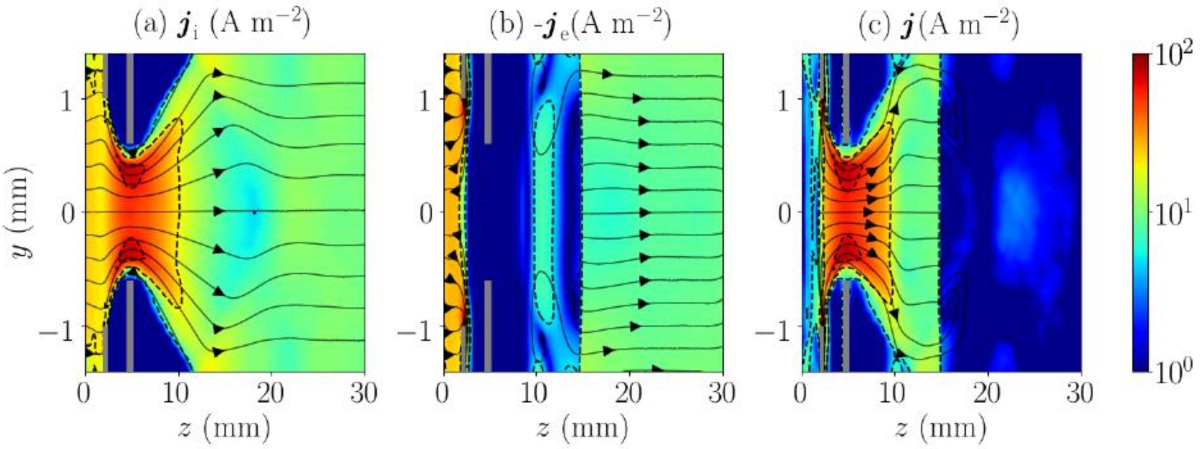

Figure 2.3: (a) Ion current density, (b) electron current density and (c) electric current density at the $x = 0$ plane, for $\Pi = 0.83$. Contour levels (dashed lines) and current streamlines (solid lines) are displayed.

grid position, where the focusing is the highest, and downstream tend to become parallel to the lateral simulation boundaries, due to the influence of the surrounding ion beamlets. The electron current density is negligible in the inter-grids region, due the screening action of the grids electric potential, so electrons barely travel through the grids. The electrons injected into the domain at $z = 0$ only travel towards the screen grid, so that $\boldsymbol{j}_e$ originates there and travels upstream inwards. The electrons emitted at the current neutralization surface, on the other hand, flow downstream to neutralize the ion beam. The resulting electric current streamlines are shown in Fig. 2.3 (c). They originate at the screen grid, flow through the grids, and disappear almost completely at the neutralizer plane.

It is important to remark here that $\boldsymbol{j}_e$ is obtained through the gradient of Φ, with Eq. 2.8. Small variations of the thermalized potential, of the order of mV, are sufficient to produce the observed $\boldsymbol{j}_e$. Therefore, the influence of Φ on Poisson's equation is negligible. Yet, the fact that the gradients of Φ and ϕ differ by several order of magnitudes does not mean that the problem of determining Φ and ϕ is ill-conditioned. In fact, Φ is directly solved for with Eq. 2.7. In this equation, the thermalized potential, and hence the electron current density, are well determined, except when $n_\mathrm{e} = 0$, or, equivalently, $\sigma_\mathrm{e} = 0$. A minimum σ_e is therefore used to avoid this numerical problem.

Fig. 2.4 shows the relative space charge of the plasma, $|n_\mathrm{i} - n_\mathrm{e}|/n_\mathrm{i}$, for two different positions of the current neutralization plane (where the reference point for the downstream

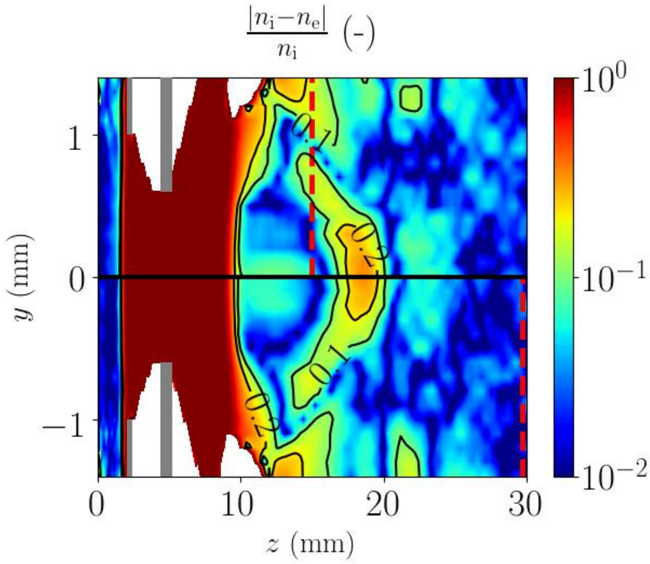

Figure 2.4: Comparison of the simulations with the neutralization surface in the position indicated in Tab. 2.2.1 (upper part of the subplots) and the neutralization surface shifted downstream to the boundary (lower part), for the same perveance case, $\Pi = 0.83$. The grey dashed lines indicate the position of the neutralization surface.

electrons population is also located). The non-neutral region is clearly not affected by the position of the neutralization surface, provided that this is located sufficiently downstream, where the plasma is essentially quasineutral. This is the consequence of the fact that the electric potential downstream is only weakly affected by this shift. On the other hand, the electric current neutralization is achieved only at the neutralization plane, as shown in Fig. 2.3 (c). This indicates that the neutralization surface position only affects significantly the current neutralization phenomena and the electric current streamlines, provided that the neutralizer is emplaced properly, i.e. it is not too far from the acceleration grid (otherwise beam stalling is expected to occur).

The extension of the space charge region downstream of the acceleration grid, $z_F - z_E$, is then shown in Fig. 2.5, as a function of the normalized perveance per hole, for both the infinite apertures (black line, square markers) and finite-apertures (blue line, triangle markers) simulations. Such a space charge extension is conventionally defined as the axial length of the region where $|n_i - n_e|/n_i > 0.1$, although farther downstream the neutrality ratio can increase again due to beamlets coalescence effects, as seen in Fig. 2.4. The infinite apertures simulations feature nearly the same space charge extension as the finite-apertures simulations, which have a very different neutralizer position, as described in Sec. 2.4, thus confirming the fact that the cathode location does not affect importantly the charge neutralization physics.

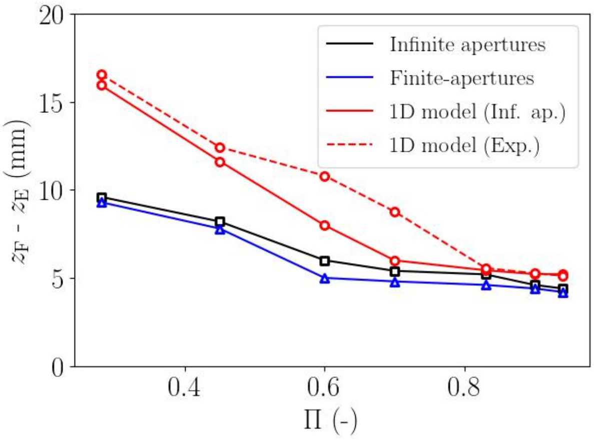

Figure 2.5: Evolution of the downstream sheath axial extension, $z_{\mathrm{F}} - z_{\mathrm{E}}$, as a function of Π, for infinite apertures (black line, square markers) and finite-apertures (blue line, triangle markers) simulations, and for the 1D model (red lines, circle markers). For the latter, the considered beam area function assumes two different divergence angle evolutions $\alpha(\Pi)$: one taken from the infinite apertures simulations (solid line) and another one from experimental measurements (dashed line).

2.3.1 Electron inertia effects

Results shown so far include the effects of the electron inertia in the momentum equation, Eq. 2.2, or the equivalent Ohm's law, Eq. 2.8. This last one can be expressed as the balance,

$$\sigma_{\mathrm{e}} \left(\nabla \phi - \nabla p_{\mathrm{e}} / (e n_{\mathrm{e}}) \right) + (\boldsymbol{j}_{\mathrm{c}} + \boldsymbol{j}_{\mathrm{e}}) - \boldsymbol{j}_{\mathrm{iner}} = \mathbf{0} \tag{2.14}$$

for electrons, among (i) the combination of pressure and electric forces, (ii) the resistive force, and (iii) the inertial force. The inclusion of $\boldsymbol{j}_{\mathrm{iner}}$ has been done through a time-consuming iterative scheme, explained before, the first step corresponding to $\boldsymbol{j}_{\mathrm{iner}} = \mathbf{0}$.

Fig. 2.6 (a)-(h) compares, for the case $\Pi = 0.83$, the terms in Eq. 2.14 and the resulting $\boldsymbol{j}_{\mathrm{e}}$ (obtained including or neglecting the electron inertia), inside the discharge chamber (subplots (a) to (d), with the grey rectangle representing the screen grid) and downstream of the neutralization plane (subplots (e) to (h), with the dashed grey line representing the neutralization plane).

The two first rows show that in both regions, inertia and resistivity are typically of the same order, so electron inertia should not be omitted, in principle, if the resistive force is kept in the momentum equation. It is also observed that inertia and resistivity force vectors are in the same direction within the discharge chamber, while they tend to oppose in the plume. The result of this is visible in the third row figures, showing $\sigma_e \nabla \Phi$. The last row of Fig. 2.6 shows the net effect of including inertia on $\boldsymbol{j}_{\mathrm{e}}$, which is not affected importantly, neither in magnitude nor in direction. This is because $\boldsymbol{j}_{\mathrm{e}}$ is rather constrained by the boundary conditions, and hence, from Eq. 2.14, the most affected term is the thermalized potential gradient, which changes to balance out the additional inertia term. This means that $\sigma_{\mathrm{e}} \nabla \Phi - \boldsymbol{j}_{\mathrm{iner}}$ is rather independent of $\boldsymbol{j}_{\mathrm{iner}}$. Yet, the effects of the

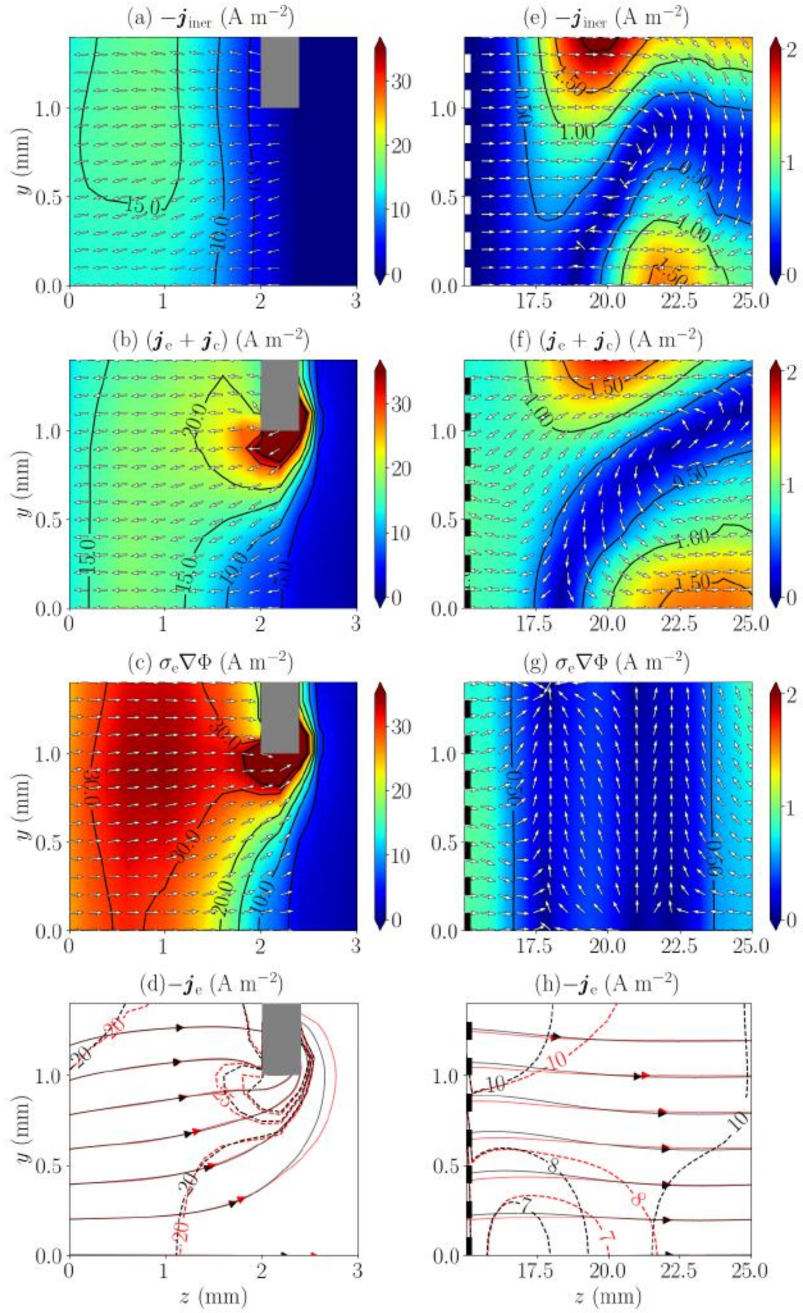

Figure 2.6: Comparison of magnitude and direction of the different terms of Eq. 2.14 for $\Pi = 0.83$: (a,e) inertial current density, (b,f) collisional force current density, and (c,g) current density associated to the thermalized potential gradient. Subplots (d,h) show the electron current density contour lines (dashed) and streamlines (solid) considering (red) or not (black) the electron inertia term. Results refer to the inside of the discharge chamber (a,b,c,d), and the plume region downstream of the neutralizer (e,f,g,h). In this latter region, the characteristic magnitude of the electron balance terms are one order of magnitude smaller than inside the chamber.

electron inertia are larger in the plume than in the discharge chamber and they tend to slightly reduce the spatial gradients and the curvature of the $\boldsymbol{j}_e$ streamlines. Finally, it is important to observe that, since $\nabla\Phi \ll \nabla\phi$, electron inertia and resistivity play no relevant role in determining the total electric field and the plasma density map.

2.4 3D case: Grids with finite apertures

The main simulation and geometric parameters considered for the finite-apertures simulations are shown in Tab. 2.2.1. Several simulations are carried out varying only the ion flux at the upstream boundary in order to assess the effect of a varying perveance. The simulation setup now consists in a whole grid assembly composed by a total of 19 hole-pairs, with square shape, forming a hexagonal pattern, as shown in Fig. 2.7, with the same grid layout as in Ref. [139]. The neutralizer is now located at $x = 0$, $z = 15$ mm, on the $y_{\max}$ lateral boundary, and has a square emission surface with 2mm side.

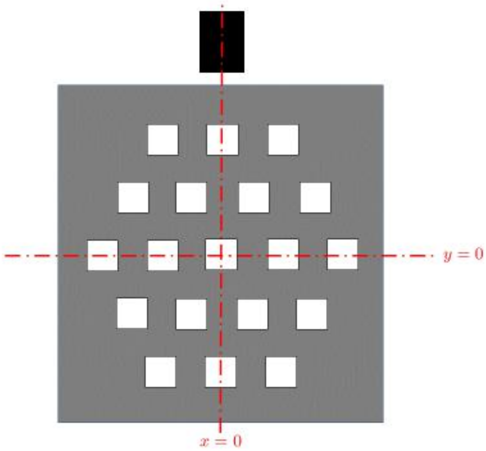

Figure 2.7: Schematic of the finite multi-apertures geometric setup. The neutralizer is actually located slightly downstream of the acceleration grid, as shown in Tab. 2.2.1.

Since the entire ion optics is simulated, the lateral boundaries in Fig. 2.1 are no more specular reflection surfaces, but simply free-loss ones (ions and neutrals traversing them are simply removed from the simulation). Moreover, the lateral walls of the ionization chamber are considered to be dielectric, thus featuring a zero normal electric current density.

In the following, results for an intermediate perveance case, $\Pi = 0.83$, are shown. Figs. 2.8 (a) and (b) show the ion density at respectively $x = 0$ and $y = 0$ while Figs. 2.8 (c) and (d) show ϕ at the same symmetry planes. The external cathode is displayed as a black rectangle, outside the computational domain, in Fig. 2.8 (b,d,f) (x=0 plane).

The formation of the ion thruster plume through the gradual coalescence of the individual beamlets into a singly-peaked plasma beam is observed just a few centimeters downstream the grids. This beam formation process occurs nearly symmetrically, around the thruster axis. Yet, a slight deviation from symmetry can be appreciated in Fig. 2.8

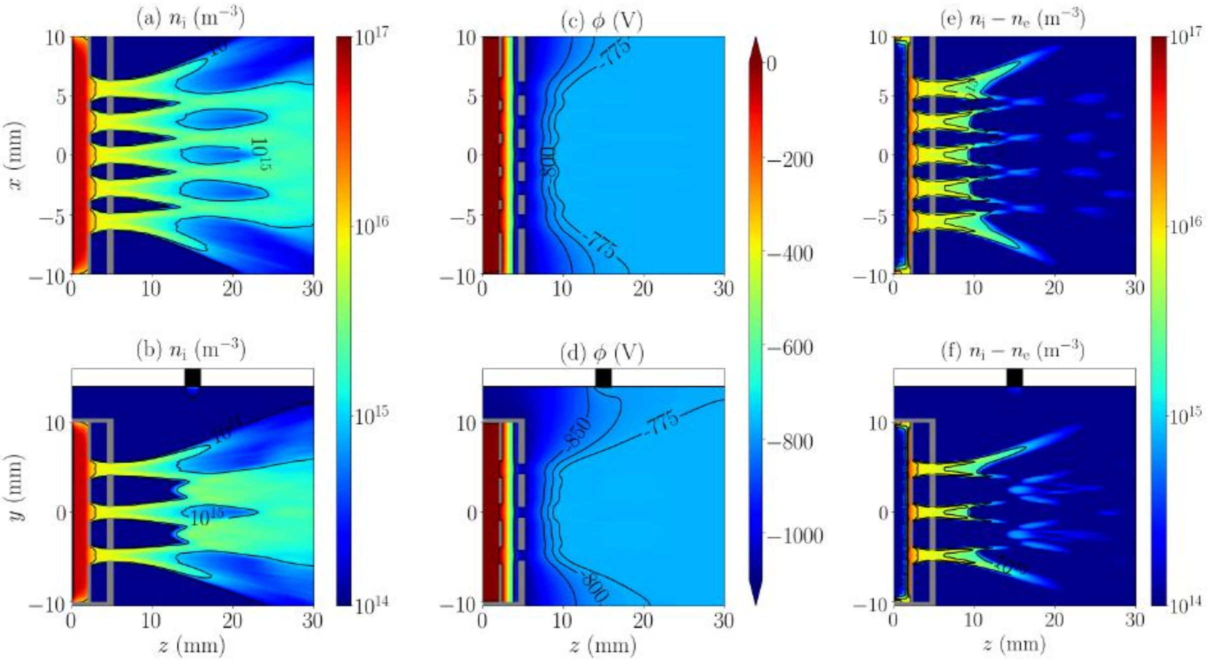

Figure 2.8: Ion density, electric potential and charge density at $y = 0$ (a, c, e), and $x = 0$ (b, d, f), for $\Pi = 0.83$.

(b) and more clearly in Fig. 2.8 (d). This is due to the presence of the cathode, which, in the considered simulation setup, is closer to the thruster than in a real scenario. For a more realistic cathode position, this disturbance is expected to be smaller. Figs. 2.8 (e) and (f) show the charge density at, respectively, $y = 0$ and $x = 0$. The central beamlets are charge-neutralized at the same distance from the acceleration grid, while boundary beamlets are neutralized slightly farther downstream. In any case, it is apparent that the charge neutralization process is almost symmetric and, thus, independent of the position of the cathode, as it will be confirmed later.

Fig. 2.9 (a) to (c) show the progressive beamlets coalescence and plume formation at increasing axial distances (12, 20 and 28 mm). At $z = 12$ mm, the beamlets have not coalesced yet and they are independent structures. Observe that their shape has become circular, in spite of the apertures being square in the present simulation, thus having short memory of its upstream extraction shape. At $z = 20$ mm, the beamlets have partially merged and finally, at $z = 28$ mm, the beamlets mixing process is almost complete and a single-peaked beam is emerging. An interesting final observation, referring to Fig. 2.8 (e) and (f), is that the beamlet coalescence process occurs when the plume is already charge-neutralized. In fact, charge neutralization is nearly complete at $z \simeq 10$ mm, while the beamlets interaction starts at higher downstream distances.

Fig. 2.10 shows the ion, electron and electric current density and streamlines at $x = 0$ (the cross-section containing the neutralizer) for the same perveance case. Referring to subplot (b), the electrons emitted by the cathode are observed to travel downstream to neutralize the ion beam, without backstreaming through the grids towards the ionization chamber. Inside the chamber, on the other hand, upstream electrons are collected by both

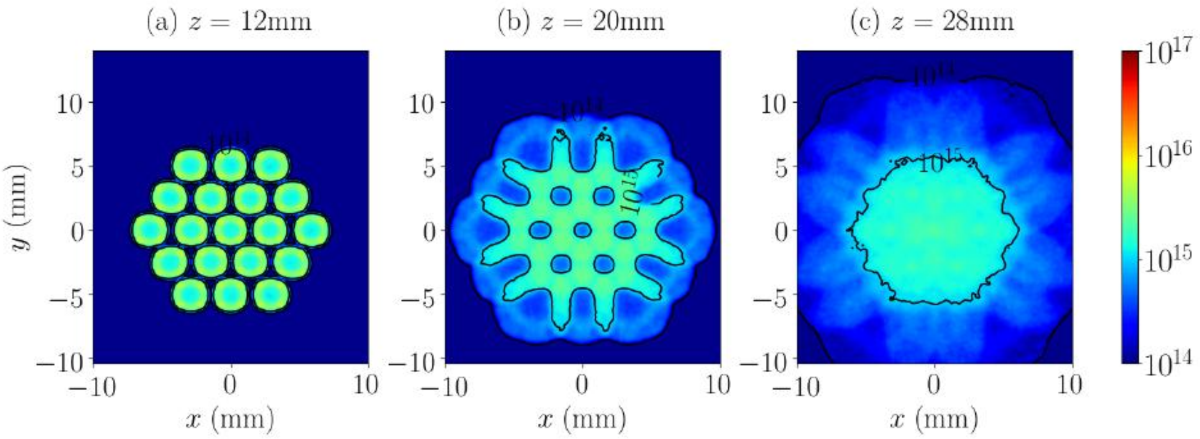

Figure 2.9: Ion density at different axial cross-sections, for $\Pi = 0.83$.

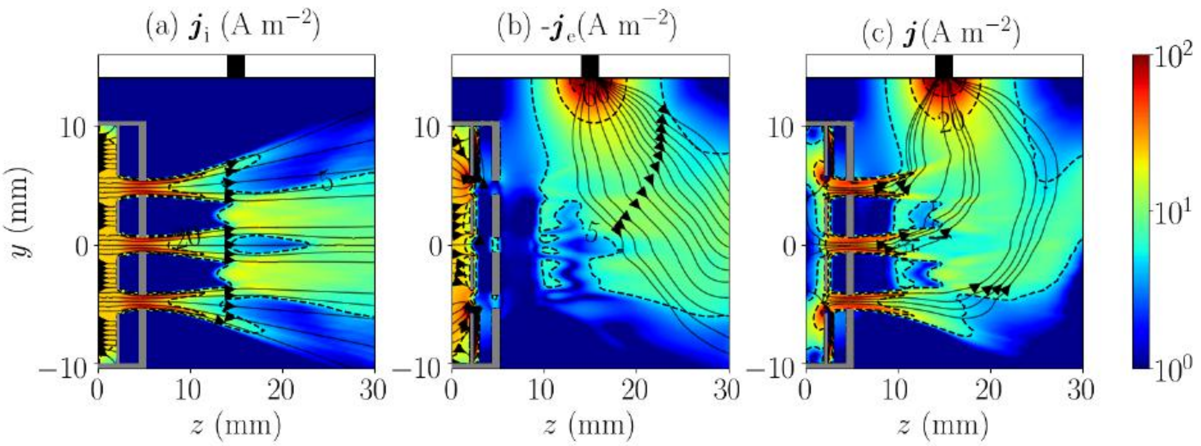

Figure 2.10: (a) Ion current density, (b) electron current density and (c) electric current density, with streamlines at $x = 0$, for $\Pi = 0.83$. Contour levels (dashed lines) and current streamlines (solid lines) are displayed.

the screen grid and the lateral thruster walls. Regarding the electric current (subplot (c)), this originates at the screen grid walls (which are an electron sink), it flows through the grids transported by the ions (subplot (a)) and is finally collected by the boundary cathode, which is an electron source. This electric circuit is completed by an external segment not shown here: the electrons collected by the screen grid are pushed towards the cathode by a "beam power" supply [142], where most of the operational thruster power is actually consumed.

Fig. 2.11 shows the ion density, the relative charge density and the electric current density at the same plane, $x = 0$, for a shifted neutralizer position. Comparing Fig. 2.11 (b) and Fig. 2.8 (f), it is clear that the charge neutralization process is nearly unaffected by the cathode position. This is not the case for the electric current neutralization. as seen by comparing Fig. 2.10 (c) and Fig. 2.11 (c): the closer the neutralizer is to the grids, the more upstream the beamlets become axially current-free. This can be considered to

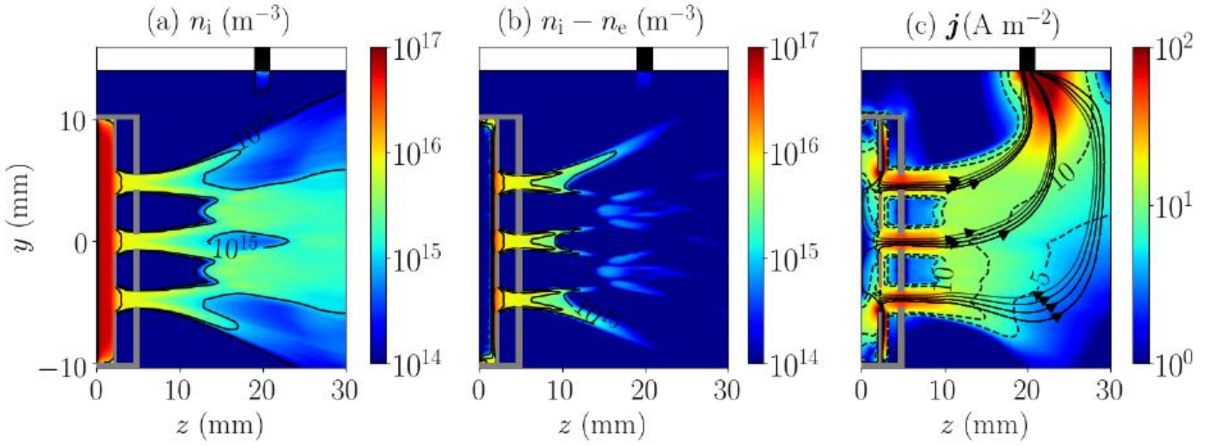

Figure 2.11: (a) Ion density, (b) charge density and (c) electric current density in the case of the cathode shifted downstream, for $\tilde{\Pi}_h = 0.83$. In (c), contour levels (dashed lines) and current streamlines (solid lines) are shown.

happen at the position where the electric current streamlines turn towards the cathode.

The observed difference between charge and current neutralization can be explained as follows. On one hand, the charge density depends on the local electron and ion densities, which are only dimly affected by the neutralizer position. In fact, the neutralizer affects the thermalized potential solution, whose gradient $-\nabla\Phi$ is negligible compared to the Boltzmann electric field $-\nabla p_e/(en_e)$. Therefore, the total electric field and hence the ion density are essentially symmetric with respect to the thruster centerline, as shown in Figs. 2.8 (a) and (b) and Fig. 2.11 (a). As a consequence, the electron number density is also symmetric, since it depends mainly on the electric potential, being $|\Delta\Phi| \ll |\Delta\phi|$ (see Eq. 2.10). On the other hand, the electron current density is ultimately determined by the asymmetric and small thermalized potential gradient $-\nabla\Phi$ (pre-multiplied by a large scalar conductivity σ_e), as shown in Eq. 2.8. Since the neutralizer is modeled as a Dirichlet surface for Φ, as explained in Sec. 2.2, both the thermalized potential and its gradient are strongly affected by the neutralizer position. This yields an asymmetric electron current density and neutralization, as shown in Fig. 2.10 (b), with an important role of the cathode position.

Finally, the effect of including the electron inertia on the $\boldsymbol{j}_e$ streamlines in this 3D case is shown in Fig. 2.12. As in the 2D case, electron inertia is a relevant contribution to the balance of Eq. 2.14, but this contribution is mostly compensated by an adjustment of $\nabla\Phi$ and the net effect on $\boldsymbol{j}_e$ is limited. Still, it is larger than the one shown in Fig. 2.6 (h) for the 2D case. When inertia is ignored, the electron streamlines that originate at the neutralizer surface tend to move near-vertically downwards until reaching the plume centerline, where they undergo an abrupt change in direction. This effect is visibly reduced when inertia is accounted for: lower spatial gradients in the electron current density and a lower curvature of the electron streamlines are appreciated.

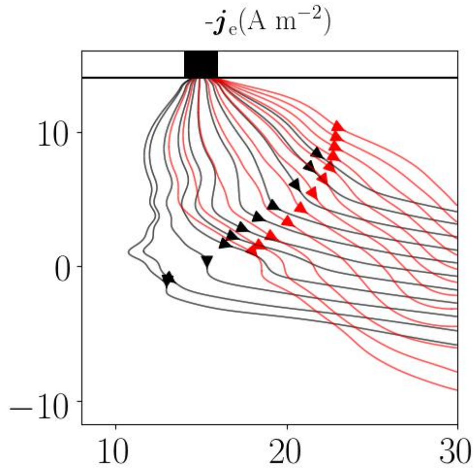

Figure 2.12: Effect of electron inertia on $\boldsymbol{j}_e$ streamlines. Red lines correspond to the full solution with electron inertia. Black lines correspond to the approximation without the contribution of electron inertia .

2.5 1D fluid model of the plume

To complement the previous 2D and 3D numerical models and extend them to the far downtream region, a 1D semi-analytical model of the plasma plume expansion, from the acceleration grid E, to infinity, is presented here. A sketch of the electric potential evolution considered for this 1D model is included in Fig. 2.13 (a).

Neutrals and collisional effects are neglected here. Ions are considered a highly supersonic population and their continuity and mechanical energy equations yield

$$u_\mathrm{i}(\phi) = \sqrt{u_\mathrm{iE}^2 - 2e(\phi - \phi_\mathrm{E})/m_\mathrm{i}} \tag{2.15}$$

$$n_\mathrm{i}(\phi, z) = \frac{I_\mathrm{i}}{eA(z)u_\mathrm{i}(\phi)}, \tag{2.16}$$

where the plume area variation $A(z)$, the total ion current I_i and the ion velocity at E, u_iE are known. The neutralizer N is modeled as a sheet, with a potential $\phi = \phi_\mathrm{N}$ and located at $z = z_\mathrm{N}$, and emits an electron current equal to I_i with a temperature T_eN. Electrons are assumed isothermal before the neutralizer, for $z < z_\mathrm{N}$, but they are considered polytropic (with $\gamma > 1$) in the downstream region $z > z_\mathrm{N}$ in order to reproduce the known far-plume cooling and to achieve a finite potential fall at infinity [73]. Thus their density satisfies

$$\frac{n_\mathrm{e}(\phi)}{n_\mathrm{eN}} = \begin{cases} \exp \dfrac{e(\phi - \phi_\mathrm{N})}{T_\mathrm{eN}} & , \quad \text{if} \quad z < z_\mathrm{N} \\ \left[1 + \dfrac{\gamma - 1}{\gamma}\dfrac{e(\phi - \phi_\mathrm{N})}{T_\mathrm{eN}}\right]^{\frac{1}{\gamma - 1}} & , \quad \text{if} \quad z \geq z_\mathrm{N} \end{cases} \tag{2.17}$$

Finally, Poisson's equation can be expressed as

$$\epsilon_0 \frac{\mathrm{d}^2\phi}{\mathrm{d}z^2} = en_\mathrm{e}(\phi) - en_\mathrm{i}(\phi, z). \tag{2.18}$$

The spatial structure of the plume is split in three subregions:

(i) a Debye sheath from the grid E to a sheath edge F, (ii) a quasineutral, zero electron current region from F to N, and (iii) a quasineutral, current-free region from N to infinity.

The Debye sheath satisfies Eq. 2.18 with boundary conditions $\phi(z_\mathrm{E}) = \phi_\mathrm{E}$ and $\epsilon_0 \mathrm{d}\phi/\mathrm{d}z|_{z_\mathrm{F}} = 0$. A simple shooting method yields the profile $\phi(z)$, including the potential at the sheath edge, ϕ_F. A practical example to be compared with the hybrid results of Fig. 2.5 is given below. Meanwhile, a rough estimate of the sheath thickness can be obtained by just approximating the electric charge on the right side of Eq. 2.18 by a constant average value $\tilde{\rho}_\mathrm{el}$, thus obtaining $\phi(\bar{z}) = \phi_E + (\tilde{\rho}_\mathrm{el}/2\epsilon_0)(2\bar{z}_\mathrm{F} - \bar{z})\bar{z}$ with $\bar{z} = z - z_\mathrm{E}$. Then, the sheath thickness is $\bar{z}_\mathrm{F} = \sqrt{2\epsilon_0(\phi_\mathrm{F} - \phi_\mathrm{E})/\tilde{\rho}_\mathrm{el}}$ or, using known parameters $\phi_\mathrm{N} - \phi_\mathrm{E}$ ($\simeq \phi_\mathrm{F} - \phi_\mathrm{E}$) and n_iE:

$$\bar{z}_\mathrm{F} \approx 3\sqrt{2\epsilon_0(\ \phi_\mathrm{N} - \phi_\mathrm{E})/en_\mathrm{iE}}, \tag{2.19}$$

with the integer 3 providing the best fit for the results of Fig. 2.5.

In the intermediate region FN, quasineutrality leads to

$$en_\mathrm{e}(\phi)u_\mathrm{i}(\phi) = I_\mathrm{i}/A(z), \tag{2.20}$$

which is the implicit equation for the monotonically-decreasing potential $\phi(z)$. Evaluating the expression between F and N, one has

$$e(\phi_\mathrm{F} - \phi_\mathrm{N}) \approx T_\mathrm{eN} \ln(A_\mathrm{N}/A_\mathrm{F}) \sim T_\mathrm{eN}, \tag{2.21}$$

thus justifying Eq. 2.19. In the far region N∞, Eq. 2.20 applies again but now $n_e(\phi)$ corresponds to the non-isothermal case in Eq. 2.17. Far downstream, $n_\mathrm{e}(z) \to 0$, and Eq. 2.17 states that the asymptotic downstream potential is

$$\phi_\infty = \phi_\mathrm{N} - \frac{\gamma}{\gamma - 1}\frac{T_\mathrm{eN}}{e}. \tag{2.22}$$

Values of $\gamma \approx 1.2$ and $T_\mathrm{eN} \approx 2$eV are suggested in the literature [141, 143] yielding a potential fall of 12V from the neutralizer sheet to infinity.

In the real case, at the exit E, the plume consists of a set of beamlets which later intersect and only downstream merge in a single beam as shown in Fig. 2.13(b). This interaction can be taken into account by properly defining the area function $A(\bar{z})$. Assuming conical beamlets of circular cross-section and divergence angle α, which start to coalesce at a distance $\bar{z}_\mathrm{C}$, a suitable expression of the area variation is the following piece-wise function:

$$A(\bar{z}) = \begin{cases} N_\mathrm{b} A'_\mathrm{E}\left(1 + \bar{z}\sqrt{\pi/A'_\mathrm{E}}\tan\alpha\right)^2, & \text{if} \quad \bar{z} \le \bar{z}_\mathrm{C}, \\ N_\mathrm{b} A'_\mathrm{C}\left(1 + (\bar{z} - \bar{z}_\mathrm{C})\sqrt{\pi/(N_\mathrm{b}A'_\mathrm{C})}\tan\alpha\right)^2, & \text{if} \quad \bar{z} > \bar{z}_\mathrm{C}, \end{cases} \tag{2.23}$$

with N_b the number of beamlets, A'_E the initial area per beamlet (or acceleration grid hole area), and $A'_\mathrm{C} = A'_\mathrm{E}\left(1 + \bar{z}_\mathrm{C}\sqrt{\pi/A'_\mathrm{E}}\tan\alpha\right)^2$ the individual beamlet area at the coalescence start point $\bar{z}_\mathrm{C}$. The coalescence coordinate $\bar{z}_\mathrm{C}$ can be obtained as a function of the geometric properties of the grid and of the divergence angle as $\bar{z}_\mathrm{C} = \arctan\left[(d_\mathrm{hc} - d_\mathrm{a})/(2\tan\alpha)\right]$.

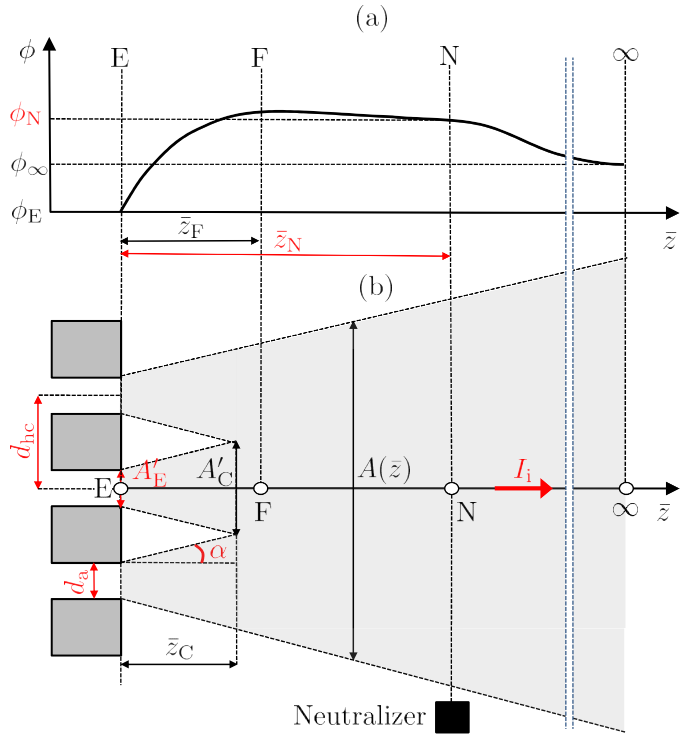

Figure 2.13: (a) Electric potential evolution along the plume centerline, and (b) a possible plume area function to include the effects of beamlets interaction. Model inputs are shown in red. In subplot (b) the plume area evolution $A(\bar{z})$ is shown by the shaded area.

Finally, the plume divergence angle is, in general, a function of the normalized perveance per hole: the evolutions $\alpha(\Pi)$ found in both the infinite-apertures simulations and in the experiments of Ref. [139] (shown by the black and red lines in Fig. 2.16) have been assumed here.

Eq. 2.23 shows that the derivative of the plume area $\mathrm{d}A(z)/\mathrm{d}\bar{z}$ is discontinuous at $\bar{z}_{\mathrm{C}}$ to account for the fact that the individual beamlets start to overlap there. In the limit of an infinite number of apertures/beamlets $N_{\mathrm{b}} \to \infty$, and the average beamlet area after point $\bar{z}_{\mathrm{C}}$ remains constant, which is consistent with the infinite-apertures 2D simulations of Sec. 2.3, where the specular reflection considered for ions crossing the lateral boundaries is equivalent to assuming a constant beamlet area.

Using the area variation of Eq. 2.23 to integrate Eq. 2.18, the profile $\phi(z)$ inside the Debye sheath and the sheath thickness $\bar{z}_{\mathrm{F}}$ are obtained. This magnitude is shown as a function of the normalized perveance by the solid and dashed red lines in Fig. 2.5, with the considered $\alpha(\Pi)$ profile (from either infinite apertures simulations or from experiments) having only a minor influence. More importantly, the predicted sheath thickness by the 1D model is in good agreement with that of the 2D and 3D hybrid models, except for low perveances. This disagreement is due to the overfocusing of the beamlets, whose area at the acceleration grid becomes quite smaller than the acceleration grid hole area, which is the one assumed in Eq. 2.23; and it is also due to the strongly non-uniform radial density profile at the grids exit induced again by the overfocusing, a feature that is not captured by the 1D nature of the model.

2.6 Model benchmarking and validation with experiments

In this section, the numerical models for 2D infinite-apertures and 3D finite-apertures setups are benchmarked one against the other and compared to the semi-analytical 1D model predictions and experimental data. For a proper comparison, the region around the central hole is considered in the finite-apertures case.

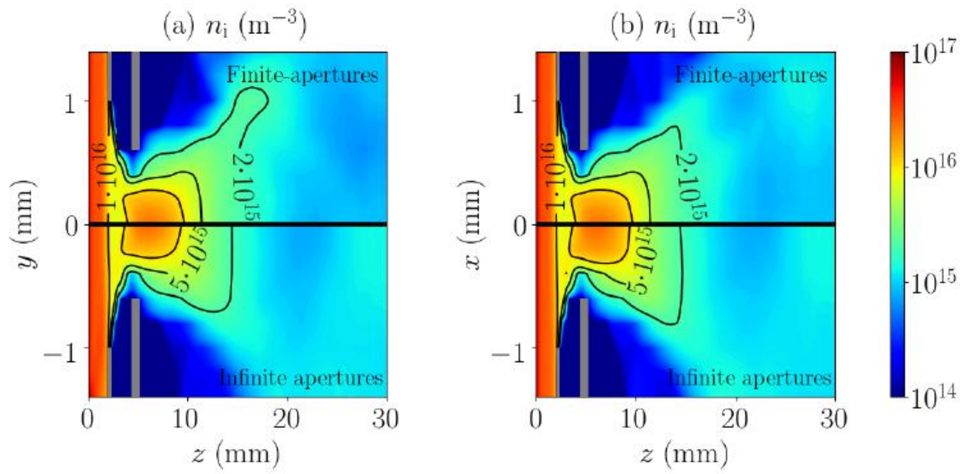

Figure 2.14: Comparison of the ion density between the infinite apertures and the finite-apertures simulation at (a) $x = 0$ and (b) $y = 0$, for $\Pi = 0.45$. The central hole-pair is considered for the finite-apertures simulation.

Fig. 2.14 compares the ion density of the 2D and 3D approaches at two planes of interest, $x = 0$ and $y = 0$, for $\Pi = 0.45$. In both planes, the solutions are qualitatively similar. However, there are also some visible discrepancies. Referring first to the $x = 0$ plane (subplot (a)), the discrepancies are explained by the fact that the symmetric boundary condition in a computational domain with square holes cannot exactly reproduce the hexagonal layout of the finite-apertures simulations, shown in Fig. 2.7. Therefore, the beamlets interaction is different in the two cases, with a consequent visible difference downstream in the ion density map. In the $y = 0$ plane (subplot (b)), on the other hand, the symmetric boundary reflection condition of the infinite-apertures simulation reproduces more accurately the beamlets interaction, so that the observed differences are smaller, and mainly related to the slight outward deviation of the beamlets surrounding the central one, as observed in the finite-apertures grid case in Fig. 2.8 (a). This three-dimensional effect, however, would vanish quickly for increasing numbers of holes (typical ion thrusters feature hundreds or thousands of holes).

The two different simulation setups discussed in detail in Secs. 2.3 and 2.4 have then been compared to the 1D semi-analytical model of Sec.2.5. While the downstream sheath size has already been compared in Fig. 2.5, with an overall good agreement, Fig. 2.15 (a) shows a quantitative comparison of the profiles, along the central hole centerline, of the ion density and electric potential, obtained with the three models.

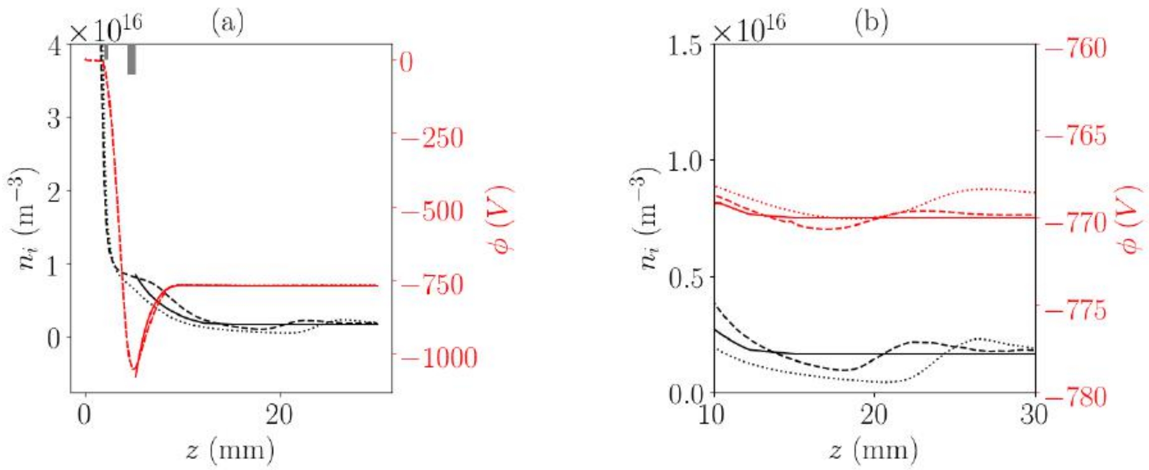

Figure 2.15: (a) 1D quantitative comparison of the ion density (in black) and electric potential (in red) for the 2D (dashed line), 3D (dotted line) and 1D (solid thick line) models, for $\Pi = 0.83$. (b) Zoom of the electric potential and density evolution, in the downstream region.

The electric potential match of the infinite and finite-apertures simulations is good, with somewhat larger differences in the ion density (due to the already mentioned reasons). Regarding the 1D model, the evolution of ϕ inside the sheath is accurate, with the exception of its minimum value (at the acceleration grid hole center), which is affected by 2D space charge effects that cannot be reproduced by a 1D model. The ion density predicted by the 1D model also behaves well, falling along the sheath in spite of the electric potential rise, thanks to the inclusion in the model of a beamlet divergence angle. Fig. 2.15 (b) finally shows a zoom of the downstream evolution of electric potential and density along the beamlet centerline. Both infinite and finite-apertures simulations show an increase in the density as we move downstream, which can be attributed to the beamlets interaction, and is accompanied by a corresponding ambipolar electric potential rise. In fact, this increment occurs farther downstream in the case of the finite-apertures because, as already shown in Sec. 2.4, the interaction between beamlets occurs with a slightly lower angle when compared to the infinite apertures case. Finally, the 1D model electric potential and ion/electron density remain roughly constant (slowly decreasing) after the beamlets coalescence with values similar to those of the numerical simulations. With the additional assumption of a polytropic coefficient $\gamma = 1.2$ for the far plume expansion, the 1D model finally predicts a potential at infinity of -782V.

The infinite and finite-apertures simulations have also been compared with the experiment in Ref. [139]. As in the finite-apertures simulations, the considered experimental setup consists of a pair of grids with 19 axially aligned holes in a hexagonal pattern. This setup also includes a set of Faraday probes located at a distance of 8 cm from the accelerator grid, in the direction of the plume. The numerical simulations and the experiment are compared in terms of a relevant performance parameter of the ion grid optics: the divergence angle α of the plume. This is mainly affected by the net acceleration voltage V_{N}, the normalized perveance per hole Π, and the geometry of the grids. The divergence angle is typically defined as the slope of the ion current streamtube that carries 95% of the total ion beam current [73]. An approximation of this angle, which is generally considered in experimental campaigns and adopted in Ref. [139], is given by:

$$\alpha = \arctan\left(\frac{R_{95} - R_{\mathrm{B,acc}}}{L}\right), \tag{2.24}$$

where R_{95} represents the radius, from the thruster axis, of the 95% ion current streamline, $R_{\mathrm{B,acc}}$ is the beam radius at the acceleration grid exit, and L is the distance between the acceleration grid and the measurement plane. The farther out the measurement plane, the more precise Eq. 2.24 in estimating the local slope of the 95% ion current streamline.

The experimentally measured divergence angle is obtained with Eq. 2.24, by measuring R_{95} at the Faraday probes location (several cm away from the thruster exit) and assuming that $R_{\mathrm{B,acc}}$ is equal to the radius of the acceleration grid. For consistency, the same formula and assumptions are considered for the computation of the divergence angle from simulation results, although a different plane is chosen for the computation of R_{95}. In the finite-apertures simulations, the measurement plane is located 1.5 cm away from the acceleration grid, i.e. at the maximum distance allowed by the considered simulation domain. In infinite apertures simulations, this plane is located before the reflection of the ion macro-particles at the lateral boundaries, so that the obtained divergence angle refers to a single beamlet and does not account for its interaction with the rest. Moreover, in this latter case, $R_{\mathrm{B,acc}}$ refers to the 95% ion current radius of a single beamlet at the acceleration grid exit plane.

Fig. 2.16 shows the results of this validation. Both simulation approaches are able to closely predict the optimal perveance value obtained experimentally. This implies that the evolution with perveance of an individual beamlet divergence is practically the same as that of the whole ion beam. Therefore, an estimation of the optimal perveance can be reasonably obtained with a limited computational effort, using the infinite-apertures simulation setup. The second point to be outlined concerns the values of the divergence angle. Overall, a good agreement between experiments and simulations can be observed. However, there are some aspects that are worth further discussion. First, the infinite-apertures divergence angle is lower than the finite-apertures one. This can be justified by the fact that, in the infinite-apertures, the divergence angle is computed at a plane where beamlets coalescence has not started yet. Second, regarding the finite-apertures simulations, the average (over the perveance range) divergence angle is close to the real one, although it is underestimates/overestimates it at low/high perveance values, with a generally flatter profile This difference might be due to the limited axial distance considered for the divergence angle estimation in finite-apertures simulations, which is quite smaller than the measurement plane distance considered in the experiments (8 cm) [139]. Another possible reason is the excessive proximity of the hollow cathode to the grids, in

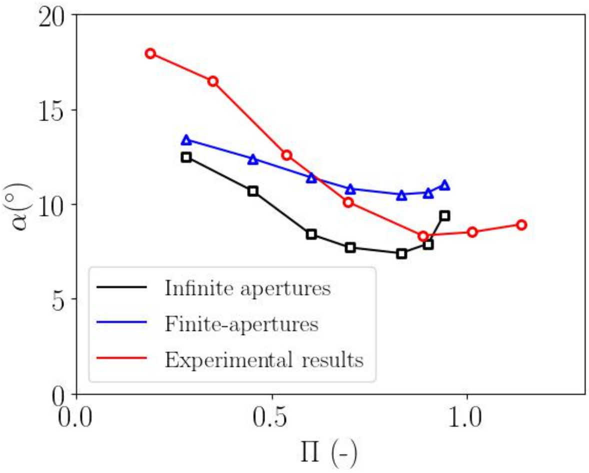

Figure 2.16: Evolution of the divergence angle α as a function of Π for infinite-apertures simulations (black line with square markers), finite-apertures simulations (blue line with triangle markers), and for the experimental campaign (red line with circle markers) of Ref. [139].

the radial direction, considered in the simulations. In Sec. 2.4, the effects of this close position were already discussed and appeared to be small. However, this might be true only for small divergence angles, as is the case in Sec. 2.4, for which the beamlets interaction with the cathode is less important. For larger divergence angles, the cathode position effects might be more important and contribute to the trend observed in Fig.2.16.

2.7 Conclusions

This paper has described a numerical hybrid model for the simulation of the grid optics of an ion thruster. While ions and neutrals are modeled as macro-particles of a particle-in-cell sub-model, both the electron properties and the electric potential are obtained by solving the coupled equations of electron momentum balance, electric continuity and Poisson's equations. With the use of a thermalized potential, the model is also capable of predicting the electron current density at the large conductivities of this weakly-collisional electron population. Indeed, electron inertia dominates over collisional effects in certain spatial regions.

Two different simulation setups have been presented, discussed and compared against both a simplified 1D model and experimental data. The first setup, the infinite-apertures one, features a periodic array of interacting beamlets and an infinite neutralizing surface. The second setup, or finite-apertures setup, features a complete grid assembly with 19 apertures and an external hollow cathode to simulate the beam neutralization. The infinite-apertures setup can be used (with a limited computational effort) to estimate the optimal perveance, in terms of beam divergence, of an ion thruster grid optics. The latter setup, on the other hand, allows to study in detail the beamlet coalescence process, and the non-symmetric electric current neutralization and its dependence on the external cathode position.

The ion extraction and charge-current neutralization physics have then been investigated. Regarding the ion extraction and focusing, this is mainly affected by the operational perveance per hole of the grids system (for a given set of operational voltages). As already indicated, an optimal perveance value exists that minimizes the divergence angle of the plume, and hence maximizes the thrust efficiency. Regarding the physics of neutralization, on the other hand, different conclusions have been obtained for what concerns the neutralization of electric charge and neutralization of current. In fact, it is found that, while the current neutralization and the electron streamlines are strongly affected by the cathode position, this has nearly no influence on both the ion trajectories and the charge neutralization process, which occurs at the same distance from the acceleration grid irrespectively of the neutralizer position. This is true provided that the neutralizer is sufficiently close to the thruster to avoid any beam stalling phenomena, and far enough to avoid perturbing the ion extraction. This conclusion is coherent with the predictions of the one-dimensional model in which the extension of the plasma sheath next to the acceleration grid (over which the charge neutralization is achieved) depends only on ion density and potential difference between the neutralizer and the acceleration grid, but not on the distance between the acceleration grid and the current neutralization plane.

The inclusion of the electron inertia in the model has the overall effect of smoothing the spatial gradients of the electron current density and reducing the curvature of the electron streamlines. The inertial force contribution in the electron momentum balance is of the same order as the collisional force, and in some downstream regions, it is even larger. However, given the boundary conditions imposed on the electron current at the simulation boundaries, the inertial effects on the electron current density are generally small. A larger effect is observed on the thermalized potential map, whose variations are nevertheless negligible with respect to the pressure gradient force. For this reason, both the ion trajectories and the plasma density are practically not affected by the electron inertia.

Chapter 3

Hybrid plasma simulations of a magnetically shielded Hall thruster

This Chapter integrally reproduces the contents of the article "Hybrid plasma simulations of a magnetically shielded Hall thruster", Journal of Applied Physics, 131 (2022) [122]. The style has been adapted to the one of this document and the references have been unified in a single bibliography at the end of the document.

Abstract

Numerical simulations of a magnetically shielded Hall effect thruster with a centrally-mounted cathode are performed with an axisymmetric hybrid particle-in-cell/fluid code, and are partially validated with experimental data. A full description of the plasma discharge inside the thruster chamber and in the near plume is presented and discussed, with the aim of highlighting those features most dependent on the magnetic configuration and the central cathode. Compared to traditional magnetic configurations, the acceleration region is mainly outside the thruster, whereas high plasma densities and low temperatures are found inside the thruster. Thus, magnetic shielding does not decrease plasma currents to the the walls, but reduces significantly the energy fluxes, yielding low heat loads and practically no wall erosion. The injection of neutrals at the central cathode generates a secondary plasma plume that merges with the main one and facilitates much the drift of electrons towards the chamber. Once inside, the magnetic topology is efficient in channeling electron current away from lateral walls. Current and power balances are analyzed to assess performances in detail.

3.1 Introduction

Magnetic shielding (MS) of a Hall effect thruster (HET) chamber has been proven an effective technique to limit both wall erosion, due to high-energy ion bombardment, and heat loads, thus enabling the design of the next generation of HETs, featuring enhanced performances and operational lifetimes [59]. Due to their recent development, just a few prototypes of MS-HETs have been experimentally tested to date. In the mid to high power range, there are the 4.5 kW BPT-4000 [144], the 12.5kW HERMeS [145], the 6kW H6MS [146], the 9kW H9 [147], the 20kW NASA-300MS [148], and SITAEL's 5 kW HT5k [149] and 20 kW HT20k [150]; then, in the low-power range ($<$ 1kW) there are the MaSMi-60 [151] and the ISCT-200 [152]. Yet, a lower number of studies comparing experimental and simulation results have been realized. Relevant ones were performed with the multi-fluid simulation code Hall2De [74] for BPT-4000 [59], H6 [153, 154], HERMeS [77, 155], H9 [156], and MaSMi-60 [157].

The relatively low numbers of MS-HET prototypes and studies, together with the lack of predictive models of HET discharges (due to the open problems on plasma-wall interaction and electron turbulence, particularly), make uncertain the direct extrapolation of results and trends from one thruster system to another.

This situation affects, for instance, the design and development of new optimized electric propulsion architectures such as the direct-drive power concept [55,56,158], which requires a precise characterization of the thruster performances and the cathode-anode electrical coupling over the nominal operation range for its appropriate integration with other subsystems [56]. Therefore, advances on the validation of simulation tools against experimental data, capable not only of providing a full characterization of a HET plasma discharge and performances, but also of addressing thermal, electrical and material issues related with its operation, are of central interest in HET research.

This work presents 2D numerical simulations of the 5kW HT5k [149], and a partial validation of the numerical model with the limited experimental data existing for this prototype. The simulations are carried out with the code HYPHEN [99, 105] and constitute its first test with a MS topology. HYPHEN is a multi-thruster, hybrid-formulation code, which uses a particle-in-cell (PIC) model for heavy species and a magnetized drift-diffusion fluid model for electrons. Contrary to other hybrid codes, relying on a quasi-1D electron model [79,96,159], whose application to MS topologies is rather complicated, HYPHEN, as Hall2De, adopts a full-2D electron fluid model on a magnetic field aligned mesh (MFAM), thus allowing a complete characterization of the electron currents, which are crucial to study, for instance, plasma-wall interaction effects. The version of HYPHEN used here is also the first one incorporating a 'wall' cathode instead of a 'volumetric' cathode. This last one worked fine for HETs with laterally-located cathodes (except for the code being axisymmetric, although electron emission becomes quickly homogeneous azimuthally [104]); however, it was not very suitable for the centrally-mounted cathode of the HT5k.

HYPHEN simulates the slow-dynamics, axisymmetric transport of the plasma discharge. This implies that two processes, involving kinetic, non-symmetric, and high-frequency aspects, need to be modeled phenomenologically in the electron fluid equations.

The first one is the estimation of the particle and energy fluxes to the thruster dielectric walls. These depend on the electron velocity distribution function (VDF), which is non-Maxwellian because of the partial depletion of the collected VDFs high-energy tail and the secondary electron emission (SEE) by the walls. Kinetic studies [87, 160, 161] and experimental evidence [162, 163] are therefore used to tune the fluxes to the walls. The second phenomenological model intends to reproduce the slow, turbulent transport of the electron fluid, resultant from averaging (on the azimuth and the high-frequency time scale) the oscillating, azimuthal forces emanating from nonlinear instabilities [164–168]. Since there is not yet an established theory of this averaged turbulence force, authors have treated it as an anomalous collisional force, calibrated, when possible, with experimental data. Still, simulations differ much on the selected strength and shape of the anomalous collision frequency [77, 93, 96, 159, 169–171].

The central goal of this work is the analysis of the 2D profiles of the discharge, the identification of the main aspects related to the MS topology and the central cathode, and the effects on thruster performances. The discussion aims at improving the understanding of the plasma physics peculiar to a MS-HET and revealing its potential advantages over a HET with a conventional magnetic topology. The document is organized as follows. Section 3.2 describes the HT5k thruster unit and the experimental data supporting this work. Section 3.3 describes the simulation model and the main settings. Subsection 3.4.1 discusses the tuning of the turbulent parameters to match the experimental data. Then, Subsections 3.4.2 and 3.4.3 analyze the 2D plasma discharge and the thruster performances. Finally, conclusions are drawn in Section 3.5.

3.2 Thruster description and experimental data

SITAEL began to develop the HT5k [Fig. 3.1 (a)] in 2013. This 5 kW-class thruster consists of two main elements: the thruster itself and the HC20 hollow cathode. Along the last years, SITAEL designed, manufactured, and tested three different development models (DMs) of the HT5k, as part of several national and international programmes. The different prototypes underwent several technical investigations [79, 149], which permitted to demonstrate low erosion, high performance, direct-drive operations, as well as performance stability in high-vacuum conditions (pressure $<10^{-5}$ mbar). The design and manufacturing process of the HT5k thruster unit engineering qualification model started in 2019, when the thruster was chosen as the main propulsive unit for the orbit raising and station keeping of the Ital-GovSatCom geostationary platform [172]. The HT5k DM3 prototype considered here implements a centrally mounted cathode and a non-conventional magnetic field topology, which is beneficial from the point of view of discharge channel erosion. Design and previous testing efforts were dedicated to enhance critical components and to optimize the thruster thermal behavior. The thruster tests were run in SITAEL's IV10 facility, reaching pressures of the order of 7×10^{-6} mbar (Xe) while firing at 4.4 kW of discharge power. The DM3 demonstrated competitive performance and showed stable and efficient operation in the 3 kW to 7 kW discharge power range, featuring anodic thrust efficiencies up to 60%.

Fig. 3.1(b) displays a sketch of the geometry of the thruster chamber and the near

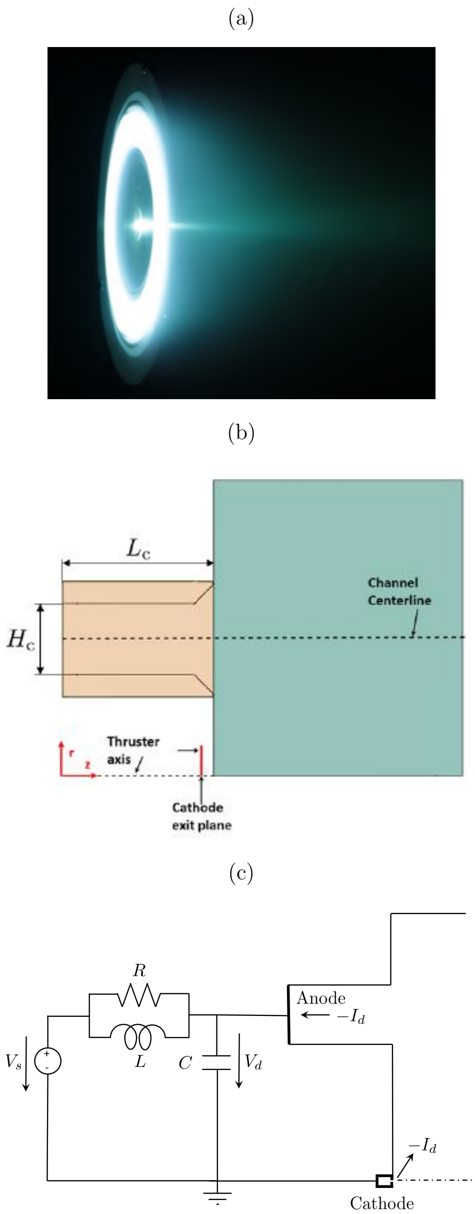

Figure 3.1: (a) HT5k thruster unit DM3 in operation. (b) HT5k thurster chamber and near plume geometry. (c) Sketch of the RLC filter unit implemented between the thruster anode wall and the cathode.

plume region. The geometrical parameters L_c and H_c correspond to the thruster chamber length and width, respectively. The plasma domain to be simulated with HYPHEN corresponds to the cylindrical axisymmetric half meridian plane, including the annular thruster chamber and the near plume region. The latter extends axially from the chamber exit plane up to $6L_c$, and radially from the symmetry axis up to $6H_c$. The position of

Case	V_{s} (V)	$\dot{m}_{\mathrm{A}}$ (mg/s)	I_{d} (A)	F (mN)
1	300	14	14.6	269
2	400	14	14.2	308
3	300	10	10.3	184
4	350	10	10.1	197
5	400	10	9.6	208

Table 3.1: Experimental data for the discharge current I_{d} and the thrust F for the five operation points under consideration. The background pressure is equal to 1.1×10^{-5} mbar for all cases.

the cathode exit plane, at the thruster symmetry axis, is also indicated in Fig. 3.1(b). Fig. 3.1(c) shows a scheme of the resistor-inductor-capacitor (RLC) filter unit connecting anode and cathode including the power source voltage V_{s}. The discharge voltage V_{d} is set between the anode and the cathode. The discharge current I_{d} flowing between anode and cathode is indicated in the sketch according to the flow direction of electrons. The values of the RLC filter elements are R = 4.7 Ω, L = 360 μH and C = 94 μF.

The experimental set-up is detailed in Refs. [79, 173]. The experimental data used in the simulations, with xenon as propellant, are listed in Tab. 3.1. Time-averaged values of the discharge current I_{d} and the thrust F are available for five operation points, hereafter referred to as Cases 1 to 5, defined by a pair (V_{s}, $\dot{m}_{\mathrm{A}}$), where V_{s} is the power source voltage and $\dot{m}_{\mathrm{A}}$ is the propellant mass flow injected through the anode to the thruster chamber. The former ranges from 300 V to 400 V and the latter from 10 mg/s to 14 mg/s. For all cases, a 7.5% of $\dot{m}_{\mathrm{A}}$ is injected through the cathode. Data repeatability (i.e. standard deviation) of the measurements is 5%. The value of the time-averaged I_{sp} ranges from 1900s to 2100s from case to case. In addition, the operation point (V_{s}, $\dot{m}_{\mathrm{A}}$) = (300 V, 14 mg/s) features an anodic thrust efficiency of 58.2%.

3.3 Simulation model and settings

3.3.1 Simulation model

Fig. 3.2(a) shows a schematic representation of the HYPHEN structure and simulation loop, which is briefly outlined next. HYPHEN is an axisymmetric, hybrid, OpenMP-parallelized code built modularly. The code version for HET simulations consists of three main modules: the Ion module (I-module), which follows a Lagrangian approach for simulating the dynamics of the PIC macroparticles of heavy species; the Electron module (E-module), which solves a fluid model for the magnetized electron population; and the Sheath module (S-module), which provides the proper coupling between the quasineutral plasma bulk, and the thruster walls. The E-module assures automatically plasma quasineutrality in the simulation domain. Thus, the Debye sheaths managed by the S-module are, in fact, discontinuity surfaces adjacent to the thruster walls. The three modules are coupled within a time-marching sequential loop.

The I-module operates on a structured mesh of the simulation domain, shown in Fig. 3.2(b). On the contrary, and in order to limit the numerical diffusion arising from the strong anisotropic transport on magnetized electrons, the E-module uses an unstructured MFAM [108], defined by the externally applied magnetic field $\boldsymbol{B}$ and shown in Fig. 3.2(c). The magnetic configuration of the MS-HT5k, which features a null magnetic point inside the channel, attempts to screen well all its internal walls.

Two reference frames are considered: one is the cylindrical frame $\{\mathbf{1}_\mathrm{z}, \mathbf{1}_\mathrm{r}, \mathbf{1}_\theta\}$, with coordinates (z, r, θ); and a second one is the magnetically aligned frame $\{\mathbf{1}_\perp, \mathbf{1}_\parallel, \mathbf{1}_\theta\}$, with $\mathbf{1}_\parallel = \boldsymbol{B}/B$ and $\mathbf{1}_\perp = 1_\parallel \times 1_\theta$, and coordinates $(\lambda, \sigma, \theta)$. The orthogonal magnetic coordinates $\lambda(z, r)$ and $\sigma(z, r)$ of the MFAM, Fig. 3.2(c), are obtained from solving $\nabla \cdot \boldsymbol{B} = 0$ and $\nabla \times \boldsymbol{B} = 0$.

Let Z_s, n_s, $\boldsymbol{u}_\mathrm{s}$, and $\boldsymbol{j}_\mathrm{s} = eZ_\mathrm{s}n_\mathrm{s}\boldsymbol{u}_\mathrm{s}$ be the charge number, particle density, macroscopic velocity, and current density of the plasma species s (i.e. electrons e, neutrals n, singly-charged ions i1, and doubly-charged ions i2); $\boldsymbol{E} = -\nabla\phi$ be the electric field, with ϕ the electric potential; and T_e the electron temperature. Every simulation step, the I-module takes as inputs $\boldsymbol{B}$, $\boldsymbol{E}$, and T_e and performs the following tasks: (i) the propagation of macroparticles one timestep Δt forward, according to the electromagnetic fields acting on them; (ii) the injection of new macroparticles into the domain and the removal of exiting ones; (iii) the interaction of macroparticles with the thruster walls, such as neutral reflection and ion recombination; (iv) the generation of new ion macroparticles due to the ionization of neutrals; and (v) the computation, through a particle-to-mesh weighting process, of the macroscopic properties characterizing each heavy species. Further details can be found in Refs. [99, 115, 174].

The E-module, taking these heavy-species magnitudes as inputs, solves a quasineutral, drift-diffusion fluid model for the magnetized electron population, obtaining ϕ, T_e, $\boldsymbol{j}_\mathrm{e}$, and the electron heat flux vector $\boldsymbol{q}_\mathrm{e}$. The electron fluid model equations are [70, 93, 175]

$$n_e = \sum_{\mathrm{s}\neq\mathrm{e,n}} Z_\mathrm{s} n_\mathrm{s}, \tag{3.1}$$

$$\nabla \cdot \boldsymbol{j}_\mathrm{e} = -\nabla \cdot \boldsymbol{j}_\mathrm{i}, \tag{3.2}$$

$$0 = -\nabla(n_\mathrm{e}T_\mathrm{e}) + en_\mathrm{e}\nabla\phi + \boldsymbol{j}_\mathrm{e} \times \boldsymbol{B} + \boldsymbol{F}_\mathrm{res} + \boldsymbol{F}_\mathrm{t}, \tag{3.3}$$

$$\frac{\partial}{\partial t}\left(\frac{3}{2}n_\mathrm{e}T_\mathrm{e}\right) + \nabla \cdot \left(\frac{5}{2}n_\mathrm{e}T_\mathrm{e}\boldsymbol{u}_\mathrm{e} + \boldsymbol{q}_\mathrm{e}\right) = -\boldsymbol{j}_\mathrm{e} \cdot \nabla\phi - Q_\mathrm{inel}. \tag{3.4}$$

$$\boldsymbol{q}_\mathrm{e} = -\bar{\bar{K}}_e \cdot \nabla T_\mathrm{e} \tag{3.5}$$

Eqs. (3.1) and (3.2), with $\boldsymbol{j}_i = \sum_{\mathrm{s}\neq\mathrm{e,n}} eZ_\mathrm{s}n_\mathrm{s}\boldsymbol{u}_\mathrm{s}$, correspond to plasma quasineutrality and the plasma current conservation equation, and the right hand sides are inputs from the I-module. The momentum equation (3.3) neglects electron inertia, assumes the pressure tensor to be isotropic, and includes the resistive force $\boldsymbol{F}_\mathrm{res}$ and the turbulent (or anomalous) force $\boldsymbol{F}_\mathrm{t}$. The resistive force satisfies

$$\boldsymbol{F}_\mathrm{res} = (m_\mathrm{e}\nu_\mathrm{e}/e)(\boldsymbol{j}_\mathrm{e} + \boldsymbol{j}_\mathrm{c}), \tag{3.6}$$

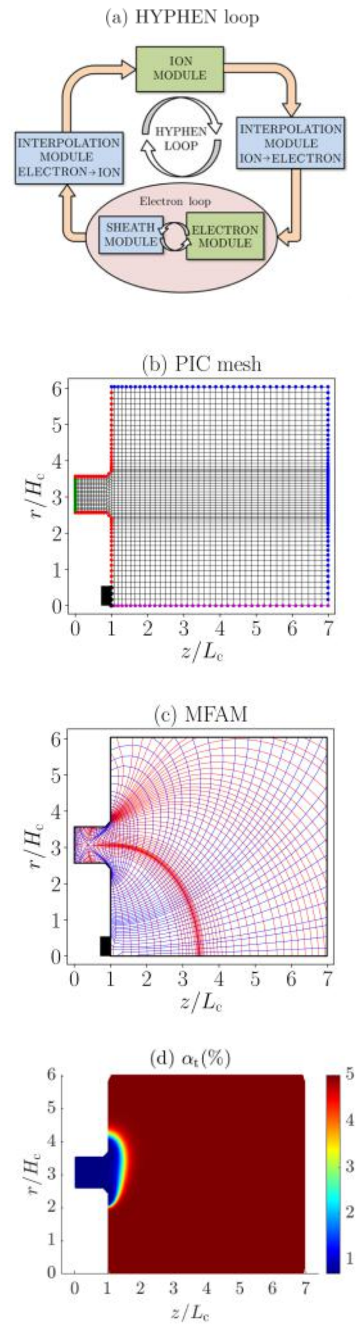

Figure 3.2: (a) Simplified description of HYPHEN time-integration loop. (b) Cylindrical mesh used by the I-module. The red, green, blue and magenta lines indicate the thruster dielectric walls, the anode, the downstream boundary, and the symmetry axis, respectively. The centrally-mounted cathode is indicated by the small black box. (c) The MFAM used by the E-module. Blue and red lines are B-parallel and B-perpendicular lines, respectively, defining the cells. (d) 2D map of α_t, particularized for Case 2.

with m_e the electron elementary mass, $\nu_e = \sum_{s\neq e} \nu_{es}$ the total momentum transfer frequency due to collisions with all heavy species, with ν_{es} the individual contributions for each heavy species s, and

$$\boldsymbol{j}_c = en_e \sum_{s\neq e} (\nu_{es}/\nu_e)\boldsymbol{u}_s \tag{3.7}$$

an equivalent heavy species collisional current density [99]. The turbulent force $\boldsymbol{F}_t$, accounting for azimuth-averaged, wave-based anomalous transport, is modeled phenomenologically as [93, 96, 169, 176]

$$\boldsymbol{F}_t \simeq -m_e \nu_t n_e u_{\theta e} \mathbf{1}_\theta, \qquad \nu_t = \alpha_t \omega_{ce}, \tag{3.8}$$

with ν_t a turbulent collision frequency, $\omega_{ce} = eB/m_e$ the electron gyrofrequency, and $\alpha_t(z, r)$ a phenomenological function representing the local turbulence level [93,96]. Turbulent-based contributions to the axial and radial momentum equations are negligible compared to the rest of forces there.

The main assumption of the electron drift-diffusion model is to neglect inertia in the momentum equation. This is justified as long as the electron kinetic energy is much less than their thermal energy, i.e. $m_e u_e^2 \ll T_e$, a condition well satisfied in HET discharges, except in localized regions and certain operation points. The great advantage of the drift-diffusion model is that the momentum equation (3.3) reduces to a generalized Ohm's law for $\boldsymbol{j}_e$ (with an electric conductivity tensor $\bar{\bar{\sigma}}_e$), which is much easier to treat numerically than the whole differential equation on $\boldsymbol{u}_e$.

The component of the Ohm's law along the local cross-field direction $\mathbf{1}_\perp$ is [177]

$$j_{\perp e} = \frac{\sigma_e}{1 + \chi\chi_t} \left[\frac{1}{en_e} \frac{\partial(n_e T_e)}{\partial \mathbf{1}_\perp} - \frac{\partial \phi}{\partial \mathbf{1}_\perp} \right] - \frac{j_{\perp c} + \chi_t j_{\theta c}}{1 + \chi\chi_t}, \tag{3.9}$$

where $\sigma_e = e^2 n_e/(m_e \nu_e)$ is the parallel electric conductivity, $\chi = \omega_{ce}/\nu_e$ is the classical Hall parameter, and $\chi_t = \chi/(1 + \alpha_t \chi)$ is the reduced Hall parameter when including ν_t. Therefore, the effective Hall parameter is $\sqrt{\chi\chi_t}$ and scales as $\propto \alpha_t^{-1/2}$ if turbulent transport dominates. The last term on the right side of Eq. (3.9) represents collisions with heavy species and is negligible generally.

Eq. (3.4) is the electron energy equation for an isotropic pressure tensor in the inertialess limit, where the second term in the left side gathers the enthalpy and heat fluxes, and the right side includes the work of the electric field and the power losses from inelastic collisions (e.g. excitation and ionization). The Fourier's law for the heat flux, Eq. (3.5), includes the thermal conductivity tensor $\bar{\bar{K}}_e = 5T_e\bar{\bar{\sigma}}_e/(2e^2)$, and corresponds to the drift-diffusion limit of the evolution equation for $\boldsymbol{q}_e$ [175].

The numerical treatment of Eqs. (3.2)-(3.5) in the unstructured, irregular MFAM was developed in Refs. [107, 108, 177]. As shown in Fig. 3.2(c), the MFAM is composed of inner and boundary cells. Inner cells are those enclosed by $\boldsymbol{B}$-parallel (blue) and $\boldsymbol{B}$-perpendicular (red) lines. Boundary cells, however, contain at least one boundary face aligned with a domain boundary, which is not a magnetic line generally. Centroids (or computational points) of both cell and faces correspond to the magnetic center or the geometric center, when the former is not available (e.g. at boundary cells). A finite volume scheme on the MFAM cells is applied to conservation Eqs. (3.2) and (3.4); and gradient reconstruction schemes, ad-hoc for the unstructured MFAM, are applied to Ohm's and Fourier's vector laws (3.3) and (3.5). For each variable ϕ and T_e, this generates one algebraic equation per MFAM cell. Additionally, boundary conditions specifying $j_\mathrm{ne} = \mathbf{1}_\mathrm{n} \cdot \boldsymbol{j}_\mathrm{e}$ and $q_\mathrm{ne} = \mathbf{1}_\mathrm{n} \cdot \boldsymbol{q}_\mathrm{e}$ (and discussed below) are imposed at each MFAM boundary face, with $\mathbf{1}_\mathrm{n}$ being the *outward* unit normal vector. This yields matrix equations for both ϕ and T_e at the centroids of the cells and of the boundary faces of the MFAM. A direct solver for sparse linear systems is used for the parallelized computation of the solution [178,179].

The reference $\phi = 0$ for the potential is set at the cathode boundary faces, so the anode potential is $\phi = V_\mathrm{d}$. The RLC filter unit, Fig. 3.1 (c), relates V_d to the imposed source voltage, V_s, and the varying discharge current, I_d, through

$$C\frac{dV_\mathrm{d}}{dt} + \frac{1}{L}\int_0^t (V_\mathrm{d} - V_\mathrm{s})d\tau + \frac{V_\mathrm{d} - V_\mathrm{s}}{R} = -I_\mathrm{d}. \tag{3.10}$$

This equation is integrated within the E-module over time with a first order numerical scheme.

The simulation domain extends up to the sheath edge of the quasineutral plasma, represented by the MFAM boundary faces. The solution for the (infinitely) thin Debye sheaths is detailed in the Appendix A. There, Eqs. (A.2) and (A.7) provide the appropriate conditions at each MFAM boundary face in the form of nonlinear relations for j_ne and q_ne versus the potential jump across the sheath, $\Delta\phi_\mathrm{sh}$.

At a dielectric wall, expressions for j_ne and q_ne are quite straightforward: a zero-collected electric current yields directly $j_\mathrm{ne} = -j_\mathrm{ni}$; Eq. (A.2) is then solved for $\Delta\phi_\mathrm{sh}$, and Eq. (A.7) yields q_ne. At the current-driving anode, with known potential V_d, the determination of j_ne and q_ne, at each anode face of the MFAM, requires to compute previously $\Delta\phi_\mathrm{sh}$ in the following way: Eq. (A.2) is combined with the Ohm's law (3.3) for j_ne yielding a non-linear implicit equation for $\phi = V_\mathrm{d} + \Delta\phi_\mathrm{sh}$ at each anode face. These equations are linearized and introduced in the matrix system yielding all ϕ; if needed, iterations on the implicit equations are run.

At the cathode boundary faces, the discharge current I_d divided by the cathode area defines the electron current density $j_\mathrm{ne}(> 0)$. The electron energy flux at each cathode face, expressed as $q_\mathrm{ne} - (5/2)T_\mathrm{e}j_\mathrm{ne}/e$, is set equal to $-2T_c j_\mathrm{ne}/e$, with $2T_c$ the average emission energy per electron. At the (quasineutral) axis, symmetry conditions imply $j_\mathrm{ne} = 0$ and $q_\mathrm{ne} = 0$; since the I-module yields $\partial n_\mathrm{e}/\partial r = 0$, one has $\partial p_\mathrm{e}/\partial r = 0$ and $\partial\phi/\partial r = 0$ too. Then, at the plume downstream (quasineutral) boundary a current-free condition $j_\mathrm{ne} = -j_\mathrm{ni}$ and a Maxwellian electron heat flux $q_\mathrm{ne} = -2T_\mathrm{e}j_\mathrm{ne}/e$ are imposed [107,177].

The time discretization of the electron equations follows a semi-implicit scheme [106], with a sub-timestep $\Delta t_\mathrm{e} = \Delta t/N_\mathrm{e}$ and $N_\mathrm{e} = O(1)$. This scheme allows to keep a linear system for T_e while reducing the value of N_e required for convergence. Finally, note that mesh interpolation of plasma variables between ion and electron modules is required.

3.3.2 Simulation settings

Figs. 3.2(b) and 3.2(c) show the PIC mesh and the MFAM used to simulate the HT5k. The main characteristics of the meshes and the relevant simulation parameters are listed in Tab. 3.2. A singular magnetic point ($\boldsymbol{B} = 0$) is located inside the thruster chamber. The green line at the left boundary in Fig. 3.2(b) represents the annular anode wall, while the small black box in Fig. 3.2(c) indicates the position of the central cathode boundary.

The prescribed xenon mass flow $\dot{m}_\mathrm{A}$ is injected from a Maxwellian reservoir through the whole annular anode featuring a flat profile with a sonic axial velocity based on its own temperature (Tab. 3.2). Considering the same injection properties, a neutral mass flow $\dot{m}_\mathrm{C} = 0.075\dot{m}_\mathrm{A}$ is injected through the cathode boundary together with an electron current equal to I_d. The emission energy of electrons at the cathode is set to $2T_c = 4.5$eV [180]; just as a sensitivity check, simulations run with $2T_c = 2.25$eV have shown no observable differences in the discharge, except naturally at the cathode neighborhood.

Wall recombination of ions contributes to the neutral density. Singly and doubly charged ions are generated volumetrically by electron-neutral collisions. Single ionization rates are obtained from the BIAGI database [181], while double ionization rates follow the Drawin model [182], including the reactions $A + e \rightarrow A^{++} + 3e$, and $A^{+} + e \rightarrow A^{++} + 2e$. Neutrals from ion recombination at walls are re-emitted diffusely considering complete ion energy accommodation at the wall, as suggested by several authors [183, 184]. Thus, the neutral emission energy is only given by the wall temperature, which is set to 850K [185]. Neutrals are reflected diffusely at the wall with zero energy accommodation; Refs. [99, 174] provide further details on the interaction of heavy-species macroparticles with walls.

The simulations monitor independently the populations of neutrals, singly-charged and doubly-charged ions. Each species population is controlled, setting a target number of 500 macroparticles per cell with a $\pm 10\%$ of tolerance [99].

The (ion) timestep in Tab. 3.2 is set so that a typical doubly-charged ion takes at least two timesteps to cross the smallest PIC cell. The simulations are started by injecting neutrals through the anode and cathode and considering a minimum background plasma density to trigger the discharge [174]. Every simulation features a total of 60000 timesteps (equivalent to 900 μs of simulation time) so that I_d undergoes a sufficiently large number of low-frequency (i.e. breathing mode) oscillation cycles. Five sub-timesteps per ion timestep ($N_\mathrm{e} = 5$) are used to integrate electron equations [99]. All the results shown in the following sections are time-averaged over several I_d cycles.

3.4 Simulation results and discussion

3.4.1 Fitting of turbulence parameters

In order to complete the electron model, the turbulence function $\alpha_\mathrm{t}(z, r)$ in Eq. (3.8) must be chosen. Since for each case in Tab. 3.1 only two experimental parameters, I_d and F, are known, the function α_t will be of the axial 'step-out' type shown in Fig. 3.2(d), with two fitting parameters only, α_t1 and $\alpha_\mathrm{t2}(> \alpha_\mathrm{t1})$, applying, respectively and approximately, inside and outside the channel. These step-out profiles have provided good

Simulation parameter	**Units**	**Value**
PIC mesh number of cells, nodes	-	2582, 2696
PIC mesh smallest grid size	mm	1
MFAM number of cells, faces	-	2848, 5830
MFAM average skewness [186]	-	0.058
Ion-moving timestep, Δt	ns	15
Total number of simulation steps	-	60000
Injected Xe velocity	ms^{-1}	300
Injected Xe temperature	K	850

Table 3.2: Main simulation parameters and mesh characteristics.

Case	V_s (V)	$\dot{m}_\mathrm{A}$ (mg/s)	$(\alpha_{\mathrm{t}1},\ \alpha_{\mathrm{t}2})$ (%)	I_d (A)	F (mN)	f_d (kHz)	$\Delta I_\mathrm{d}/I_\mathrm{d}$ (%)
1	300	14	(0.8, 8.0)	15.0	276	20.1	±13.0
2	400	14	(0.7, 5.0)	14.8	319	23.7	±6.8
*2**	*400*	*14*	*(0.8, 8.0)*	*16.7*	*335*	*26.2*	*± 7.2*
3	300	10	(0.8, 7.0)	9.8	187	17.8	±7.1
4	350	10	(0.7, 6.0)	9.8	203	15.2	±4.6
5	400	10	(0.7, 3.5)	9.4	213	18.2	±7.4

Table 3.3: Simulation results for the best fit of the turbulence parameters (column 4th), except Case 2*. Simulated results for I_d and F (5th and 6th columns) are within a 5% error of the values in Tab. 3.1. Frequency and relative half-amplitude of oscillation of I_d are listed in 7th and 8th columns.

fittings in previous studies [170, 184, 187, 188]. Hereafter, a particular step-out profile is referred to as $(\alpha_{\mathrm{t}1},\ \alpha_{\mathrm{t}2})$.

For each of the cases of Tab. 3.1, the pair $(\alpha_{\mathrm{t}1},\ \alpha_{\mathrm{t}2})$ has been tuned to reproduce (I_d, F) with a relative error smaller than 5%, thus consistent with the repeatability of the experimental data. The results are in Tab. 3.3 and Fig. 3.3. Turbulent transport is larger in the plume by nearly one order of magnitude, in line with the existing literature. Also aligned with previous studies for MS-HETs [154] and traditional HETs [188], there is a moderate change of the turbulence parameters with the operation point. The parameter $\alpha_{\mathrm{t}2}$ features the largest variation, increasing as V_s decreases and $\dot{m}_\mathrm{A}$ increases. The obtained turbulence fitting for (I_d, F) turns out to be also good reproducing the main oscillations of I_d, those known as the breathing mode [166, 176, 189, 190] and listed in Tab. 3.3. For instance, for Case 1, simulations yield an oscillation frequency $f_\mathrm{d} = 20.1$ kHz, close to the 22 kHz reported in experiments. For all cases, ΔI_d ranges between 4-13% of I_d, also consistent with experiments.

It is known that the thrust and, mainly, the discharge current are rather sensitive to the turbulence parameters. This is illustrated here by Case 2* in Tab. 3.3, which

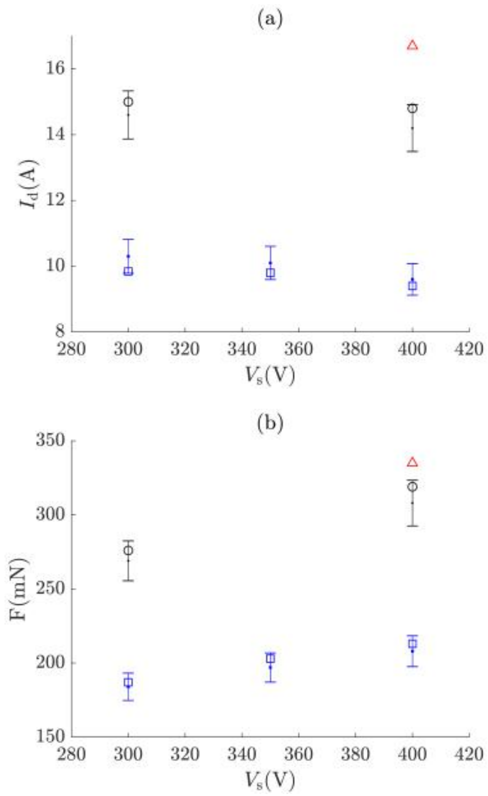

Figure 3.3: Comparison of experimental (error bars) and simulation results (empty markers) for (a) the I-V curve and (b) the F-V curve. The black circle and blue square markers correspond to $\dot{m}_{\mathrm{A}} = 14$ mg/s (Cases 1 and 2) and 10 mg/s (Cases 3 to 5), respectively. The red triangle marker corresponds to Case 2* in Tab. 3.3.

corresponds to the operation point of Case 2 but using the turbulent fitting of Case 1. Simulation errors with respect to experimental data are about 18% for I_{d} and 9% for F.

Nonetheless, these differences in performances do not change the main trends of the 2D discharge. Fig. 3.4(a)-(d) show the 1D axial profiles of ϕ, $E_{\mathrm{z}} \equiv -\partial\phi/\partial z$, T_{e} and n_{e}, along the thruster channel midline and for Cases 1, 2, and 2*. For Case 1, most of the ion acceleration occurs in the near plume along 2-3 channel lengths. This agrees with existing experimental measurements for a previous HT5k prototype [191]. In Case 2, with higher V_{s}, the total potential fall spans over a broader axial region, which would explain the slightly higher plume divergence we observe and is in line with previous numerical [154] and experimental [151, 152] studies. The peaks of T_e and E_z are outside the channel and move slightly downstream for higher V_{s}, in line with previous numerical studies too [154]. This behavior of E_{z} follows some experimental results reported in Ref. [152] but differs from those observed in Ref. [192], suggesting that the observed mild trends with V_{s} depend, at least partially, on the prototype and the operational conditions.

The change of turbulent collisionality from Case 2 to 2* in Fig. 3.4, results mainly in steeper gradients of ϕ and T_{e} in the region where α_t is transitioning from α_{t1} to α_{t2}, but plasma variables behave very similarly for Cases 2 and 2*, and typical MS effects are

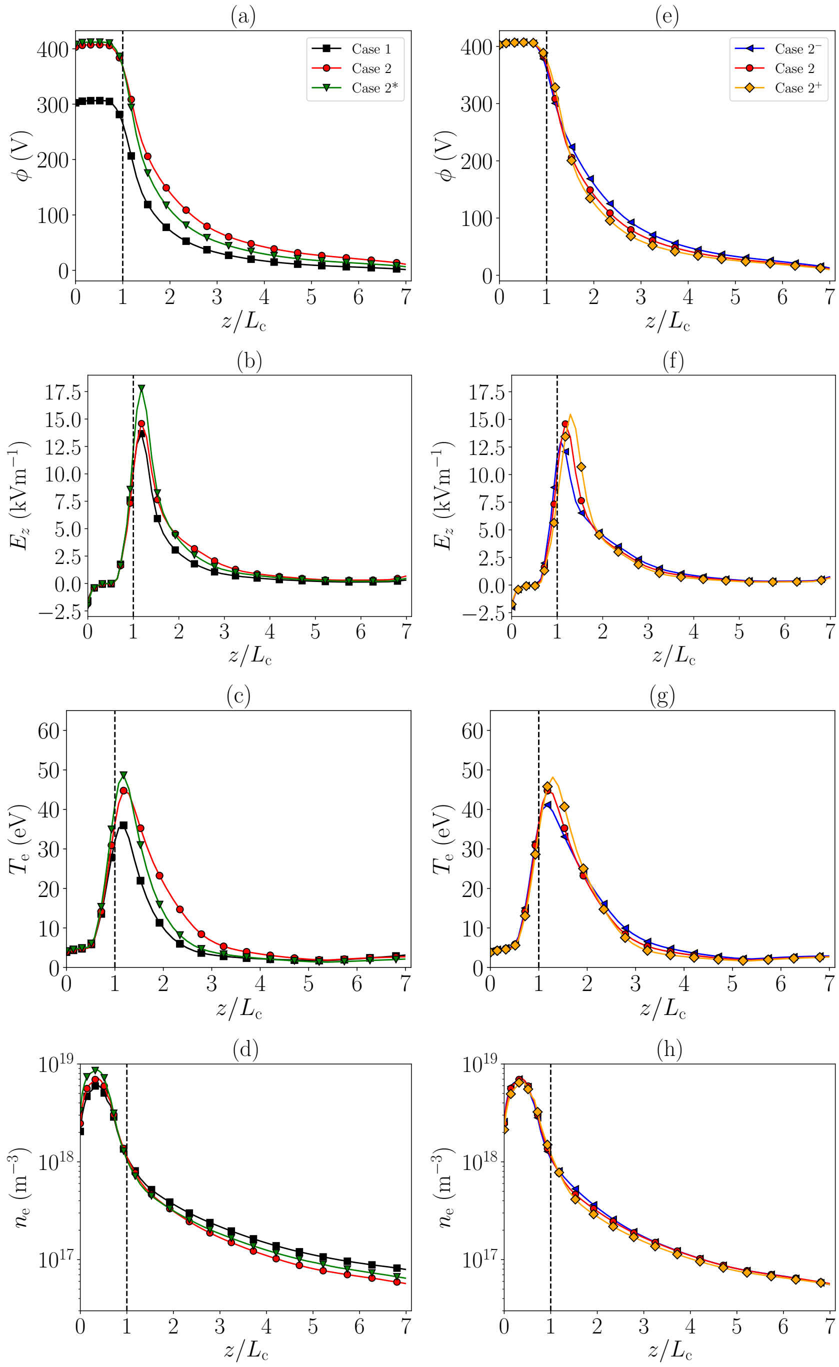

Figure 3.4: Time-averaged axial profiles along the thruster chamber midline (a)-(d) for Cases 1, 2 and 2* and (e)-(h) for Cases 2^-, 2 and 2^+ with ϕ, E_z, T_e and n_e, respectively, for each column.

reproduced in both cases, in line with the numerical studies of Refs. [157, 193].

Figures 3.4(e)-(h) show the effect on the discharge of moving the transition point $(\alpha_{t1} + \alpha_{t2})/2$ upstream or downstream. For Case 1 and at the mid-channel radius, that point was placed at $z/L_c = 1.46$ (for reference, the peak of the magnetic field is at

$z/L_\mathrm{c} = 1.29$). Cases 2^- and 2^+ displace the transition point to $z/L_\mathrm{c} = 1.28$ and 1.59, respectively. The variations of I_d are small, within the accepted range of 5%, while the value of F remains practically constant. Changes in the 2D discharge inside the chamber are barely perceptible, but mild changes on the location and values of the maximum E_z are observed. This suggests that the location of the transition point can be used to fit the location of the peak of E_z.

The strength of the maximum E_z can be adjusted using a third fitting parameter $\alpha_{\mathrm{t}3}$ around the peak of the magnetic field, as it is done in 'quenched turbulence models', in general with $\alpha_{\mathrm{t}3} < \alpha_{\mathrm{t}1}, \alpha_{\mathrm{t}2}$ [194–196]. One stage ahead in fitting techniques is due to Mikellides *et al.* [77], who adjust a multi-piecewise function α_t with a larger set of experimental plasma data. Interestingly, the resultant function α_t resembles a 'step-out plus quenched model', with $\alpha_{\mathrm{t}3} < \alpha_{\mathrm{t}1} < \alpha_{\mathrm{t}2}$.

In any case, all these are just numerical attempts to adjust time-averaged experimental data, without a firm theoretical basis (not even for extrapolating the function α_t from one operation point to another). The fitting problem is more severe for fully-2D MS topologies than for the traditional ones, which feature quasi-radial magnetic lines. Fortunately, this weakness in modeling accurately the slow turbulent transport of electrons does not preclude the study of other central features of the plasma discharge.

3.4.2 Analysis of the 2D plasma discharge

Case 1 in Tab. 3.3 is chosen for this analysis. Fig. 3.5 shows the 2D (z,r) maps of relevant time-averaged plasma properties inside the thruster chamber (left column) and in the whole simulation domain (right column). The neutral density map, Figs. 3.5(a)-(b), illustrates the effects of gas ionization plus the wall-born neutrals from ion recombination. The neutral density exhibits a decrease of about two orders of magnitude inside the thruster chamber, corresponding to a large propellant utilization. In addition, plot (b) shows well the injection and partial ionization of the neutral gas injected through the cathode. Then, the enhanced electron-neutral collisionality favours the coupling of cathode electrons with the main ion beam. The plasma density [Figs. 3.5(c)-(d)] inside the chamber is higher and more uniform than in conventional HETs, due likely to the acceleration region being moved outwards from the chamber. As usually, the plasma density presents its maximum at a central location inside the chamber, here close to the magnetic null point. As shown in Fig. 3.4, the increase of the T_e peak at higher V_s enhances gas ionization, augmenting slightly the peak of n_e inside the chamber. In contrast, the lower n_e in the near plume at higher V_s, is due to the larger ion acceleration. The right plot shows the secondary plasma plume created by ionization of cathode neutrals, which merges downstream with the main plume.

The electric potential [Fig. 3.5(e)-(f)] also presents a maximum close to the singular magnetic point. Potential variations are rather small inside the chamber, as expected in an MS-HET configuration. As commented already, the MS moves the acceleration region outside the chamber and equipotential lines follow approximately the magnetic lines there. Inside, the magnetic null point and the pressure gradients uncouple equipotential lines from magnetic ones. The electron temperature [Fig. 3.5(g)-(h)] peaks in the near plume, rather close to the maximum E_z. Temperature isolines follow closely magnetic lines and temperature gradients are very pronounced when the electron flow enters into the chamber. The temperature is below 5 eV near all chamber walls, which is indeed one of the main achievements of MS topologies [153, 154, 159] and leads to small energy losses to the walls.

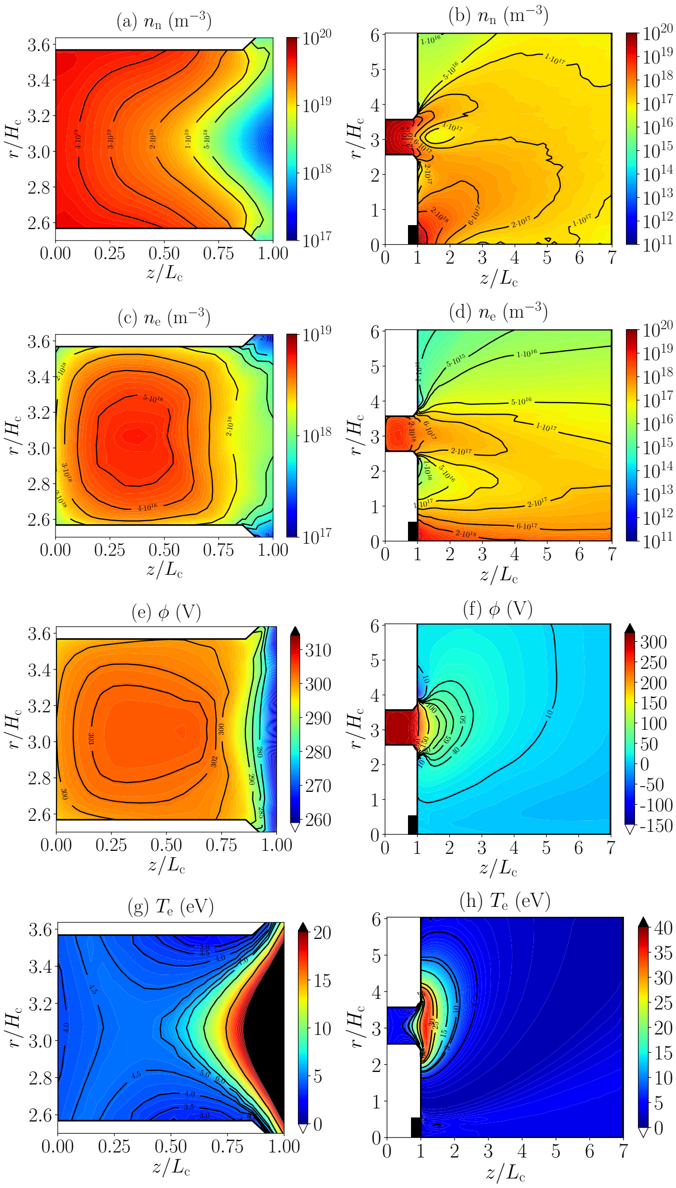

Figure 3.5: Time-averaged 2D (z,r) contour maps for Case 1. (a)-(b) Neutral density n_n, (c)-(d) plasma density n_e, (e)-(f) electric potential ϕ and (g)-(h) electron temperature T_e. The left column plots show magnitudes inside the thruster chamber, while the right column plots correspond to the whole simulation domain. The centrally-mounted cathode is indicated by the small black box.

Fig. 3.6 depicts 2D vector maps for the longitudinal components of the ion, electron,

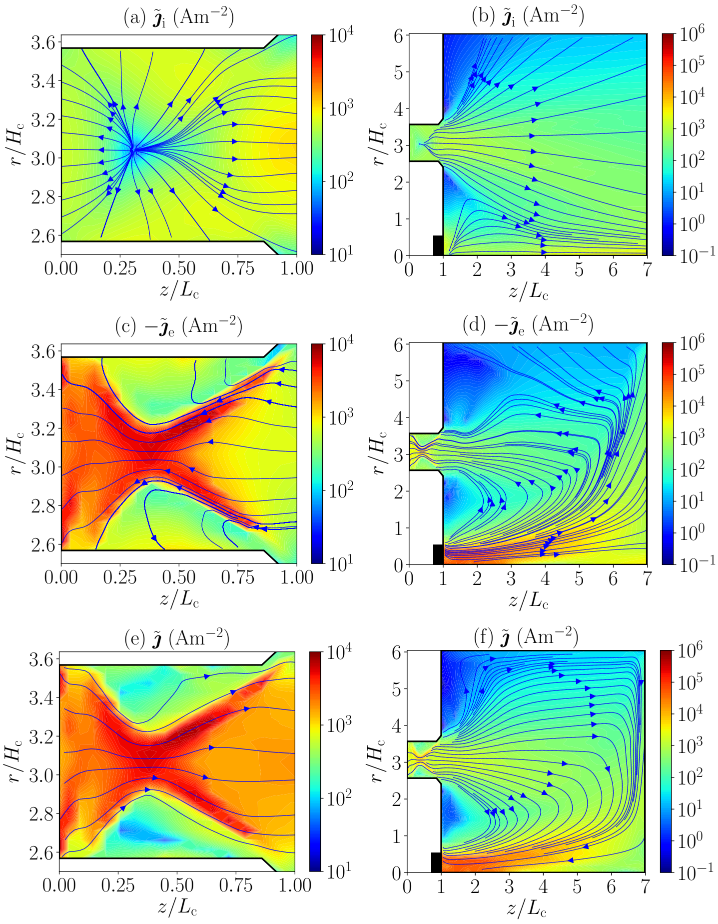

Figure 3.6: Time-averaged 2D (z,r) contour maps for Case 1. Magnitude of the longitudinal (a)-(b) ion current density vector $\tilde{\boldsymbol{j}}_{\mathrm{i}}$, (c)-(d) electron current density vector $\tilde{\boldsymbol{j}}_{\mathrm{e}}$ and (e)-(f) electric current density vector $\tilde{\boldsymbol{j}}$. Blue lines with arrows depict the streamlines of (a)-(b) $\tilde{\boldsymbol{j}}_{\mathrm{i}}$, (c)-(d) $-\tilde{\boldsymbol{j}}_{\mathrm{e}}$ and (e)-(f) $\tilde{\boldsymbol{j}}$. The left column plots show magnitudes inside the thruster chamber, while the right column plots correspond to the whole simulation domain. The centrally-mounted cathode is indicated by the small black box close to the axis.

and electric currents, defined as $\tilde{\boldsymbol{j}}_i = \boldsymbol{j}_i - j_{\theta \mathrm{i}} \mathbf{1}_\theta$ and so on. The ion current is obtained from a particle-to-mesh weighting algorithm, while the electron current comes out directly from the fluid model. The ion streamlines, Fig. 3.6(a)-(b), reflect the existence of backward, forward, and lateral ion flows. Although there is a point with $\tilde{\boldsymbol{j}}_i = 0$, notice that the ionization source is distributed in the whole channel volume and the streamlines represent the ion macroscopic behavior. Ions, practically unmagnetized, follow the electric field and are not prevented from impacting the channel walls. Interestingly, plot (a) shows nearly wall-parallel ion current streamlines close to the channel exit, a fact also observed experimentally [147]. Ion streamlines moving into the far plume present the expected divergence outside the thruster chamber. Plot (b) shows again how the secondary ion beam created around the cathode combines with the main beam downstream.

The longitudinal electron streamlines, Fig. 3.6(c)-(d), are all born from the cathode but they are split into one beam directed to the far downstream region, which neutralizes the main ion beam, and one beam moving into the interior of the thruster. This second beam follows first the magnetic lines, but then enters the chamber almost perpendicular to the magnetic field, and finally it is again channeled by the convergent-divergent magnetic lines. Interestingly, this last configuration does not constitute at all a magnetic nozzle [197] (the magnetic strength is null at the 'throat', instead of maximum) but it channels the electrons anyway. Still some electron streamlines are driven into lateral walls to cancel the ion flows there. It has also been realized that the neutral injection through the cathode enhances much the diffusive cross-field transport of the inward beam and the electric coupling of the cathode with the main beam. Finally, Figs. 3.6(e)-(f) show the 2D streamlines of the longitudinal electric current. The zero net collected current condition imposed at the dielectric walls and along the downstream boundary (which is assumed current-free locally) yields the expected current loops connecting anode and cathode.

To complete the description of the discharge, Figs. 3.7(a)-(c) plot the main plasma magnitudes along the thruster internal walls. The abscissa length s runs from the inner corner at the exit of the chamber towards the anode corner, continues along the anode, and finishes along the outer, interior wall of the chamber. Fig. 3.7(a) shows the electron temperature at the sheath edge and the sheath potential fall, $\Delta\phi_{\mathrm{sh}}$, this last one computed from the S-module. The temperature near all internal walls is rather low ($\sim$3-4 eV) and the ratio $e\Delta\phi_{\mathrm{sh}}/T_e$ is between 1 and 3. This ratio is affected by the SEE and the partially-depleted VDF of primary electrons, at the dielectric walls, and by the need to control the local flux of electrons, at the anode. The low T_{e} makes the SEE yield small: it is $\delta_{\mathrm{s}} \approx 0.2$ for $T_{\mathrm{e}} = 5$ eV.

Fig. 3.7(b) plots the electron and ion currents towards the walls (which are constant across the Debye sheaths). The plotted electron current density is the net one, i.e. the difference between the currents of primary and secondary electrons at the wall. Ion and electron current densities are identical at dielectric walls. At the anode, the backward ion current density is around a 20% of the electron current, which is a percentage larger than desirable. Fig. 3.7(c) plots the average ion and electron energy at the wall, per net particle impacting the wall, computed from Eqs. (A.5) and (A.8). The low values of $\Delta\phi_{\mathrm{sh}}$ yield ion-impact energies, $\mathcal{E}_{\mathrm{i,wall}}$, well below typical threshold values for wall erosion [154, 198], which is the main advantage expected from MS topologies.

3.4.3 Current and power balances

The ion current balance at steady state can be expressed as

$$I_{\mathrm{prod}} = I_{\mathrm{i}\infty} + I_{\mathrm{iD}} + I_{\mathrm{iA}} + I_{\mathrm{iC}}, \tag{3.11}$$

where: I_{prod} is the current of ions generated by ionization in the simulation domain; I_{iD}, I_{iA} and I_{iC} are the ion currents impacting the dielectric, anode and cathode walls, respectively [and defined in Fig. 3.2(b)]; and $I_{\mathrm{i}\infty}$ is the ion beam current leaving the domain at plume

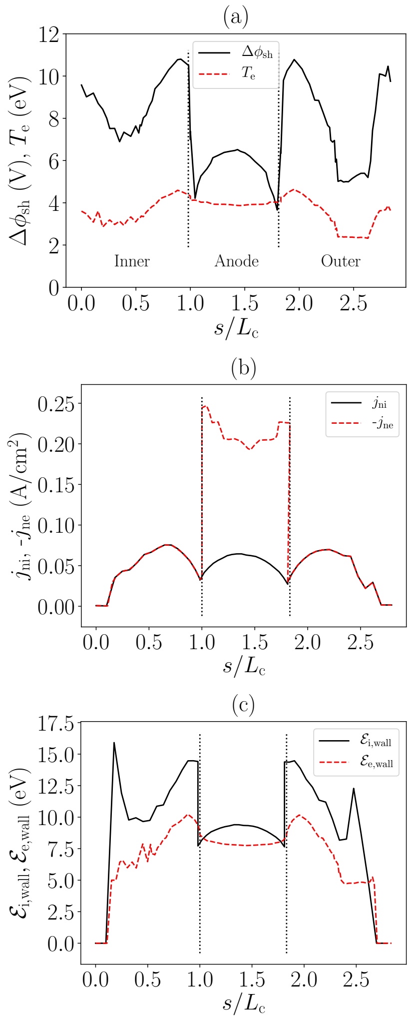

Figure 3.7: Time-averaged simulation results for Case 1 in Ref. 3.3. Coordinate s runs along the thruster chamber walls. Profiles of (a) potential fall across the sheath edge, $\Delta\phi_{\rm sh}$ and electron temperature, Te; (b) ion, $j_{\rm ni}$, and electron, $j_{\rm ne}$, current normal to the walls; and (c) ion, $\mathcal{E}_{\rm i,wall}$, and electron, $\mathcal{E}_{\rm e,wall}$, wall-impact energy.

boundaries, the only one contributing to thrust. All currents are defined as positive; $I_{\rm prod}$ comes out from a volumetric integration, and the other ones are computed from surface integrals at the domain boundaries.

Tab. 3.4 details $I_{\rm prod}$ for Cases 1 to 5 and how it is distributed among the different boundaries; $I_{\rm iC}$ is about one order of magnitude lower than $I_{\rm iA}$ and has not been included. The table also includes the propellant utilization, the current efficiency, and the charge efficiency, defined as

$$\eta_{\rm u} = \frac{\dot{m}_{\rm i\infty}}{\dot{m}}, \qquad \eta_{\rm cur} = \frac{I_{\rm i\infty}}{I_{\rm d}}, \qquad \eta_{\rm ch} = \frac{e\dot{m}_{\rm i\infty}}{m_{\rm i} I_{\rm i\infty}}, \tag{3.12}$$

respectively. Here $\dot{m} = \dot{m}_{\rm A} + \dot{m}_{\rm C}$, and $\dot{m}_{\rm i\infty}$ is the total ion mass flow across the plume

Case	V_s (V)	$\dot{m}_A$ (mg/s)	I_{prod} (A)	$I_{i\infty}/I_{prod}$	I_{iD}/I_{prod}	I_{iA}/I_{prod}	η_u	η_{cur}	η_{ch}
1	300	14	27.6	0.42	0.39	0.18	0.94	0.77	0.90
2	400	14	33.0	0.36	0.42	0.21	0.94	0.78	0.89
3	300	10	17.4	0.45	0.37	0.17	0.91	0.79	0.92
4	350	10	18.6	0.42	0.38	0.19	0.90	0.79	0.91
5	400	10	18.1	0.44	0.37	0.18	0.92	0.85	0.85

Table 3.4: Value of I_{prod} and fractions of I_{prod} corresponding to the different contributions to the current balance in Eq. (3.11) for Cases 1 to 5. Values of η_u, η_{cur} and η_{ch} for Cases 1 to 5.

Case	V_s (V)	$\dot{m}_A$ (mg/s)	P (kW)	η	P_{inel}/P	P_D/P	P_A/P	P_∞/P ($=\eta_{ene}$)	η_{div}	η_{disp}
1	300	14	4.43	0.57	0.15	0.07	0.05	0.74	0.89	0.87
2	350	14	5.73	0.57	0.13	0.07	0.04	0.74	0.86	0.90
3	300	10	2.91	0.56	0.14	0.06	0.05	0.74	0.88	0.85
4	350	10	3.40	0.56	0.13	0.06	0.05	0.75	0.85	0.88
5	400	10	3.76	0.57	0.11	0.05	0.04	0.78	0.84	0.86

Table 3.5: Value of P and fractions of P corresponding to different contributions to the power balance in Eq. (3.13) for Cases 1 to 5. Values of η, η_{ene}, η_{div} and η_{disp} for Cases 1 to 5.

boundaries. The trends of these partial efficiencies with source voltage and mass flow are the usual ones. Compared to a typical discharge in a conventional HET, η_u and η_{cur} are rather good, and the relative amount of doubly-charged ions, measured by η_{ch}, is similar. The relative current losses to the lateral walls, I_{iD}/I_{prod}, are similar to conventional HETs, because of the compensation of two trends: a higher plasma density and a lower electron temperature. For this prototype, the relative current losses to the anode, I_{iA}/I_{prod}, are high, likely due the existence of the null point not far way from the anode. Although further analyses would be needed, the conclusion here on the current balance is that the MS topology of the HT5k does not present clear advantages over a more conventional one. However, this is not going to be the conclusion with the power balance.

The plasma power balance for the steady state discharge is

$$P = P_\infty + P_D + P_A + P_{inel}, \tag{3.13}$$

where $P = I_d V_d + P_C$ is the total power deposited into the plasma discharge, sum of the discharge power and the net power delivered through cathode electron emission (P_C amounting to 1-2% of P); P_∞ is the plasma energy flow through the plume boundaries; P_D and P_A are the power losses at the dielectric walls and anode, respectively; and P_{inel} corresponds to the power losses due to inelastic (ionization and excitation) collisions. All powers are defined as positive. P_{inel} is obtained from a volumetric integral, P_∞ comes from a surface integral at the plume boundary, and P_D and P_A are computed from surface integrals at the respective walls (not at the Debye sheath edges). Eqs. (3.11) and (3.13) have also served to check that the numerical errors given by HYPHEN simulations are acceptable (below 2%).

Inelastic losses correspond entirely to electrons and they are roughly proportional to I_{prod} (notice that single and double ion creation has different ionization energies). Energy losses to walls D and A present contributions of ions and electrons, which were discussed in Sec. 3.4.2, and they are proportional to their respective currents I_{iD}, I_{iA} and $I_{\mathrm{eA}} = I_{\mathrm{d}} + I_{\mathrm{iA}}$. The downstream energy flow P_∞ corresponds mainly to ions but it also includes the residual electron energy flow in the far plume.

Tab. 3.5 lists the main contributions to the power balance and some related magnitudes for Cases 1 to 5. Observe that while the current losses to the lateral walls amount to about a 40% of I_{prod}, the energy losses to these walls amount to a mere 7%. Adding the energy losses to the anode, the total energy losses to the walls are just 9-12%, which can be considered an important achievement of MS topologies. Inelastic losses are consistent with the ion production: the ratio $P_{\mathrm{inel}}/I_{\mathrm{prod}}$ yields 23 eV as effective single-ionization cost (including the contribution from excitation collisions).

The thrust efficiency is defined and then factorized as

$$\eta = \frac{F^2}{2\dot{m}P} \equiv \eta_{\mathrm{ene}}\eta_{\mathrm{div}}\eta_{\mathrm{disp}}, \tag{3.14}$$

where F is the thrust, measured from plasma properties at the plume boundary. The energy, divergence, and dispersion efficiencies are defined, respectively, as

$$\eta_{\mathrm{ene}} = \frac{P_\infty}{P} \qquad \eta_{\mathrm{div}} = \frac{P_{\mathrm{z}\infty}}{P_\infty}, \qquad \eta_{\mathrm{disp}} = \frac{F^2}{2\dot{m}P_{\mathrm{z}\infty}}, \tag{3.15}$$

with $P_{\mathrm{z}\infty}$ being the flow of axial plasma (ion and electron) energy across the plume boundaries. Here: η_{ene} quantifies the relative power in the downstream plume, η_{div} assesses the plume divergence based on axial energy and total energy flows, and η_{disp} quantifies the level of velocity dispersion of all plasma species (which would be one for a mono-velocity gas). Plume energy flows include the residual energy of electrons, coming from their incomplete expansion in the finite simulation domain, but this is quite low: about 4% of P_∞ for Case 1.

Setting $\cos^2\alpha_{\mathrm{div}} = \eta_{\mathrm{div}}$, the half-divergence angles in these simulations are $\alpha_{\mathrm{div}} \sim$ 22-25 deg. As commented already, plume divergence increases slightly for higher V_{s}. The corresponding decrease in η_{div} is compensated by η_{ene} and η_{disp}, thus yielding mild variations of η. Previous studies for a different HET prototype also reported slight changes of η in the range V_{s} = 300-700 V [154]. Here, we find $\eta \sim$ 56% (or $\sim$ 61% if the 'anodic' thrust efficiency is used), the overestimate relative to measured values being just attributed to the slight overestimate of the simulated F.

3.5 Conclusions

The numerical simulations of the HT5k prototype with HYPHEN have allowed the testing of this code with MS topologies and a centrally-located cathode, and its partial validation with the limited experimental data available.

Turbulence transport has been modeled with a step-out profile of a phenomenological anomalous frequency, which has been fitted with experimental data of I_d and F. The observed trends and the moderate changes of the fitting with the operation point tend to agree with previous works in the literature. Oscillations of the discharge current agree well with experimental ones. A larger set of experimental data would allow a finer tuning of the turbulent transport, but it would probably not alter the present comprehension of the physics of the MS-HET.

A detailed picture of the plasma discharge has been shown for one operation point. The discussion has been focused on those aspects highlighting the effects introduced by the MS topology and the central cathode, over conventional thrusters with lateral cathodes. The MS topology shifts the acceleration region outwards and keeps a high-density, low-temperature plasma inside the chamber. This combination of plasma properties explains that plasma flows to walls are similar to those in conventional HETs. The low plasma temperature in the chamber implies low electric fields, small Debye sheaths around lateral walls, and low SEE, leading to a small energy deposition at the walls and small ion impact energies, well below the usual threshold for material sputtering.

In the near plume, a central cathode with both electron and neutral emission has been simulated. A secondary plasma plume is generated, which merges with the main one downstream. A fraction of the electron emission drifts towards the interior of the thruster perpendicular to the magnetic lines but, once inside, this current is again channeled by the magnetic lines until crossing the null point, except for a small part leaking with ions to the lateral walls.

Finally, detailed experimental measurements of the plasma discharge, in progress, would allow to validate more firmly the present simulation tool, especially those aspects where phenomenological approaches are still important, such as turbulent transport, plasma-wall interaction, and downstream boundary conditions.

Appendix A: The sheath model

The S-module of HYPHEN solves a planar, unmagnetized, collisionless, kinetic model of the thin Debye sheaths developing around the walls. The model includes SEE and retains other non-Maxwellian features of the electron VDF [199]. The S-module provides the appropriate boundary conditions for the quasineutral electron fluid equations, specifying, at each quasineutral MFAM boundary face (i.e. Debye sheath edge), the perpendicular electron current and heat flux.

Taking as reference a ceramic material with large SEE, the electric current density of primary (p) electrons from the quasineutral plasma into the wall is assumed to follow

$$j_\mathrm{np} = -(1-\delta_\mathrm{r})\sigma_\mathrm{rp}\, e\frac{n_\mathrm{e}\bar{c}_\mathrm{e}}{4}\exp\frac{-e\Delta\phi_\mathrm{sh}}{T_\mathrm{e}}, \tag{A.1}$$

which corresponds to a partially-depleted, partially-reflected Maxwellian VDF [199]. Here: $\Delta\phi_\mathrm{sh}$ is the potential fall in the sheath, $\bar{c}_\mathrm{e} = \sqrt{8T_\mathrm{e}/(\pi m_\mathrm{e})}$, δ_r is the fraction of primary electrons reaching the wall but being reflected back elastically by it; and σ_rp estimates the replenishment fraction of the VDF tail corresponding to impacting electrons. If δ_s is the SEE yield, the net, local electron current density to the wall is

$$j_{\rm ne} = j_{\rm np}(1-\delta_{\rm s}). \tag{A.2}$$

Kinetic studies of plasma-wall interaction [87, 160] show that $\sigma_{\rm rp} < 1$ because of the weak electron collisionality. Simulations results with $\sigma_{\rm rp}$ between 0.05 and 0.30 have revealed small effects on thruster performances and relevant plasma profiles. This is in agreement with experimental results evidencing a reduced influence of plasma-wall interaction on the plasma discharge in magnetically shielded thrusters [162, 163]. Based on this, $\sigma_{\rm rp} = 0.1$ is set for all simulations here, leaving further sensitivity analyses or more accurate models to further work.

For a conducting wall, such as the anode, we just take $\delta_{\rm s}, \delta_{\rm r} \approx 0$. For the lateral ceramic walls, $\delta_{\rm r}$ and $\delta_{\rm s}$ are modeled according to [199–203]

$$\delta_{\rm r}(T_e) = \delta_{\rm r0}E_{\rm r}^2/(T_{\rm e}+E_{\rm r})^2, \tag{A.3}$$

$$\delta_{\rm s}(T_{\rm e}) = \min\left(2T_{\rm e}/E_1, \delta_{\rm s}^*\right), \tag{A.4}$$

with δ_{r0}, E_r and E_1 being material dependent parameters, and $\delta_{\rm s}^*$ the effective upper-bounded SEE yield, corresponding to a space-charge limited (SCL) sheath. For the Boron Nitride walls of our thruster, the following values were taken: $\delta_{\rm r0} = 0.4$, $E_{\rm r} = 40$ eV, $E_1 = 50$ eV, and $\delta_{\rm s}^* = 0.986$.

The local net power density deposited by the whole electron population at the wall is

$$P''_{\rm ne,wall} = -\frac{j_{\rm ne}}{e}\mathcal{E}_{\rm e,wall}, \quad \mathcal{E}_{\rm e,wall} = \frac{2T_e - 2T_s\delta_s}{1-\delta_{\rm s}}, \tag{A.5}$$

where $\mathcal{E}_{\rm e,wall}$ is the average energy per net collected electron, and $2T_{\rm s}$ is the average energy per wall-emitted electron (equal to 4eV in the simulations here). Then, the net power density of electrons at the sheath edge is

$$P''_{\rm ne,edge} = P''_{\rm ne,wall} - j_{\rm ne}\Delta\phi_{\rm sh}. \tag{A.6}$$

At that edge the kinetic electron model inside the sheath is matched with the fluid electron model of the outer quasineutral domain. The matching of $j_{\rm ne}$ is obvious, but for the energy fluxes, the 'kinetic' one, $P''_{\rm ne,edge}$ of Eq. (A.6), is matched to the 'fluid' one, $-5T_{\rm e}j_{\rm ne}/(2e) + q_{\rm ne}$. This yields the heat flux at the sheath edge as

$$q_{\rm ne} = -\frac{j_{\rm ne}}{e}\left(e\Delta\phi_{\rm sh} + \mathcal{E}_{\rm e,wall} - \frac{5}{2}T_e\right), \tag{A.7}$$

which is used as boundary condition on the quasineutral domain for the electron fluid.

For ions, the PIC solution in the quasineutral domain is also matched to the kinetic sheath model at the sheath edge. Dedicated particle-to-surface weighting schemes for the PIC formulation of ions [99, 204, 205] yield directly the net ion power density at (the PIC side of) the sheath edge, $P''_{\rm ni,edge}$. Then, the power density deposited at the wall is $P''_{\rm ni,wall} = P''_{\rm ni,edge} + j_{\rm ni}\Delta\phi_{\rm sh}$ and the average energy per wall-impacting ion is

$$\mathcal{E}_{\rm i,wall} = \frac{eP''_{\rm ni,edge}}{j_{\rm ni}} + e\Delta\phi_{\rm sh}. \tag{A.8}$$

Chapter 4

Simulations of driven breathing modes of a magnetically shielded Hall thruster

This Chapter integrally reproduces the contents of the article "Simulations of driven breathing modes of a magnetically shielded Hall thruster", Plasma Sources Science and Technology, 32 (2023) [123]. The style has been adapted to the one of this document and the references have been unified in a single bibliography at the end of the document.

Abstract

The operation of a 5 kW-class magnetically shielded Hall effect thruster with sinusoidal modulation of the discharge voltage is investigated through simulations with a 2D axisymmetric hybrid (particle-in-cell/fluid) code. The dynamic response of the thruster for different modulation amplitudes and frequencies is presented and discussed. The analysis of partial efficiencies contributing to thrust efficiency allows identifying counteracting effects limiting net gains in performance figures. Voltage modulation enhances the amplitude of plasma oscillations and can effectively control their frequency when the modulation frequency is close to that of the natural breathing mode (BM) of the thruster. The 2D plasma solution reveals that the dynamics of the ionization cycle are governed by the electron temperature response, enabling a driven BM at the modulation frequency. For modulation frequencies far from the natural BM one, voltage modulation fails to control the plasma production via the electron temperature, and the natural BM of the thruster is recovered. High order dynamic mode decomposition applied to the 2D plasma solution permits analyzing the complex spatio-temporal behavior of the plasma discharge oscillations, revealing the main characteristics of natural and externally driven modes.

4.1 Introduction

The Hall effect thruster (HET) is a mature electric propulsion technology, with relatively high efficiency and thrust. However, in spite of its successful flight history, there currently exist significant efforts to increase HETs efficiency and lifetime in response to new, on-going, ambitious space missions, including the deployment of near-Earth satellite mega-constellations for fast and far-reaching telecommunications, or the colonization of the Moon and Mars. Magnetic shielding (MS) of the channel walls [59] is an effective technique that is enabling the design of the next HET generation, featuring enhanced performances and operational lifetimes compared to classical HET designs such as the Stationary Plasma Thruster (SPT) [25, 206], which relies on a magnetic lens type topology inside the channel.

The plasma discharge in both conventional and MS-HETs is characterized by the presence of the so-called breathing mode (BM), a low frequency (of the order of tens of kHz) discharge oscillation, which was first identified in the 1970s [207], and that has been typically linked to a predator-prey type ionization instability, involving an axial displacement of the ionization front inside the thruster chamber [166, 176, 189]. While the underlying physical mechanisms behind the onset and growth of the BM are still topics of present debate [208–212], several numerical and experimental studies have shown that, depending on the operating parameters, the BM can yield significant oscillations in the discharge current, I_d, with amplitudes of the order of its DC value, which can greatly affect the thruster performance [188, 190, 213–218]. Moreover, the external anode-to-cathode circuit is known to have a significant impact on the discharge oscillations. Barral *et al.* [219], analyzed resistor-inductor-capacitor (RLC) networks connecting anode and cathode and proportional-integral-derivative closed-loop control of the discharge voltage V_d or of the applied magnetic field intensity as active means for achieving nearly oscillation-free operation. Wei *et al.* [220] have reported experimental measurements showing a noticeable effect of the amplitude of I_d oscillation on the thruster performance by changing only the capacitor value of a RLC filter unit connected between anode and cathode. Therefore, the assessment of the impact of the BM on the discharge performance continues to be of central importance in HET research.

Recent works have explored the so-called externally driven BM operation of the thruster by applying some external modulation to V_d. These studies are motivated by different reasons. First, adding a sinusoidal voltage component to the anode potential with a frequency close to that of the natural (i.e., unmodulated) BM of the thruster has been proven effective to obtain time-coherent breathing oscillations, which have permitted the successful validation of time-resolved laser induced fluorescence (LIF) diagnostic techniques with application to HET discharges [221–226].

Second, a novel power processing unit (PPU) concept for HETs relying on a pulsating drive of the anode voltage through a pulsating boost chopper circuit demonstrated a good performance and reduced size and weight compared to conventional PPUs for a 1kW-class HET, thus making it attractive for high power applications [227]. A recent study has proven the pulsating boost chopper power supply (chopper PS) effective for controlling the frequency of the driven discharge oscillations for the case of a 1 kW-class anode-layer-type HET, which can greatly simplify electromagnetic interference (EMI) mitigation strategies on modern spacecrafts [228].

Moreover, several numerical and experimental studies of a modulated HET discharge have reported enhanced performance. Tamida *et al.* [229] applied a chopper PS on a conventional HET prototype with a frequency close to that of the natural BM and with a modulation amplitude ranging between 10% and 50% of the average value of V_d. Operating at 200 W, measurements indicate up to a 30% relative increase in thrust efficiency with respect to the unmodulated operation, the latter featuring a thrust efficiency of about 20%. Yamamoto and coworkers [227] reported 23% and 16% relative increases on the thrust efficiency and the thrust-to-power ratio, respectively, with respect to the unmodulated discharge at $V_\mathrm{d} = 150$ V (featuring values of 22% and 50 mN/kW), for a 1 kW-class HET operated with a chopper PS, when V_d is modulated at a frequency close to that of the natural BM. The enhanced thrust performance is attributed to the synchronization between the predator-prey oscillation mechanism and the PPU, which optimizes the plasma production and the ion acceleration processes. Measurements in the plasma plume of the same thruster reported a negligible effect of the modulation on the plume divergence and a wider ion energy distribution function in pulsating operation [230].

Romadanov *et al.* [231] studied the discharge and plasma plume characteristics of a 200 W cylindrical Hall effect thruster (CHT), operating with a sinusoidal V_d modulation, through experimental measurements and numerical simulations using a time-dependent 1D axial fluid model of the discharge including neutrals, electrons and singly-charged ions. The time-averaged voltage was set to 220 V, and the peak-to-peak modulation amplitude was varied from 8 to 50 V, while the modulation frequency was varied from 6 to 18 kHz, close to the 13 kHz natural BM frequency of the thruster. This type of modulation was proven effective to externally drive the BM resulting in enhanced I_d oscillations. The amplitude of the I_d oscillations and its root mean square (RMS) value were shown to depend on the modulation amplitude. Two distinct, linear and non-linear, response regimes were identified. Moreover, a resonant behavior of the discharge was observed, with maximum I_d oscillation amplitude and RMS value at modulation frequencies close to that of the natural BM. The resonant frequency was also shown to depend on the modulation amplitude, ranging from 10 to 13 kHz. RMS values of the propellant utilization and current efficiencies are found to increase in modulated operation. Close to the resonant frequency, and at large modulation amplitude (half-peak values around 9-11% of the time-averaged value) the authors report a total increase of up to a 20% in the product of the RMS values of the propellant utilization and current efficiencies compared to unmodulated operation. Enhanced oscillation and phase alignment of the ion velocity and ion density were postulated as one of the main reasons behind the observed behavior. The beam divergence is found almost unaffected by the external modulations. An experimental study [232] carried out with the same thruster showed that the rotating spoke instability, which could contribute to electron turbulent transport across the magnetic field, can be suppressed in the non-linear regime in externally driven BM operation, thus suggesting that voltage modulation can increase current efficiency.

A theoretical analysis demonstrated that for modulated operation, an increase of thrust can be obtained if the ion beam current and energy oscillate in-phase [233]. In

Ref. [234], time-dependent measurements of the ion current and ion energy in the plume of the CHTpm2, a permanent magnet version with magnetic shield of the low power (100-200 W) CHT mentioned above, operating with sinusoidal V_d modulation, revealed a decrease in the phase angle between these two signals when the modulation frequency was close to that of the natural BM, which is optimal for high thrust production. However, recent experiments and 1D axial hybrid numerical simulations of the modulated CHTpm2 have reported lower than expected thrust gains due to increased plume divergence and lower ion energy amplitude close to the resonant frequency of the modulation [235]. Moreover, thrust gains are counteracted by gains in discharge power, thus the anticipated net increase in thrust efficiency is not achieved.

Therefore, further analysis of the complex spatio-temporal behavior of main plasma magnitudes inside the thruster chamber is required to advance in the understanding of the modulated HET response. In particular, the dynamics of the ionization and acceleration regions, which are highly coupled in a classical HET discharge, play an essential role in determining the spectral characteristics and phase-frequency relationships of relevant plasma magnitudes. Accurate numerical simulations are of particular importance in this context, since experimental measurements of plasma profiles inside thruster chamber are scarce and challenging. Reduced 1D axial simulation models used in previous studies [231,235] reproduced the main features of the experimental results, although they present several important limitations. First, they have not been able to reproduce accurately the natural BM of the thruster; second, they miss important 2D effects and are not directly applicable to complex MS topologies of new low erosion MS-HET designs; third, they rely on approximate models for plasma-wall interaction, which determine plasma losses to the walls and thus the discharge performance; and fourth, they do not include double ionization collisions, whose contribution is generally non-negligible.

This work presents 2D numerical simulations of the dynamic response of a MS-HET operating with an external sinusoidal modulation of V_d. The simulations are carried out with the code HYPHEN [99, 105], a 2D axisymmetric multi-thruster simulator with a hybrid formulation featuring a particle-in-cell (PIC) model for heavy species (including neutrals, singly and doubly charged ions), and a magnetized drift-diffusive fluid model for electrons. In a recent work [122], HYPHEN capabilities were extended to the simulation of MS-HET discharges, and partial code validation was made against the HT5k prototype [149,173], in terms of discharge current and thrust for five different operation points, without any external modulation and using xenon as propellant. Taking as reference the simulation results for one of these unmodulated operation points, a parametric investigation of the modulated response of the thruster for different modulation amplitudes and frequencies is presented. The central goal is to assess the effect of modulation in this new, high-efficiency, 5 kW-class MS-HET prototype, which greatly differs from HET designs analyzed in previous modulation studies, and to advance in the understanding of the externally driven BM operation, which could be advantageous for high-power applications. The simulation results presented here are shown to be in good qualitative agreement with those reported in previous numerical and experimental studies, thus confirming that modulated MS-HET discharges also follow main trends found for conventional HETs. The 2D solution for the electron temperature, plasma density, neutral density and ionization production term inside the thruster chamber is analyzed to explain the impact of modulation in the discharge performance, and the transition between the externally driven and the natural BM is investigated. To the authors' knowledge, there are no previous full 2D numerical studies on a modulated MS-HET discharge.

The document is organized as follows. Section 4.2 summarizes the simulation model and settings and presents the natural BM of the thruster characterizing the unmodulated discharge. Section 4.3 discusses the effect of voltage modulation on main performance figures when compared to the unmodulated case. Parametric studies in terms of modulation amplitude and frequency are presented in Sections 4.3.1 and 4.3.2, respectively. Section 4.4 analyzes the 2D plasma solution to get a deeper insight on the dynamics of the modulated response. Section 4.5 studies the transition between the natural and the externally driven BM. Finally, conclusions are drawn in Section 4.6.

4.2 The natural breathing mode response to constant discharge voltage

The present study uses the same simulation model and main settings detailed in Ref. [122], which are briefly outlined here. Fig. 4.1 presents a sketch of the simulation domain, which corresponds to the cylindrical axisymmetric half meridian plane of the thruster, including the thruster chamber, with length L_c and width H_c, and the near plume region, with axial and radial extensions equal to $6L_\mathrm{c}$ and $6H_\mathrm{c}$, respectively. The electric circuit connecting the anode and the centrally-mounted cathode is also depicted in Fig. 4.1. Both the anode wall and cathode exit planes correspond to boundaries of the simulation domain. A discharge voltage V_d is imposed between the anode and the cathode. The reference $\phi = 0$ for the electric potential is set at the cathode boundary, so the anode potential is $\phi = V_\mathrm{d}$. The discharge current I_d flowing from cathode to anode through the external circuit is indicated in Fig. 4.1 according to the flow direction of positive charges.

A prescribed xenon neutral mass flow $\dot{m}_\mathrm{A}$ is injected through the anode wall. The xenon neutral mass flow injected through the central cathode is $\dot{m}_\mathrm{C} = 0.075\dot{m}_\mathrm{A}$. Simulations include singly-charged and doubly-charged ions generated through ionization collisions in the bulk plasma. Plasma recombination at the thruster walls contributes to neutral density. Charge-exchange collisions generating radially-expanding, slow ions and fast neutrals in the near plume are not considered in this study, since their effect on the discharge performance was found negligible for the present case.

The code version for HET simulations consists of three main modules coupled within a time-marching sequential loop: the Ion module (I-module), which follows a Lagrangian approach for simulating the neutral and ion species; the Electron module (E-module), which applies quasineutrality and solves a fluid model for the magnetized electron population; and the Sheath module (S-module), which provides the proper coupling between the quasineutral plasma bulk, and the thruster walls. While the I-module operates on a structured mesh of the simulation domain, the E-module uses an unstructured magnetic field aligned mesh (MFAM) [108], defined by the externally applied magnetic field $\boldsymbol{B}$ to limit the numerical diffusion arising from the strong anisotropic transport of magnetized

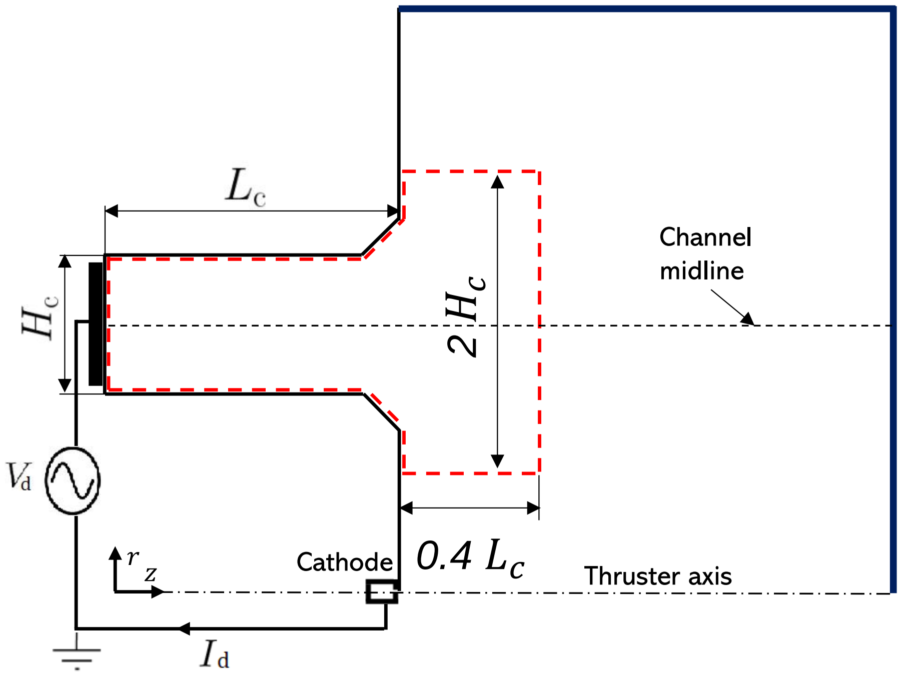

Figure 4.1: Sketch of the simulation domain and the anode-to-cathode external electrical circuit. The downstream plume boundary is indicated with a thick dark-blue line. The dashed red lines limit the region used for global magnitudes in Secs. 4.4 and 4.5.

electrons. The details of both meshes are provided in Ref. [122] and omitted here.

Every simulation timestep, the I-module takes as inputs the externally applied magnetic field $\boldsymbol{B}$, the electric field $\boldsymbol{E} = -\nabla\phi$, and the electron temperature T_e and performs the following tasks: (i) the propagation of macroparticles one timestep Δt forward, according to the electromagnetic fields acting on them; (ii) the injection of new macroparticles into the domain and the removal of exiting ones; (iii) the interaction of macroparticles with the thruster walls, such as neutral reflection and ion recombination; (iv) the generation of new ion macroparticles due to the ionization of neutrals; and (v) the computation, through a particle-to-mesh weighting process, of the macroscopic properties characterizing each heavy species, including the neutral density n_n, the plasma density $n_e = \sum_{s\neq e} Z_s n_s$ and the net ion current density $\boldsymbol{j}_i = \sum_{s\neq e} eZ_s n_s \boldsymbol{u}_s$, with Z_s, n_s and $\boldsymbol{u}_s$ the charge number, particle density and macroscopic velocity of the s^{th} ion population, including singly and doubly charged ions. Further details can be found in Refs. [99, 115, 174]. The E-module, taking these heavy-species magnitudes as inputs, solves a quasineutral, drift-diffusion fluid model for the magnetized electron population, including the plasma current conservation, a generalized Ohm's law solving for ϕ and the electron current density vector $\boldsymbol{j}_e = -en_e\boldsymbol{u}_e$, and the electron energy equation solving for T_e with a Fourier's law for the electron heat flux vector $\boldsymbol{q}_e$. The electron model is further detailed in Refs. [99, 107, 110], and it has been recently upgraded for the simulation of MS-HET discharges in Ref. [122].

HYPHEN E-module models the azimuth-averaged, wave-based electron anomalous

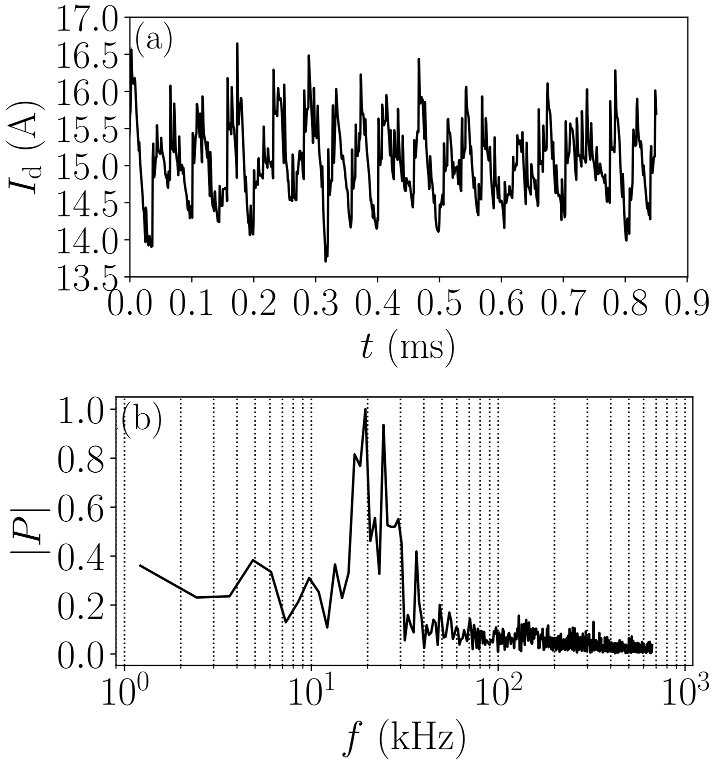

Figure 4.2: Natural BM of the unmodulated discharge for $V_{\mathrm{d}} = 300$ V and $\dot{m}_{\mathrm{A}} = 14$ mg/s, taken as reference for this work. (a) Time response of I_{d}. (b) Normalized frequency spectrum of I_{d}.

transport through a turbulent electron collisionality $\nu_{\mathrm{t}} = \alpha_{\mathrm{t}}\omega_{\mathrm{ce}}$, where $\alpha_{\mathrm{t}}(z, r)$ is a phenomenological function representing the electron local turbulence level and ω_{ce} is the electron cyclotron frequency [93, 96, 169, 176]. In Ref. [122], five different operation points were considered, defined by a pair (V_{d}, $\dot{m}_{\mathrm{A}}$). The former ranged from 300 to 400 V, and the latter from 10 to 14 mg/s. For each operation point, only two experimental measurements were available: the time-averaged values of the thrust and the discharge current $\bar{F}$ and $\bar{I}_{\mathrm{d}}$, respectively. Therefore, to complete the electron model, an axial step-out type function for $\alpha_{\mathrm{t}}(z, r)$, which has provided good fittings in previous studies [170, 184, 187, 188], was chosen, featuring two fitting parameters only: α_{t1} and $\alpha_{\mathrm{t2}}(> \alpha_{\mathrm{t1}})$ acting approximately inside and outside the thruster chamber, respectively. For each operation point, the pair (α_{t1}, α_{t2}) was tuned to reproduce the experimental values ($\bar{I}_{\mathrm{d}}$, $\bar{F}$) with relative errors below 5%. The obtained turbulent fittings yielded numerical results in good agreement with experimental measurements of plasma magnitudes for a similar prototype [79, 191], and turned out to be also good reproducing the main oscillations of I_{d}, which correspond to the natural BM of the thruster, as described later. Previous studies have successfully developed more advanced empirically-calibrated models for $\alpha_{\mathrm{t}}(z, r)$, informed by local plasma properties [77, 236, 237]. Moreover, non-invasive time-resolved measurements have recently shown a direct correlation between the anomalous collision frequency and breathing cycle [238]. Despite current remarkable efforts, the precise characterization and modeling of the anomalous electron transport still remains an open problem in HET research, subject to several challenges that block the development of predictive simulation tools, including the non-uniqueness of empirically-calibrated more elaborated models [77, 239]. Here, the experimental data availability for the MS-HET prototype limits the tuning of more complex turbulent models.

The present work takes as reference the simulation case 1 of Ref. [122]. For simplicity, the RLC filter unit connecting anode and cathode in Ref. [122] is not included in this work (since its effect on I_{d} was proven negligible). Therefore, this unmodulated simulation case features $V_{\mathrm{d}} = 300$ V (constant with time) and $\dot{m}_{\mathrm{A}} = 14$ mg/s. For this case, the fitting process yields $(\alpha_{\mathrm{t1}}, \alpha_{\mathrm{t2}}) = (0.8, 8)\%$. The oscillations of I_{d} are shown in Fig. 4.2(a). The time-averaged value of the discharge current is $\bar{I}_{\mathrm{d}} = 15$ A, and it features a half-peak amplitude ΔI_{d} of about 6.7% of $\bar{I}_{\mathrm{d}}$, consistent with experiments. Fig. 4.2(b) shows the normalized frequency spectrum of I_{d}. The dominant frequency $f_{\mathrm{BM}} = 20$ kHz corresponds to the natural BM, which is close to the 22 kHz reported in experiments. The frequency spectrum in Fig. 4.2(b) reveals the spectral complexity of I_{d}, with several peaks at frequencies close to f_{BM}. This result suggests that the natural discharge oscillations can be represented by a non-harmonic cluster of several modes, similar to those identified in a recent study through high order dynamic mode decomposition (HODMD) for a conventional SPT-100-like HET discharge [240]. The application of HODMD to this unmodulated reference case is left for Sec. 4.4. In the rest of the paper, simulation cases including V_{d} modulation are compared with this unmodulated reference case.

4.3 Effect of voltage modulation on main performance figures

The sinusoidal modulation applied on the anode-to-cathode discharge voltage (refer to Fig. 4.1) is defined as

$$V_{\mathrm{d}}(t) = \bar{V}_{\mathrm{d}} \left[1 + \varepsilon \sin\left(2\pi f_{\mathrm{s}} t\right)\right], \tag{4.1}$$

where $\bar{V}_{\mathrm{d}}$ is the constant time-averaged discharge voltage value, ε is the relative half-peak modulation amplitude, and f_{s} is the modulation frequency.

In order to compare with the unmodulated reference case presented in Sec. 4.2, all modulated cases analyzed in this work consider the same operation point, characterized by the pair $(\bar{V}_{\mathrm{d}}, \dot{m}_{\mathrm{A}}) = (300$ V, 14 mg/s). Each modulation case is defined by the pair $(f_{\mathrm{s}}, \varepsilon)$; the unmodulated reference case will be referred to as $f_{\mathrm{s}} = 0$ or $\varepsilon = 0$. Secs. 4.3.1 and 4.3.2 present parametric studies on ε and f_{s}, respectively. Time-averaged values of main performance figures, including a valuable set of partial efficiencies (defined below), are reported for all simulated cases.

Computing efficiencies in a highly oscillating HET discharge requires special care. Here, meaningful estimations of the thrust efficiency and a set of partial efficiencies will be obtained considering time-averaged quantities over a sufficiently large number of complete discharge oscillation cycles. The thrust efficiency is defined and factorized, in terms of the time-averaged variables, as

$$\eta = \frac{\bar{F}^2}{2\dot{m}\bar{P}_{\mathrm{d}}} \equiv \eta_{\mathrm{u}}\eta_{\mathrm{cur}}\eta_{\mathrm{vol}}\eta_{\mathrm{div}}\eta_{\mathrm{disp'}}, \tag{4.2}$$

being $\bar{P}_{\mathrm{d}} = \overline{I_{\mathrm{d}}V_{\mathrm{d}}}$ the time-averaged discharge power deposited into the plasma (the net power delivered through cathode electron emission is around 1-2% of $\bar{P}_{\mathrm{d}}$ and has been neglected here). The propellant utilization and the current efficiency are defined as

$$\eta_{\mathrm{u}} = \frac{\bar{\dot{m}}_{\mathrm{i}\infty}}{\dot{m}}, \qquad \eta_{\mathrm{cur}} = \frac{\bar{I}_{\mathrm{i}\infty}}{\bar{I}_{\mathrm{d}}}, \tag{4.3}$$

respectively, where $\dot{m} = \dot{m}_{\mathrm{A}} + \dot{m}_{\mathrm{C}}$, $\bar{\dot{m}}_{\mathrm{i}\infty}$ and $\bar{I}_{\mathrm{i}\infty}$ are the time-averaged ion mass flow and ion beam current across the downstream plume boundary, respectively, and m_{i} and e are the xenon atom mass and the electron charge, respectively. The voltage, divergence, and dispersion efficiencies are defined, respectively, as

$$\eta_{\mathrm{vol}} = \frac{\bar{P}_{\infty}/\bar{I}_{\mathrm{i}\infty}}{\bar{P}_{\mathrm{d}}/\bar{I}_{\mathrm{d}}},\ \eta_{\mathrm{div}} = \frac{\bar{P}_{\mathrm{z}\infty}}{\bar{P}_{\infty}},\ \eta_{\mathrm{disp'}} = \frac{\bar{F}^2}{2\bar{\dot{m}}_{\mathrm{i}\infty}\bar{P}_{\mathrm{z}\infty}}, \tag{4.4}$$

with $\bar{P}_{\infty}$ and $\bar{P}_{\mathrm{z}\infty}$ the time-averaged flows of total and axial plasma energy across the downstream plume boundaries, respectively, and $e\bar{P}_{\infty}/\bar{I}_{\mathrm{i}\infty}$ the time-averaged effective energy of ions downstream. The values of $\bar{F}$, $\bar{P}_{\infty}$ and $\bar{P}_{\mathrm{z}\infty}$ are computed from the corresponding surface integrals at the downstream plume boundary considering all plasma species (the contributions of neutrals and electrons are found negligible in all cases). The product $\eta_{\mathrm{cur}}\eta_{\mathrm{vol}}$ quantifies the fraction of $\bar{P}_{\mathrm{d}}$ transferred to the downstream plume; η_{div} assesses the plume divergence based on axial energy and total energy flows; and $\eta_{\mathrm{disp'}}$ quantifies the level of velocity dispersion of all plasma species (which would be one if only axial mono-energetic ions contribute to thrust and power downstream).

Additionally, the charge efficiency,

$$\eta_{\mathrm{ch}} = \frac{e\bar{\dot{m}}_{\mathrm{i}\infty}}{m_{\mathrm{i}}\bar{I}_{\mathrm{i}\infty}}, \tag{4.5}$$

is equal to one if no doubly-charged ions are generated, and decreases with the production of doubly-charged ions.

To show the effect of discharge oscillations on the performance figures estimations, and to establish a fairer comparison with the results reported in Ref. [231], RMS values of I_{d} and F, and estimations of the efficiencies above using RMS values of the involved quantities are also reported in this work. For any time series $y_1, \ldots, y_K \in \mathbb{R}$, its RMS value is defined as

$$y_{\mathrm{RMS}} = \sqrt{\frac{1}{K}\sum_{k=1}^{K} y_k^2}. \tag{4.6}$$

$\bar{I}_{\mathrm{d}}$ (A)	$\Delta I_{\mathrm{d}}/\bar{I}_{\mathrm{d}}$ (%)	$\bar{F}$ (mN)	$\Delta F/\bar{F}$ (%)	η	η_{u}	η_{cur}	η_{vol}	η_{div}	$\eta_{\mathrm{disp'}}$	η_{ch}
15.0	±6.7	280	± 15.1	0.578	0.932	0.763	0.947	0.907	0.946	0.897

Table 4.1: Performances for the unmodulated case operating at $(\bar{V}_{\mathrm{d}}, \dot{m}_{\mathrm{A}}) = (300$ V, 14 mg/s). RMS and time-averaged values are approximately the same for this case.

4.3.1 Modulation amplitude parametric study

A parametric investigation on the effects of the modulation amplitude is presented in this section. For all modulated simulation cases analyzed here, the modulation frequency is set equal to that of the natural BM characterizing the unmodulated discharge presented in Sec. 4.2, so that $f_{\mathrm{s}} = f_{\mathrm{BM}} = 20$ kHz. Results for four modulated discharges with relative half-peak amplitude ε =2.5, 6.25, 12.5 and 25% are presented and compared with the unmodulated reference case in Sec. 4.2 ($\varepsilon = 0$).

The results for the time-averaged and RMS values of I_{d} and F, and their oscillation amplitudes are in Fig. 4.3. Tab. 4.1 contains these data only for the unmodulated case. A monotonic growth of I_{d} and F RMS values and their oscillation amplitudes with the modulation amplitude is found, in line with the results reported in Ref. [231]. As expected, RMS values are noticeably higher than their corresponding (arithmetic) time-averaged values when signal oscillations are large. In Refs. [225, 231], the linear and non-linear

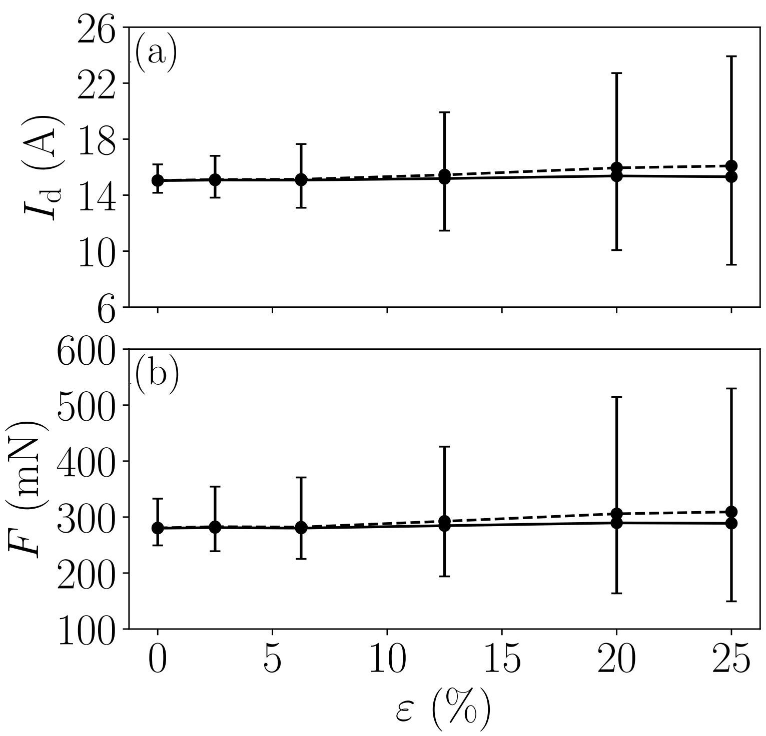

Figure 4.3: Time-averaged (solid lines) and RMS values (dashed lines) of (a) I_{d} and (b) F versus the modulation relative half-amplitude ε. Vertical bars indicate signals maxima and minima, thus yielding the oscillation amplitude ΔI_{d} and ΔF.

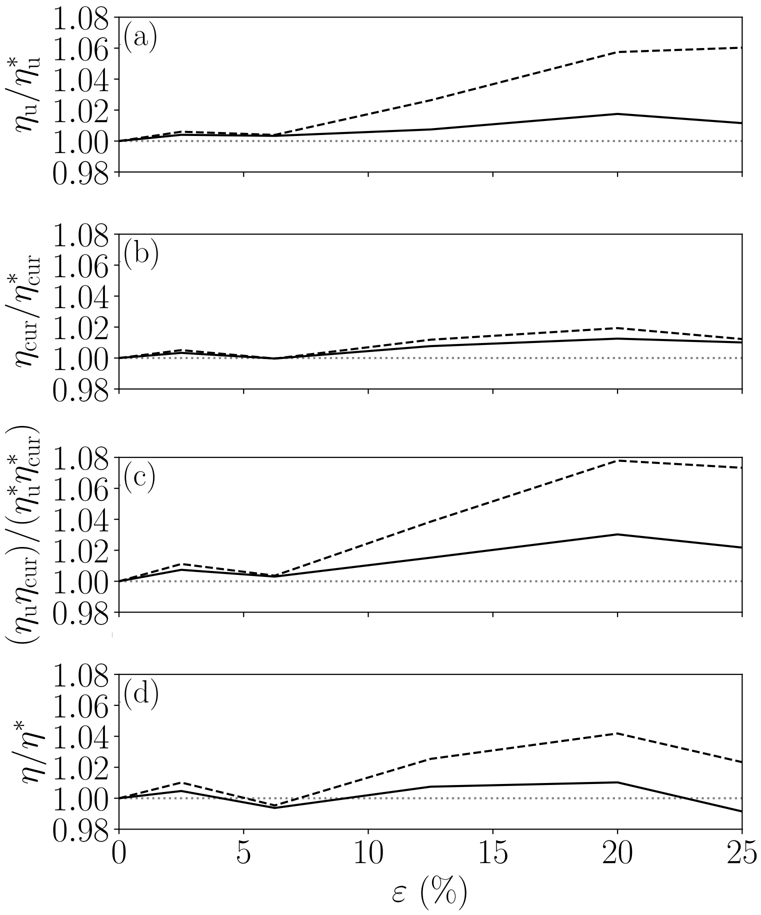

Figure 4.4: Total and partial efficiencies, relative to the unmodulated case (with asterisk and detailed in Tab. 4.1), versus the amplitude of oscillation, for f_s = 20 kHz. Time-averaged (solid lines) and RMS values (dashed lines) are plotted.

responses of a 200 W CHT prototype against the amplitude of the anode voltage modulation were identified. In the linear regime, at low modulation amplitude (up to $\varepsilon \sim 5\%$), the amplitude of the I_d oscillations increases linearly with the modulation amplitude while the RMS values remain nearly constant. In the non-linear regime, at higher modulation amplitudes, I_d oscillation amplitude and RMS values exhibit a superlinear growth with the modulation amplitude. Interestingly, these two regimes are also observed in Fig. 4.3(a).

The time-averaged and RMS values for the enhanced F shown in Fig. 4.3(b) in the non-linear regime are consistent with the results presented in Refs. [233–235], where it is shown that, for modulated operation, an increase in F can be obtained when oscillations of the ion beam current and energy are high and their phase shift is low. These aspects are analyzed in Refs. [234] and [235] considering modulated discharges with different modulation frequencies (close to the natural BM) at a constant modulation amplitude, an analysis which is undertaken in the next section.

Fig. 4.4 compares the total and partial efficiencies of modulated cases with the unmodulated case of Tab. 4.1, identified there by an asterisk. The trends of η_{u} and η_{cur} with the modulation amplitude are in good qualitative agreement with the experimental measurements and numerical results reported in Ref. [231] (propellant utilization values reported there correspond to our ratio $\eta_{\mathrm{u}}/\eta_{\mathrm{ch}}$).

Section 4.4 will show that ionization is enhanced by external modulation, thus corresponding to a larger η_{u}. A similar behavior, but with slighter changes, is found for η_{cur}. The increase in η_{cur} (especially in the non-linear regime) is due to an enhancement of the ion beam current $I_{\mathrm{i}\infty}$ with the voltage modulation. 1D numerical simulations and experiments reported in Refs. [231, 235] indicate that the enhanced $I_{\mathrm{i}\infty}$ is related to the increase in ε and the phase alignment of the ion density and energy at the near plume (i.e. end of the acceleration region). The same behavior (not shown) is found in our simulations. Finally, since $\eta/\eta^* < (\eta_{\mathrm{u}}\eta_{\mathrm{cur}})/(\eta^*_{\mathrm{u}}\eta^*_{\mathrm{cur}})$, the product $\eta_{\mathrm{vol}}\eta_{\mathrm{div}}\eta_{\mathrm{disp}'}$ decreases with ε increasing, thus concluding that voltage modulation has a small effect on thrust efficiency due to the different trends of the partial efficiencies.

The comparison of solid lines (time-averaged values) and dashed lines (RMS values) in Fig. 4.4 indicates that using RMS values to estimate efficiencies does not seem appropriate in scenarios with high discharge oscillations, and it may lead to significant misestimation of the performance figures. This is particularly the case for η_{u} defined in Eq. (4.3), which is reported to increase up to a 6% if estimated with RMS values, and only up to a 2% if obtained with time-averaged quantities. Discrepancy between these particular values is induced by oscillations in $\dot{m}_{\mathrm{i}\infty}$ exclusively.

4.3.2 Frequency parametric study

Setting the amplitude modulation to $\varepsilon = 25\%$, this section presents simulation results for f_{s} ranging from half to double the dominant frequency of the natural BM, $f_{\mathrm{BM}} = 20$ kHz. Fig. 4.5(a) shows the normalized frequency spectrum of I_{d} and Fig. 4.5(b) its quasi-periodic time response for three modulated cases: $f_{\mathrm{s}} = 10$, 18 and 40 kHz. These results reveal several aspects. First, the low-frequency I_{d} oscillations are driven by the V_{d} modulation, presenting a dominant frequency equal to f_{s}. Second, the modulated cases exhibit a much simpler I_{d} frequency spectrum than that of the unmodulated one in Fig. 4.2: a single prominent peak at f_{s} is found, corresponding to highly coherent I_{d} oscillations. This result is in line with experimental studies reporting that sinusoidal voltage modulation close to the natural BM yields quasi-periodic discharge oscillations [221, 225, 226].

In Fig. 4.5(b) the modulated discharge exhibits a clear capacitive/inductive character for $f_{\mathrm{s}} = 10/40$ kHz, with I_{d} ahead/behind V_{d}, respectively. A similar behavior has been reported in experimental studies for a 1kW-class HET operated with a chopper PS [227], and in experimental and numerical studies for the CHTpm2 prototype with sinusoidal voltage modulation [235].

As already seen in Sec. 4.3.1, modulated cases feature higher I_{d} oscillation amplitude than the unmodulated one. To further investigate this aspect, Fig. 4.6 shows the I_{d} and F response for several frequencies between 10 and 40 kHz. Interestingly, the oscillations of

I_d and F exhibit a non-monotonic behavior with f_s. In fact, the modulated response exhibits a resonant-kind behavior similar to that reported in experiments and 1D numerical simulations for the 200 W electromagnetic CHT [231] and its permanent magnet version CHTpm2 [234, 235]. This resonant response of the thruster is characterized by enhanced I_d and F oscillations for an interval of f_s close to f_{BM}.

In Ref. [231], the resonant modulation frequency f_r, is defined as the modulation frequency for which the I_d oscillation amplitude and its RMS value are maximum. The value of f_r is shown to depend on the modulation amplitude, being slightly lower than f_{BM} for high modulation amplitude ($\varepsilon = 9\%$), and approximately equal to f_{BM} for low modulation amplitude ($\varepsilon < 5\%$). At resonance, for both the electromagnetic and the permanent magnet versions of the 200W CHT, it is found $\Delta I_d/I_d \sim \pm 100\%$ for $\varepsilon = 9\%$ [231] and $\varepsilon = 18.2\%$ [235], respectively. For the latter, $\bar{I}_d$ and $\bar{F}$ are found to increase a 6% and 4% with respect to the unmodulated case, respectively [235].

Here, for $\varepsilon = 25\%$, the maximum oscillation amplitude of I_d is $\Delta I_d/I_d \sim \pm 50\%$ at $f_s = 18$ kHz, while RMS values are maximum at $f_s = 17$ kHz. Therefore, there exists a resonance region centered at a resonant frequency f_r ~17-18 kHz, slightly lower than $f_{BM} = 20$ kHz, with a width of 2-3 kHz, shaded in blue in Fig. 4.6. Within this resonance region $\bar{I}_d$ and $\bar{F}$ are shown to increase a 3% and 5% with respect to the unmodulated reference case, respectively. Interestingly, doubling and halving f_s with respect to f_{BM} leads to roughly the same decrease in I_d oscillation amplitude and RMS value. At lower modulation amplitudes, f_r is found to approach f_{BM}. In particular, for

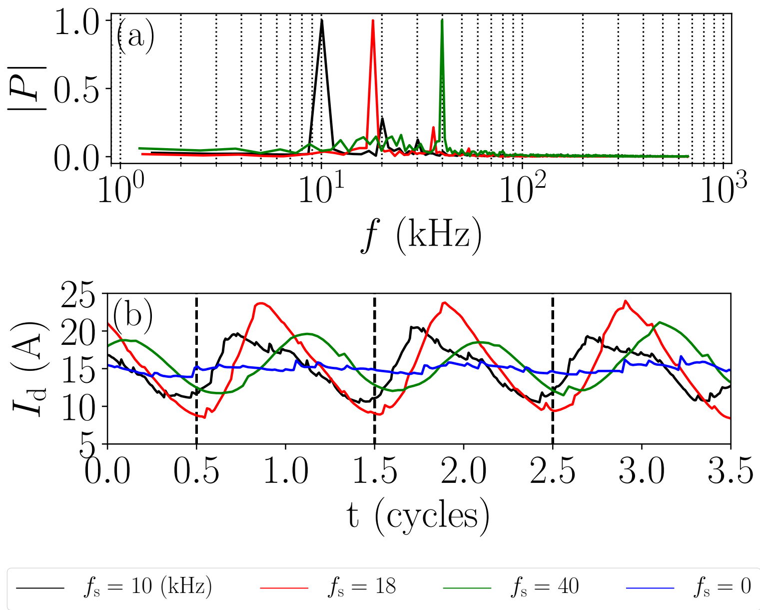

Figure 4.5: Modulated cases with $\varepsilon = 25\%$ and $f_s = 10$, 18 and 40 kHz (black, red and green solid lines, respectively) and $f_s = 0$ (blue). (a) Normalized frequency spectrum of I_d. (b) Time response of I_d for 3.5 modulation cycles, or 3.5 natural BM cycles for $f_s = 0$; dashed vertical lines mark the minima of $V_d(t)$ for $f_s \neq 0$.

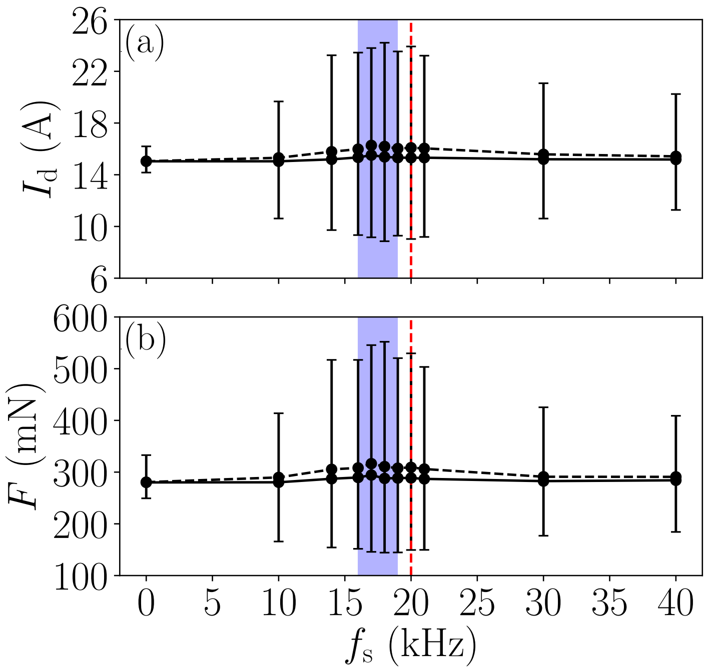

Figure 4.6: Time-averaged (solid lines) and RMS values (dashed lines) of (a) I_d and (b) F versus the modulation frequency f_s. Vertical bars indicate signals maxima and minima, yielding their corresponding oscillation amplitude, ΔI_d and ΔF. The blue, shaded region indicates the approximate location and extension of the resonant region and the red, dashed line corresponds to f_BM. The oscillations for $f_\mathrm{s} = 0$ are plotted too.

$\varepsilon = 6.25\%$, we find $f_\mathrm{r} = f_\mathrm{BM}$. These results reveal the prominence of the natural BM of the thruster over the external modulation on the low-frequency discharge oscillations for low modulation amplitude. The transition between the natural and externally driven BM at lower modulation amplitude is detailed in Sec. 4.5.

Fig. 4.7 shows the changes in efficiencies for modulated cases with respect to $f_\mathrm{s} = 0$ versus the modulation frequency. Slight changes (of about 3-4% maximum) are found in all efficiency figures, in line with the results in Ref. [235]. The non-monotonic behavior of the thrust efficiency η close to resonance is also in good agreement with numerical and experimental results reported there. The maximum η gains with respect to the unmodulated reference case occur within the resonance region and are limited to $\sim$2% only, as a consequence of counteracting contributions of all the partial efficiencies in Eq. (4.4), as described next.

The maximum of η_u is close to the resonance frequency, as in Refs. [231, 235]. The current and voltage efficiencies, η_cur and η_vol, do not exhibit here clear trends with f_s. Experimental studies in Ref. [231] do not report a clear trend of η_cur either, while η_cur is found to remain nearly constant in Ref. [235]. All modulated cases feature a smaller $\eta_{\mathrm{disp}'}$ than the unmodulated case, with a minimum in the resonance region, thus indicating a larger velocity dispersion in the ion velocity distribution function (VDF) for those cases.

For a given species, the time-averaged axial flux-VDF of particles leaving the domain

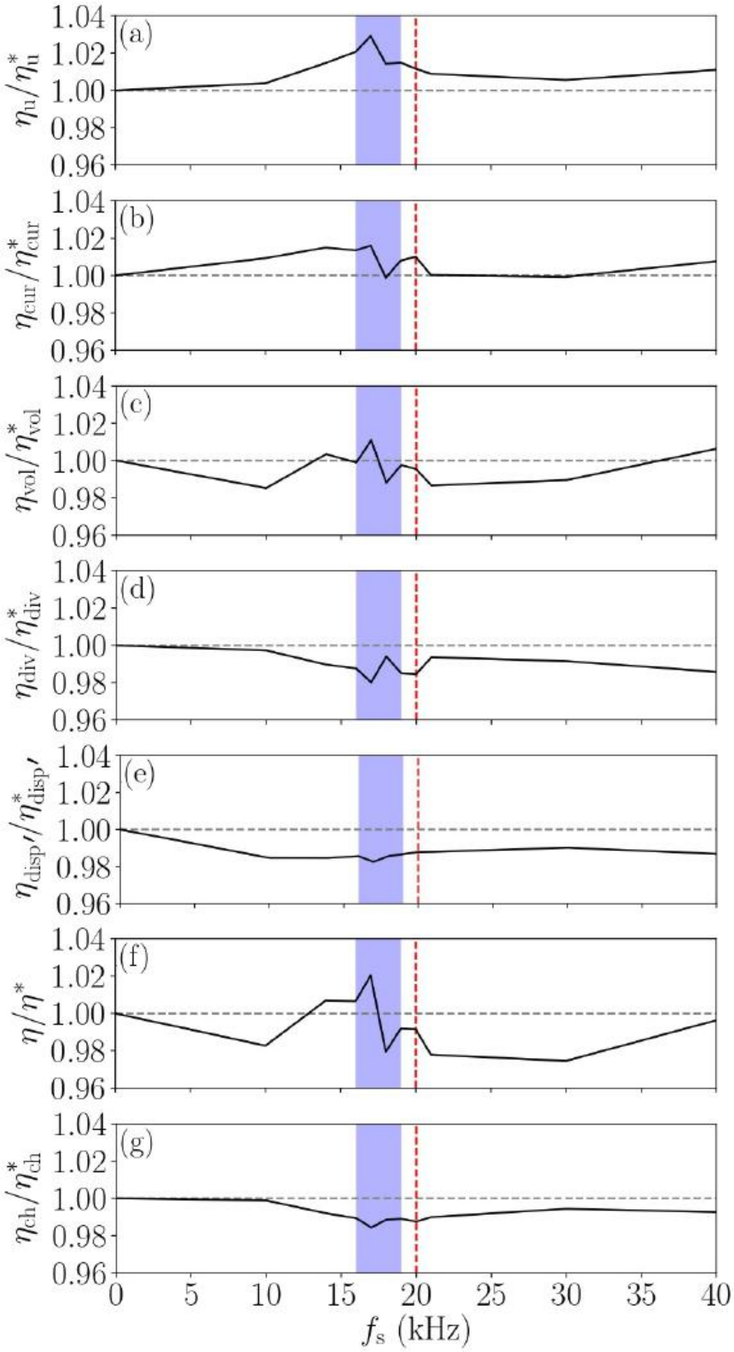

Figure 4.7: Total and partial efficiencies relative to the unmodulated case versus f_s for $\varepsilon = 25\%$. The blue, shaded region indicates the approximate location and extension of the resonant region, and the red dashed line corresponds to f_{BM}.

through the downstream boundary is defined as

$$\mathcal{F}_z(v_z) = \int_{-\infty}^{\infty} dv_r \int_{-\infty}^{\infty} v_z \mathcal{F}(v_r, v_\theta, v_z) dv_\theta, \tag{4.7}$$

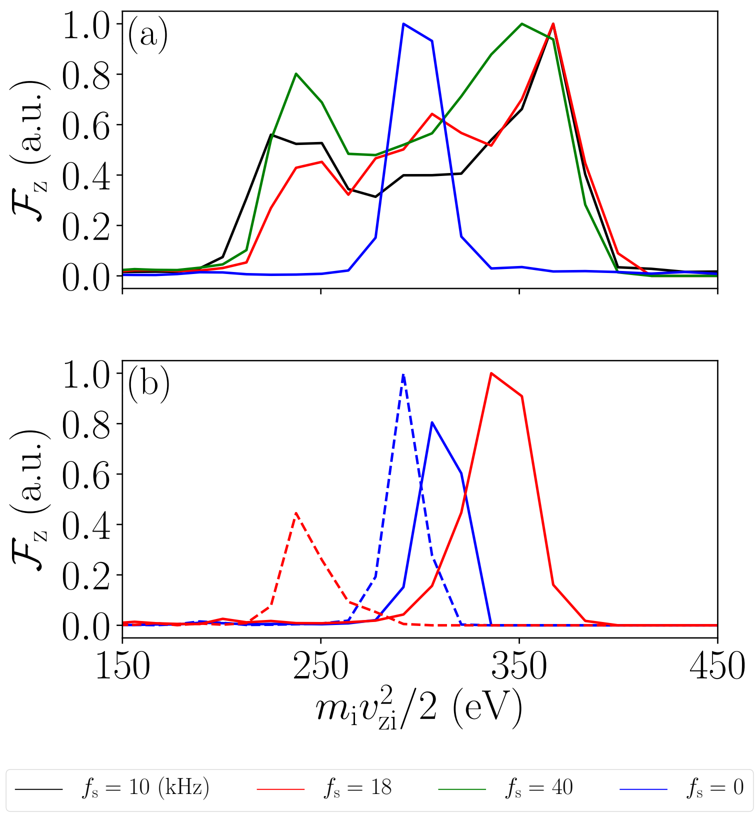

Figure 4.8: Normalized axial-flux VDF of singly-charged ions at the downstream boundary of the channel midline for $\varepsilon = 25\%$ and $f_\mathrm{s} = 0$, 10, 18, and 40 kHz (blue, black, red and green solid lines, respectively). (a) Time-averaged VDFs (b) VDFs at maximum $\mathcal{E}_{\mathrm{zi}\infty}$ (solid line) and at minimum $\mathcal{E}_{\mathrm{zi}\infty}$ (dashed line), for $f_\mathrm{s} = 0$ and 18 kHz.

with $\mathcal{F}(v_\mathrm{r}, v_\theta, v_\mathrm{z})$ the species VDF. Fig. 4.8(a) shows $\mathcal{F}_\mathrm{z}$ for singly-charged ions at the downstream boundary at the channel midline for $f_\mathrm{s} = 0$, 10, 18 and 40 kHz. For the unmodulated case, $\mathcal{F}_\mathrm{z}$ presents a single dominant peak at 290 eV and a much lower ion velocity dispersion (consistent with a higher $\eta_{\mathrm{disp}'}$) than for the modulated cases. For all modulated cases, the ion-flux VDF exhibits two main peaks near 225 eV and 375 eV, the minimum and maximum values of the modulated $V_\mathrm{d}(t)$. Interestingly, the dominant peak is the one with the highest energy. Compared to cases at $f_\mathrm{s} = 10$ and 40 kHz, the results for $f_\mathrm{s} = 18$ kHz show a lower velocity dispersion of the singly-charged ion population, in line with Ref. [233]. A similar double peak behavior for modulated cases is found for doubly-charged ions.

The behavior of $\eta_{\mathrm{disp}'}$ is also related to that of η_ch [Figs. 4.7(e) and (g)], since the presence of doubly-charged ions contributes to the velocity dispersion of the ion population. The lower η_ch values near resonance indicate that a larger fraction of doubly-charged ions is produced at these conditions. This is consistent with the higher T_e around f_r reported by experiments [235]; this aspect is further analyzed in Sec. 4.4. The decrease in η_div within the resonance region indicates higher plume divergence, in line with results in

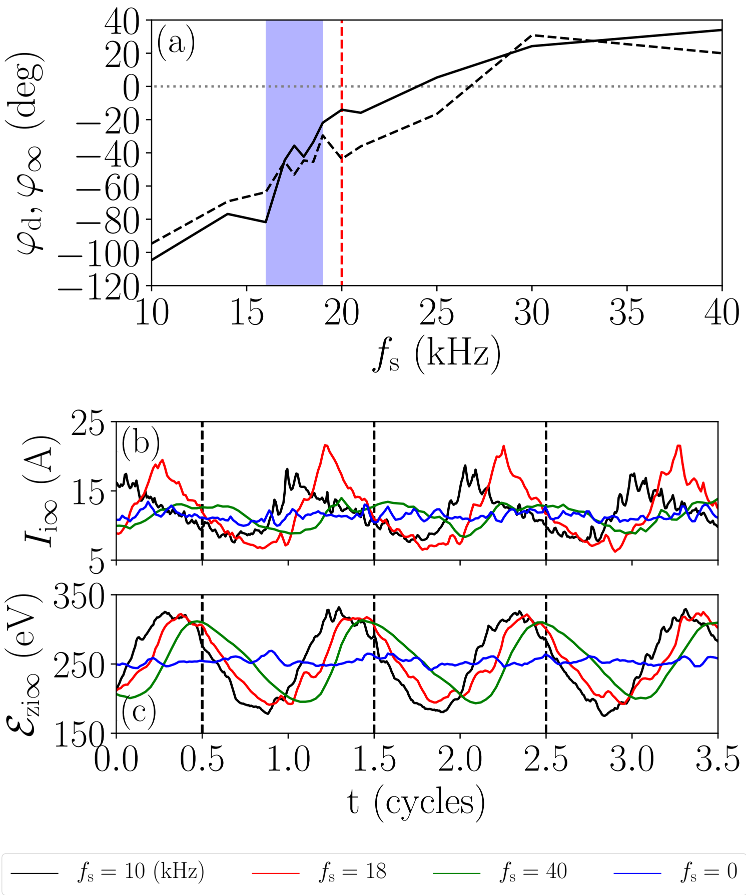

Figure 4.9: Case $\varepsilon = 25\%$. (a) Phase difference φ_d, between I_d and V_d (solid black line), and φ_∞, between $I_{\mathrm{i}\infty}$ and $\mathcal{E}_{\mathrm{zi}\infty}$ (dashed black line), versus f_s. Red line and shaded region as in Fig. 4.6. Time response of (b) $I_{\mathrm{i}\infty}$ and (c) $\mathcal{E}_{\mathrm{zi}\infty}$, for 3.5 modulation cycles for $f_\mathrm{s} =$ 10, 18 and 40 kHz (black, red and green solid lines, respectively), and natural BM cycles for $f_\mathrm{s} = 0$ (blue line). Other lines as in Fig. 4.5(b).

Ref. [235], and, along with $\eta_{\mathrm{disp}'}$ decrement, partially compensates the gains in $\eta_\mathrm{u}\eta_\mathrm{cur}$.

The increase in the product $\eta_\mathrm{cur}\eta_\mathrm{vol}\eta_\mathrm{div} \approx \bar{P}_{\mathrm{zi}\infty}/\bar{P}_\mathrm{d}$ is also limited, where $\bar{P}_{\mathrm{zi}\infty}$ corresponds to the dominant ion contribution to $\bar{P}_{\mathrm{z}\infty}$ [refer to Eq. (4.4)]. This aspect is further analyzed as follows. For sinusoidally oscillating quantities, $\bar{P}_\mathrm{d}$ and $\bar{P}_{\mathrm{zi}\infty}$ can be expressed as

$$\bar{P}_\mathrm{d} = \bar{V}_\mathrm{d}[\bar{I}_\mathrm{d} + \varepsilon \Delta I_\mathrm{d} \cos(\varphi_\mathrm{d})/2], \tag{4.8}$$

$$\bar{P}_{\mathrm{zi}\infty} = [\bar{\mathcal{E}}_{\mathrm{zi}\infty}\bar{I}_{\mathrm{i}\infty} + \Delta\mathcal{E}_{\mathrm{zi}\infty}\Delta I_{\mathrm{i}\infty}\cos(\varphi_\infty)/2]/e, \tag{4.9}$$

where $\mathcal{E}_{\mathrm{zi}\infty} = eP_{\mathrm{zi}\infty}/I_{\mathrm{i}\infty}$ is the average axial energy per ion crossing the downstream plume boundary; and $\varphi_\mathrm{d}, \varphi_\infty \in [-180, 180]$ deg are phase shifts between I_d and V_d, and between $I_{\mathrm{i}\infty}$ and $\mathcal{E}_{\mathrm{zi}\infty}$, respectively, referred to as discharge phase and ion phase. A negative phase shift means that the first signal of the pair (the currents, in this case) is ahead of the other signal. Assuming that time-averaged values remain nearly constant with f_s, and that $\varphi_\mathrm{d}, \varphi_\infty \in (-90, 90)$ deg (i.e., $\cos\varphi_\mathrm{d}, \cos\varphi_\infty > 0$), both $\bar{P}_\mathrm{d}$ and $\bar{P}_{\mathrm{zi}\infty}$ increase for higher oscillation amplitude and phase alignment of the involved signals.

Fig. 4.9(a) shows φ_d and φ_∞ versus f_s. Figs. 4.9(b) and (c) present the time response of $I_{\mathrm{i}\infty}$ and $\mathcal{E}_{\mathrm{zi}\infty}$, respectively, while the one corresponding to I_d is in Fig. 4.5(b). Two main facts are revealed by these results. First, the behavior of $I_{\mathrm{i}\infty}$ is found similar to that of I_d: it exhibits a non-monotonic behavior in terms of oscillation amplitude and time-averaged values, with both quantities peaking near resonance; and second, the absolute value of both φ_d and φ_∞ are shown to decrease near resonance, indicating a phase alignment of signals I_d and V_d, and $I_{\mathrm{i}\infty}$ and $\mathcal{E}_{\mathrm{zi}\infty}$, respectively. Indeed, both curves $\varphi_\mathrm{d}, \varphi_\infty(f_\mathrm{s})$ are nearly coincident, and full phasing (i.e. $\varphi = 0$) is found for $f_\mathrm{s} \sim 25$ kHz, thus above the resonance region (and f_BM). The results for $\varphi_\mathrm{d}(f_\mathrm{s})$ confirm the capacitive/inductive character of the discharge commented above for f_s lower/higher than 25 kHz. A similar behavior is reported in Ref. [235]. These findings indicate that near resonance both $\bar{P}_{\mathrm{zi}\infty}$ and $\bar{P}_\mathrm{d}$ increase, thus limiting the product $\eta_\mathrm{cur}\eta_\mathrm{vol}\eta_\mathrm{div} \approx \bar{P}_{\mathrm{zi}\infty}/\bar{P}_\mathrm{d}$ and, consequently, the gains in η induced by modulation.

Previous studies for a voltage modulated thruster [233–235] have shown that high oscillation amplitude and low phase shift between ion current and energy is optimal for thrust production. Here, we find maximum F near resonance [refer to Fig. 4.6(b)], where $I_{\mathrm{i}\infty}$ oscillations are maximum and φ_∞ is low. While average values of $\mathcal{E}_{\mathrm{zi}\infty}$ (about 251-253 eV) are found to barely change with f_s (maximum change is about 0.8% with respect to the unmodulated case) its oscillation amplitude is shown to decrease at resonance with respect to its level at low f_s (see black and red curves in Fig. 4.9(c) corresponding to $f_\mathrm{s} = 10$ and 18 kHz, respectively). This fact, along with the higher plume divergence discussed above, limits thrust production, in line with Ref. [235]. Furthermore, the combination of the sub-optimal F with the aforementioned enhanced P_d yields limited η gains for modulated resonant discharges.

Finally, Fig. 4.8(b) shows $\mathcal{F}_\mathrm{z}$ for singly-charged ions at the downstream boundary at the thruster channel midline computed at the time instants with maximum and minimum $\mathcal{E}_{\mathrm{zi}\infty}$ for a given discharge oscillation cycle. Results are presented for the unmodulated reference case described in Sec. 4.2 (blue curves) and for the modulated case with $f_\mathrm{s} =$ 18 kHz (red curves). The axial flux-VDFs present two peaks at energies consistent with the time response of $\mathcal{E}_{\mathrm{zi}\infty}$ in Fig. 4.9. Interestingly, while both the high and low-energy peaks in the unmodulated case are similarly populated, the high-energy peak clearly dominates in the modulated case. This result indicates that voltage modulation near resonance enhances and optimizes the acceleration of the ion population, thus favoring F production, as commented above. These aspects are further analyzed next.

4.4 Further insights on the 2D plasma response

In this section we analyze the time-dependent response of the plasma variables in order to discuss the predator-prey character of the driven modes. First we will consider a 0D analysis with global variables, then we will look at 1D and 2D behaviors.

4.4.1 Global response

In order to define globally-averaged values of the plasma variables we consider the domain in Fig. 4.1 bounded by the red line, which covers the portion of the simulation domain where most ionization takes place, extending axially up to z/L_c =1.4, thus including the thruster chamber and the position of T_e and E_z peaks downstream [122]. Spatially-averaged values within this region of any magnitude ζ are denoted as $\tilde{\zeta}$.

The ion continuity equation states

$$\frac{\partial n_e}{\partial t} + \nabla \cdot (\boldsymbol{j}_i/e) = S_e, \tag{4.10}$$

where

$$S_e = n_e \sum_{\kappa} n_\kappa \Delta Z_\kappa R_\kappa(T_e) \tag{4.11}$$

is the net ionization production term, including single and double ionization between electrons and heavy species (ions and neutrals) with, for each ionization process κ (i.e., $Xe \rightarrow Xe^+$, $Xe \rightarrow Xe^{2+}$ and $Xe^+ \rightarrow Xe^{2+}$): n_κ the heavy species involved, ΔZ_κ the heavy species charge number jump in the process, and $R_\kappa(T_e)$ the corresponding ionization rate, which is a non-linear function of the electron temperature. Ion current oscillations are therefore governed by oscillations of S_e, which in turn depend on the dynamics of T_e, n_n and n_e. Current continuity in the quasineutral plasma relates the produced ion and electron current densities,

$$\nabla \cdot \boldsymbol{j}_e = -\nabla \cdot \boldsymbol{j}_i. \tag{4.12}$$

The surface integral of the electric current (i.e., $\boldsymbol{j} = \boldsymbol{j}_i + \boldsymbol{j}_e$) collected at the anode wall provides I_d, while the surface integral of the ion current collected at the downstream plume boundary provides $I_{i\infty}$.

On the other hand, T_e is determined from the inertialess electron energy equation for an isotropic pressure tensor,

$$\frac{\partial}{\partial t}\left(\frac{3}{2} n_e T_e\right) + \nabla \cdot \boldsymbol{P}''_e = P'''_{elec} - P'''_{inel}. \tag{4.13}$$

where $\boldsymbol{P}''_e = -5T_e\boldsymbol{j}_e/(2e) + \boldsymbol{q}_e$ is the electron energy flux gathering the enthalpy and heat fluxes; $P'''_{elec} = \boldsymbol{j}_e \cdot \boldsymbol{E}$ is the work of the electric field over fluid electrons per unit volume and time, corresponding to the the main energy source term for electrons; and P'''_{inel} accounts for the power losses per unit volume from inelastic collisions (e.g., excitation and ionization).

Fig. 4.10 shows the phase shifts and the time response of several plasma variables for the same simulations than Figs. 4.5 and 4.9. Interestingly, the results for the modulated discharge found here for the MS-HET are in good qualitative agreement with those reported in Ref. [235] for the CHTpm2. This fact suggests that the same fundamental phenomena drive the modulated response in both prototypes, and indicates that anode voltage modulation seems a robust technique to control the frequency and the phasing between current and voltage across different HET designs.

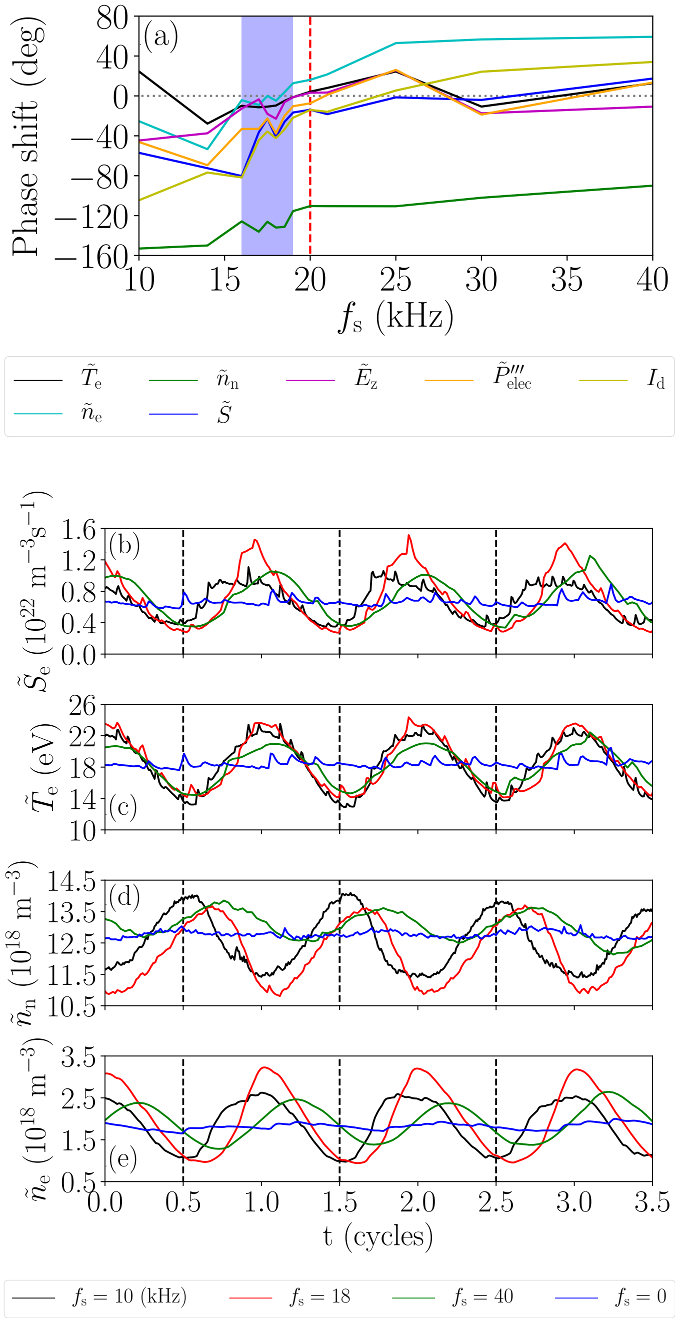

Figure 4.10: Modulated case $\varepsilon = 25\%$. (a) Phase shift of different magnitudes with respect to V_d. Red line and shaded region as in Fig. 4.6 (b)-(e) Time response of different magnitudes for $f_\mathrm{s} = 0$, 10, 18 and 40 kHz (blue, black, red and green solid lines, respectively). Other details as in Fig. 4.5.

For modulated cases, a quasi-periodic time response with dominant frequency equal to f_s is found for all magnitudes in Fig. 4.10, with significantly larger oscillation amplitudes than for the unmodulated case, in line with the behavior of I_d. The ionization of neutrals is triggered by a combination of the rise of $\tilde{T}_\mathrm{e}$ and the level of neutral replenishment, yielding an increase in plasma density until the neutral population is depleted and $\tilde{T}_\mathrm{e}$ decreases. The ionization then drops until neutrals are replenished and $\tilde{T}_\mathrm{e}$ rises again, leading to another cycle. For all cases, $\tilde{n}_\mathrm{n}$ is ahead of $\tilde{n}_\mathrm{e}$, the phase lag between signals ranging from 100 to 150 deg. This behavior is typical of a predator-prey type ionization instability [176,189], and suggests that the main discharge oscillations in modulated cases correspond to an externally driven BM (this aspect is further assessed later). For low and high f_s, far from the resonant region, $\tilde{n}_\mathrm{n}$-V_d phase shift exhibits an asymptotic behavior, typical of resonant oscillators. A similar trend is found for $\tilde{n}_\mathrm{e}$-V_d and $\tilde{S}_\mathrm{e}$-V_d phase shifts.

For $f_\mathrm{s} = 18$ kHz, $\tilde{S}_\mathrm{e}$ exhibits much larger oscillations yielding higher neutral depletion and plasma density peaks. The enhanced averaged plasma production (it increases up to a 6% from the unmodulated case) is in line with the increase in η_u with respect to the unmodulated discharge observed in Fig. 4.7(a). Near resonance, the $\tilde{S}_\mathrm{e}$-V_d phasing (Fig. 4.10) has a central impact on the discharge performance, as described next. First, it is responsible for both the discharge and ion phasing (i.e. the decrease of $|\varphi_\mathrm{d}|$ and $|\varphi_\infty|$) discussed in Sec. 4.3.2, since (1) S_e is the source of both ion and electron currents contributing to I_d and $I_{\mathrm{i}\infty}$ [refer to Eqs. (4.10) and (4.12)], and (2) V_d ultimately determines $\mathcal{E}_{\mathrm{zi}\infty}$ in Fig. 4.9(c). The similar phase-frequency characteristic found for φ_d and φ_∞ in Fig. 4.9(a) is a consequence of the coupling between the plasma generation and acceleration in the HETs, which limits the performance improvement in the modulated discharge (especially in terms of η). On the one hand, both F and $P_{\mathrm{zi}\infty}$ are maximized if $\tilde{S}_\mathrm{e}$ and V_d are maximum at the same time every discharge cycle. On the other hand, the higher F (or $P_{\mathrm{zi}\infty}$) is accompanied by higher P_d.

Considering only modulated cases, the $\tilde{S}_\mathrm{e}$-V_d phasing near resonance also contributes to the lower ion velocity dispersion observed in Fig. 4.8(a) for $f_\mathrm{s} = 18$ kHz (red line): if the peaks of both $\tilde{S}_\mathrm{e}$ and V_d occur closer within the cycle, then the majority of the ions will go across a similar potential fall when accelerating downstream ($\partial V_\mathrm{d}/\partial t \approx 0$ near its maximum). Furthermore, this phasing is behind the fact that the high energy peak of $\mathcal{F}_\mathrm{z}$ in Fig. 4.8(b) is much more populated than the lower one.

The electron temperature response is determined by the energy balance for electrons in Eq. (4.13), including P'''_elec as the main energy source, and is found to oscillate nearly in-phase with V_d for all f_s values. This is consistent with the fact that (1) MS of the channel walls limits power losses to the walls and avoids T_e saturation [241]; and (2) the period of the modulation ($\sim 10^{-4}$ s) is much longer than the electron residence time ($\sim 10^{-6}$-10^{-7} s), so that $\boldsymbol{j}_\mathrm{e}$ quickly adapts to V_d changes (with f_s). The larger $\tilde{T}_\mathrm{e}$ peak near resonance (it increases from about 20 to 24 eV from the unmodulated case to the case with $f_\mathrm{s} = 18$ kHz) favors double ionization collisions, and is thus in line with the slight decrease in η_ch and $\eta_{\mathrm{disp}'}$, as indicated in Sec. 4.3.2.

For f_s near f_BM, T_e is found to govern S_e (and n_n) dynamics and, therefore, is the main factor responsible for the control of the dominant frequency of the modulated discharge oscillations. As commented above, $\tilde{T}_\mathrm{e}$ oscillates nearly in-phase with V_d for all f_s values (Fig. 4.10). On the other hand, $\tilde{n}_\mathrm{n}$ oscillates nearly out-of-phase with V_d for $f_\mathrm{s} = 10$ kHz, and their phase shift decreases (in absolute value) for higher f_s. The rise in $\tilde{S}_\mathrm{e}$ depends on that of $\tilde{T}_\mathrm{e}$ and the level of neutral replenishment in the chamber. For $f_\mathrm{s} = 10$ kHz, neutrals have longer time available to replenish the chamber before $\tilde{T}_e$ begins to rise, and they trigger the ionization before the rise of $\tilde{T}_e$. For $f_s = 18$ and 40 kHz, neutrals have shorter time to replenish the chamber, and a lower value of $\tilde{n}_n$ is found at the initial rise of $\tilde{S}_e$, which is now triggered mainly by the rise of $\tilde{T}_e$. Near resonance, at $f_s = 18$ kHz, the ionization is enhanced by an optimal combination of $\tilde{n}_n$ and $\tilde{T}_e$, yielding the maximum peak of $\tilde{S}_e$ and $\tilde{n}_e$, and the highest level of neutral depletion.

4.4.2 Local response

Fig. 4.11 shows the axial-temporal contour maps over several modulation cycles of radially-averaged plasma magnitudes (denoted with circumflex accent). For $f_s = 10$ kHz, the ionization front, identified with the peak of $\hat{S}_e$, is formed on every cycle at $z/L_c \approx 0.8$, and moves upstream towards the anode along the cycle. The larger neutral replenishment in the chamber in this case triggers the ionization close to the chamber exit, where $\hat{T}_e$ is higher, and the ionization front is formed well before $\hat{T}_e$ reaches its maximum value. Then, the ionization front travels upstream, as neutrals are consumed (and the electron temperature increases), and stays near the anode a significant part of the cycle, until $\hat{T}_e$, which oscillates nearly in-phase with V_d, decreases with time and the ionization front vanishes. For the case with $f_s = 18$ kHz the ionization front appears at a distance from the anode similar to the case with $f_s = 10$ kHz, while for $f_s = 40$ kHz the front forms closer to the anode (at $x/L_c \approx 0.7$) due to the lower level of downstream neutral replenishment. For both $f_s = 18$ and 40 kHz, the ionization front is triggered by the rise in the electron temperature. Near resonance (e.g., at $f_s = 18$ kHz), an optimal phasing between neutral replenishment and electron temperature is found every cycle, yielding the highest ionization production, as commented above. The upstream motion of the ionization front towards the anode is much more evident for $f_s = 18$ than for $f_s = 40$ kHz, and in both cases the ionization extinguishes when the electron temperature drops within the cycle. These results confirm that, for modulated cases with f_s close to f_{BM}, the dynamics of T_e are the main factor responsible for slowing down or speeding up the inherent ionization cycle of the unmodulated discharge, yielding an externally driven BM at f_s.

To have a full 2D picture of the dominant spatio-temporal modes we apply the HODMD [242, 243] data-driven technique, which expands a spatio-temporal dataset into dynamics-relevant modes identifying involved frequencies, amplitudes and growth rates, and that allows to separate transient behaviors from asymptotic oscillations. HODMD extends standard DMD [244] capabilities for the application to non-linear system with high spectral complexity, and overcomes the limitations of standard DMD when dealing with noisy data. A recent study [240] has already demonstrated the capabilities of HODMD to identify and characterize the natural BM and the ion transit time [166, 188, 245] from HYPHEN simulations of a SPT-100-like HET.

Given a set of spatio-temporal data composed of K snapshots of dimension N, i.e., $\boldsymbol{x}_1, \ldots, \boldsymbol{x}_K \in \mathbb{R}^N$, each of them representing the values of a physical variable of interest x at the N spatial mesh points involved in the numerical simulations for a given time

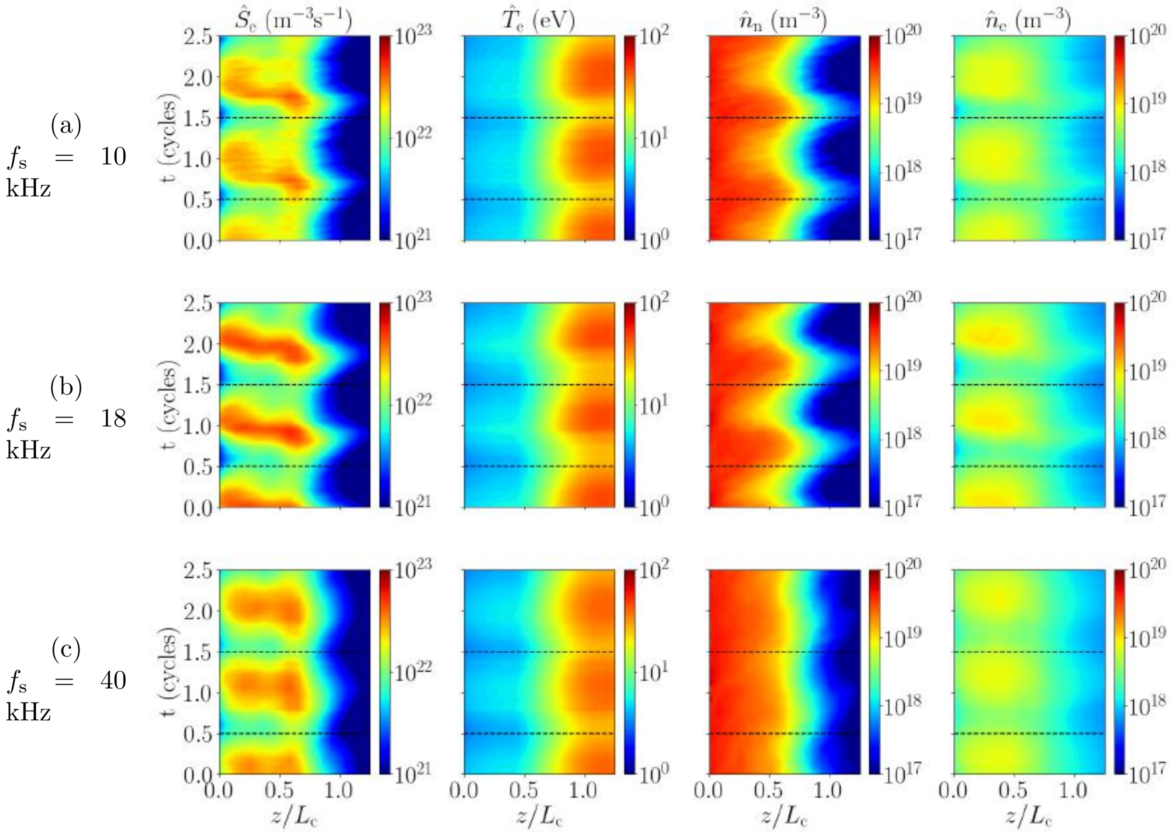

Figure 4.11: Modulated cases $\varepsilon = 25\%$. Axial-temporal contour maps over 2.5 modulation cycles of radially-averaged values of $\hat{S}_e$, $\hat{T}_e$, $\hat{n}_n$ and $\hat{n}_e$ (from left to right column), for f_s = 10, 18 and 40 kHz (from top to bottom row). The black dashed lines correspond to the minima of V_d.

instant k, i.e., $\boldsymbol{x}_k = \boldsymbol{x}(t_k)$, HODMD aims at decomposing each snapshot $\boldsymbol{x}_k$ as

$$\boldsymbol{x}_k \approx \boldsymbol{x}_k^{\mathrm{DMD}} = \sum_{m=1}^{M} a_m \boldsymbol{\psi}_m e^{\Omega_m t_k} \tag{4.14}$$

where $\boldsymbol{\psi}_m$ are the complex spatial modes (normalized with RMS-norm), Ω_m their corresponding complex frequencies and $a_m > 0$ are their real amplitudes. Here, only purely oscillating modes are considered for the analysis and a_m assesses their dynamical relevance. The accuracy of the HODMD reconstruction of the original data, $\boldsymbol{x}_k$, depends on the number M of modes considered and a tunable parameter d that defines the number of "delayed" snapshots to be used in the analysis [242]. In order to identify an adequate value for M and d, a similar procedure to the one in Ref. [240] is followed: M and d are varied until the relative RMS error in the reconstruction is found small enough (between 5% and 15%); once this is achieved, it is checked that small variations of the resulting d parameter do not affect the output HODMD modes. Results shown next are for $M = 40$ (including complex conjugates) and $d = 600$.

Fig. 4.12 shows the normalized amplitude spectrum resulting from the application of HODMD to the spatio-temporal data of $S_\mathrm{e}(z,r,t)$ within the red-bounded region of Fig. 4.1 for unmodulated and modulated cases. For the unmodulated case, the largest-amplitude mode corresponds to the natural BM frequency $f_\mathrm{BM} = 20$ kHz, but there are non-negligible contributions of several modes with frequencies close to f_BM, and which are not harmonics of f_BM. In particular, the amplitudes of the second and the fifth-largest modes, at 29.5 and 70.2 kHz, respectively, are just 18% and 42% lower than that of the largest one. Therefore, the natural BM cannot be reconstructed within a selected accuracy by a simple spatio-temporal sinusoidal term (nor the superposition of several sinusoidal harmonics). Instead, a wide non-harmonic breathing mode cluster is found, which confirms the rich spectral complexity of the natural BM for this thruster, in line with the I_d time response and frequency spectrum shown in Fig. 4.2.

Modulated cases show a simpler spectrum, with a more prominent role of the mode at f_s. This result is consistent with the quasi-periodic I_d response shown in Fig. 4.5 for these cases. Yet, cases with $f_\mathrm{s} = 10$ and 18 kHz show non-negligible contributions of 2-3 harmonic modes, and several non-harmonic *secondary* modes with frequencies close to f_s.

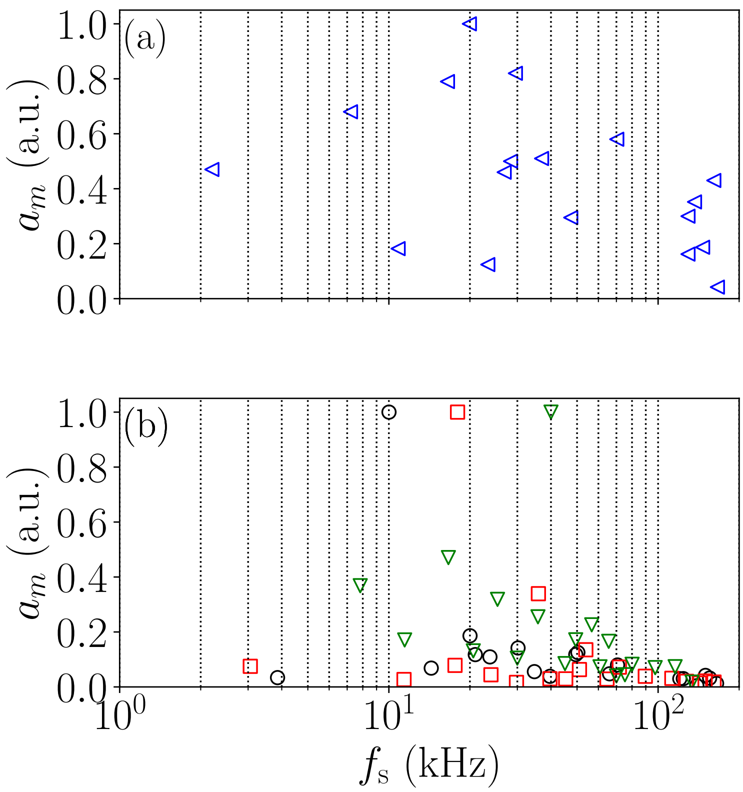

Figure 4.12: Normalized amplitude versus frequency diagram for the HODMD modes of S_e within the red-bounded domain of Fig. 4.1 for (a) the unmodulated case and (b) the modulated cases with $\varepsilon = 25\%$ and $f_\mathrm{s} = 10$, 18 and 40 kHz (black circle, red square and green triangle markers, respectively).

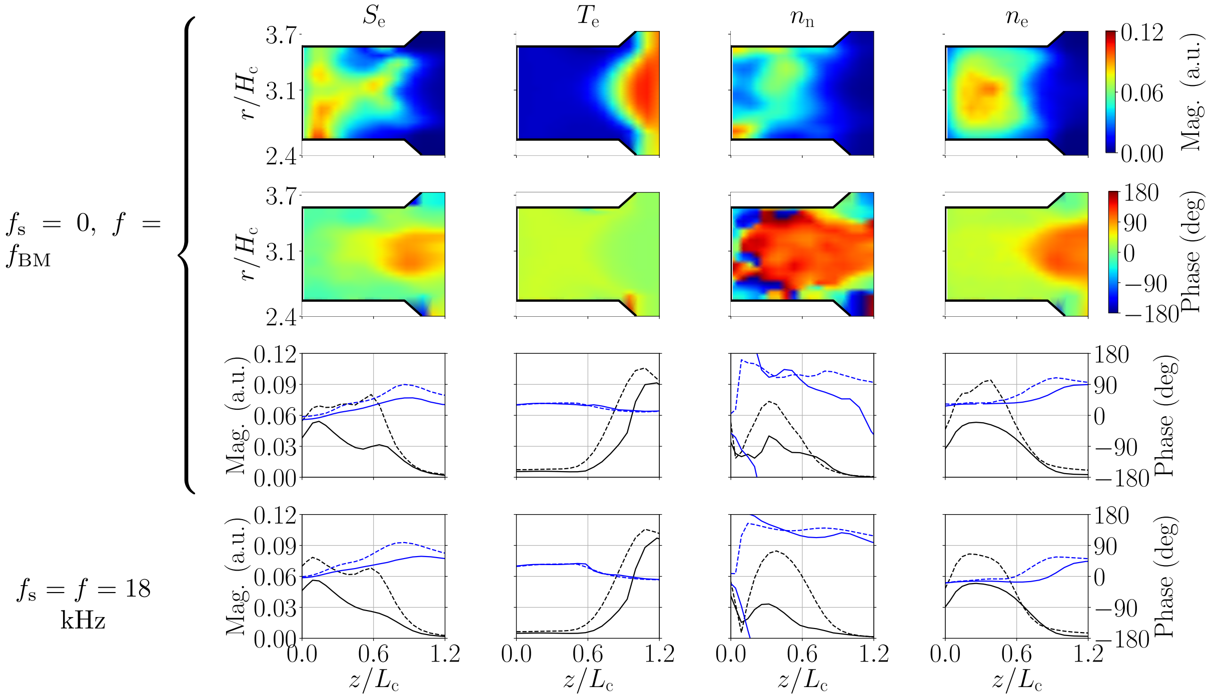

Figure 4.13: Dominant HODMD mode for the unmodulated case, corresponding to $f_{BM} = 20$ kHz (first three rows), and for the modulated one with $f_s = 18$ kHz and $\varepsilon = 25\%$ (last row), for S_e, T_e, n_n and n_e (from left to right columns). Row 1: mode magnitude in arbitrary units. Row 2: mode phase angle. Rows 3 and 4: axial profiles of mode magnitude (black lines and left y-axis) and phase angle (blue lines and right y-axis); solid lines correspond to radially averaged quantities, while dashed lines indicate quantities along the thruster channel midline.

Interestingly, for $f_s = 40$ kHz ($> f_{BM}$), the mode-amplitude hierarchy contains modes with frequencies close to f_{BM}.

Fig. 4.13 shows the spatial structure of the dominant HODMD mode of S_e, T_e, n_n, and n_e, in terms of its magnitude and phase angle within the region of analysis depicted in Fig. 4.1. The first three rows of Fig. 4.13 show results for the unmodulated reference case. 2D contour maps of mode magnitude and phase angle are depicted in the first and second row. The third row shows 1D axial profiles of magnitude (black lines and left y-axis) and phase angle (blue lines and right y-axis). While dashed lines correspond to values along the thruster channel midline, solid lines, corresponding to radially averaged values, are included to emphasize the spatial non-uniform 2D character of the modes. The reference for the phase angle (i.e. 0 deg) is set to the phase of the S_e mode at the midpoint of the anode wall. Results for the modulated discharge with $f_s = 18$ kHz are found qualitatively similar to those of the unmodulated discharge. Therefore, 2D contour maps are omitted, and only 1D axial profiles of magnitude and phase angle are reported in the fourth row of Fig. 4.13, in the same fashion as for the unmodulated case. The information in Fig. 4.13 must be interpreted as follows: the magnitude plots indicate where the oscillation takes place; the phase plots describe the standing or progressive structure of the wave and allow identifying the phase relation between the different plasma variables.

Magnitude 2D maps and 1D axial profiles in the first column of Fig. 4.13 show that, for both the unmodulated reference case and the modulated case with $f_\mathrm{s} = 18$ kHz, the region where S_e oscillates extends from the anode to $z/L \approx 0.8$. This result is consistent with the spatio-temporal contour maps of $\hat{S}_\mathrm{e}$ depicted in Fig. 4.11(b) for $f_\mathrm{s} = 18$ kHz, showing that the ionization front, identified with the peak of $\hat{S}_\mathrm{e}$, forms at $z/L \approx 0.8$ and travels upstream towards the anode during the modulation cycle. In fact, in this region S_e exhibits an upwards progressive-wave structure (i.e. traveling to the left in the diagrams), indicated by the positive slope of the 1D axial phase profiles (blue lines in the third and fourth rows of the first column of Fig. 4.13). Its characteristic axial phase velocity is 2.68 km/s for the unmodulated reference case and 2.63 km/s for the modulated case with $f_\mathrm{s} = 18$ kHz. The main oscillations of n_n and n_e (third and fourth columns of Fig. 4.13) are also found between the anode and $z/L \approx 0.8$, indicating that the ionization region is contained there. In contrast, T_e is found to oscillate downstream the ionization region, mainly outside the thruster chamber, where most of the ion acceleration takes place. A similar behavior is found for E_z (not shown). T_e has essentially a constant phase through the analyzed region, indicating a dominant standing-wave character. The 1D axial profiles along the channel midline for the phase of n_n and n_e indicate that the former leads by 75-135 deg within the ionization region, and that both present a dominant standing-wave character.

The spatial non-uniformity of the modes in the thruster channel is especially evident for the case of n_n. The radial non-uniformity of S_e is mainly due to the ion recombination at the thruster walls, which significantly contributes to n_n, and it is partially responsible for that of n_e. For the n_n mode, radially averaged 1D profiles of magnitude and phase along the channel (solid lines) greatly differ from those along the thruster channel midline (dashed lines). Interestingly, the radially averaged n_n mode corresponds to an apparent 1D axial wave travelling downstream along the thruster channel from the anode wall (i.e., solid blue lines with negative slopes) This behavior is consistent with $\hat{n}_\mathrm{n}$ maps in Fig. 4.11, in which the downstream travelling of neutrals is more evident for cases with $f_\mathrm{s} = 10$ and 18 kHz. The phase characteristics of this axial wave allows to identify two different regions. On the one hand, near the anode, the characteristic axial phase velocity is mainly a result of the competition between neutral injection and ionization: for the unmodulated case, which features lower ionization near the anode, the HODMD mode for n_n recovers the expected convective axial wave dominated by neutral injection from the anode, and the phase velocity is 0.31 km/s, close to macroscopic axial injection velocity for neutrals, set to 0.3 km/s; for the modulated case with $f_\mathrm{s} = 18$ kHz, the phase velocity is of the same order of magnitude but smaller, 0.15 km/s, due to the enhanced ionization and the phasing between S_e and n_n, which decrease the effective neutral replenishment rate. On the other hand, further downstream the anode wall, for $z/L_\mathrm{c} > 0.2$-0.3, neutral fluxes from ion recombination along the lateral walls yield an apparent axial phase velocity of 1.76 km/s (unmodulated case) and 1.51 km/s (modulated case), about 5-6 times larger than the macroscopic axial velocity of neutrals.

4.5 Transition from driven to natural breathing mode

Voltage modulation at relatively high modulation amplitudes (e.g., $\varepsilon = 25\%$) was found to yield limited gains in thrust efficiency, but, it has been proven to be an effective strategy to control the frequency of the discharge oscillations for $f_\mathrm{s} \approx f_\mathrm{BM}$. While this feature can help reduce EMI on modern spacecrafts, the enhanced I_d oscillations obtained in the non-linear regime [Fig. 4.3(a)] may pose issues to other subsystems. Therefore, anode modulation at relatively low amplitudes within the linear regime (e.g., $\varepsilon = 5-10\%$) seems an interesting compromise allowing to control the frequency of the oscillations while keeping low current oscillation amplitudes. However, operating at low ε may result in a loss of control over the discharge oscillations and the reappearance of a dominant natural BM if f_s is sufficiently far from f_BM [228].

For a given modulation amplitude, the natural BM is expected to dominate over driven oscillations if f_s far enough from f_BM.

The transition between the driven and the natural BM of the thruster is here investigated for a relatively low modulation amplitude within the linear regime, set to $\varepsilon = 6.25\%$. Two limit simulation cases are run with $f_\mathrm{s} = 3$ kHz and 110 kHz, one order of magnitude lower and larger than f_BM, respectively. Fig. 4.14 shows the normalized frequency spectrum of I_d and main plasma magnitudes for $f_\mathrm{s} = 3$ kHz and 110 kHz. The results for I_d reveal that the natural BM of the thruster at $f_\mathrm{BM} = 20$ kHz is present in the response as the dominant mode (for $f_\mathrm{s} = 3$ kHz) or a co-dominant one (for $f_\mathrm{s} = 110$ kHz). Therefore, voltage modulation fails to control the main oscillations of the plasma discharge for both $f_\mathrm{s} = 3$ kHz and 110 kHz. Moreover, I_d response deviates from a quasi-periodic one at f_s, characterizing modulated discharges with $f_\mathrm{s} \approx f_\mathrm{BM}$. Instead, a higher spectral complexity is found, similar to that of the unmodulated case.

As discussed in Sec. 4.4, when f_s is close to f_BM, T_e is found to govern the dynamics of S_e, thus enabling the control of the discharge oscillation frequency. Here, for f_s far from f_BM, a quasi-periodic time response at f_s is still found for $\tilde{T}_\mathrm{e}$. However, the main oscillations of $\tilde{S}_\mathrm{e}$ occur now at f_BM, thus uncoupled from T_e dynamics, and its response presents a higher spectral complexity, similar to that of I_d, with a secondary mode at f_s. Similar results are found for $\tilde{n}_\mathrm{n}$ and $\tilde{n}_\mathrm{e}$. Therefore, the natural ionization cycle of the discharge at f_BM, governed by the dynamics of heavy species (i.e., neutrals and ions), which, contrary to electrons, cannot adapt to V_d changes when f_s is far from f_BM, is recovered, and it is only partially modulated by V_d through T_e dynamics.

For both modulation cases with $f_\mathrm{s} = 3$ and 110 kHz, the HODMD modes corresponding to $f_\mathrm{BM} = 20$ kHz for S_e, T_e, n_n, n_e present a similar structure and spatio-temporal characteristics as those of the natural BM of the thruster shown in Fig. 4.13. For the same plasma magnitudes, Fig. 4.15(a) and (b) show the 3 kHz and 110 kHz modes for modulated cases with $f_\mathrm{s} = 3$ kHz and $f_\mathrm{s} = 110$ kHz, respectively. In addition to their frequency, several aspects reveal that these modes are induced by the voltage modulation and do not present the features of a predator-prey type ionization instability typically associated to the BM characterizing HET operation. First, the roughly flat axial profile of the phase of S_e corresponds to global oscillations inside the thruster channel, and the progressive-wave structure travelling upwards towards the anode, which characterizes

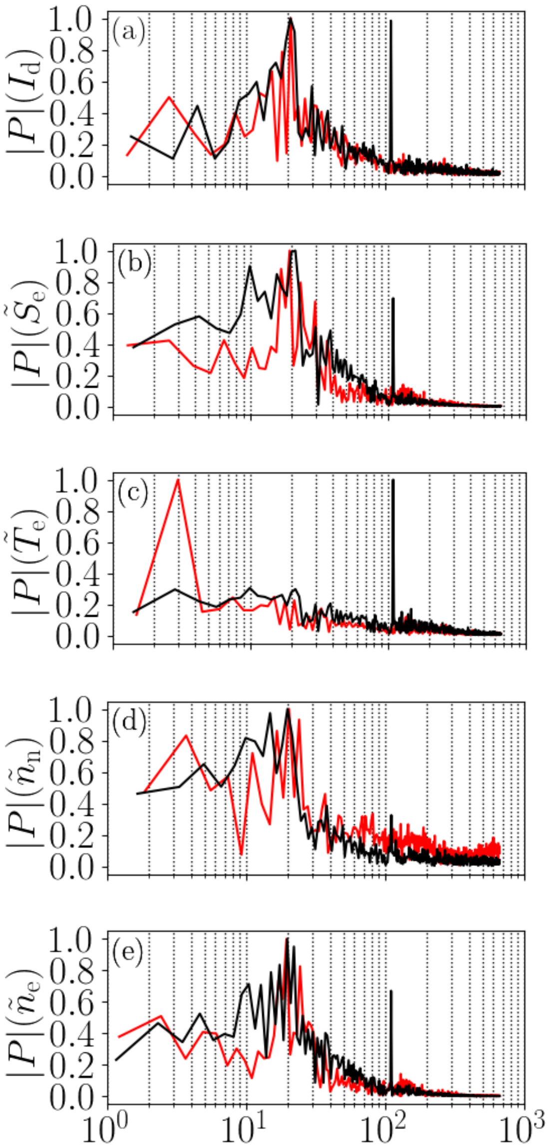

Figure 4.14: Normalized frequency spectrum of I_d and several plasma variables for $f_\mathrm{s} = 3$ kHz (red lines) and 110 kHz (black lines), with $\varepsilon = 6.25\%$.

both the natural and driven BM in Fig. 4.13 is not present. Second, the spatial distribution of the magnitude of the 110 kHz n_n mode reveals that the main neutral density oscillations at that frequency take place only within a very localized region close to the chamber walls. These n_n oscillations are due to slow neutrals from ion recombination at the walls at $f_\mathrm{s} = 110$ kHz, which become ionized before reaching the center of the channel. Finally, even though n_n oscillations take place in the bulk plasma for the 3 kHz mode, n_e oscillations are found to lead those of n_n in most of the domain, contrary to the case of a BM. This result for the $f_\mathrm{s} = 3$ kHz case seems to indicate that, throughout the slow modulation cycle, the growth in plasma density within the channel is limited by the T_e decay and ion recombination at the walls, which later promotes a neutral density peak

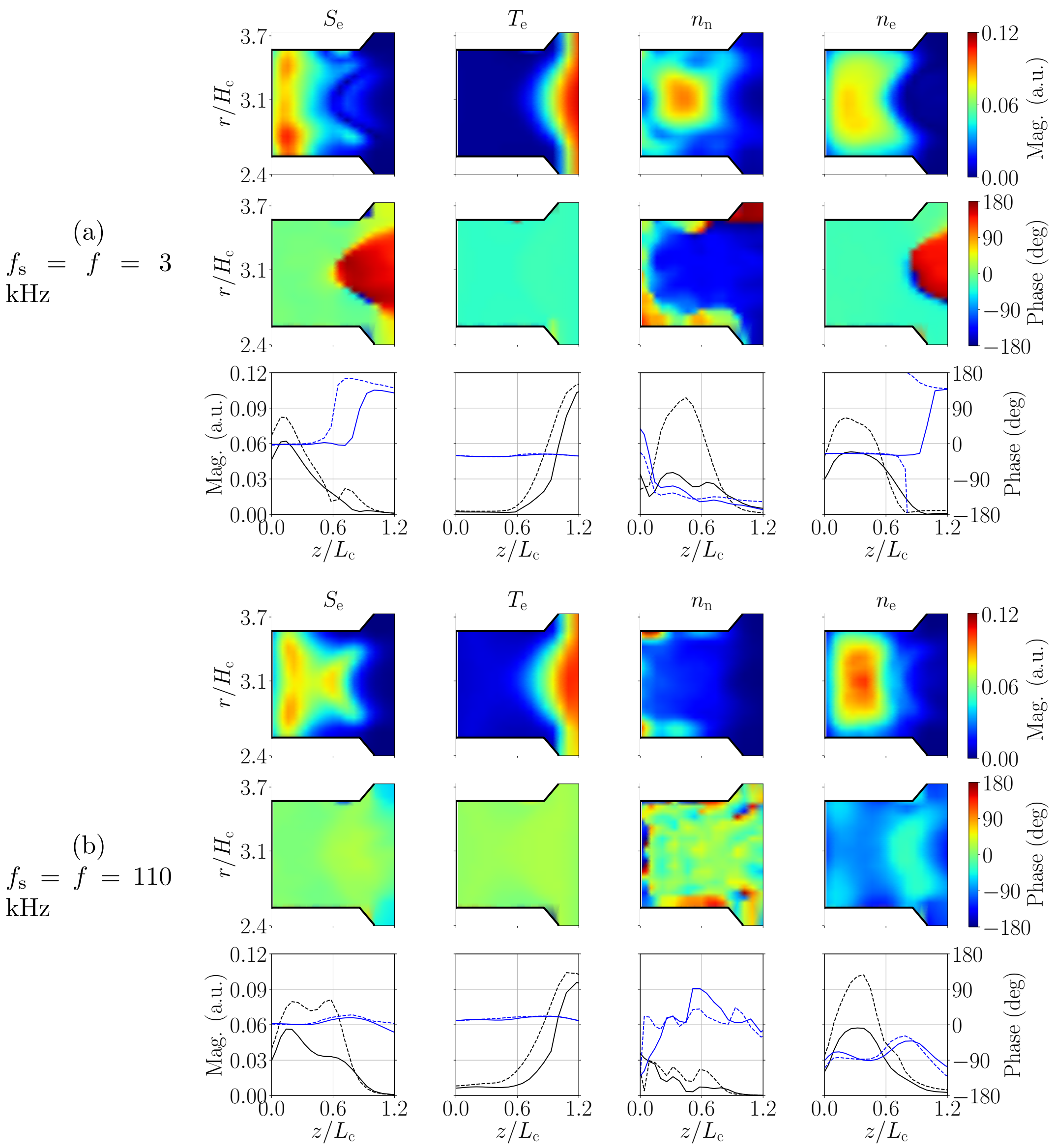

Figure 4.15: (a) 3 kHz and (b) 110 kHz HODMD modes for the modulated cases with $f_s = 3$ and 110 kHz, respectively, and $\varepsilon = 6.25\%$, for S_e, T_e, n_n and n_e (from left to right columns). For each panel (a) and (b): rows 1 and 2 present the mode magnitude (in arbitrary units) and phase angle; row 3 shows the axial profiles of mode magnitude (black line and left y-axis) and phase angle (blue line and right y-axis); solid lines correspond to radially averaged quantities, while dashed lines indicate quantities along the thruster channel midline.

inside the thruster vessel.

4.6 Conclusions

The dynamic response of a MS-HET with sinusoidally modulated discharge voltage has been investigated through 2D (axial-radial) simulations of the discharge, then assessed through Fourier analysis and HODMD techniques. Parametric analyses for several modulation amplitudes and frequencies show a good qualitative agreement with experimental measurements and 1D numerical results reported in previous studies for CHT prototypes in the low power range (<1kW), suggesting that the same fundamental phenomena drive the modulated response across different designs. The ubiquitous presence in these ExB devices, including also conventional and anode-layer-type HETs [228, 229], of the BM oscillations of the discharge current, attributed to the same fundamental predator-prey type ionization instability in which the electron temperature solution inside the vessel plays an essential role, could explain this interesting result. The role of plasma-wall losses could be another reason behind the similar modulated response across these prototypes: on the one hand the surface-to-volume ratio of the MS-HET is comparable to those of the low-power CHT and HETs of the previous modulation studies; on the other hand, the MS topology considered here (which to some extent is much more similar to that of the CHTpm2 than to that of a conventional HET) significantly limits plasma-wall interaction.

For constant modulation frequency, time-averaged values and oscillation amplitudes of I_d and F increase with the amplitude of modulation and a linear and a non-linear regime are observed in the response for low and high modulation amplitude, respectively. For highly oscillating discharges, the computation of efficiency figures based on time-average quantities is shown to avoid misestimations induced by RMS values. Within the non-linear regime, a resonant-like response is found for frequencies close to the natural BM. The analysis of partial efficiencies has revealed that anode modulation yields only limited gains in thruster performance (about 2% in thrust efficiency) due to counteracting effects inherent to the coupling between plasma production and acceleration processes characterizing HET operation.

The 2D solution for relevant plasma variables reveals that, for modulation frequencies close to the natural BM, the electron temperature governs the ionization production dynamics, and is therefore the main factor responsible for the control of the dominant frequency of the modulated discharge oscillations, enabling the externally driven BM induced by anode voltage modulation. The complex spatio-temporal structure of the 2D plasma solution is analyzed through the HODMD technique, which has revealed the travelling character of the ionization production wave inside the thruster channel, common to the natural and driven BM. Ion recombination at the lateral walls of the thruster channel significantly contributes to neutral replenishment in the thruster vessel and gives rise to an apparent 1D axial neutral density wave travelling downstream with phase velocity about 5-6 times larger than the macroscopic axial velocity of neutrals.

For low modulation amplitudes within the linear regime, the natural BM of the thruster reappears as a dominant or co-dominant mode of the discharge current oscillations when the modulation frequency is far from the natural BM one. The transition from a driven BM to the natural one occurs when the electron temperature, which oscillates at the modulation frequency, loses control over the dynamics of the ionization production, and the natural ionization cycle of the discharge, governed by heavy species dynamics, is recovered. The main oscillations of the plasma production inside the thruster vessel then correspond to the natural BM, and secondary modes at the modulation frequency, induced by the discharge voltage through the electron temperature dynamics, do not exhibit the features of a predator-prey type ionization instability.

Discharge voltage modulation has been proven an effective technique to control the frequency of the discharge oscillations in a range close to the natural BM of the thruster without loss in performance, thus presenting interesting applications for EMI mitigation and for plasma diagnostics. The analysis of the effects of anode modulation for different operating conditions covering the nominal operation range of the thruster would permit evaluating its impact on the performance map and I-V characteristics.

Chapter 5

Analysis of a 20 kW-class Hall effect thruster

The initial research of this Chapter was presented in the 37th International Electric Propulsion Conference, held in Boston (MA) [246]. A journal paper based on the final results of this research is under preparation.

This Chapter presents the results of the HYPHEN simulations of SITAEL's HT20k plasma discharge, for different operation points with xenon and krypton as propellants. It comprises six different sections. Section 5.1 briefly describes the thruster and presents the experimental data. Section 5.2 introduces the simulation settings and some differences in the modeling with respect to Chs. 3 and 4. In Section 5.3, the different operation points with Xe are compared in terms of performance figures, global balances and efficiencies, and also in terms of plasma properties in the bulk and along the thruster walls. In Section 5.4, the same analysis is performed with Kr as propellant, and comparison is established with Xe. In Section 5.5, sensitivity analyses concerning plasma plume-related parameters are performed, to study the robustness of the simulation results. Finally, in Sec. 5.6, the most relevant conclusions are drawn.

5.1 Thruster description and experimental data

The HT20k is a high-power (20kW-class) HET developed by SITAEL, which operates with an internally-mounted hollow cathode, SITAEL's HC60 [247]. The development activities of the thruster started in 2015 [150], after having considered the benefits of high-power HETs, the potential market demand (for both commercial and scientific missions) and the lack of development of this technology in Europe, with a few notable exceptions [248].

The first development model of the HT20k thruster (DM1) was experimentally characterized along 2017. The design of the second development model (DM2), in 2018, under the CHEOPS (Consortium for Hall Effect Orbit Propulsion System) H2020 project and a ESA/GSTP (General Support Technology Programme) project, incorporated the MS topology to the thruster, for the extension of its lifetime. Then, an engineering model (EM) was designed and manufactured from the knowledge acquired from SITAEL's HT5k and the previous HT20k models [249]. The EM is the thruster model which has been simulated along the Thesis, mainly within the framework of the ASPIRE H2020 project.

The sketch of the geometry of the HT20k thruster chamber and the near plume region, defined for simulation purposes, is the same as in the HT5k simulations [see Fig. 3.1(b)]. The geometrical parameters L_c and H_c correspond, in this case, to the HT20k thruster chamber length and chamber width, respectively. The simulated plume region extends in the axial direction from the chamber exit plane up to $6L_c$; and in the radial direction from the axis of symmetry up to approximately $6H_c$, with the thruster chamber midline coinciding with the near plume region midline. The HT20k thruster features the same RLC filter circuit as the HT5k, which is schematically depicted in Fig. 3.1(c). Nevertheless, the RLC filter is not experimentally activated in any of the HT20k operation points discussed here and, therefore, is not considered in the simulations. This implies that $V_s = V_d$.

Case	$\dot{m}_A$ (mg/s)	$\dot{m}_C$ (mg/s)	V_s (V)	p_{Xe}(mbar)	B_{max} (mT)	I_d (A)	F (mN)	P (kW)	η_A (%)
Xe1	20	1.5	300	8.8E-6	21	20.5	373	6.15	56.6
Xe2	25	2.0	300	1.2E-5	21	26.8	477	8.04	56.6
Xe3	30	2.3	300	1.3E-5	22	33.3	580	9.99	56.1
Xe4	25	2.0	500	1.2E-5	27	23.9	603	11.95	60.9
Xe5	30	2.3	500	1.4E-5	27	31.0	760	15.50	62.1
Xe6	35	2.6	500	1.6E-5	27	38.2	908	19.10	61.7
Kr1	20	1.8	300	1.6E-5	15	28.0	422	8.4	53.0
Kr2	25	2.0	300	1.7E-5	20	37.2	547	11.16	53.6
Kr3	20	1.8	400	1.9E-5	24	28.2	501	11.28	55.6

Table 5.1: Experimental data for operation points with xenon or krypton as propellant defined in terms of anodic mass flow rate, $\dot{m}_A$, cathode mass flow rate, $\dot{m}_C$, source voltage, V_s, background pressure, p_{Xe}, and strength of the magnetic field peak, B_{max}. The main performance figures are the time-averaged discharge current, I_d; thrust, F; total power, P; and anodic thrust efficiency, η_A.

Tab. 5.1 gathers the experimental data provided by SITAEL for the different operation points with xenon and krypton, respectively. The magnetic topology is the same for all the cases, but the intensity of B is scaled proportionally with the strength of the magnetic field peak, B_{max}. Tab. 5.1 also lists time-averaged experimental values provided for the following thruster performance figures: the discharge current, I_d, the thrust, F, the discharge power, P_d and the anodic thrust efficiency, η_A.

5.2 Simulation model and settings

The HYPHEN model considered for the HT20k simulations is the same as for the HT5k simulations, described in 3.3.1, except for an improvement in the plume downstream boundary condition. The plume downstream boundary, P, is represented by a blue line in Fig. 5.1(a). There, the local null current condition is substituted by a global downstream matching layer (GDML) model. The GDML yields expressions for $j_{\rm ne}$ and $q_{\rm ne}$, and it is defined as a thin boundary layer providing the jump conditions for relevant electron magnitudes between P and infinity, where a final electric potential far downstream, ϕ_∞, is determined from the global current free condition, $I_\infty = 0$ [250]. A first version of the GDML (partially similar to a classical Debye sheath) has been implemented in HYPHEN [250], so that the final potential ϕ_∞ is obtained by imposing a global zero current condition at P, such that $I_{\rm e,\infty} = -I_{\rm i,\infty}$. Compared to the local null current condition, implemented for the HT5k simulations, the GDML model limits plume truncation effects and provides an electron current solution in the near plume more representative of the still magnetized electron population there, while not affecting significantly the plasma solution inside the thruster chamber nor the estimated discharge performance. [250].

Figs. 5.1(a) and (b) show the PIC mesh and the MFAM considered for the modeling of the HT20k discharge. Regarding the PIC mesh, the number of cells and nodes is, respectively, 5328 and 5475, being the smallest grid size equal to 1 mm. Regarding the MFAM, the number of cells and faces is, respectively 3980 and 7794, with the average skewness (see Ref. [186]) being 0.059. The HT20k exhibits a magnetic topology similar to the one of the HT5k, as deduced from the comparison of Figs. 5.1(b) and 3.2(c). In Fig. 5.1(a), the annular anode wall is represented with a green line on the left, while the small black box in Figs. 5.1(a) and (b) indicates the position of the central cathode boundary.

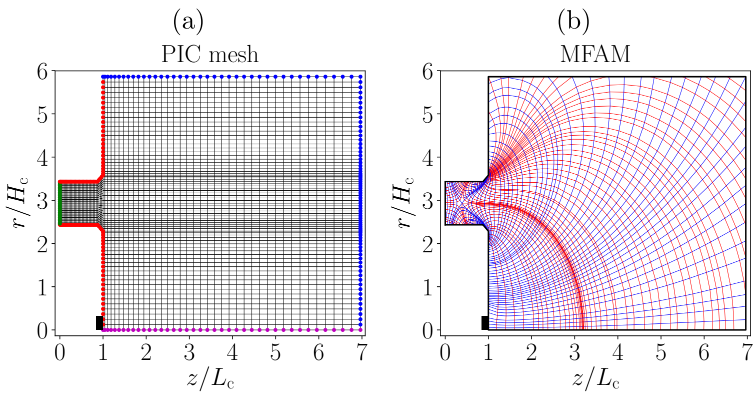

Figure 5.1: (a) Cylindrical mesh used by the I-module. The red, green, blue and magenta lines indicate the thruster dielectric walls, the anode, the plume downstream boundary P, and the symmetry axis, respectively. The centrally-mounted cathode is indicated by the small black box. (b) The MFAM used by the E-module. Blue and red lines are B-parallel and B-perpendicular lines, respectively, defining the cells.

The corresponding anodic mass flow, $\dot{m}_{\rm A}$, is injected from a Maxwellian reservoir through, unlike in the HT5k simulations, only a portion of the anode surface, from $r/H_{\rm c} =$ 2.74 to 3.12, but with the same injection temperature (see Tab. 3.2). Similarly also to the HT5k cases, a sonic drift injection velocity is considered. This velocity varies from Xe to Kr cases accordingly to the square root of the ratio of the atomic masses of the propellants. With the same injection properties as in the anode, the cathode neutral mass flow, $\dot{m}_{\rm C}$, reported from experiments (see Tab. 5.1), is injected. The emission energy of electrons at the cathode, as in Sec. 3.3.2, is set to be $2T_c = 4.5$eV [180].

Both singly and doubly charged ions are simulated. The type of collisions and the particle-wall interaction settings considered in the HT20k simulations are the same as in Sec. 3.3.2. The same occurs for the sheath module settings, since the lateral dielectric walls of the HT20k thruster chamber are made of boron nitride, as the HT5k ones. The replenishment fraction of the high energy tails of the electron VDF, σ_{rp}, is set to 0.1 by default. The metallic anode features no SEE. The (ion) timestep, the total number of timesteps and the number of electron-fluid subiterations are the same as in the HT5k simulations, in Sec. 3.3.2. All the results in this chapter, except in the case of time-series, are time-averaged over an interval which spans a sufficiently large integer number of I_{d} cycles.

5.3 Operation with xenon

In this section, simulations of the HT20k plasma discharge for the operation points in Tab. 5.1, with xenon as propellant, are analyzed. Sec. 5.3.1 presents the fitting of the turbulent parameters for each of the simulated cases. Then, Sec. 5.3.2 analyzes the plasma discharge, including 2D plasma maps and 1D profiles along the thruster chamber axis and along the walls. Finally, in Sec. 5.3.3, the global balances and efficiencies are discussed.

5.3.1 Adjustment of turbulent profiles

For each operation point, the pair $(\alpha_{\mathrm{t}1},\ \alpha_{\mathrm{t}2})$ is tuned to match the experimental data for I_{d} and F, in Tab. 5.1, with a relative error below 5% (the experimental data repeatability). The tuning process has revealed the following trends: on the one hand, $\alpha_{\mathrm{t}1}$ has been found to mainly affect I_{d}, which increases with $\alpha_{\mathrm{t}1}$, while F is not very sensitive to changes in this parameter; on the other hand, both I_{d} and F increase when $\alpha_{\mathrm{t}2}$ increases. The results of the fitting process are summarized in Tab. 5.2.

Case	V_{s} (V)	$\dot{m}_{\mathrm{A}}$ (mg/s)	$(\alpha_{\mathrm{t}1},\ \alpha_{\mathrm{t}2})$ (%)	I_{d} (A)	F (mN)	f_{d} (kHz)	$\Delta I_{\mathrm{d}}/I_{\mathrm{d}}$ (%)
Xe1	300	20	(1.3, 12.0)	21.4	381	13.6	±2.9
Xe2	300	25	(1.2, 13.0)	27.6	492	14.3	±2.5
Xe3	300	30	(1.2, 14.0)	34.1	606	17.7	±2.3
Xe4	500	25	(1.1, 4.0)	24.6	619	12.6	±3.7
Xe5	500	30	(1.1, 7.0)	31.8	768	14.4	±2.1
Xe6	500	35	(1.1, 5.0)	37.5	909	14.9	±5.7

Table 5.2: Simulation results for the best fit of the turbulence parameters (4th column). Simulated results for time-averaged I_{d} and F (5th and 6th columns) are within a 5% error of the experimental values, in Tab. 5.1. Frequency and relative half-amplitude of oscillation of I_{d} are listed in 7th and 8th columns.

Although the fitting of the turbulent parameters targets the pair (I_d,F) only, there exists a good agreement between the simulated values of the dominant frequency of the I_d oscillations (i.e., the frequency of the breathing mode [176]), f_d, and the experimental one: the experimentally reported f_d values range from 6.3 to 18.8 kHz, while the simulated ones range from 12.6 to 17.7 kHz, as seen in Tab. 5.2. The adjusted values of $\alpha_{\mathrm{t}1}$ and $\alpha_{\mathrm{t}2}$, in Tab. 5.2, are slightly larger than the ones obtained in the HT5k discharge (see Sec. 3.4.1) for the same V_s, especially outside the thruster chamber. The turbulent parameters also exhibit similar trends as those found for the HT5k prototype. They seem to have stronger dependence on V_s than on $\dot{m}_\mathrm{A}$. In particular, both $\alpha_{\mathrm{t}1}$ and $\alpha_{\mathrm{t}2}$ decrease with increasing V_s, while there does not exist a clear trend with $\dot{m}_\mathrm{A}$.

Tab. 5.2 shows that both I_d and F increase with $\dot{m}_\mathrm{A}$. This is the expected trend, given that the higher the neutral injection rate, the larger the amount of generated plasma, which ends up being accelerated to the anode and the plasma plume. When V_s increases from 300 V to 500 V: F increases because of the higher kinetic energy of the expelled ions; I_d slightly decreases, indicating a more efficient operation of the thruster.

5.3.2 Plasma discharge maps

In this section, the HT20k plasma discharge is analyzed in terms of 2D maps and 1D axial and wall profiles of the most relevant plasma magnitudes. As previously indicated, the results are time-averaged over an integer number of breathing-mode cycles.

2D plasma maps

Fig. 5.2 and 5.3 show the 2D maps of relevant time-averaged plasma magnitudes of the discharge, including the interior of the thruster chamber and the near plume regions, for the case Xe1. In both Figs. 5.2 and 5.3, the left columns show the plasma properties only inside the thruster chamber, while the right columns present the whole simulation domain. In Fig. 5.2, the plasma magnitudes shown are the neutral density n_n, the plasma density n_e, the electric potential ϕ, and the electron temperature T_e. Fig. 5.3 shows the in-plane ion $\tilde{\boldsymbol{j}}_\mathrm{i}$, electron $\tilde{\boldsymbol{j}}_\mathrm{e}$ and electric $\tilde{\boldsymbol{j}}$ current densities. The 2D plasma maps of the HT20k discharge are qualitatively similar to the ones of the HT5k, in Figs. 3.5 and 3.6, given the similar magnetic topologies. For this reason, the discussion about Figs. 5.2 and 5.3 is focused on their differences with, respectively, Figs. 3.5 and 3.6.

Fig. 5.2(a) shows the 2D map of n_n inside the thruster chamber, which exhibits qualitative differences with respect to the HT5k discharge near the anode wall. This occurs because the neutral gas is injected, unlike in the HT5k, through only a portion of the anode wall in the HT20k configuration. Nevertheless, neutrals soon lose memory of their injection conditions and the differences between both thrusters disappear close to the chamber exit and further downstream in the plume, as shown in Fig. 5.2(b). In both the HT20k and HT5k discharges, the decrease in neutral density inside the thruster chamber indicates a large propellant utilization, as typical in high power HETs, given their beneficial upscaling [53]. In terms of n_e, no significant differences between the discharges of both thrusters are observed in Fig. 5.2(c) and (d). As with the HT5k, the peak of n_e is located around the position of the magnetic singular point inside the chamber.

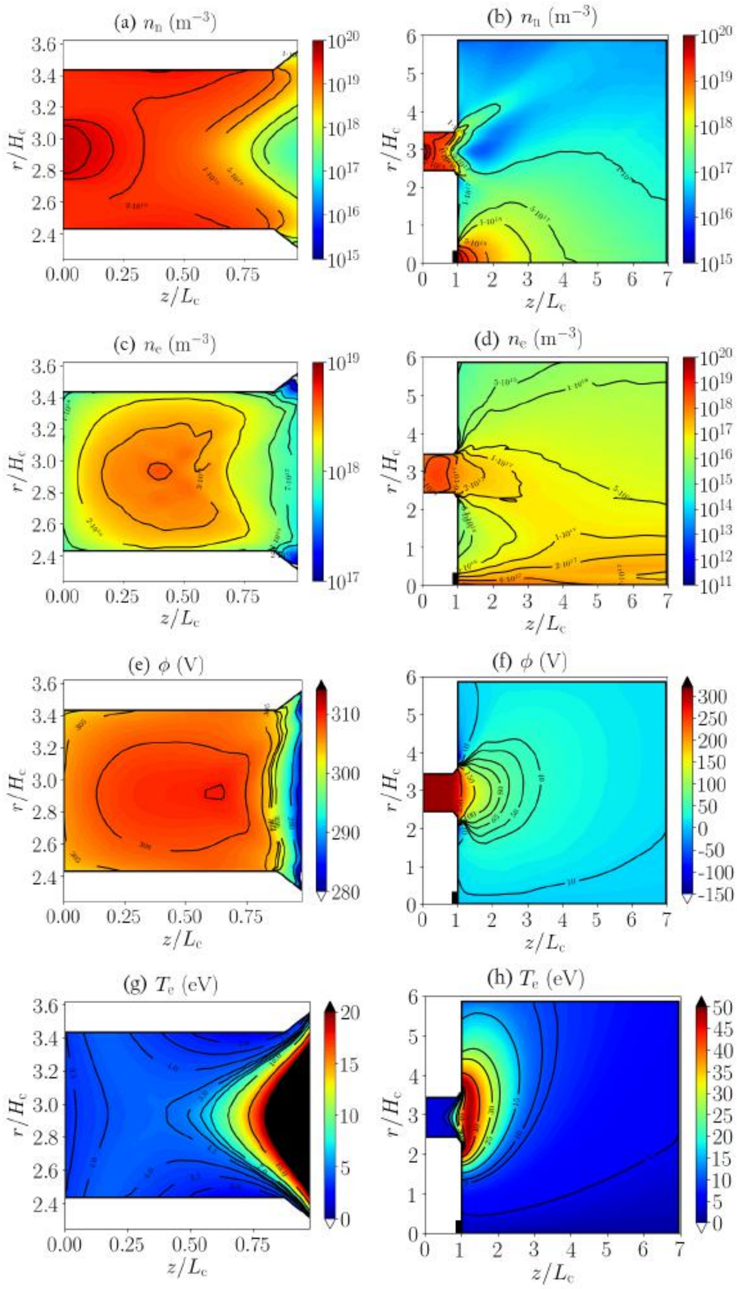

Figure 5.2: Time-averaged 2D (z,r) contour maps for the case Xe1. (a)-(b) Neutral density n_n, (c)-(d) plasma density n_e, (e)-(f) electric potential ϕ and (g)-(h) electron temperature T_e. The left column plots show magnitudes inside the thruster chamber, while the right column plots correspond to the whole simulation domain. The centrally-mounted cathode is indicated by the small black box.

As a consequence of the MS topology and the outward shifting of the acceleration zone, the profile of ϕ is practically flat inside the chamber, as seen in Fig. 5.2(e). In the plume region, Fig. 5.2(f) shows that ϕ falls down to 50 V in an axial distance of around two chamber lengths from the exit plane, as in the HT5k discharge [see Fig. 3.4(a)].

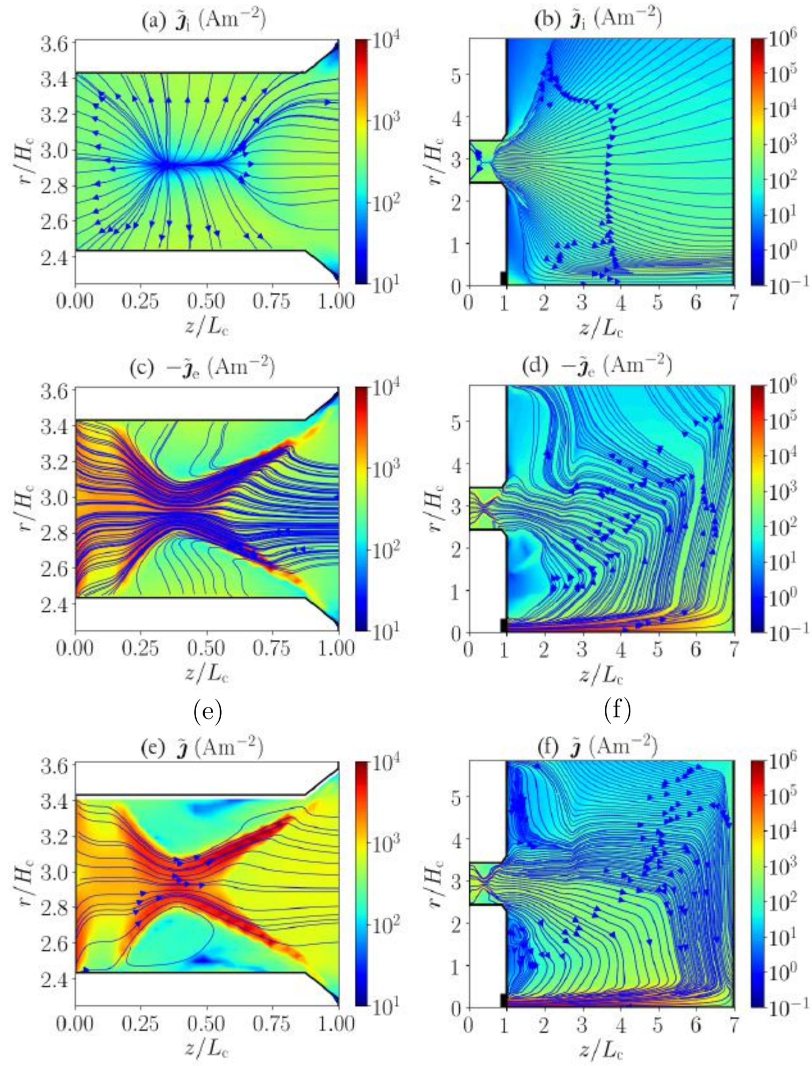

Figure 5.3: Time-averaged 2D (z,r) contour maps for the case Xe1. Magnitude of the longitudinal (a)-(b) ion current density vector $\tilde{\boldsymbol{\jmath}}_{\rm i}$, (c)-(d) electron current density vector $\tilde{\boldsymbol{\jmath}}_{\rm e}$ and (e)-(f) electric current density vector $\tilde{\boldsymbol{\jmath}}$. Blue lines with arrows depict the streamlines of (a)-(b) $\tilde{\boldsymbol{\jmath}}_{\rm i}$, (c)-(d) $-\tilde{\boldsymbol{\jmath}}_{\rm e}$ and (e)-(f) $\tilde{\boldsymbol{\jmath}}$. The left column plots show magnitudes inside the thruster chamber, while the right column plots correspond to the whole simulation domain. The centrally-mounted cathode is indicated by the small black box close to the axis.

Compared also to Fig. 3.4(a), the axial gradient of ϕ in the plume is less steep, taking into account normalization by $L_{\rm c}$. Fig. 5.2(h) shows that $T_{\rm e}$ peaks at a value slightly larger than 40 eV downstream the channel exit. Although the $T_{\rm e}$ peak is higher than in the HT5k discharge (with the same $V_{\rm s}$), Fig. 5.2(g) shows that the thruster chamber walls are, also in the HT20k case, effectively shielded: electron temperature near the walls is very low ($T_{\rm e} \approx$ 3-4 eV).

Fig. 5.3(a) shows the ion streamlimes of the HT20k discharge. These streamlines have their origin where $\tilde{\boldsymbol{\jmath}}_{\rm i} = 0$, around the chamber midline from $z/L_{\rm c} = 0.25$ to $z/L_{\rm c} = 0.75$.

This region extends further downstream than in the HT5k discharge, in Fig. 3.6(a). The fact that $\tilde{\boldsymbol{j}}_{\mathrm{i}}$ remains 0 closer to the chamber exit implies that acceleration and ionization are shifted downstream in the HT20k discharge. Figs. 5.3(a), (c) and (e) reveal that, as with the HT5k, electron current dominates over ion current inside the thruster chamber. Again, the magnetic field channeling of $\tilde{\boldsymbol{j}}_{\mathrm{e}}$ is observed. Compared to the HT5k discharge, the $\tilde{\boldsymbol{j}}_{\mathrm{e}}$ streamlines in Fig. 5.3(d) exhibit relatively abrupt turns near the downstream boundary. This result suggests that, although the electron transport across $\boldsymbol{B}$ lines is enhanced thanks to the cathode neutral injection, the simulation domain might have to be slightly extended downstream to better capture the cathode-beam coupling. It must be noted that these abrupt turns in the $\tilde{\boldsymbol{j}}_{\mathrm{e}}$ streamlines are not observed in the HT20k operation points with $V_{\mathrm{s}} = 500$ V. A possible explanation for this is given in the analysis of Fig. 5.4, but further investigations would be needed to clarify it.

Fig. 5.3(f) shows that, unlike in the HT5k simulations, where the local null current is imposed, there exist current loops closing outside the simulation domain, as a result of the GDML condition decoupling ion and electron local current densities. Across the lateral plume boundary, electric current comes into the domain, because of the dominance of j_{ne} over j_{ni} there. This incoming current is compensated by the current leaving across the vertical downstream plume boundary (close to the symmetry axis), where j_{ni} dominates over j_{ne}. The net electric current leaving the domain is null, as imposed with the GDML condition.

1D axial profiles

The axial profiles of the main plasma variables along the thruster chamber midline are displayed in Fig. 5.4, for the cases in Tab. 5.2 with $\dot{m}_{\mathrm{A}} = 25$, 30 mg/s at $V_{\mathrm{s}} = 300$, 500 V. The largest differences in the 1D profiles of the magnitudes are found between cases with different V_{s}.

In Fig. 5.4(a), the comparison of the different operation points shows that n_{n} is smaller in the plume for $V_{\mathrm{s}} = 500$ V. This indicates a higher η_{u} for higher V_{s}, as occurs in conventional US thrusters [251]. The improved neutral gas ionization is linked to the higher electron temperature, as seen in Fig. 5.4(d). The plasma density profiles for all cases, in Fig. 5.4(b), are qualitatively similar. The cases with higher $\dot{m}_{\mathrm{A}}$ (Xe3 and Xe5) exhibit larger density peaks inside the chamber. Fig. 5.4(c) shows that ϕ is higher in the plume along the midline for the cases with $V_{\mathrm{s}} = 500$ V. This can explain why the abrupt turns in the $\tilde{\boldsymbol{j}}_{\mathrm{e}}$ streamlines, in Fig. 5.3(d), disappear at higher V_{s} operation: the increase in the radial $\boldsymbol{E}$ strength (a proportionally larger increase than the one in the $\boldsymbol{B}$ strength) enhances cathode-to-plume radial electron fluxes. There is also an outward displacement of the acceleration zone with increasing V_{s}, as observed in Fig. 5.4(d), indicated by the fact that the T_{e} peak (as well as the electric field peak, not shown here) moves downstream for larger V_{s}.

Plasma-wall interaction

To study in more detail the effects of the MS topology in the HT20k discharge, Fig. 5.5 displays the profiles of relevant time-averaged plasma variables at the thruster chamber

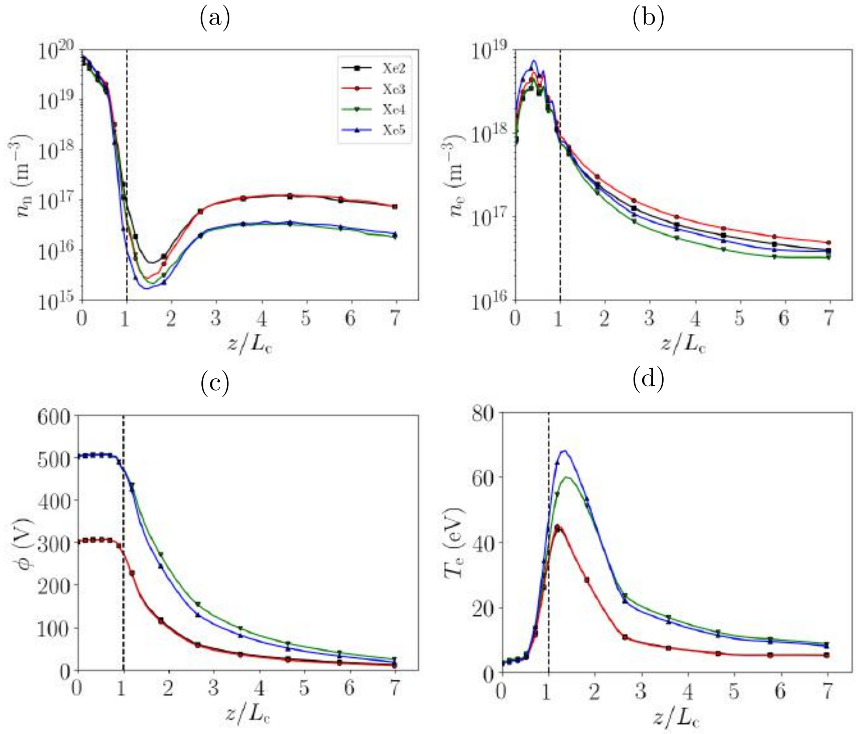

Figure 5.4: Time-averaged 1D axial profiles along the thruster chamber midline of xenon operation points with $\dot{m}_A = 25$ and 30 mg/s in, respectively, black and red lines for $V_s =$ 300 V and green and blue lines for $V_s = 500$ V. Magnitudes are (a) neutral density n_n, (b) plasma density n_e, (c) electric potential ϕ and (d) electron temperature T_e.

walls. The length coordinate s runs from the inner chamfer end to the outer chamfer end. For all the operation points, the profiles are qualitative and quantitatively similar to each other. A qualitative similarity exists also with the HT5k discharge, in Fig. 3.7. In Fig. 5.5(a), the electric potential at the sheath edge, ϕ_Q, exhibits, for all cases, a flat profile over the whole chamber wall. The value of ϕ_Q is everywhere along this surface close to V_s (= 300 V). This confirms that the MS configuration is shifting most of the acceleration zone to the near plume region, out of the thruster chamber. Only at the outer corner of both chamfers, it is found that ϕ_Q decreases to values smaller than 300 V, by several dozens of volts.

Figs. 5.5(b) shows the sheath potential fall, $\Delta\phi_{sh}$, and Fig. 5.5(c) shows the electron temperature at the sheath edge. The electron temperature, as already observed in Fig. 5.3(g), is relatively low (∼2-5 eV) and the ratio $e\Delta\phi_{sh}/T_e$ ranges from 1.0 to 3.0. The HT5k features the same range of values for $e\Delta\phi_{sh}/T_e$, since the wall material and the local T_e are the same in the discharge of both thrusters (see Eqs. A.1 and A.2 in Ch. 3). The low value of T_e results in a small SEE yield, δ_s ($\sim$ 0.1-0.2), along all the thruster walls. Fig. 5.5(f) shows the profile of the average energy per net collected electron, $\mathcal{E}_{e,wall}$. Since T_e and δ_s have low values on the walls, and so $\Delta\phi_{sh}$, $\mathcal{E}_{e,wall}$ is also small (see Eq. A.5).

Fig. 5.5(d) plots the electron and ion current densities towards the walls. At the anode wall, similarly to the HT5k discharge, the backward j_{ni} amounts to approximately

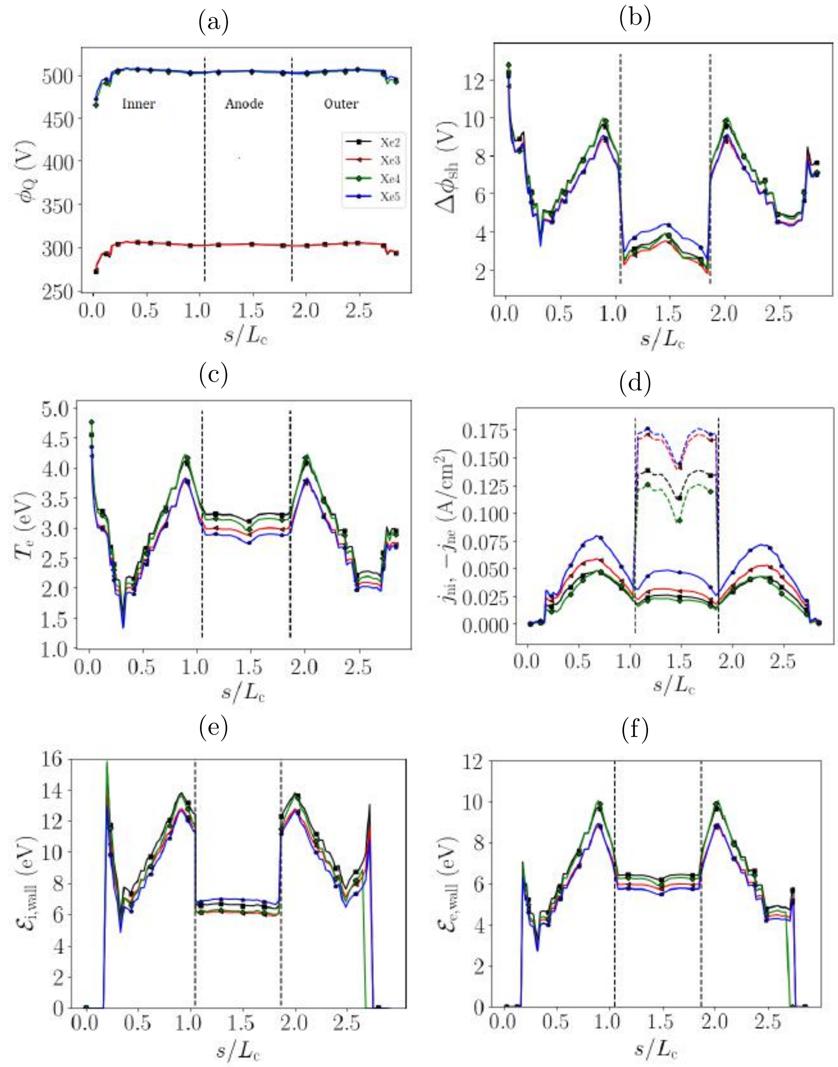

Figure 5.5: Time-averaged 1D profiles along the thruster chamber walls of xenon operation points with $\dot{m}_A = 25$ and 30 mg/s in, respectively, black and red lines for $V_s = 300$ V and green and blue lines for $V_s = 500$ V. Coordinate s runs from the inner chamfer end to the outer chamfer end. Magnitudes of (a) electric potential at the sheath edge, ϕ_Q; (b) potential fall across the sheath edge, $\Delta\phi_{sh}$; (c) electron temperature at the sheath edge, T_e; (d) ion (solid line), j_{ni}, and electron (dashed line), j_{ne}, current normal to the walls; (e) ion wall-impact energy, $\mathcal{E}_{i,wall}$; and (f) impact energy per net collected electron, $\mathcal{E}_{e,wall}$.

a 15-25% of j_{ne}. Unlike in the HT5k, j_{ne} exhibits a sudden drop at the center of the anode surface, also visible in Fig. 5.3(c), which may be a consequence of the neutral injection profile [see Fig. 5.3(a)]. Fig. 5.5(e) shows the profile of the average energy per ion particle reaching the wall $\mathcal{E}_{i,wall}$. The low values of $\Delta\phi_{sh}$, in Fig. 5.5(b), results in ion-impact energies below typical thresholds for erosion of boron nitride walls [154, 198], along most of the chamber walls. This further confirms that the MS topology of the HT20k is effective for the operational range under study. Nevertheless, since there is a drop in ϕ near the outer corners of both chamfer walls [see Fig. 5.5(a)], $\mathcal{E}_{i,wall}$ increases there. Then, its value becomes zero right at the outer corners because, as shown in Fig. 5.5(d), j_{ni} is negligible on that part of the surface, thanks to the ion streamlines running nearly parallel to those walls, as seen in Fig. 5.3(b). In the HT5k discharge, j_{ni} behaves in the same way, as observed in Fig. 3.7(c).

Back in Fig. 5.5, the largest quantitative differences among the HT20k simulation points are found in terms of j_{ni} and j_{ne}. Unlike the axial profiles along the chamber midline, in Fig. 5.4, the magnitudes at the walls does exhibit a dependence on $\dot{m}_{\mathrm{A}}$. In Fig. 5.5(c), the cooling effect of a higher $\dot{m}_{\mathrm{A}}$ [252] is visible in the case Xe3 (as compared to Xe2) and Xe5 (as compared to Xe4), and $\Delta\phi_{\mathrm{sh}}$ and $\mathcal{E}_{\mathrm{e,wall}}$ are smaller for those cases [see Figs. 5.5(b) and (f)]. For these same cases, j_{ni} and j_{ne} are maximum in Fig. 5.5(d), because n_{e} inside the chamber [see Fig. 5.4(b)] is higher.

5.3.3 Global balances and efficiencies

Tabs. 5.3 and 5.4 contain the terms of the current and power balances in Eqs. (3.11) and (3.13), respectively, and the partial efficiencies defined in Eqs. (3.12) and (3.15), for the different operation points with Xe. The amount of ion current to the cathode, I_{iC}, is negligible compared to I_{iA}, and is not included. The relative current losses to the lateral walls, $I_{\mathrm{iD}}/I_{\mathrm{prod}}$, are large compared to a US HET, and also higher than those found in the HT5k discharge (see Tab. 3.4). The relative ion current losses to the anode, $I_{\mathrm{iA}}/I_{\mathrm{prod}}$, are similar to those in a US HET discharge. With respect to the HT5k case (see Tab. 3.4), $I_{\mathrm{iA}}/I_{\mathrm{prod}}$ is observed to be lower in the HT20k, because numerical simulations have shown that ionization occurs closer to the thruster channel exit in the HT20k discharge. From the point of view of ion current losses to walls, as it occurs with the HT5k, the MS topology is not advantageous with respect to the US one.

In Tab. 5.3, all the operation points exhibit high values of η_{u} (the same as in the HT5k discharge at 300 V), which are enhanced at 500 V, as anticipated in Sec. 5.3.2 from Fig. 5.4. The current efficiency, η_{cur}, is, in average, also high relative to conventional US HETs under the usual operational regime [253]. It is observed that η_{cur} grows with V_{s}, as reported from other HETs, both US and MS ones [254–256], including the HT5k [see Tab. 3.4]. This growing trend could be associated to an improvement in the electron confinement inside the discharge chamber [3] and is in line with the decrease in α_{t1} at higher V_{s}, in Tab. 5.2. Regarding η_{ch}, this is observed to decrease with increasing $\dot{m}_{\mathrm{A}}$ and V_{s}, as reported experimentally for US HET's [253,254]. This implies that the doubly-charged ion fraction increases with $\dot{m}_{\mathrm{A}}$ and V_{s}.

In Tab. 5.4, the beneficial impact of MS in the HT20k is evidenced by the terms in the power balance: although $I_{\mathrm{iD}}/I_{\mathrm{prod}}$ is 46-52%, the corresponding relative power losses (which also includes the contribution of electrons), P_{D}/P, is only a 3-5% of the total input power. Moreover, the total energy losses to the thruster chamber walls, adding the ones to the anode, amount only to a 4-7%. The ratio $P_{\mathrm{inel}}/I_{\mathrm{prod}}$, which represents an effective single-ionization cost, yields 23-25 eV. This value, nearly the same as in the HT5k discharge, is 1.9 times greater than the first ionization energy of Xe, as a consequence of double ionization and excitation processes. The fraction of beam power, $P_{\infty}/P \equiv \eta_{\mathrm{ene}}$ (with negligible contribution from electrons), raises with V_{s}. This trend is

Case	V_s (V)	$\dot{m}_A$ (mg/s)	I_{prod} (A)	$I_{i\infty}/I_{prod}$	I_{iD}/I_{prod}	I_{iA}/I_{prod}	η_u	η_{cur}	η_{ch}
Xe1	300	20	35.1	0.49	0.46	0.05	0.93	0.81	0.85
Xe2	300	25	45.9	0.49	0.46	0.05	0.94	0.81	0.83
Xe3	300	30	57.0	0.49	0.46	0.05	0.95	0.82	0.80
Xe4	500	25	44.9	0.50	0.44	0.06	0.98	0.91	0.86
Xe5	500	30	67.6	0.41	0.52	0.07	0.98	0.87	0.84
Xe6	500	35	73.7	0.46	0.47	0.07	0.99	0.89	0.82

Table 5.3: Different contributions to the current balance in Eq. (3.11) and related partial efficiencies, defined in Eq. (3.12).

Case	V_s (V)	$\dot{m}_A$ (mg/s)	P (kW)	η	P_{inel}/P	P_D/P	P_A/P	P_∞/P ($=\eta_{ene}$)	η_{div}	η_{disp}
Xe1	300	20	6.38	0.52	0.13	0.05	0.02	0.80	0.78	0.83
Xe2	300	25	8.29	0.54	0.14	0.04	0.02	0.80	0.80	0.84
Xe3	300	30	10.23	0.56	0.14	0.03	0.02	0.81	0.81	0.85
Xe4	500	25	12.32	0.57	0.09	0.03	0.02	0.86	0.77	0.86
Xe5	500	30	15.91	0.58	0.10	0.03	0.01	0.86	0.78	0.86
Xe6	500	35	18.74	0.59	0.09	0.03	0.01	0.87	0.77	0.88

Table 5.4: Different contributions to the power balance in Eq. (3.13), and related partial efficiencies, defined in Eqs. (3.14) and (3.15).

driven by the enhancement in η_{cur}, in Tab. 5.3, since η_{vol} remains approximately constant for all cases ($\eta_{ene} \equiv \eta_{vol}\eta_{cur}$). Measurements of the high-power MS H9 thruster also reveal little variation of η_{vol} across Xe operation points [256], whereas this efficiency is clearly enhanced with increasing V_s in the high-power US NASA-173Mv2 (although its η_{vol} also quantifies plume divergences) [254]. These differences among prototypes cannot be directly attributed to the dissimilar magnetic topologies: geometrical factors or the cathode position (unlike the H9 and the HT20k, the NASA-173Mv2 has a externally-mounted cathode) may play a significant role [257,258].

To estimate the divergence of the plume, proceeding as in Sec. 3.4.3, we set $\cos^2\alpha_{div} = \eta_{div}$. From this equality, the mean half-divergence angle of the plasma plume is $\alpha_{div} \approx 27.6$ deg, slightly larger than in the H9 discharge [256]. It is in terms of η_{div} that the largest disagreement ($\approx 8\%$) is found between the HT20k and the HT5k discharges. The HT20k exhibits larger divergence partly due to the downstream shift, relative to the HT5k discharge, of its acceleration zone, as reported from simulations. Similarly to η_{vol}, η_{div} barely changes from case to case in Tab. 5.4. The ratio η_{disp}/η_u, which characterizes the level of kinetic energy dispersion of the plasma species in the plume, remains around 0.88-0.89 for all Xe cases. The thrust efficiency, η, ranges from 0.52 to 0.59. In terms of anodic efficiency, $\eta_A = (\dot{m}/\dot{m}_A)\eta \approx [0.57,\ 0.63]$, the performance of the HT20k with Xe is similar to that of other US and MS high-power HETs, under similar operating conditions [248,253,254,256,259].

5.3.4 Plasma-wall interaction sensitivity analyses

An analysis of the sensitivity of the simulation results to some plasma-wall interaction parameters is presented. The MS topology is expected to affect the sensitivity of the simulation to the plasma-wall parameters. In particular, the influence of (*i*) the replenishment fraction of the electron VDF, σ_{rp}, and (*ii*) the parameter E_{r}, which appears in the expression for the yield of elastically reflected electrons in Eq. (A.3), is studied. The operation point Xe1, from Tab. 5.1, is taken as baseline case for the analysis.

Electron VDF replenishment fraction

A value of the electron VDF replenishment fraction parameter, σ_{rp}, close to 1 represents a small depletion of the high energy tail of the electron VDFs near the thruster walls. On the contrary, a value of σ_{rp} close to 0 means a large depletion of the tails of the electron VDFs. This parameter can have a significant influence on the particle and energy fluxes deposited to the thruster chamber walls.

Case	I_{prod} (A)	P (kW)	η	$I_{\mathrm{iD}}/I_{\mathrm{prod}}$	P_{D}/P	η_{u}	η_{cur}	η_{ene}	η_{div}
$\sigma_{\mathrm{rp}} = 0.1$	35.3	6.42	0.53	0.46	0.05	0.94	0.81	0.80	0.78
$\sigma_{\mathrm{rp}} = 0.5$	33.8	6.41	0.52	0.45	0.06	0.93	0.81	0.80	0.80
$\sigma_{\mathrm{rp}} = 1.0$	33.3	6.40	0.52	0.44	0.07	0.93	0.80	0.80	0.80

Table 5.5: Value of I_{prod} and fractions of I_{prod} corresponding to the different contributions to the current balance in Eq. (3.11). Values of η_{u}, η_{cur} and η_{ch}.

Three different values σ_{rp} are considered for the sensitivity study: 0.1 (baseline case), 0.5 and 1. Over this range of values of σ_{rp}, all the main performance metrics exhibit variations of just a 1 or 2% (see Tab. 5.5), and the 2D maps of the most relevant plasma variables are barely affected. In Fig. 5.6, the profiles of the main plasma magnitudes at the thruster walls are shown. The black line with square markers corresponds to the baseline case, with $\sigma_{\mathrm{rp}} = 0.1$ (see Fig. 5.5). The red and green lines correspond, respectively, to the cases with $\sigma_{\mathrm{rp}} = 0.5$ and 1. Figs. 5.6(a) and (b) evidence the increase in the sheath potential fall, $\Delta\phi_{\mathrm{sh}}$, at the thruster walls, as σ_{rp} is augmented. As the high energy tails of the electron VDF are more replenished, the flux of electrons to the walls rises and $\Delta\phi_{\mathrm{sh}}$ must increase to counteract this effect, and keep the electron current equal to the ion one. Nevertheless, the change in ϕ is relative small, around $0.02V_{\mathrm{d}}$. As $\Delta\phi_{\mathrm{sh}}$ increases, so does $\mathcal{E}_{\mathrm{i,wall}}$ in Fig. 5.6(e). This variation is very slight and $\mathcal{E}_{\mathrm{i,wall}}$ remains below the erosion threshold for all cases. Unlike $\mathcal{E}_{\mathrm{i,wall}}$, $\mathcal{E}_{\mathrm{e,wall}}$ decreases as σ_{rp} grows, as seen in Fig. 5.6(f) following T_{e} in Fig. 5.6(c). All the changes are, nevertheless, very slight, thanks to the reduction of the plasma-wall interaction in MS thrusters [59].

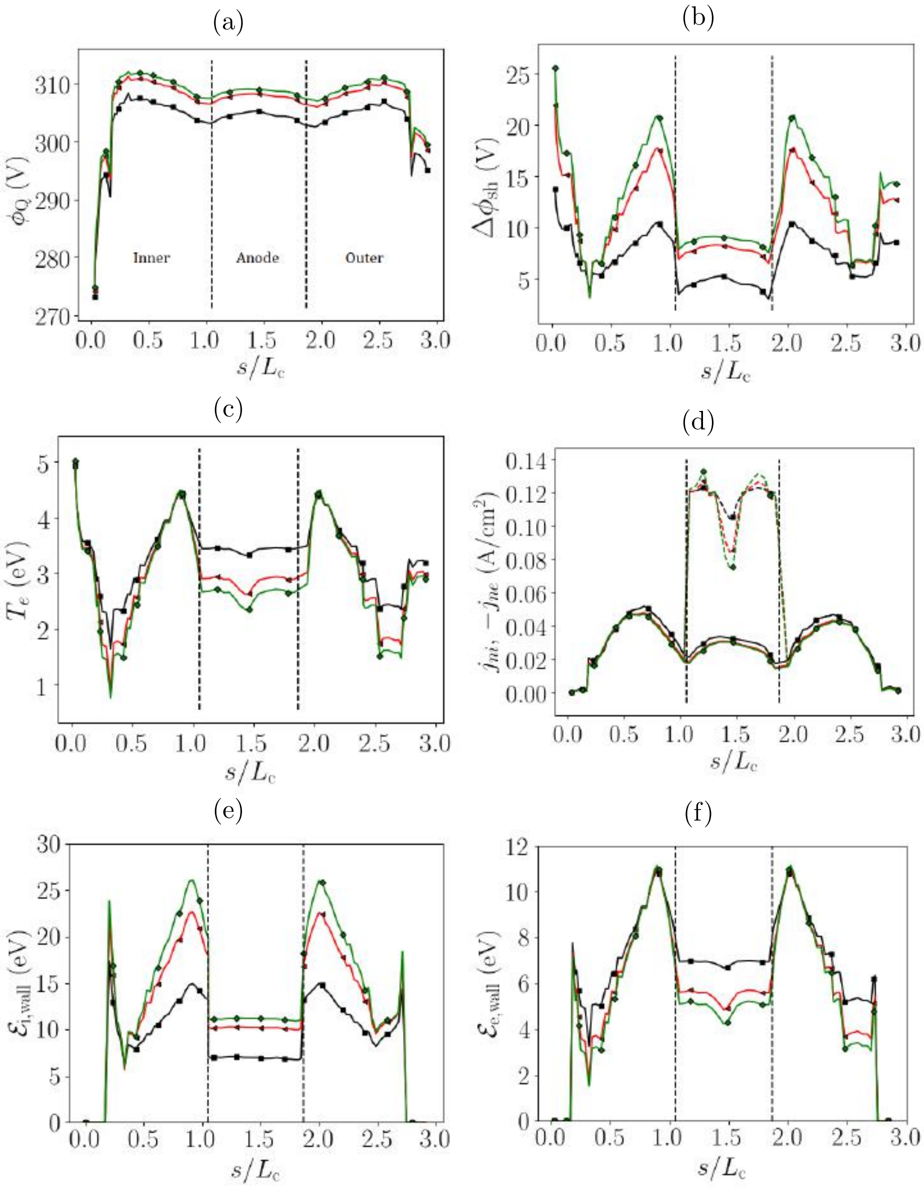

Figure 5.6: Time-averaged 1D profiles along the thruster chamber walls for simulation cases with $\sigma_{rp} = 0.1$ (black line with square markers), $\sigma_{rp} = 0.5$ (red line with triangle markers) and $\sigma_{rp} = 1.0$ (green line with diamond markers). Coordinate s runs from the inner chamfer end to the outer chamfer end. Magnitudes description as in Fig. 5.5.

Elastically reflected electrons

The yield for elastically reflected electrons, δ_r, is a function of the parameter E_r at the dielectric walls, according to Eq. (A.3). For a given T_e, δ_r grows with E_r. Two different cases are simulated in this section: one with $E_r = 20$ eV (baseline case in Sec. 5.3), and another one with $E_r = 40$ eV.

Fig. 5.7 shows the time-averaged 1D profiles of δ_r and T_e along the thruster chamber walls. The black line corresponds to the case with $E_r = 20$ eV, and the red line to the

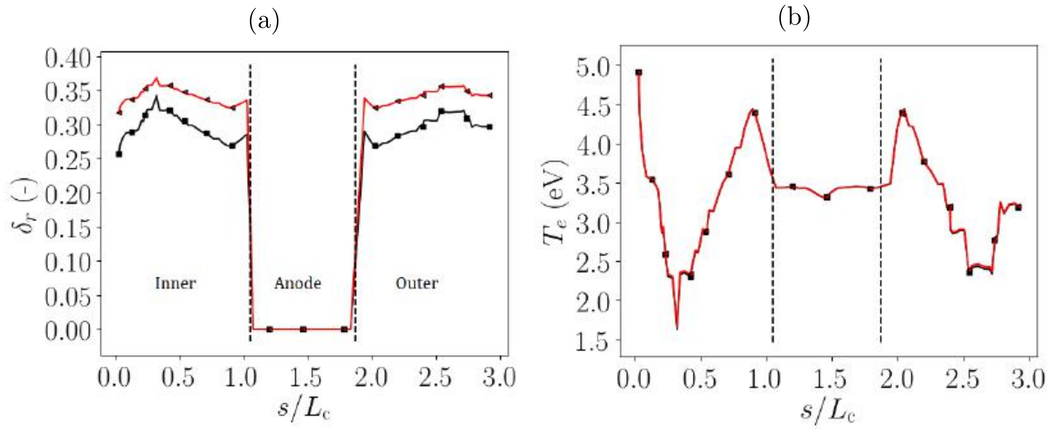

Figure 5.7: Time-averaged 1D profile along the thruster chamber walls for simulation cases with $E_\mathrm{r} = 20$ eV (black line with square markers), $E_\mathrm{r} = 40$ eV (red line with triangle markers). Coordinate s runs from the inner chamfer end to the outer chamfer end. Profiles of (a) reflected electrons yield δ_r and (b) electron temperature T_e.

one with $E_\mathrm{r} = 40$ eV. Since the electron temperature remains the same from one case to the other, as seen in Fig. 5.7(b), δ_r increases with E_r at the dielectric walls, in Fig. 5.7(a). Doubling the value of E_r leads to a 15% increment in δ_r. Given the low energy of electrons reaching the walls, this variation in δ_r does not have any significant effect in the global energy balance and, thus, in the performance. This is again a consequence of the MS topology.

5.4 Operation with krypton. Comparison with Xe

In this section, the simulation results for several operation points with krypton as propellant are presented and analyzed, and compared to the xenon discharge. The same simulation settings of Sec. 5.3 are considered, except for the propellant injection velocity, which is modified according to the square root of the ratio of the Xe and Kr atomic masses, assuming that the reservoir temperature is kept constant from case to case. The turbulent parameters fitting is presented in Sec. 5.4.1. Then, Sec. 5.4.2 analyses the 2D plasma maps of the discharge. Finally, global balances and efficiencies are introduced and discussed, in Sec. 5.4.3.

Given the dissimilar atomic weights of the propellants [$A_\mathrm{r}(\mathrm{Xe}) = 131.29\mathrm{u}$ and $A_\mathrm{r}(\mathrm{Kr}) = 83.80\mathrm{u}$], three different Xe-Kr comparison scenarios have been considered in the literature: (i) with the same V_s and (similar) P; (ii) with the same V_s and (similar) volumetric flow rate, Q_A; and (iii) with the same V_s and $\dot{m}_\mathrm{A}$. In first place, regarding the comparison scenario with the same V_s and P, in Ref. [260] the authors have experimentally compared Xe and Kr performance with the M3 magnetic configuration (shielded) of the HT5k-DM2 prototype (details about the HT5k-DM2 prototype can be found in Ref. [149]), keeping P constant at 2.5 kW and 4.5 kW and $V_\mathrm{s} = 300$ V. A study on the NASA-173Mv1 HET (5kW thruster with conventional magnetic topology and a trim coil [261, 262]), has been performed to compare Xe and Kr performance also with the same P [253]. The latter experiments have been carried out at operating voltages higher than nominal (700V, with $P = 6$ and 8 kW), as Kr would be preferred over Xe in high $I_{\rm sp}$ missions. Su et. al [256] studies this comparison scenario with the high-power MS H9 thruster. In second place, in Ref. [253], beyond the comparison at the same P, they have also compared Xe and Kr cases with the same $Q_{\rm A}$ and $V_{\rm s}$. The same approach has been followed with the 50kW-class HET NASA-457M [263] and the NASA-400M [259], an improved version of NASA-475M optimized for Kr operation. Finally, there is the comparison of Xe and Kr operation with the same $\dot{m}_{\rm A}$ and $V_{\rm s}$. This comparison scenario can be found, for instance, in Ref. [264]. In this experimental work, they test a conventional SPT-100 with both propellants over an operational envelope ranging from 800 kW to 3.5kW.

The discussion that follows through the next sections is common to all the different Xe-Kr comparison scenarios, although some particularities of each of them are also addressed.

5.4.1 Adjustment of turbulent profiles

The same fitting process described for Xe operation points is repeated here for Kr, yielding the results shown in Tab. 5.6. The experimental values of $f_{\rm d}$ for the three cases are in the range of 13.2 to 14.1 kHz, while the simulated ones range from 9.9 to 13.5 kHz, as seen in Tab. 5.6.

Case	$V_{\rm s}$ (V)	$\dot{m}_{\rm A}$ (mg/s)	$(\alpha_{\rm t1}, \alpha_{\rm t2})$ (%)	$I_{\rm d}$ (A)	F (mN)	$f_{\rm d}$ (kHz)	$\Delta I_{\rm d}/I_{\rm d}$ (%)
Kr1	300	20	(1.4, 4.0)	28.4	429	11.7	±3.9
Kr2	300	25	(1.5, 6.0)	36.5	557	13.5	±3.8
Kr3	400	20	(1.5, 5.0)	28.4	513	9.9	±4.2

Table 5.6: Simulation results for the best fit of the turbulence parameters (4th column). Simulated results for time-averaged $I_{\rm d}$ and F (5th and 6th columns) are within a 5% error of the experimental values, in Tab. 5.1. Frequency and relative half-amplitude of oscillation of $I_{\rm d}$ are listed in 7th and 8th columns.

In Tab. 5.6, $I_{\rm d}$ and F exhibit the same trends observed in the Xe cases (see Tab. 5.2). The anomalous transport parameter in the plume, $\alpha_{\rm t2}$, is clearly lower with Kr than with Xe, for all cases at same $V_{\rm s}$ (i.e. cases with $V_{\rm s} = 300$ V). Whether this behavior is related or not to an underlying physical mechanism is beyond the scope of this study. In spite of the differences, each of the anomalous transport coefficients, $\alpha_{\rm t1}$ and $\alpha_{\rm t2}$, keep the same order of magnitude across discharges with Xe and Kr, and across different prototypes too [HT20k vs. HT5k (see Tab. 3.3)]. This fact denotes certain robustness in the phenomenological anomalous transport model.

5.4.2 Plasma discharge maps

Fig. 5.8 compares time-averaged axial profiles along the thruster chamber midline and 2D contour maps of the relevant plasma magnitudes of the operation points Xe3 (black

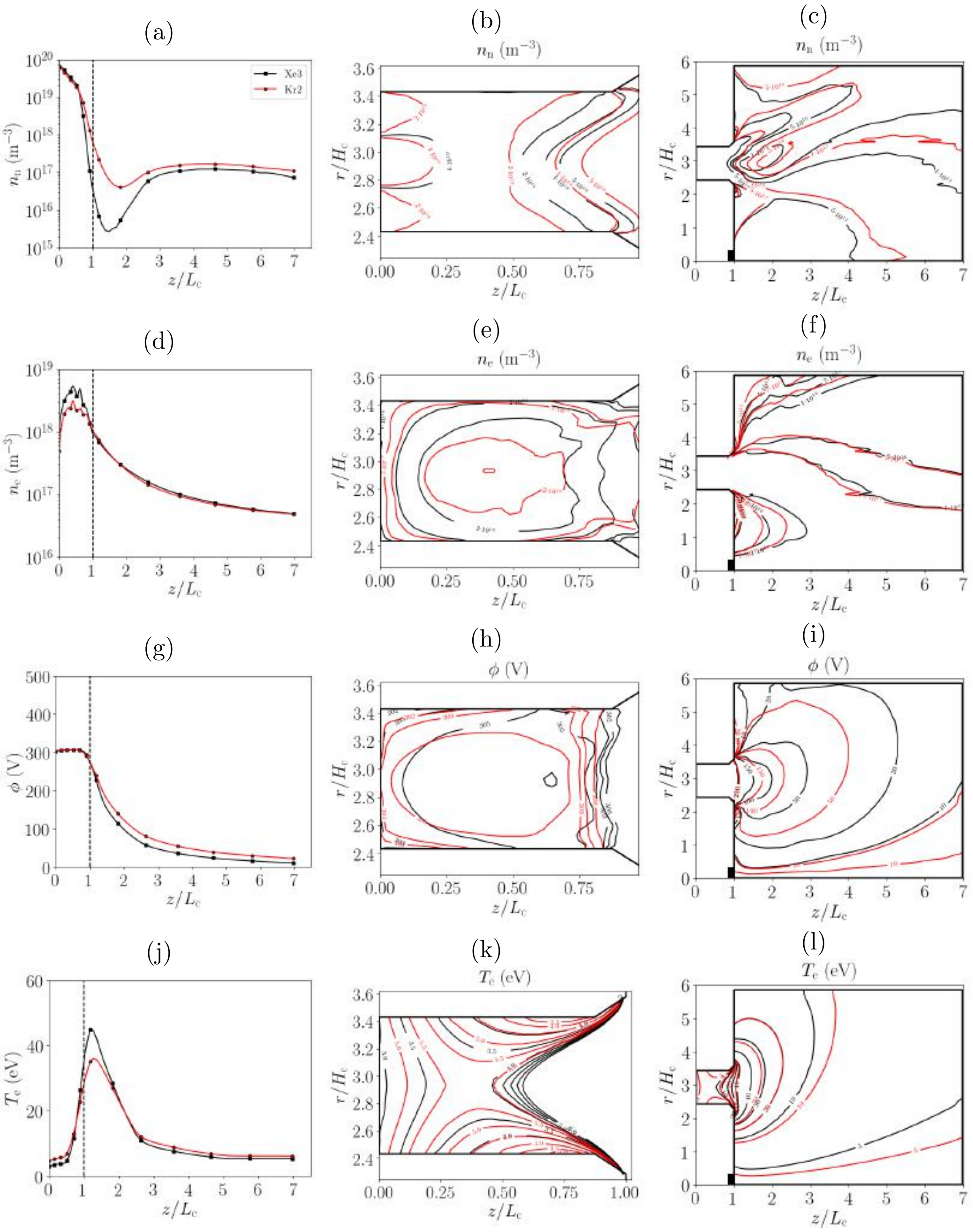

Figure 5.8: Time-averaged 1D axial profiles along the thruster chamber midline (left column) and 2D contour maps inside the thruster chamber (central column) and the whole simulation domain (right column) of the operation points with Xe3 (black line) and Kr2 (red line). Magnitudes of (a-c) n_n, (d-f) n_e, (g-i) ϕ, and (j-l) T_e. Xe3 and Kr2 cases feature the same values of V_s and (similar) P.

line) and Kr2 (red line). These cases features the same value of V_s and (similar) P. The comparison of any other two Xe and Kr cases is qualitative similar.

Fig. 5.8(a) shows that n_n is larger in the plume with Kr. This may be attributed to

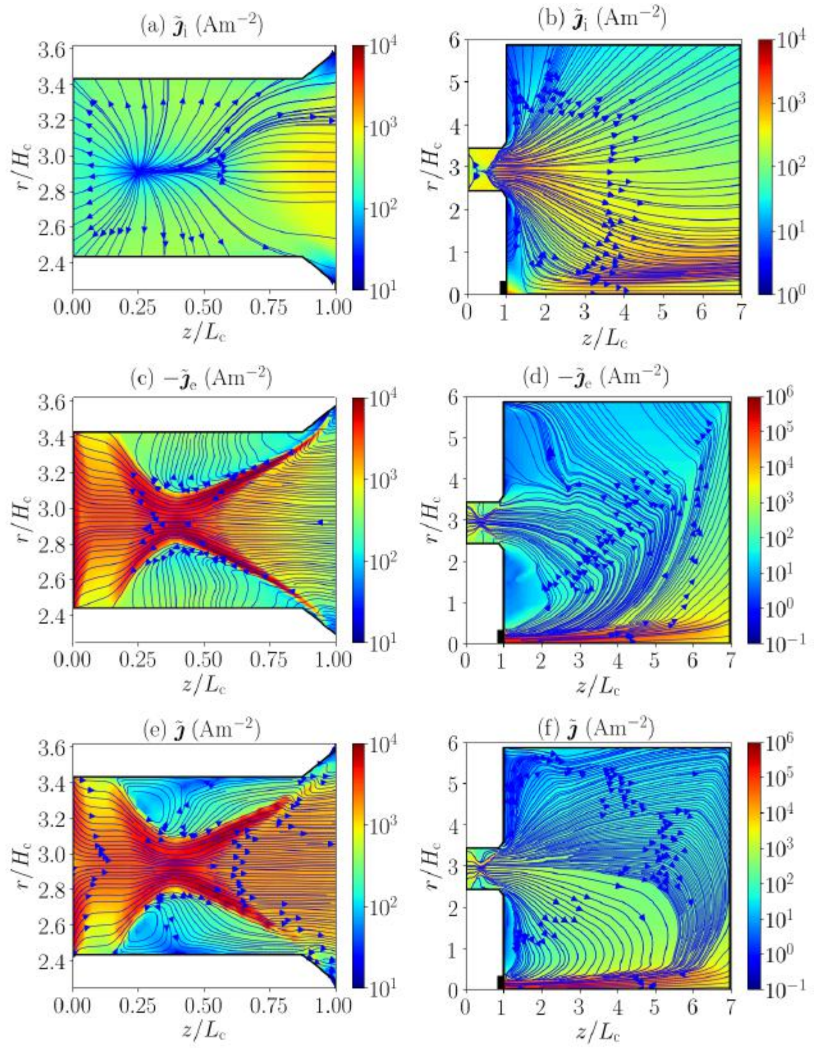

Figure 5.9: Time-averaged 2D (z,r) contour maps for case Kr2. Magnitudes description as in Fig. 5.3. The left column plots show magnitudes inside the thruster chamber, while the right column plots correspond to the whole simulation domain. The centrally-mounted cathode is indicated by the small black box close to the axis.

the larger volumetric flow rate and the lower ionization levels in the case Kr2. The latter is evidenced by Fig. 5.8(d), with the case Xe3 exhibiting larger plasma density inside the chamber. Also inside the chamber, the case Xe3 features higher n_n close to the anode [see Fig. 5.8(b)], because the Xe atoms move slower than the Kr ones. In Fig. 5.8(a), both profiles feature a downstream increase of n_n, which is due to the neutrals coming from the cathode, as observed in Fig. 5.8(c), and already reported from Fig. 5.4. In the plume region, n_e is similar for both cases, with more significant differences in the lateral parts of the plume, as seen in Fig. 5.8(f).

In Fig. 5.8(g), ϕ remains higher in the plume for the case Kr2, which can be attributed to a smaller turbulent transport coefficient in the plume, $\alpha_{\mathrm{t}2}$. The case Kr2 features a higher coupling voltage, V_{cc}, which is defined as the voltage drop necessary to bring

Case	V_s (V)	$\dot{m}_A$ (mg/s)	I_{prod} (A)	$I_{i\infty}/I_{prod}$	I_{iD}/I_{prod}	I_{iA}/I_{prod}	η_u	η_{cur}	η_{ch}
Kr1	300	20	42.1	0.60	0.36	0.04	0.91	0.88	0.91
Kr2	300	25	53.9	0.60	0.36	0.04	0.92	0.89	0.88
Kr3	400	20	47.6	0.55	0.40	0.05	0.93	0.93	0.89

Table 5.7: Different contributions to the current balance in Eq. (3.11) and related partial efficiencies, defined in Eq. (3.12).

electrons from the cathode to the HET plume, and therefore, is a loss mechanism [265]. Here, V_{cc} can be approximated as the downstream (rightmost) value of ϕ in Fig. 5.8(g), yielding $V_{cc}^{Xe3} = 9.5$ V and $V_{cc}^{Kr2} = 21.7$ V. Fig. 5.8(h) shows that the gradients of ϕ within the chamber are very small for both cases, as a result of the MS topology [153]. Also due to MS, T_e remains low close to the thruster chamber walls. Fig. 5.8(i) shows that the acceleration region expands downstream when moving from Xe to Kr, as previously observed experimentally [266].

The T_e peak in Fig. 5.8(j) is lower in the Kr discharge, as experimentally observed in Ref. [260]. In spite of having a smaller T_e peak, in the Kr2 discharge electrons are able to penetrate within the thruster chamber with larger thermal energy. This can be seen in Fig. 5.8(k), where T_e along the walls is higher for the case Kr2, decreasing slightly the effectiveness of MS. This effect is also reported in Ref. [260], and is attributed to the smaller collisional cross-section of Kr with respect to Xe for electron-neutral interactions.

Fig. 5.9 shows the 2D maps of the plasma currents and their corresponding streamlines, for the operation point Kr2. The main difference with respect to the Xe discharge (see Fig. 5.3) is found in terms of $\tilde{\boldsymbol{j}}_i$ inside the thruster chamber, in Fig. 5.9(a). In the Kr discharge, the ion streamlines exhibit a more pronounced inclination towards the chamber exit than in the Xe case, indicating that acceleration takes place deeper into the chamber. This is in agreement with Andreussi et al. [260], which experimentally observes a widening of the acceleration region when moving from Xe to Kr. In Figs. 5.9(d) and (f), the current streamlines from the cathode are smoother than in the Xe discharge: in spite of having lower anomalous transport in the plume, the Kr discharge has a larger gradient $\frac{\partial \phi}{\partial \mathbf{1}_\perp}$ in the vicinity of the cathode injection surface, as observed in Fig. 5.8(i).

5.4.3 Global balances and efficiencies

In this section, the HT20k discharges with xenon and krypton are compared in terms of their global current and power balances and partial efficiencies. Tabs. 5.7 and 5.8 contain the terms of the current and power balances and their corresponding partial efficiencies, for the simulated operation points with Kr. These data are compared with the ones in Tabs. 5.3 and 5.4

Regarding the current balance terms in Tab. 5.7, the relative current losses to walls, I_{iD}/I_{prod} and I_{iA}/I_{prod}, are smaller in average for Kr operation points than for Xe ones. This may be a consequence of the ionization region extending further downstream with Kr, as observed in Fig. 5.10. A widening of the ionization region with Kr has also been reported in previous experimental measurements of the HT5k discharge [260].

The mean value of η_{cur} for Xe and Kr at 300 V is, respectively, $\eta_{\mathrm{cur}}^{\mathrm{Xe,300V}} \approx 0.81$, while $\eta_{\mathrm{cur}}^{\mathrm{Kr,300V}} \approx 0.89$. The better performance of Kr in terms of current efficiency in the HT20k discharge, which is confirmed by experimental measurements by SITAEL, is not observed in the discharge of the H9 thruster [256]. In fact, the H9 features smaller η_{cur} with Kr than with Xe. On the other hand, Ref. [253] reports no significant differences between propellants in terms of η_{cur} in the US NASA-173Mv2 discharge. These results seem to indicate that the relation between η_{cur} and propellant type is somehow thruster-dependent. The limited knowledge about turbulent transport in HETs impedes further physical insights into this matter.

From Tabs. 5.6 and 5.7, the average ratio $I_{\mathrm{prod}}/I_{\mathrm{d}}$ at V_{d}= 300 V is calculated and found smaller for Kr (≈ 1.48) than for Xe (≈ 1.66). This is partly due to the lower ionization potential of Xe molecules [267], which results in a more efficient plasma production process and, in turn, leads to a superior propellant utilization, η_{u}, as seen in Tab. 5.3. The latter observation has been made on previous HET designs and across different operating conditions [253, 256, 268, 269]. Although higher with Xe, the obtained η_{u} with Kr is relatively high (~ 0.92). This is not the case for conventional low-power HETs [270]. This can be attributed, in first place, to the relatively low surface-to-volume ratio [271], $\frac{S}{V}$, of the HT20k ($< \frac{1}{2}(\frac{S}{V})^{\mathrm{SPT100}}$), with the current density (I_{d} vs. thruster area) being kept within the typical range [0.10, 0.15] A/cm^2 [3]. In second place, the increment in T_{e} along the thruster chamber midline, associated with MS topologies with respect to US ones [146], can improve the poorer ionization performance of Kr. Unlike η_{u}, η_{ch} is higher with Kr as propellant: in average, $\eta_{\mathrm{ch}}^{\mathrm{Xe}} \approx 0.83$, while $\eta_{\mathrm{ch}}^{\mathrm{Kr}} \approx 0.89$. Previous works have also reported the same behavior, which is attributed to the second ionization energy of Kr being higher than the Xe one [253, 256].

Tab. 5.8 contains the terms of the power balance and its related efficiencies for the Kr operation points. The mean value for P_{inel}/P is approximately 9%. This results in an effective single-ionization cost for Kr, estimated as $P_{\mathrm{inel}}/I_{\mathrm{prod}}$, equal to 18-19 eV. This value is: *i*) higher than the first ionization energy of Kr by a 30% and *ii*) lower than

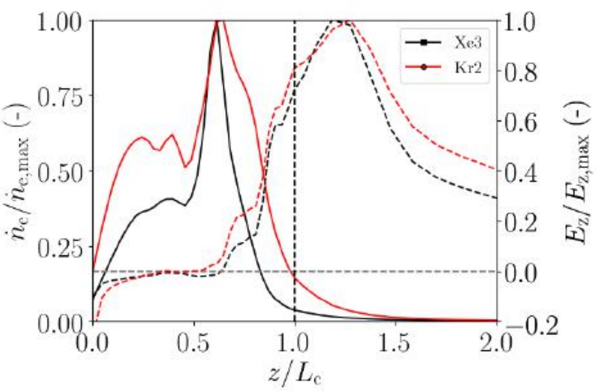

Figure 5.10: 1D axial profiles inside the thruster chamber of the non-dimensional (solid line) ionization production term, $\dot{n}_{\mathrm{e}}/\dot{n}_{\mathrm{e,max}}$ and (dashed line) axial electric field, $E_{\mathrm{z}}/E_{\mathrm{z,max}}$, for cases Xe3 (black line) and Kr2 (red line)

Case	V_s (V)	$\dot{m}_A$ (mg/s)	P (kW)	η	P_{inel}/P	P_D/P	P_A/P	P_∞/P ($=\eta_{ene}$)	η_{div}	η_{disp}
Kr1	300	20	8.53	0.50	0.09	0.05	0.04	0.82	0.76	0.80
Kr2	300	25	10.94	0.52	0.09	0.05	0.04	0.82	0.78	0.82
Kr3	400	20	11.35	0.53	0.08	0.04	0.03	0.85	0.77	0.82

Table 5.8: Different contributions to the power balance in Eq. (3.13), and related partial efficiencies, defined in Eqs. (3.14) and (3.15).

P_{inel}/I_{prod} for Xe by 4-5 eV. The latter result is in line with the superior η_{ch} of Kr with respect to Xe, which means reduced double-ion generation losses. Despite the noticeably smaller values of I_{iD}/I_{prod} and I_{iA}/I_{prod}, Kr cases exhibit relative power losses to walls similar (or higher) to the Xe ones, as observed in Tab. 5.8. This occurs because Kr induces larger T_e isolines near the thruster chamber walls [as explained for Fig. 5.8(k)] and, as a result, power deposition per unit flux is increased.

In Tab. 5.8, the fraction of power delivered to the plume, η_{ene}, is similar for both Xe and Kr operation points with the same V_d: the higher η_{cur} of Kr cases is compensated by their lower η_{vol} ($\eta_{vol} \equiv \eta_{ene}/\eta_{cur}$). The lower voltage efficiency of Kr stems mainly from the following causes: the wider overlap between the ionization and acceleration regions, as observed in Fig. 5.10; and the larger coupling voltage, V_{cc}, ($V_{cc}^{Xe3} = 9.5$ V $< V_{cc}^{Kr2} = 21.7$ V), in Fig. 5.8(g). This is in agreement with Hargus et al. [272], who observe that energy conversion in the US BHT-600 discharge is smaller with Kr than with Xe. In Refs. [253, 256], instead, no significant difference in terms of η_{vol} is found between both propellants. Regarding η_{div}, a comparison at similar discharge power levels, $\eta_{div}^{Xe3} = 0.81 > \eta_{div}^{Kr2} = 0.78$, reveals a poorer performance of Kr in terms of beam divergence, as observed in Ref. [253]. The same conclusion is reached from the comparison at similar Q_A (Xe1 vs. Kr3), or same $\dot{m}_A$ (Xe2 vs. Kr2). The lower η_{div} with Kr can be partly attributed to the downstream widening of the ionization, as observed in Fig. 5.10, and acceleration zones and the lower atomic weight of the propellant [260].

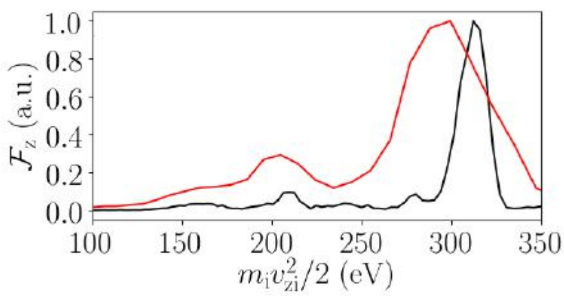

Figure 5.11: Normalized axial-flux VDF of singly-charged ions at the downstream boundary of the channel midline for the cases Xe3 (black line) and Kr2 (red line)

The amount of velocity dispersion of the plasma species, quantified as η_{disp}/η_u, is practically the same for Xe and Kr operation points ($\sim$ 0.88-0.89) . For a physical insight into this result, the time-averaged axial flux-VDF, $\mathcal{F}_z$, of singly-charged ions leaving the domain through the downstream boundary, as defined in Eq. 4.7 is analyzed. Fig. 5.11 shows $\mathcal{F}_z$ for singly-charged ions at the downstream boundary for the operation points Xe3 (black line) and Kr2 (red line). Fig. 5.11 evidences that, for a given species, velocity dispersion is larger with Kr, in line with the greater overlapping of the ionization and acceleration zones in Fig. 5.10. Then, the fact that $\eta_{\mathrm{disp}}/\eta_{\mathrm{u}}$ remains similar with both propellants may be attributed to the penalty for dispersion associated to the larger fraction of doubly-charged ions in Xe discharges.

In terms of η, the efficiency gap between Xe and Kr is minimum when two cases with the same V_{s} and $\dot{m}_{\mathrm{A}}$ are compared: η^{Xe2} - $\eta^{\mathrm{Kr2}} = 2\%$, from Tabs. 5.4 and 5.8. This observation is in line with a previous experimental work on a SPT-100 [268], which shows that performance with Kr can be close to that with Xe at similar V_{s} and $\dot{m}_{\mathrm{A}}$. Moreover, this comparison scenario is the only one in which the Kr discharge exhibits higher F than the Xe one, with $F^{\mathrm{Kr2}}/F^{\mathrm{Xe2}} \approx 1.13$, as observed in Ref. [264]. This is a consequence of the higher exhaust velocity of Kr and the similar η_{u} in both discharges. The largest thrust efficiency gap between Xe and Kr is found when two cases with the same V_{s} and Q_{A} are considered: η^{Xe3} - $\eta^{\mathrm{Kr1}} = 6\%$. This is, at the same time, the comparison scenario with the largest difference in terms of anodic mass flow rate: $\dot{m}_{\mathrm{A}}^{\mathrm{Xe3}}$ - $\dot{m}_{\mathrm{A}}^{\mathrm{Kr1}} = 10$ mg/s.

5.5 Plume effects

In this section, the simulation sensitivity to different plume-related parameters and settings is evaluated. Sec. 5.5.1 studies the effect of the neutral gas injection through the centrally-mounted cathode. In Sec. 5.5.2, CEX collisions are turned on to quantify its impact on the performance and local plasma properties of the discharge. Sec. 5.5.3 analyzes the sensitivity of the simulation results to the downstream boundary conditions. In Sec. 5.5.4, the effect of background pressure over the thruster discharge performance and physics is assessed, using the injection of neutral macroparticles from the downstream boundary.

5.5.1 Effects of cathode injection mass flow

In Fig. 5.12, time-averaged 1D profiles along the thruster channel midline of the main plasma magnitudes are shown; with black lines with square markers corresponding to the case Xe1 with neutral gas injection through the cathode, and red lines with circle markers corresponding to the same case without cathode gas injection. In Fig. 5.12(b), n_{e} along the thruster channel midline is practically not affected by the cathode neutral injection. On the other hand, Fig. 5.12(a) shows that the rise in n_{n} downstream the channel exit only takes place when cathode neutral injection is activated, because it is caused by the neutrals coming from the cathode. A similar effect is found for p_{n} in the near plume, as seen in Fig. 5.12(e). In the case without cathode neutral injection, the reduced electron Joule heating around the thruster chamber exit results in a lower T_{e} peak there, as seen in Fig. 5.12(c). Moreover, Fig. 5.12(d) shows that the case without cathode neutral injection exhibits a lower potential fall, which implies a weaker coupling

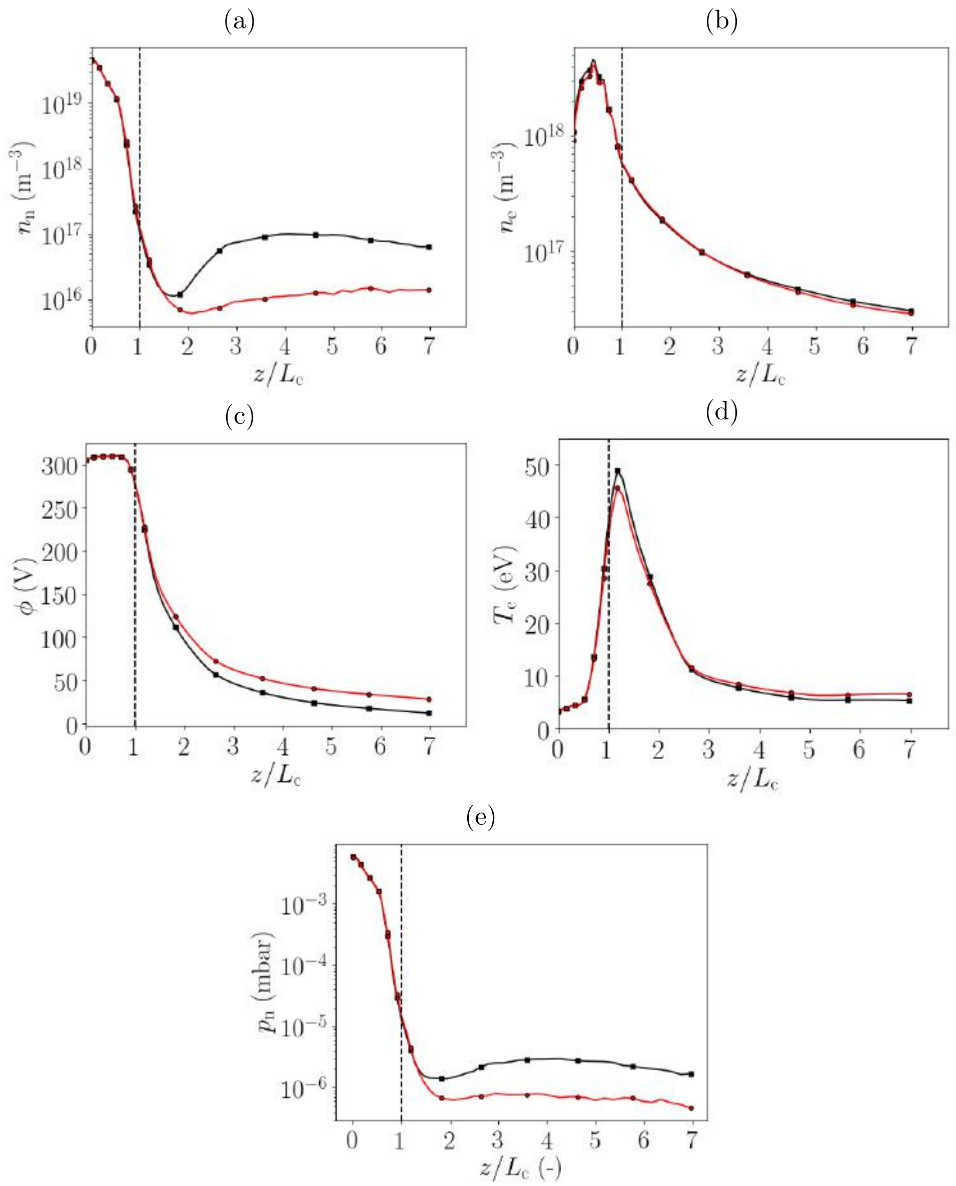

Figure 5.12: Time-averaged 1D axial profiles along the thruster chamber midline for cases with cathode injection (black line with square markers) and without cathode injection (red line with circle markers). Magnitude of (a) neutral density n_n, (b) plasma density n_e, (c) electric potential ϕ, (d) electron temperature T_e and (e) neutral pressure, p_n.

between the cathode electrons and the ion beam. This leads to a 4% decrease in F with respect to the case with neutral injection. A 2% decrease in I_d is also found.

5.5.2 Effects of charge-exchange collisions

Fig. 5.13 shows time-averaged 1D axial profiles along the thruster chamber midline of the relevant plasma magnitudes for case Xe1 without (solid line) and with (dashed line) CEX collisions. Figs. 5.13(a), (b), and (d) reveal that the presence of CEX ions

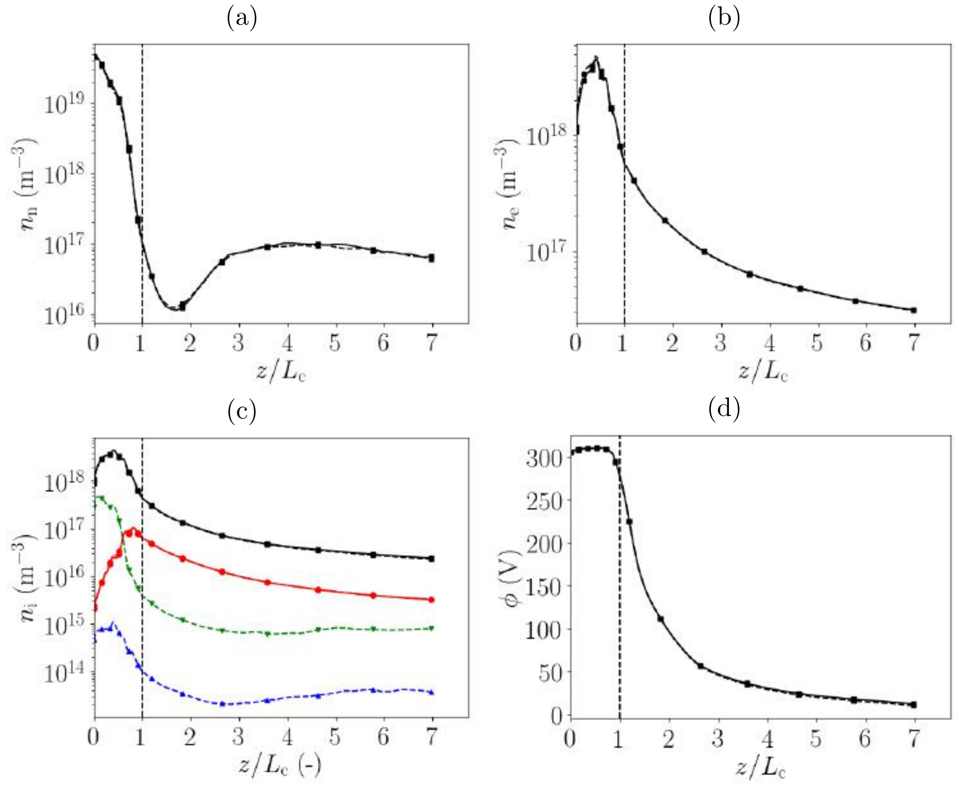

Figure 5.13: Time-averaged 1D axial profiles along the thruster channel midline for cases without CEX (solid line) and with CEX (dashed line). (a) Neutral density n_n, (b) plasma density n_e, (c) density of singly-charged ions, n_i1, (black line with square markers), doubly-charged ions, n_i2, (red line with circle markers), singly-charged CEX ions, n_i3, (green line with down triangle markers), doubly-charged CEX ions, n_i4, (blue line with up triangle markers) and (d) electric potential ϕ.

in the discharge does not produce any noticeable change in the time-averaged plasma properties along the thruster chamber midline. As a result, I_d and F only vary a 1-2% after the activation of CEX collisions in the simulations. Fig. 5.13(c) shows that, inside the thruster chamber, the densities of singly and doubly-charged CEX ions (produced from CEX collisions) can amount to a 20-30% of the corresponding singly and doubly charged ion populations produced from ionization collisions. However, the effect in the overall performance is small, because ions from ionization collisions have low velocities inside the thruster chamber, and thus, they are kinetically indistinguishable from CEX ions there.

Fig. 5.14(a) shows the time-averaged 2D contour of the density ratio of singly charged CEX ions ("i3") and singly charged ionization ions ("i1"). In the main plasma plume, from the thruster chamber, the CEX ion density is below 15-20% of the ionization ion density. The largest value of the fraction $n_\mathrm{i3}/n_\mathrm{i1}$ is found in each of the sides of the plume, where n_n is higher [see Fig. 5.14(b)]. Again in Fig. 5.14(a), near the symmetry axis, in the region corresponding to the cathode plasma plume, n_i1 and n_i3 exhibit similar values, and even $n_\mathrm{i3}/n_\mathrm{i1}$ is close to 1 near the cathode surface. The large fraction of CEX ions

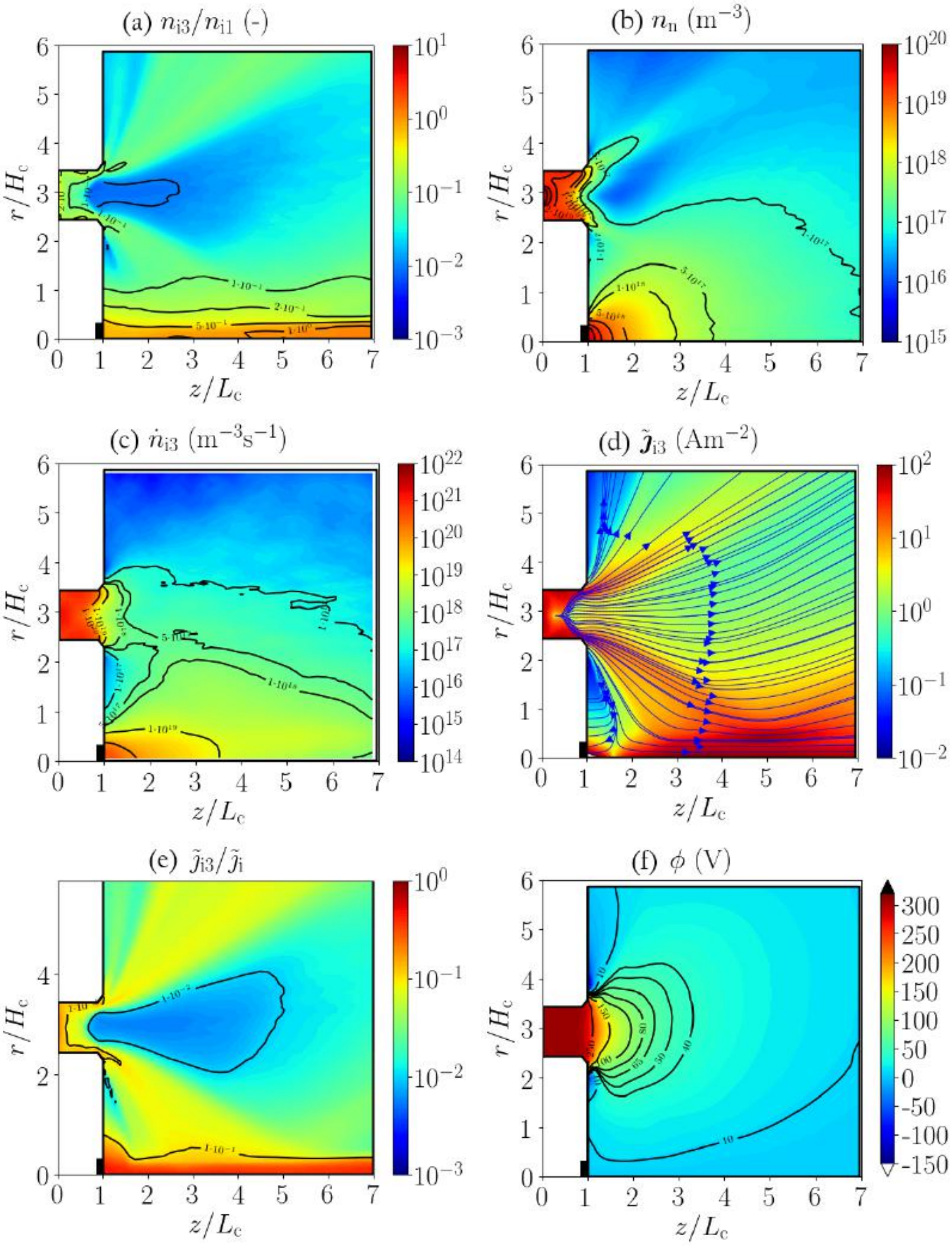

Figure 5.14: Time-averaged 2D maps of (a) ratio of n_{i3}/n_{i1}, (b) neutral density n_n, (c) production rate of singly-charge CEX ions, $\dot{n}_{i3}$, (d) in-plane current density of singly-charged CEX ions, $\tilde{\boldsymbol{\jmath}}_{i3}$, (e) ratio of $\jmath_{i3}$ and the total in plane current density, $\jmath_i$ and (f) electric potential, ϕ; for the case with CEX collisions.

near the symmetry axis stems from the combined contribution of the two main CEX ion sources, observed in Fig. 5.14(c): the thruster chamber (including its near plume) and the cathode plume region. The majority of CEX ions originated in the thruster chamber and the near plume, see Fig. 5.14(d), gain a significant amount of kinetic energy before reaching the symmetry axis, while the CEX ions generated in the cathode plume are barely accelerated. This is reason why the high CEX ion fraction near the symmetry axis can be mainly attributed to CEX collisions in the cathode plume, whose low velocity ions remain confined around the axis, due to the radial gradient of ϕ [see Fig. 5.14(f)].

In Fig. 5.14(d), the current of singly-charged CEX ions, $\tilde{\boldsymbol{j}}_{i3}$, to the inner pole and cathode surfaces can be observed. The intensity of the flux of CEX ions to these surfaces is higher near the symmetry axis. In this region, Fig. 5.14(e) shows that $\tilde{j}_{i3}$ is the dominant term in the total ion current, $\tilde{j}_{i}$. This result may be particularly important in what regards the erosion of the cathode keeper. To a lesser degree, in Fig. 5.14(e), there exists a significant fraction of $\tilde{j}_{i3}$ near the thruster chamber walls, due to the intense CEX production there, as observed in Fig. 5.14(c). However, as indicated before, CEX ions produced inside the chamber are roughly indistinguishable from ionization ions, from a kinetic perspective. The ratio $\tilde{j}_{i3}/\tilde{j}_{i}$ is small in the rest of the simulation domain, particularly in the core of the main plasma plume.

5.5.3 Far plume boundary conditions

In Fig. 5.15, the plume downstream boundary, P, is represented by the thick blue line. The GDML approach, summarized in Sec. 5.2, is applied at the P boundary . The three different simulation cases for the sensitivity analysis are defined in Tab. 5.9. The case Xe1 is contained in the first row of Tab. 5.9. For this case, the electric potential at infinity, $\phi_\infty = \phi_{\infty,0}$ reaches a value of -2.8 V, such that the collected electric current at infinity, I_∞, is equal to 0 at any time instant. The second and third rows of Tab. 5.9 correspond to two simulation cases with, respectively, $\phi_\infty = 1.2\phi_{\infty,0}$ and $\phi_\infty = 0.8\phi_{\infty,0}$. As ϕ_∞ is set different to $\phi_{\infty,0}$, a certain electric current I_∞ is collected at the P boundary, as schematically represented in Fig. 5.15.

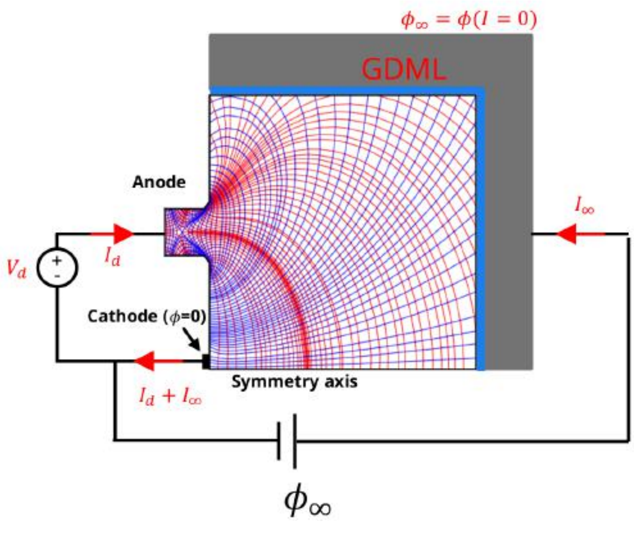

Figure 5.15: Sketch representing the infinity-to-cathode bias ϕ_∞ obtained through the GDML condition.

Case	ϕ_∞ (V)	I_∞ (A)	I_∞/I_d (%)	$I_\mathrm{d}(A)$
$\phi_\infty = \phi_{\infty,0}$	-2.8	0.0	0.0	21.4
$\phi_\infty = 1.2\phi_{\infty,0}$	-3.4	-1.16	-5.5	21.3
$\phi_\infty = 0.8\phi_{\infty,0}$	-2.3	0.64	2.8	21.3

Table 5.9: Results for the simulation cases with different infinity-to-cathode potential bias, ϕ_∞. Values of the electric current collected at P boundary, I_∞; fraction of electric current collected vs. discharge current, I_d; and I_d

It must be noted that, with this simulation setup, I_∞ does not necessarily correspond to the so-called stray currents [158, 273], which are present in the discharge of HETs in direct-drive configuration. The main goal with this study is not the characterization of stray currents, but the assessment of the performance of the GDML approach for the downstream boundary conditions. This implies evaluating the sensitivity of the simulation results to variations in the parameter ϕ_∞.

In Tab. 5.9, the time-averaged I_d does not significantly change (ΔI_d ∼1%) when $\Delta\phi_\infty = \pm\, 0.2\ \phi_{\infty,0}$. For these cases, the current flowing between the P boundary and the cathode is I_∞ ∼5-6%I_d. Positive and negative contributions to I_∞ correspond, respectively, to electron and ion fluxes. Since I_d is barely sensitive to variations in ϕ_∞, it can be stated that the anode-to-cathode plasma bridge is not significantly affected by the conditions at the P boundary . Notice that, while $\Delta I_\infty \approx 1$ A, the change in I_d is not larger than 0.1 A. This occurs because the energy spent in bringing electrons from the cathode to the P boundary is relative small (electric resistance is low because electrons do not have to cross $\boldsymbol{B}$ lines), compared to the cost of moving electrons from the cathode to the anode. Regarding the time-averaged 2D plasma maps of the discharge, they do not exhibit noticeable changes from case to case.

Fig. 5.16 shows the main plasma magnitudes along the P boundary for the simulation cases contained in Tab. 5.9. The coordinate s runs along the entire extension of the P boundary, from the leftmost corner of the lateral P boundary to the bottom corner of the downstream P boundary, and then to the other side of the symmetry axis at $s = 0$ (not simulated). The separation between the lateral and the vertical P boundary is indicated by black dashed lines in Fig. 5.16. The variations in the profile of ϕ, observed in Fig. 5.16(a), are orders of magnitudes smaller than the average downstream ion energy. Therefore, the ion acceleration process is not sensitive to variations in ϕ_∞. In Fig. 5.16(b), the T_e profile also presents negligible changes as ϕ_∞ is modified. The comparison between Fig. 5.16(c) and Fig. 5.16(d) reveals that, while j_ni is barely affected by ϕ_∞, j_ne is controlled by the P-to-infinity electric potential drop. In particular, the smaller the value of ϕ_∞, the lower the amount of electrons collected at infinity per unit time (i.e., the lower j_ne). The surface integral over P of the profiles in Fig. 5.16(e) yields I_∞ in Tab. 5.9.

The profile of j_ni in the three simulation cases, in Fig. 5.16(c), exhibits a sudden depression at the symmetry axis, which is also observed in the near plume of the discharge of other HETs [258,274]. This double peak structure in the j_ni profile is the consequence of the HET being a double ion source, from a purely radial perspective, around the symmetry

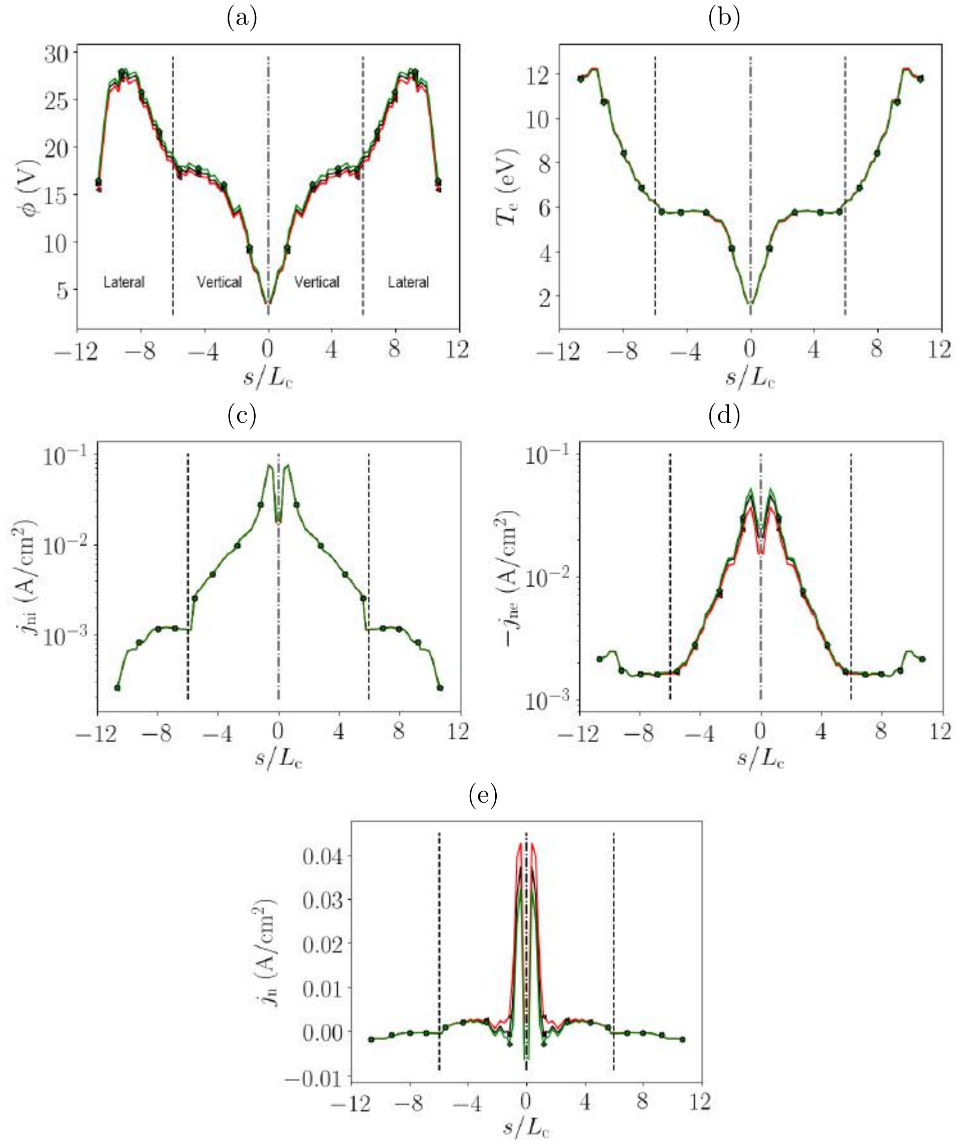

Figure 5.16: Time-averaged 1D axial profiles along P for $\phi_\infty = \phi_{\infty,0}$ (black line with square markers), $\phi_\infty = 1.2\phi_{\infty,0}$ (red line with triangle markers) and $\phi_\infty = 0.8\phi_{\infty,0}$ (green line with diamond markers). The coordinate s runs from the leftmost corner of P to the bottom corner of P. The vertical dashed line indicates the separation between lateral and vertical downstream plume boundaries. Profiles of (a) electric potential, ϕ, (b) electron temperature, T_e (c) normal ion current, j_{ni}, (d) normal electron current, j_{ne}, and (e) normal electric current, j_n.

axis. Also in Fig. 5.16(c), there is a jump in j_{ni} at the separation line of the lateral and vertical boundaries, because $\tilde{\boldsymbol{j}}_i$ is mostly axial there.

5.5.4 Background pressure effects

BP within vacuum chambers is well known for affecting the on-ground performance characterization of HET prototypes, increasing both I_d and F, with respect to the in-space HET operation [275–277]. This has been typically associated to background neutrals ingestion by the thruster chamber, which would act as an additional effective input mass flow rate [278, 279]. However, this effect cannot completely explain the change in performance [280]. Therefore, other mechanisms have been recently investigated, such as: changes in the coupling voltage [281–283], or in the acceleration region of the plasma discharge [284]. The complexity of the problem requires numerical simulations to understand the physics of BP and quantify its impact on performance.

Case	V_s (V)	$\dot{m}_A$ (mg/s)	$(\alpha_{t1}, \alpha_{t2})$ (%)	I_d (A)	F (mN)	f_d (kHz)	$\Delta I_d/I_d$ (%)	$I_{i\infty}$ (A)	P (kW)	η (-)	η_{ene} (-)	η_{div} (-)	η_{disp} (-)
Xe1 Low BP	300	20	(1.3, 12.0)	21.4	381	13.6	± 2.9	17.3	6.38	0.52	0.80	0.78	0.83
Xe1 High BP	300	20	(1.2, 12.0)	22.2	403	15.1	± 2.1	18.9	6.67	0.57	0.77	0.83	0.89
Xe5 Low BP	500	30	(1.1, 7.0)	31.8	768	14.4	± 2.1	27.7	15.91	0.57	0.86	0.78	0.86
Xe5 High BP	500	30	(1.1, 7.0)	32.7	804	15.5	± 2.8	30.3	16.35	0.61	0.82	0.82	0.91

Table 5.10: Cases with low and high background pressure. Simulated results for time-averaged I_d and F (4th and 5th columns). Frequency and relative half-amplitude of oscillation of I_d are listed in 6th and 7th columns. The values of the total power, P, and the thrust efficiency, η, are in the 8th and 9th columns.

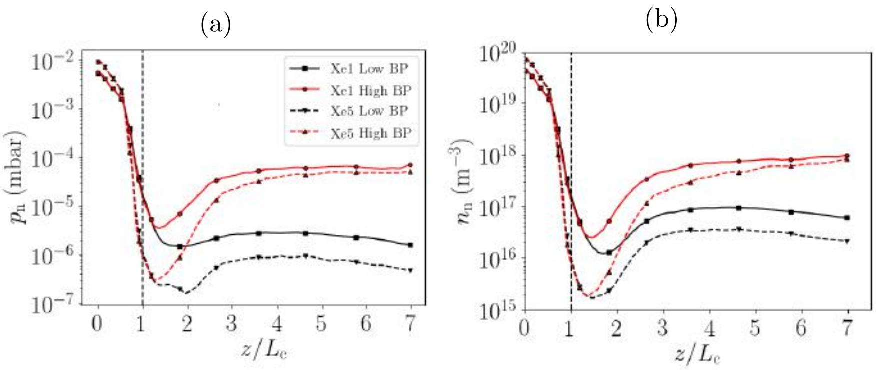

Figure 5.17: Time-averaged 1D axial profiles along the thruster chamber midline of the operation points Xe1 (solid line) and Xe5 (dashed line) with low BP (black lines) and high BP (red lines). Magnitudes of (a) neutral pressure p_n and (b) neutral density n_n.

In the present numerical study, two different operation points are considered with Xe as propellant, at low and high V_s. These cases are Xe1 Low BP and Xe5 Low BP. The other cases, in rows 2 and 4 of Tab. 5.10, are denoted as "High BP" cases. For each of the High BP cases, a mass flow of neutrals, $\dot{m}_{back}$, is injected through the downstream plume boundary with a temperature, T_{back}, equal to the standard ambient temperature (25 °C). This input mass flow is augmented until an increase in I_d or F of around a 5% (the repeatability of the experimental measurements) is observed with respect to the

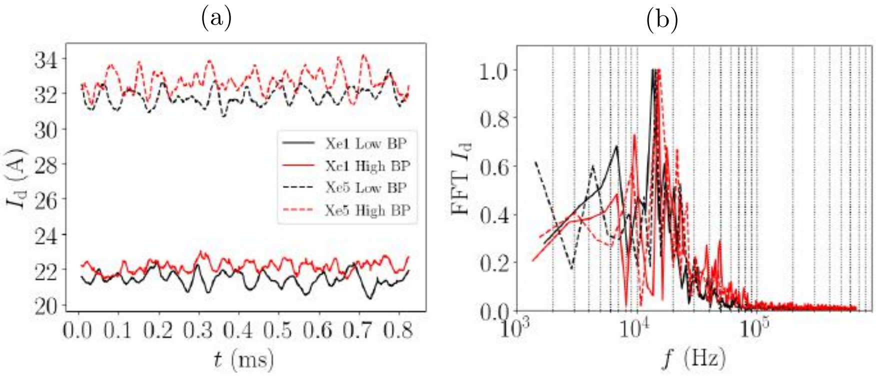

Figure 5.18: (a) Time evolution of I_{d} and (b) I_{d} normalized amplitude for operation points Xe1 (solid line) and Xe5 (dashed line) with low BP (black line) and high BP (red line).

corresponding Low BP case. This approach permits a qualitative analysis of some of the physical mechanisms by which BP impacts performance measurements in on-ground HET testing.

Fig. 5.17 shows the time-averaged 1D axial profiles along the thruster chamber midline of the neutral pressure, p_{n}, and n_{n}. The resultant profiles indicate that the influence of BP is small within the thruster chamber, where p_{n} and n_{n} are relatively high. However, downstream the chamber exit, where the neutral gas from the anode has been ionized and is accelerating and expanding, background neutrals are non-negligible and can modify the local plasma properties and the thruster performance.

Fig. 5.18 features the time evolution and FFT of I_{d} for the cases without (black line) and with injection (red line) of background neutrals. In Fig. 5.18(a), the increase in I_{d} due to BP is observed. Moreover, the value of f_{d} also grows with BP, as seen in Fig. 5.18(b). The latter result has been reported previously from experimental studies of different thrusters operated at 300 V [277, 285]. The proposed explanation for this trend is that background neutrals would accelerate the replenishment of the ionization region, but this requires that background neutral density is important within the chamber, which is not observed in Fig. 5.17. In Fig. 5.18(a), the amplitude of the I_{d} oscillations remain constant from low to high BP, which does not agree with previous experimental works [277, 285], where they observe that ΔI_{d} grows with BP. This disagreement may be explained by the fact that BP can affect the anomalous transport [285], and this is not considered in the present simulations.

Fig. 5.19 shows the time-averaged 1D axial profiles along the thruster chamber midline of n_{e}, ϕ and T_{e}. In Fig. 5.19(a), n_{e} is higher at $z > 2L_{\mathrm{c}}$ for the high BP cases. And there is also a slight increment of n_{e} within the chamber, indicating extra ionization at higher BP, which may be linked to the increase in T_{e} in Fig. 5.19(c). In Figs. 5.19(b) and (c), the profiles of ϕ and T_{e} in the acceleration region are compressed towards the interior of thruster chamber when BP is increased. This can be associated to a change in the electron mobility caused by the increase of the electron-neutral collision frequency, which, in Ref. [285], is mostly attributed to changes in the anomalous collision frequency, while here is only due to classical collision mechanisms. Figs. 5.19(b) shows that the final potential of the plume, taken as an estimation of V_{cc}, is almost the same with

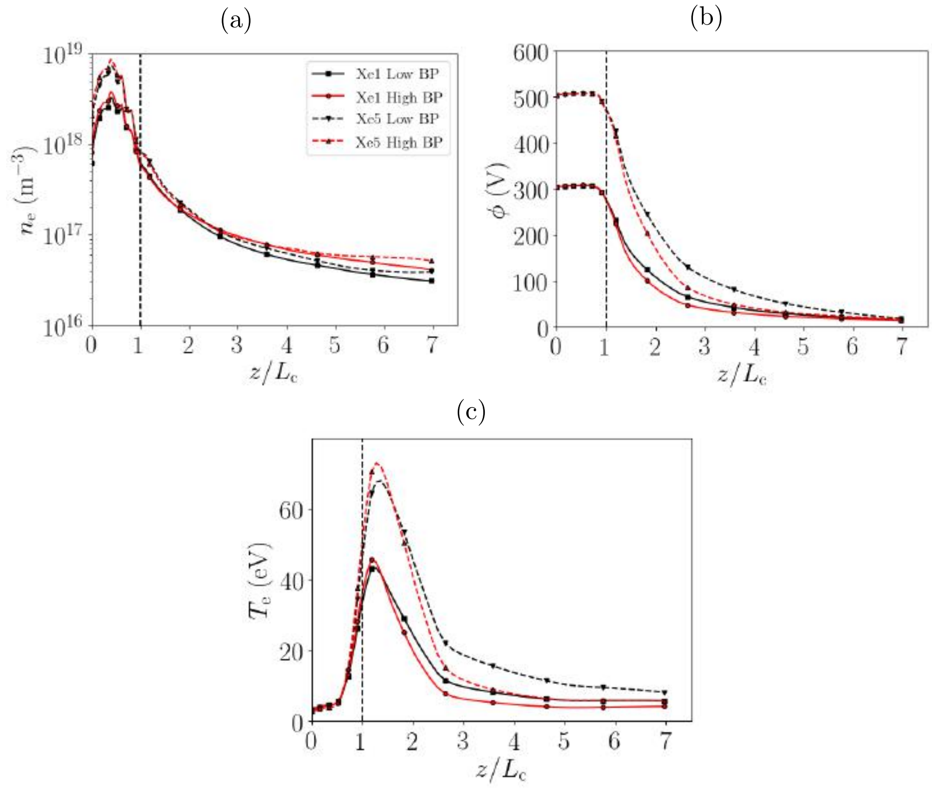

Figure 5.19: Time-averaged 1D axial profiles along the thruster chamber midline of the operation points Xe1 (solid line) and Xe5 (dashed line) with low BP (black line) and high BP (red line). Magnitudes of (a) plasma density n_e, (b) electric potential ϕ, and (c) electron temperature T_e.

low and high BP. Yet, a change in V_{cc} due to BP has been observed experimentally in previous works [283, 286]. Although these changes are typically of the order of units of volts and may not even impact significantly the downstream kinetic energy of ions [287], the numerical modelling of this aspect would require to account for the dependence of anomalous transport on BP [265, 282, 283].

The erosion of the inner pole region is a topic of concern in MS HETs and has been subject of recent numerical 2D simulations [236]. Although the erosion rate of the inner pole walls has been reported to be orders of magnitude smaller than the usual one of the channel walls of a conventional HET, it is dominant in a MS HET [288]. Fig. 5.20 shows the profiles along the inner pole of the plasma variables relevant for erosion, for the case Xe1 at low (in black) and high (in red) BP, without (solid line) and with (dashed line) CEX collisions. The variable s runs, in this case, from the thruster symmetry axis ($r = 0$) upwards, along the whole inner pole surface. Two different aspects of Fig. 5.20 are analysed: on the one hand, the potential impact on erosion of the profiles of the plotted magnitudes; on the other hand, the influence of BP and CEX ions on the profiles.

Regarding the first aspect, in Fig. 5.20(a), at $s/H_c \approx 2.0$, there is a large negative value of ϕ_Q, caused by the small local n_e. As a result, ions can be strongly accelerated from the plume to impact the pole and cause erosion there. This potentially negative effect is aggravated by the large local $\Delta\phi_{\mathrm{sh}}$ (around 40 V in Fig. 5.20(b)) due to the high electron temperature in Fig. 5.20(c). All this results in a maximum impact kinetic energy of the ions, $\mathcal{E}_{\mathrm{i,wall}}$, of around 200 V at $s/H_{\mathrm{c}} \approx 2.0$. Yet, there are few ions that reach that

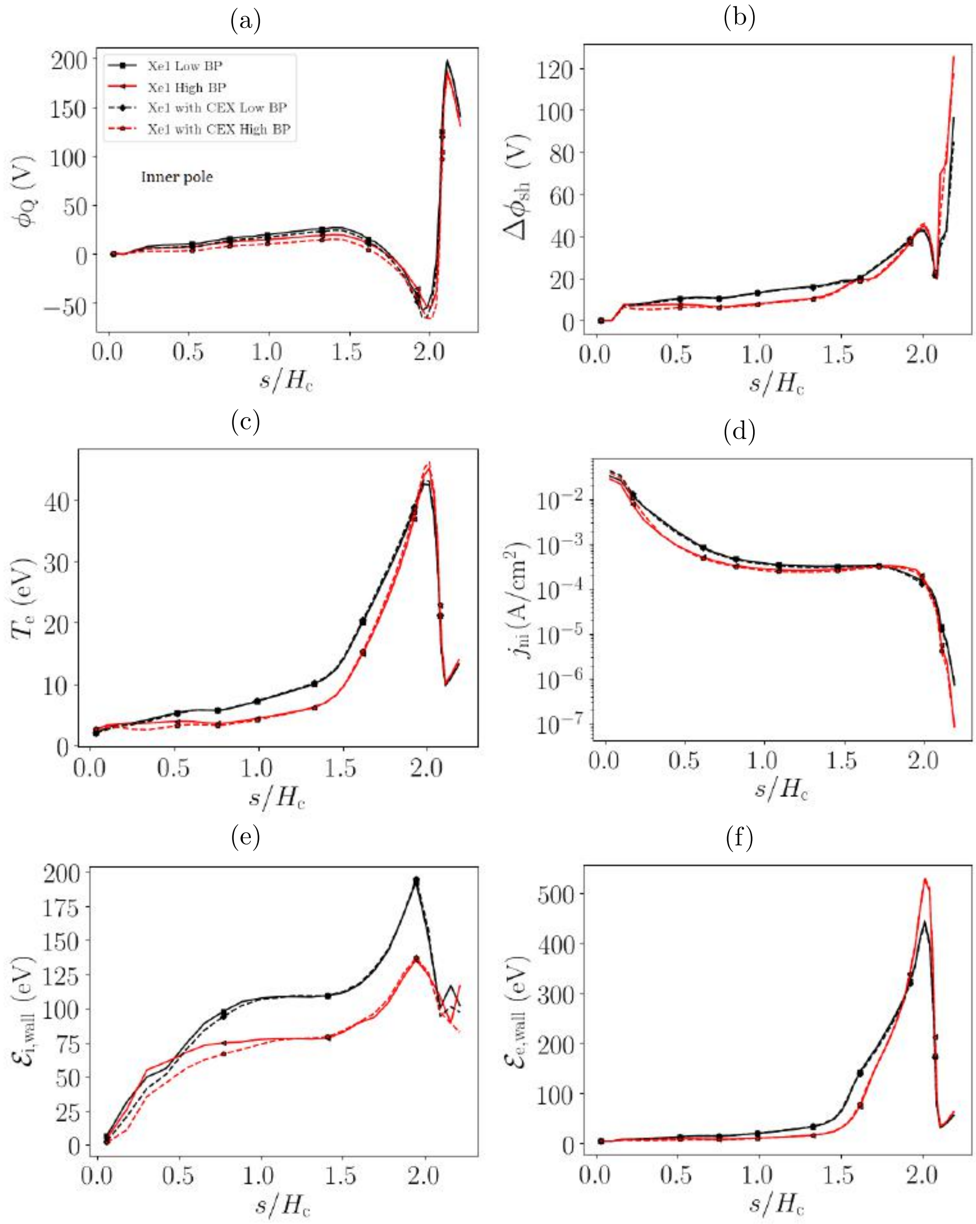

Figure 5.20: Time-averaged 1D profiles along the thruster inner pole for the case Xe1 at low (in black) and high (in red) BP, without (solid line) and with (dashed line) CEX collisions. Coordinate s runs along the inner pole of the thruster, starting from the cathode position ($r = 0$). Profiles of (a) electric potential at the sheath edge, ϕ_{Q}; (b) potential fall across the sheath edge, $\Delta\phi_{\mathrm{sh}}$; (c) electron temperature at the sheath edge, T_{e}; (d) ion current normal to the walls, j_{ni} ; (e) ion wall-impact energy, $\mathcal{E}_{\mathrm{i,wall}}$; and (f) electron wall-impact energy, $\mathcal{E}_{\mathrm{e,wall}}$.

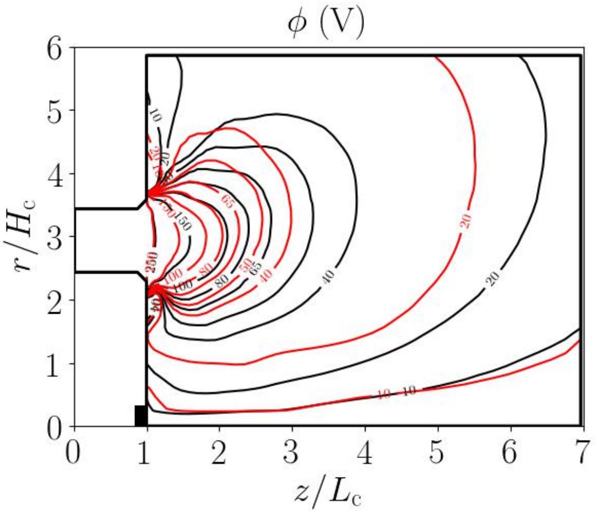

Figure 5.21: Time-averaged 2D contour plot of ϕ for the cases Xe1 with low BP (in black) and high BP (in red) without CEX collisions.

zone, not even CEX, as evidenced by Fig. 5.20(d), where j_{ni} is two orders of magnitudes smaller than at the cathode, where the current is maximum but $\mathcal{E}_{i,wall}$ has its lowest value (around 10 eV).

The influence of CEX collisions (at low and high BP) is, in general, negligible. Yet, Fig. 5.20(d) shows that, near the cathode (around $s/H_c = 0$), j_{ni} grows when CEX collisions are included. This increase in j_{ni} may be due to the CEX ions coming from the sides of the plume, as observed in Fig. 5.14(d). The effect of BP over the plasma profiles along the inner pole is more significant. As seen in Fig. 5.20(e), $\mathcal{E}_{i,wall}$ noticeably decreases at high BP for $s/H_c > 0.5$. This behavior can be partially attributed to the lower T_e at high BP observed in Fig. 5.20(c). Another reason for the decrease of $\mathcal{E}_{i,wall}$ at high BP can be found in Fig. 5.21. There, the high BP isolines (in red) feature lower values of ϕ than the ones for low BP (in black) at the same axial and radial position in the near plume. Therefore, the ions generated in the plume, which can impact with the wall, have lower potential energy in the high BP case. In Fig. 5.20(d), j_{ni} is also found to decrease with higher BP, mainly for $s/H_c < 1.5$. This can be due to the compression of the acceleration region, observed in Fig. 5.19(b) and Fig. 5.21, which decreases the plume divergence (compare η_{div} from the first and second rows of Tab. 5.10) and therefore reduces the ion fluxes to the inner pole. Fig. 5.20(f) shows that $\mathcal{E}_{e,wall}$ is only slightly affected by BP and CEX collisions. For all the operation points, $\mathcal{E}_{e,wall}$ features relative high values from $s/H_c = 1.5$ to $s/H_c = 2.0$. The reason for this is the high T_e and δ_s (see Eq. A.5), which is around 0.7-0.8, on that segment of the wall.

5.6 Conclusions

HYPHEN numerical simulations of SITAEL's HT20k prototype with MS topology and a central cathode for several operation points with xenon and krypton as propellant have been presented in this chapter.

The electron turbulent transport model has been fitted to satisfactorily match the experimental data, (I_d, F), for each of the operation points. The breathing mode frequency is approximately reproduced by the simulations, while the output oscillation amplitude is far from the experimental one at high voltages. HT5k and HT20k discharges with Xe have similar efficiencies and global balances, due to their similar magnetic topologies. The main difference between both thrusters is that the HT5k exhibits a larger current fraction to the anode, because ionization takes place deeper into the chamber. Both xenon and krypton discharges exhibit similar behaviors with V_s and $\dot{m}_\mathrm{A}$. For a higher V_s, the propellant utilization efficiency, the current efficiency and the energy efficiency are found to increase. For both propellants and all the operation points, the magnetic shielding remains effective, achieving low ion impact energies and reduced energy losses to the thruster walls.

Regarding the Xe-Kr comparison, Kr features a thrust efficiency comparable to the one obtained with Xe. This is partially due to the improved utilization efficiency of Kr in high power HETs. In any case, the propellant utilization is still worse with Kr than with Xe. There exits a widening towards the plume of the ionization and acceleration in the Kr cases, as compared to Xe ones. Thus, Kr operation points exhibit higher divergence and species-wise velocity dispersion at the downstream boundary. While the Kr discharges have higher current and charge efficiencies, they have worse voltage utilization, being the latter associated with a worse cathode-plume coupling. Most of the numerical results are in good agreement with previous experimental observations on other conventional or magnetically shieleded HETs, but some of them seem to be thruster dependent.

Sensitivity analyses of relevant plasma-wall related parameters have shown their limited influence on the plasma discharge and thruster performance, due to the magnetic shielding topology. The injection of neutrals through the cathode has been shown to improve the cathode-beam coupling in the near plume and to yield a higher thrust. Although CEX ions do not affect significantly the performance of the HT20k, they can be dominant in localized regions of the discharge. Inside the thruster chamber, their density is comparable to that of ions from ionization. Nevertheless, both ion populations are rather indistinguishable from a kinetic point of view in that region. The ion current density in the symmetry axis and, particularly, towards the central cathode is dominated by CEX ions, which can increase the erosion of this device. In the rest of the domain, the CEX ion current is, at least, one order of magnitude smaller than the total ion current.

A sensitivity analysis of the GDML model for the downstream plume boundary condition has been carried out. The infinity-to-cathode bias, ϕ_∞, has been varied around $\phi_{\infty,0}$, which is the value at which no current is collected at infinity: $I_\infty = 0$. The main result of the analysis is that I_d is barely affected by variations of ϕ_∞. The effect of background pressure has been studied by injecting an increasing mass flow of neutrals through the downstream plume boundaries until a noticeable effect on performances is observed in the simulations. Although the relative density of background neutrals is small within the thruster chamber, they can dominate in the acceleration region, modifying the local plasma properties. Therefore, the acceleration region is found to be compressed when the background pressure increases. This compression of the acceleration region is only due to changes in the classical electron-neutral collisionality, because the present simulations do not account for changes in anomalous transport with background pressure. The need for a model that relates anomalous transport and background pressure has been identified, but such model does not exist yet

The study of the plasma properties at the inner pole surface has revealed a high ion impact energy along this wall (mainly close to the thruster chamber exit), due to the combined effect of the local plasma potential and the electron temperature. Nevertheless, the total ion current reaching this surface is very small, and it is not significantly affected by the presence of CEX ions (with the exception of the region around the cathode). An increase in the background pressure is found to reduce the ion impact energy on the inner pole walls. Moreover, the ion current to this wall is also reduced due to compression of the acceleration region, which decreases the beam divergence.

Chapter 6

WET-HET thruster modeling

This Chapter describes the work developed during the three month-long research stay of the PhD candidate at the Imperial Plasma Propulsion Laboratory (IPPL), Imperial College London (ICL), under the supervision of Prof. Aaron Knoll, and in collaboration with Jesús Manuel Muñoz Tejeda (PhD student). The contents of this Chapter are part of a journal article under preparation, which is devoted to the numerical analysis of the water-fuelled WET-HET discharge

This Chapter is devoted to the numerical study of the discharge of the IPPL WET-HET thruster. This Hall effect thruster is designed to operate with (i) water vapour through the anode and any other propellant through the cathode, or (ii) water electrolysis products, injecting molecular oxygen through the anode and hydrogen through the cathode. The axial-radial version of the IPPL in-house full-PIC code PlasmaSim is upgraded and used for the numerical analysis of the WET-HET operation.

The present Chapter is organized as follows. Section 6.1 briefly describes the code PlasmaSim from IPPL. Section 6.2 explains the main changes implemented in PlasmaSim for a more faithful modelling of the WET-HET discharge. Section 6.3 contains some simulation results of the WET-HET discharge and their discussion. Finally, in Section 6.4, the main conclusions of the numerical study are presented.

6.1 PlasmaSim code

PlasmaSim is a quasi-2D electrostatic full-PIC code for the numerical simulation of HETs [67]. The main simulation loop of PlasmaSim is represented in Fig. 6.1. During the execution of the code, the loop is repeated over and over until the actual simulation time reaches the maximum simulation time imposed by the user.

Starting the loop from its top part, the mesh size and time step are automatically updated by PlasmaSim, considering the current plasma properties within the simulation domain, which have been weighted to the computational cells. Then, Poisson's equation is solved and the electric field is computed, which is subsequently, interpolated from the cells centers to the macroparticles position (together with the magnetic field). After

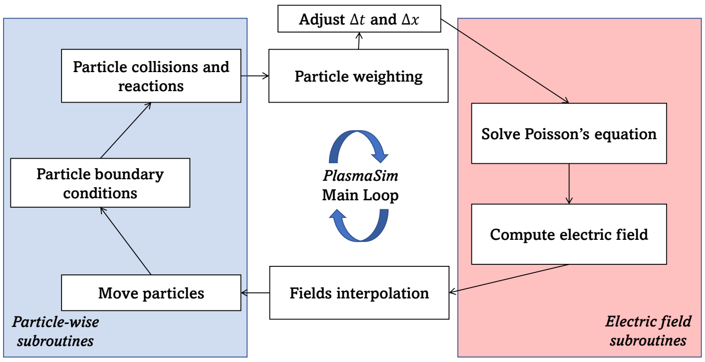

Figure 6.1: Main loop of a PlasmaSim simulation step

this, on the left-hand side of the loop, the particle-wise subroutines start. In first place, particles are moved under the influence of the electric and magnetic fields. Then, if the surface crossing of a macroparticle is detected, the particle-wall interaction subroutine operates on the macroparticle, applying to it the corresponding boundary condition. And finally, collision and ionization events are evaluated and the corresponding particles are created, removed or modified. The simulation cycle starts again with the weighting of the macroparticles properties, for a new update of Δt and Δx.

The most relevant PlasmaSim subroutines and algorithms within the main simulation loop are briefly described here. Detailed information about them can be found in Ref. [67]. PlasmaSim tracks the particles in a 3D volume, with the shape of a rectangular parallepiped. However, only in the axial and radial directions Poisson's equation is solved and so only in these two directions the electric field is defined. PlasmaSim uses adaptive time and spatial steps to ensure the fulfillment of the numerical constraints associated to the time and spatial resolution in plasma simulations and to ensure convergence [67]. The particle pusher subroutine is in charge of the motion of neutrals and charged macroparticles. Neutrals follow a ballistic trajectory until a collision with another macroparticle or an interaction with any surface takes place. The kinematic state of charged particles is updated under the effect of Lorentz's force. $\boldsymbol{E}$ is consistently computed every time step, while $\boldsymbol{B}$ is kept constant along the simulation time, since the self-induced magnetic field is negligible. Boris pusher is the algorithm used to integrate the trajectory of macroparticles [289]. This method has been successfully used in other works in the literature [67].

Fig. 6.2 shows an axial-radial section of the PlasmaSim simuation domain. This includes the anode and cathode boundaries, the outer and inner walls of the thruster chamber and the lateral and vertical free loss surfaces, past the channel exit plane (indicated with a black dashed line). The information concerning the particle-boundary interaction in PlasmaSim is gathered in Tab. 6.1. At the anode, electrons are collected, while ions are recombined into neutrals and neutrals are simply reflected. At the cathode boundary, all types of macroparticles are removed as in the rest of free loss surfaces.

At the same time, through the cathode, an uniformly distributed electron current equal to the net collected current at the anode is injected (recirculation condition). There, electrons are injected following a semi-Maxwellian distribution with the user-defined temperature. At the lateral dielectric walls of the thruster chamber, macroparticles undergo

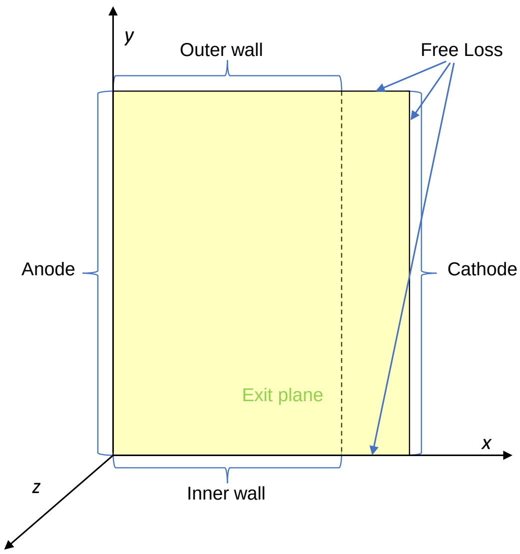

Figure 6.2: Schematic representation of the different types of boundaries in a PlasmaSim simulation.

the same type of interaction as on the anode wall. Finally, the boundaries perpendicular to the azimuthal direction feature periodic boundary conditions. This implies that any macroparticle crossing one of these two boundaries is reinjected through the other conserving its velocity vector.

Location	**Electrons**	**Ions**	**Neutrals**
Anode	Removed	Recombined	Reflected
Cathode/ Free loss	Recirculation/ removed	Removed	Removed
Lateral free loss	Removed	Removed	Removed
Dielectric Walls	Removed	Recombined	Reflected
Azimuthal direction	Periodic	Periodic	Periodic

Table 6.1: PlasmaSim boundary conditions

PlasmaSim includes electron-neutral and electron-ion ionization collisions as well as elastic collisions of the type electron-neutral, ion-neutral and neutral-neutral; all this for Xe as propellant. All the collision types in PlasmaSim are modelled by using the Monte Carlo Collisions (MCC) approach [290]. For an ionization collision type, the ion macroparticle conserves the velocity vector of the ionized neutral macroparticle, whose size is reduced an amount equal to the size of the input electron. The output electron macroparticle, instead, is created with a velocity that follows a 3D Maxwellian distribution at a fixed temperature set by the user. This is done to stabilize the plasma discharge.

Poisson solver and electric field subroutine

The most distinctive feature of PlasmaSim is its novel approach for the solution of the electric potential. The quasi-2D method for the solution of the electric potential, ϕ, permits reducing the dimensionality of Poisson's equation, by partially decoupling the different dimensions. The main computational advantages of this approach over standard full PIC codes are: (a) the savings in terms of computational time in the solution of Poisson's equation due to the dimensionality reduction and (b) the relaxation of the constraint in the number of particles per cell, since the dimensionality reduction implies the integration of the charge density, ρ, along the different sections perpendicular to each of the dimensions. This last aspect will be clarified later.

The quasi-2D approach of PlasmaSim assumes a certain form of the electric potential, of the following type:

$$\phi = \phi_1(x) + \phi_2(y) \tag{6.1}$$

where ϕ_1 is only a function of x and ϕ_2 is only a function of y. This is a strong assumption whose accuracy may be limited in certain scenarios. Nevertheless, the formulation in Eq. 6.1 is the simplest form of the quasi-2D approach: the simulation domain can be divided axially (and/or radially) in subdomains, Ω_i, for which there exist different $\phi_2^i(y)$ (and/or $\phi_1^i(x)$). This is at the cost of losing a fraction of the computational speedup, but it has been shown that the quasi-2D method approaches the exact 2D solution as the number of subdomains grows [118]. The single-subdomain formulation from Eq. 6.1 is the one considered here.

The application of the Laplacian operator to Eq. 6.1 yields the following expression:

$$\nabla\phi(x,y) = \frac{\partial^2\phi_1(x)}{\partial x^2} + \frac{\partial^2\phi_2(y)}{\partial y^2} \tag{6.2}$$

Next, the quasi-2D approach states that the second order derivative of both ϕ_1 and ϕ_2 has the following form:

$$\frac{\partial^2\phi_1(x)}{\partial x^2} = -c^{\mathrm{x}}\frac{\rho^{\mathrm{x}}(x)}{\varepsilon_0}; \qquad \frac{\partial^2\phi_2(y)}{\partial y^2} = -c^{\mathrm{y}}\frac{\rho^{\mathrm{y}}(y)}{\varepsilon_0}; \tag{6.3}$$

where

$$\rho^{\mathrm{x}}(x) = \frac{1}{L_{\mathrm{y}}}\int_0^{L_{\mathrm{y}}} \rho(x,y)dy; \quad \rho^{\mathrm{y}}(y) = \frac{1}{L_{\mathrm{x}}}\int_0^{L_{\mathrm{x}}} \rho(x,y)dx; \tag{6.4}$$

and with c_1 and c_2 being non-dimensional weighting parameters whose sum must be equal to 1: in PlasmaSim, $c_1 = \frac{\Delta x}{\Delta x+\Delta y}$ and $c_2 = \frac{\Delta y}{\Delta x+\Delta y}$. The sensitivity of the simulation results to these weighting coefficients is studied in Ref. [116]. The boundary conditions for Eq. 6.3 are: (a) Dirichlet for both $x = 0$ and $x = L_x$, and (b) symmetric boundary conditions for $y = 0$ and $y = L_y$. A direct solver for tridiagonal matrices from the LAPACK library [291] is used for the coefficient matrix inversion.

The calculation of the electric field, $E(x, y)$, is carried out every time step. The gradient of ϕ, taken from Eq. 6.1, is computed numerically with a centered-difference discretization scheme.

6.2 PlasmaSim upgrade

This section describes the main upgrades made to PlasmaSim in the framework of the research stay at ICL. These include: the parallelization of the code, the improvement of the boundary conditions, the implementation of a new version of the quasi-2D formulation and the addition of water as a new propellant to the code. The purpose of these developments is to enable the modelling of the WET-HET discharge with water vapour and water electrolysis products as propellants.

Parallelization

Although the quasi-2D formulation leads to a significant reduction of the computational cost, as explained in Sec. 6.1, the parallelization of PlasmaSim has been deemed necessary to deal with plasma discharges with molecular propellants. These are characterized by the large number of species involved and the numerous types of collisions and reactions that must be modelled. This imposes a significant penalty to full-PIC codes in terms of computational cost.

The parallelization process of PlasmaSim has followed two different complementary paths. On one side, specific libraries and functionalities of Unreal Engine (UE) for multithreading have been used. On the other side, in order to overcome some limitations of UE for massive parallelization, the UE interface (for the simulation set-up and main loop) is substituted by new `C++` subroutines and OpenMP [292] is implimented.

The first path consists on the usage of existing UE classes for multithreading, since external libraries for parallelization, like OpenMP, are found to be incompatible with UE. There exist several UE-specific classes and templates commonly used for tasks distribution among threads. In all the approaches, two qualitatively different threads can be distinguished: the main thread and the worker threads. The main thread triggers and controls the execution of the worker threads. Within a parallel loop, the main thread acts as another worker thread.

- **Runnable threads**: in this approach, a worker thread is an instance of the class called *FRunnableThread*, for a particular object of the *FRunnable* class. The main advantage of this method is its relatively simple implementation. The main drawback is the automatic destruction of the worker thread objects upon the realization of its parallel task. This can cause an overhead problem associated with the continuous creation and destruction of threads, unless the predefined parallel tasks are relatively long.

- **Queued pool threads**: a *FQueuedThread* class can be instantiated into a pool of threads, to which tasks are assigned using the method *AddQueuedWork*. This approach does not have an overhead problem, because worker threads exist independently of the task assignment. However, some control over threads and task assignment is lost. But its main drawback is the lack of specific functionalities for shared memory access.

- **ParallelFor**: *ParallelFor* is a function that mimics a *for* loop, and permits the execution in parallel of a given number of statements. It works similarly to OpenMP. It includes the possibility of using *FCriticalSection* to prevent the simultaneous update of a certain memory location by different worker threads. The only drawback is the loss of control over threads management, which is controlled by UE.

The *ParallelFor* approach has been the one implemented in PlasmaSim, given its numerous advantages and the fact that is programatically more natural than the other possibilities. The computational gain achieved consists, for a typical simulation scenario, on more than a 60% reduction of the computational time in a laptop with 4 cores. However, any further improvements are limited by the incompatibility of PlasmaSim with the high performance computers of ICL. This, in turn, limits the number of accessible cores for simulation and is the main reason to pursue a second parallelization strategy.

The second path implies the translation into `C++` of the UE interface for the simulation set-up and main loop, to enable the access to the resources of high performance computers. To that end, a PlasmaSim.cpp file has been created for: (a) the reading of the user's inputs, (b) the set-up of the simulation and (c) the control of the main loop of PlasmaSim. The user's inputs are contained in a new file called set_inp.txt. OpenMP directives are mainly implemented on the particle-wise subroutines, where parallelization can be leveraged. The simulation results in Sec. 6.3 are obtained with this version, without the UE interface.

Improvement of boundary conditions

Two of the boundary conditions for electron macroparticles, contained in Tab. 6.1, have been significantly modified, for an improved modelling of the WET-HET discharge. These are the cathode recirculation condition and the dielectric removal condition.

In first place, the cathode recirculation condition has been observed to lead to the formation of an artificial sheath along the Cathode/Free loss surface, in line with previous numerical simulations with similar scenarios [168]. To prevent the formation of an artificial non-neutral region, the quasineutrality condition (QNC) has been proposed [118]. This condition consists on the injection, through the cathode boundary, of a variable electron current to compensate at every time step the positive charge accumulated in the cells adjacent to the cathode surface. This input electron flux is uniformly distributed in space. The velocity of injection follows a semi-Maxwellian distribution with a temperature set by the user.

In second place, the removal condition for electrons at the dielectric walls (see Tab. 6.1) is substituted by two different models of SEE. They are implemented as in Ref. [86]:

- **Constant SEE model**: when an electron macroparticle crosses a dielectric surface, the possibility of an elastic reflection is evaluated in first instance. A random number, R, is generated and compared to δ_{r}, which is the elastic reflection yield and has a constant value defined by the user, such that $0 < \delta_{\mathrm{r}} < 1$. If $R < \delta_{\mathrm{r}}$, the macroparticle is elastically reflected. If not, the evaluation of the possibility of SEE takes place. This process is analogous to the elastic reflection one. The constant SEE yield, δ_{SEE}, is also set by the user. The SEE emission is performed with an electron temperature of 1 eV [86]. In case the SEE does not occur, the electron macroparticle is simply removed.

- **Linear SEE model**: the first stage of this model consists again on the evaluation of the possibility of elastic reflection. This is done in the same way as in the constant SEE model. Now, δ_{SEE} is not constant anymore, but a function of the energy per incident electron [202]:

$$\delta_{\mathrm{SEE}}(\mathcal{E}_{\mathrm{e,wall}}) = \max\left[\delta_0 + \frac{\mathcal{E}_{\mathrm{e,wall}}}{\mathcal{E}_{\mathrm{e}}^*}(1-\delta_0), \delta_{\max}\right] \tag{6.5}$$

where $\mathcal{E}_{\mathrm{e}}^*$ is the crossover energy, δ_0 the probability of attachment and $\delta_{\max}$ the maximum SEE yield. The value of these constants depend on the type of material of the thruster dielectric walls. For Boron-Nitride ceramic walls, as is the case of the WET-HET: $\mathcal{E}_{\mathrm{e}}^* = 35.04$ eV, $\delta_0 = 0.578$, and $\delta_{\max} = 2.9$ [293,294]. In case $\delta_{\mathrm{SEE}} > 1.0$, a SEE electron macroparticle is injected, and then $\delta_{\mathrm{SEE}} = \delta_{\mathrm{SEE}} - 1.0$. The same process is repeated until δ_{SEE} becomes smaller than 1.0. Then, the SEE injection probablity is evaluated as usual. The injection temperature of SEE electrons is again 1eV.

Enabling anomalous collisionality

The possibility of considering anomalous collisionality in a PlasmaSim simulation has been added. This extra anomalous collisionality, associated to azimuthal-wise fluctuations and affecting only electron macroparticles, is modeled as in Ref. [295]. The anomalous collisional frequency is defined, in this case, as:

$$\nu_{\mathrm{t}} = k\frac{\omega_{\mathrm{ce}}}{16} \tag{6.6}$$

where the value of the parameter k must be set by the user, informed by experimental data. If an electron experiences a collision of this type in the code, the macroparticle undergoes an elastic isotropic-like scattering. The present model does not consider anisotropy in the anomalous scattering, which have been studied in previous works [161].

Implementation of updated quasi-2D formulation

The updated version of the quasi-2D formulation has been implemented in PlasmaSim. This new formulation has been introduced in Ref. [118]. Starting from the separation of

ϕ into the sum of $\phi_1(x)$ and $\phi_2(y)$, in Eq. 6.1, Poisson equation can be written as:

$$\frac{\partial^2\phi_1(x)}{\partial x^2}+\frac{\partial^2\phi_2(y)}{\partial y^2}=-\frac{\rho(x,y)}{\varepsilon_0}. \tag{6.7}$$

Now, the integration of Eq. 6.7 along each of the directions results in two 1D ordinary differential equations:

$$\frac{d^2\phi_1(x)}{dx^2}L_\mathrm{y}+\left.\frac{d\phi_2(y)}{dy}\right|_{L_\mathrm{y}}-\left.\frac{d\phi_2(y)}{dy}\right|_0=-\frac{1}{\varepsilon_0}\rho^x(x) \tag{6.8}$$

$$\frac{d^2\phi_2(y)}{dy^2}L_\mathrm{x}+\left.\frac{d\phi_1(x)}{dx}\right|_{L_\mathrm{x}}-\left.\frac{d\phi_1(x)}{dx}\right|_0=-\frac{1}{\varepsilon_0}\rho^y(y) \tag{6.9}$$

with

$$\rho^\mathrm{x}(x)=\frac{1}{L_\mathrm{y}}\int_0^{L_\mathrm{y}}\rho(x,y)dy \quad \rho^\mathrm{y}(y)=\frac{1}{L_\mathrm{x}}\int_0^{L_\mathrm{x}}\rho(x,y)dx. \tag{6.10}$$

The boundary conditions for Eqs. 6.9 and 6.10 are the same as in the old formulation, in Sec. 6.1. It must be noted that now Eqs. 6.9 and 6.10 are coupled through the first order derivatives (which are discretized with forward and backward 1^{st} order differences) at the boundaries. Therefore, they must be solved together and the matrix of coefficients to be numerically inverted has a size of $N_\mathrm{cell}+N_\mathrm{cell}$. The order of the problem is still significantly reduced compared to a full 2D model (N^2_cell). The matrix of coefficients is stored as a sparse matrix and inverted using the Eigen libraries for linear algebra [296]. In previous works, Eqs. 6.9 and 6.10 have been decoupled by moving the first order derivatives to the RHS, obtaining their values from the previous time step [118].

Implementation of water propellant

The addition to PlasmaSim of O_2 and H_2O propellants (and the derived species) and their associated collisions and reactions (dissociation, ionization, attachment and excitations) is presented here. The complete list of all the reactions modelled by PlasmaSim for O_2 and H_2O propellants is contained in Tabs. 6.2 and 6.3. The second column of the tables includes the information of the energy loss associated to each of the reactions. The most relevant excitation collisions have been included in the modelling of the discharge. Previous works have shown that power losses associated to the mechanism of vibrational excitation can be considered negligible for O_2 and other diatomic molecular propellants [295]. Electronic excitation, on the contrary, may play an important role in the power balance, and must be considered in the simulations of diatomic molecules. In order to allow the user to turn off and on the different collision types, a dedicated input file, named 0_<Prop>_ReducedModel.txt is created.

In Tab. 6.2, the O_2-dissociation reaction data is taken from Itikawa [297], which provides the total dissociation cross section. Molecular ionization data is obtained from the same reference. For the ion dissociation double reaction of O_2, the lost energy is estimated as the sum of the dissociation reaction of O_2 (5.1 eV) and the double ion ionization of O (48.6 eV). In the event of a dissociative attachment collision, all the energy

Reaction	Energy loss
Elastic: $O_2 + e \rightarrow O_2 + e$	-
Dissociation: $O_2 + e \rightarrow O + O + e$	5.10 eV [Ref. 306]
Ionization: $O_2 + e \rightarrow O_2^+ + 2e$	12.1 eV [Ref. 307]
Dis. ionization (+): $O_2 + e \rightarrow O^+ + O + 2e$	18.8 eV [Ref. 307]
Dis. ionization (++): $O_2 + e \rightarrow O^{++} + O + 3e$	53.7 eV
Dissociative attachment: $O_2 + e \rightarrow O^- + O$	K_e [Ref. 297]
Excitation 1: $O_2(X^3\Sigma_g^-) + e \rightarrow O_2(a^1\Delta_g) + e$	0.98 eV [Ref. 308]
Excitation 2: $O_2(X^3\Sigma_g^-) + e \rightarrow O_2(b^1\Sigma_g^+) + e$	4.05 eV [Ref. 308]
Excitation 3: $O_2(X^3\Sigma_g^-) + e \rightarrow O_2(A^3\Sigma_u^+,\ A'^3\Delta u,\ c^1\ \Sigma_u^-) + e$	6.12 eV [Ref. 308]
Excitation 4: $O_2(X^3\Sigma_g^-) + e \rightarrow O_2(B^3\Sigma_u^-) + e$	6.12 eV [Ref. 308]
Elastic: $O + e \rightarrow O + e$	-
Ionization: $O + e \rightarrow O^+ + 2e$	13.6 eV [Ref. 307]
Double ionization: $O + e \rightarrow O^{++} + 3e$	48.6 eV [Ref. 309]
Attachment: $O + e \rightarrow O^-$	K_e [Ref. 298]
Excitation 1: $O(^3P) + e \rightarrow O(^1D) + e$	1.96 eV [Ref. 299]
Excitation 2: $O(^3P) + e \rightarrow O(^1S) + e$	4.18 eV [Ref. 299]
Excitation 3: $O(^3P) + e \rightarrow O(^3P^0) + e$	9.20 eV [Ref. 299]
Excitation 4-6: $O(^3P) + e \rightarrow O^* + e$	$>$ 12.0 eV [Ref. 299]

Table 6.2: Water Electrolysis (O_2), reactive model.

of the colliding electron, K_e, is lost. Six different types of molecular excitation collisions from the ground state ($X^3\Sigma_g^-$) are considered. Following Ref. [297], excitation to the states $A^3\Sigma_u^+$, $A'^3\Delta u$ and $c^1\ \Sigma_u^-$ are considered together: they have similar threshold energies. In the case of atomic oxygen, cross section data for elastic, ionization and attachment collisions is taken from Ref. [298], while for the excitation ones from Ref. [299]. In Tab. 6.3, the cross sections for the different electron-H_2O collisions are taken from Ref. [300]. As for the derived species, the collisional data is obtained from: Ref. [301] for OH, Ref. [302] for H_2 and Ref. [303] for H. The excitation collisions included (not shown in Tab. 6.3) are: H_2O first four rotational modes and stretching and bending modes [300], H_2O six lowest-energy electronic transitions [304, 305], OH three lowest-energy electron transitions [301], H electronic excitations up to n = 4 (included) [303]. Although collisional data are gathered for H_2 [302], they are not implemented given the small fraction of H_2 reported from preliminary simulations. O_2 and O collisional data are taken from Tab. 6.2.

In the new version of the code, the energy lost in the i^{th} reaction event, E^i_{loss}, is subtracted to the kinetic energy of the electron involved in the collision, $E^i_{\text{k,in}}$, to obtain the output energy. This remaining energy is equally distributed among the outcoming electrons (scattered and ejected) [311]:

$$E^i_{\text{k,out}} = \left(E^i_{\text{k,in}} - E^i_{\text{loss}}\right)/N^i \tag{6.11}$$

Reaction	**Energy Loss**
Elastic: H_2O + e → H_2O + e	-
Dissociation I: H_2O + e → OH + H + e	5.1 eV [Ref. 306]
Dissociation II: H_2O + e → O + H_2 + e	7.1 eV [Ref. 310]
Ionization: H_2O + e → H_2O^+ + 2e	12.6 eV [Ref. 307]
Ion dissociation I: H_2O + e → OH^+ + H + 2e	18.1 eV [Ref. 307]
Ion dissociation II: H_2O + e → OH + H^+ + 2e	18.3 eV [Ref. 307]
Ion dissociation III: H_2O + e → O^+ + H_2 + 2e	19.0 eV [Ref. 307]
Ion dissociation IV: H_2O + e → O + H_2^+ + 2e	20.7 eV [Ref. 307]
Double ion dissociation: H_2O + e → O^{++} + H_2 + 3e	55.7 eV
Dissociative attachment I: H_2O + e → OH^- + H	K_e
Dissociative attachment II: H_2O + e → OH + H^-	K_e
Dissociative attachment III: H_2O + e → O^- + H_2	K_e
OH-elastic: OH + e → OH + e	-
OH-ionization: OH + e → OH^+ + 2e	13.0 eV [Ref. 307]
OH-dissociation: OH + e → O + H + e	4.4 eV [Ref. 306]
OH-attachment: OH + e → OH^-	K_e
H-elastic: H + e → H + e	-
H-ionization: H + e → H^+ + 2e	13.6 eV [Ref. 307]
H-attachment: H + e → H^-	K_e
O-elastic: O + e → O + e	-
O-ionization I: O + e → O^+ + 2e	13.6 eV [Ref. 307]
O-ionization II: O + e → O^{++} + 3e	48.6 eV [Ref. 309]
O-attachment: O + e → O^-	K_e
H_2-elastic: H_2 + e → H_2 + e	-
H_2-ionization: H_2 + e → H_2^+ + 2e	15.4 eV [Ref. 307]
H_2-dissociation: H_2 + e → H + H + e	4.5 eV [Ref. 306]
H_2-ion dissociation: H_2 + e → H^+ + H + 2e	18.0 eV [Ref. 307]
H_2-attachment: H_2 + e → H_2^-	K_e

Table 6.3: Water Vapour (H_2O) reactive model. Excitation reactions are not included in this table

where $E^i_{\mathrm{k,out}}$ stands for the kinetic energy per output electron. There exist other models for the energy partition (beyond deterministic equipartition) among the output electrons, which distinguish between the scattered electron and the ejected electrons. In Ref. [312], a deterministic model is proposed where equipartition is kept until a certain energy threshold, above which the energy of ejected electrons remains constant. A simple probabilistic approach consisting on the uniformly random partition of the energy is implemented in Ref. [313]. Moreover, Ref. [314] uses a more sophisticated probabilistic model based on the differential cross-sections of the collisions. In PlasmaSim, the accuracy of the energy equipartition approach is considered sufficient provided the quasi-2D approximation.

The generation of the velocity vectors of the outcomming electrons is also kept simple. The vectors are independently sampled from the surface of a sphere using Marsaglia's algorithm [315]. There exist others methods in the literature with a higher degree of complexity, based on assumptions that do not necessarily hold in the real collisional processes. In Ref. [316], they assume that the incident and the outcomming electron vectors are coplanar, with the scattered and the ejected one being perpendicular to each other. Chew *et al.* [317] impose that the ejected electron velocity vector is randomly generated from a hemisphere, whose equatorial plane is perpendicular to the incident velocity vector. The remaining kinetic energy after the inelastic collision is equally split among the scattered and the ejected particles.

Updated PlasmaSim architecture

The updates presented in the previous sections and the realization of other minor changes have lead to a modified overall structure of the code. The updated PlasmaSim architecture is depicted and compared to the old one in Fig. 6.3.

(a)

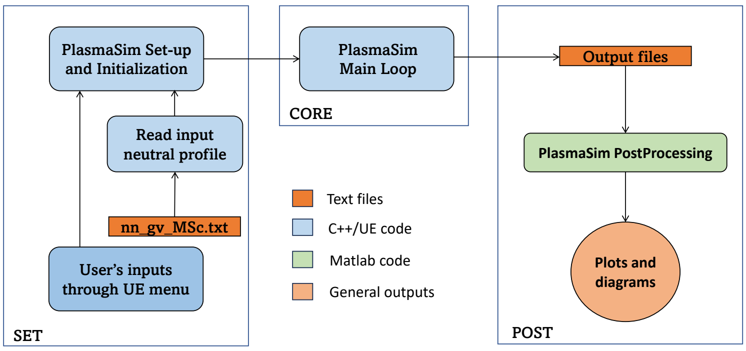

(b)

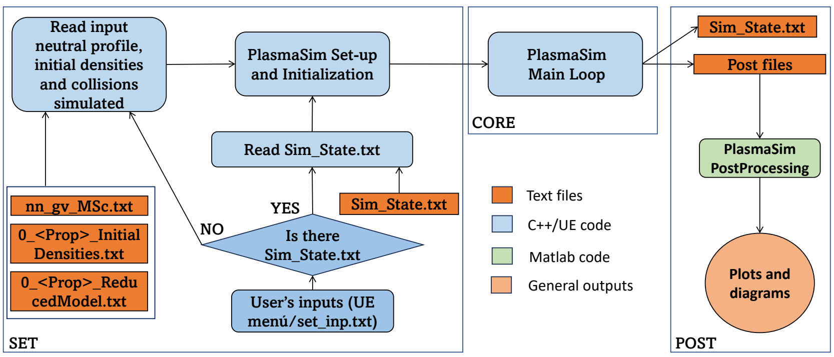

Figure 6.3: (a) Old and (b) updated overall PlasmaSim architecture

In the old version of PlasmaSim, in Fig. 6.3(a), the user defines the simulation set-up through an interactive menu built with Unreal Engine. Upon the simulation initialization, the UE interface reads the user inputs, builds the simulation domain, and randomly creates electron, ion and neutral macroparticles with an uniform distribution in space and a Maxwellian distribution for the initial velocities. If the user includes in the simulation folder a file called nn_gv_MSc.txt, which contains an input neutral axial profile, neutrals are not created following an uniform spatial distribution, but according to the user-defined profile. Then, the main loop of the simulation starts, which corresponds to the CORE block (coded in `C++`), and whose main subroutines have been briefly described in Sec. 6.1. Finally, the output .txt files from the CORE block are postprocessed within the POST block.

In the updated version of the code, in Fig. 6.3(b), user's inputs can now be introduced through the new file set_input.txt, which is shown below.

```
########################### SET INPUT ###########################
######### This file contains the input parameters for a #########
#########              PlasmaSim simulation             #########
#################################################################

#### GENERAL SIMULATION SETTINGS ####

Output_path = /home/jpera95/Repositories/PlasmaSimNoUE/sims/SimOxygen/ //
Number_of_threads = 20          //
Maximum_Time = 5e-6 //;1.0e-10  // [s]
Time_Step_Print = 1.0e-8        // [s]
Recording_Start = 0.0           // [s]
Recording_Stop = 50e-6          // [s]
Particles_species = 180000      // [s]
Anode_Voltage = 300             // [V]
Mass_flow = 1.0                 // [mg/s]
Simulation_type = HallThruster  //
Electron_Temperature = 5.0      // [eV]
Ion_Temperature = 0.1           // [eV]
Neutrals_Temperature = 700.0    // [K]
NeutralSizeLimit = 1e8          // Upper limit for the size of neutrals
ChargeSizeLimit = 1e8           // Upper limit for the size of charged species
Electron_Number_Density = 3.0e19 // [m - 3]
Neutral_Number_Density = 5.0e20  // [m - 3]
Permittivity = 8.854187813e-12  // [F m - 1]
Cathode_Voltage_Ampl = 0.0      // [V]
Cathode_Freq = 0.0              // [Hz]
Reactive_Model = 2              //
Reactive_Stages = 2             //
Propellant = 1                  // 0: Xenon; 1: Oxygen; 2: Water
Poisson_solver = 1              // 0: Original Quasi-2D approach;
                                // 1: Updated Quasi-2D approach
Acc_steps = 1                   // Number of steps for variable accumulation
```

```
#### MAGNETIC FIELD SETTINGS ####

Maximum_B = 0.016                // [T]
Location_peak_B = 0.024          // [m]
Location_half_B = 0.04           // [m]

#### GEOMETRICAL PARAMETERS ####

Channel_Length = 0.035           // [m]
Channel_Width = 0.005            // [m]
Channel_Diameter = 0.025         // [m]
Sim_Domain_Length = 0.04375      // [m]

#### BOUNDARY CONDITIONS ####

SEE_flag = 2          // 0: no SEE (electrons are elastically reflected);
                      // 1: constant SEE model; 2: linear SEE model
SEE_Temp = 1.0        // [eV]
SEE_yield = 0.5       // [-] SEE yield used in the constant SEE model
refl_yield = 0.5      // [-] Reflection yield used in the constant SEE model
cath_BC = 1           // 0 - recirculation condition at the cathode;
                      // 1 - quasineutrality condition at the cathode cell
```

The set_input.txt contains all the available options that the user can edit to create a certain simulation set-up. It must be placed within the simulation folder, so that the PlasmaSim executable can read it. After its correct reading, PlasmaSim will look for a Sim_State.txt file also within the simulation folder. The Sim_State.txt contains the state of a previous simulation at a certain time step. Such simulation state is stored as a set of the kinematic states of all the macroparticles within the domain. If PlasmaSim finds this file, the simulation will start from this stored state. If not, the initialization of the simulation takes place with the information contained in nn_gv_MSc.txt and 0_<Prop>_InitialDensities.txt. The latter is a new input file that allows the user to specify the initial densities of each species. Then, the main loop starts, which prints or updates the Sim_State.txt file every given number of steps.

6.3 WET-HET simulations

As indicated previously, the advances in PlasmaSim presented in the previous sections have the ultimate goal of enabling the simulation of the WET-HET thruster operated with O_2 and/or H_2O as propellants. In this section, a simulation of the O_2-fuelled WET-HET discharge is presented. Sec. 6.3.1 presents the simulation set-up. In Sec. 6.3.2, the simulation results are shown and discussed.

6.3.1 Simulation set-up

Tab. 6.3.1 gathers the main settings, related to physical parameters, of the WET-HET simulation with O_2 as propellant. The other species considered in the simulation are O_2^+, O^+, O; then, O^{++} and O^- have been excluded because they have been found negligible in previous simulations, which is in agreement with [295]. The channel length is equal to 0.035 m. The domain is extended in the axial direction approximately half of a chamber, up to 0.053 m. The operation point, defined in terms of the discharge voltage and the anodic mass flow rate, is $V_d = 300$ V and $\dot{m}_A = 1.1$ mg/s. Neutrals are injected through the anode with a uniform spatial profile and their velocity is sampled from a semi-Maxwellian distribution function with a temperature of 300 K and an axial drift velocity of 750 m/s. In a similar way, electrons are injected from the downstream cathode boundary with a temperature equal to 5 eV.

Simulation parameter	**Units**	**Value**
Propellant (anode inj.)	-	O_2
Other species	-	O_2^+, O^+, O
Channel length	m	0.035
Channel width	m	0.005
Channel diameter	m	0.025
Domain length	m	0.053
Discharge voltage (V_d)	V	300
Anodic mass flow ($\dot{m}_A$)	mg/s	1.1
O_2 inj. temperature	K	300
O_2 inj. drift	m/s	750
Electron inj. temperature	eV	5
B peak intensity	G	250
B peak axial position	m	0.032
SEE temperature	eV	1.0
Electron reflection yield	-	0.5
Anomalous transport coeff., k	-	0.01 [71]

Table 6.4: Simulation settings: physical parameters

The magnetic field, B, which is purely radial has a maximum intensity of around 250 G. The axial position of the B peak is 0.032 m. The axial profile of the intensity of B can be observed in Fig. 6.4 (a). The profile reproduces approximately the one set in the real thruster, measured along the thruster chamber midline. Regarding the SEE, the linear model presented in Sec. 6.2 is considered. The value of the elastic reflection yield of electrons at the wall is set to 0.5 [318]. Tab. 6.5 contains the information of the numerical parameters of the WET-HET simulation. Notice that the density of macroparticles is expressed in a per axial/radial cell-basis. The reason for this is that, as explained in Sec. 6.2, the quasi-2D formulation of PlasmaSim allows to solve for two different artificial electric potentials, an axial and a radial one, which approximate the real 2D ϕ.

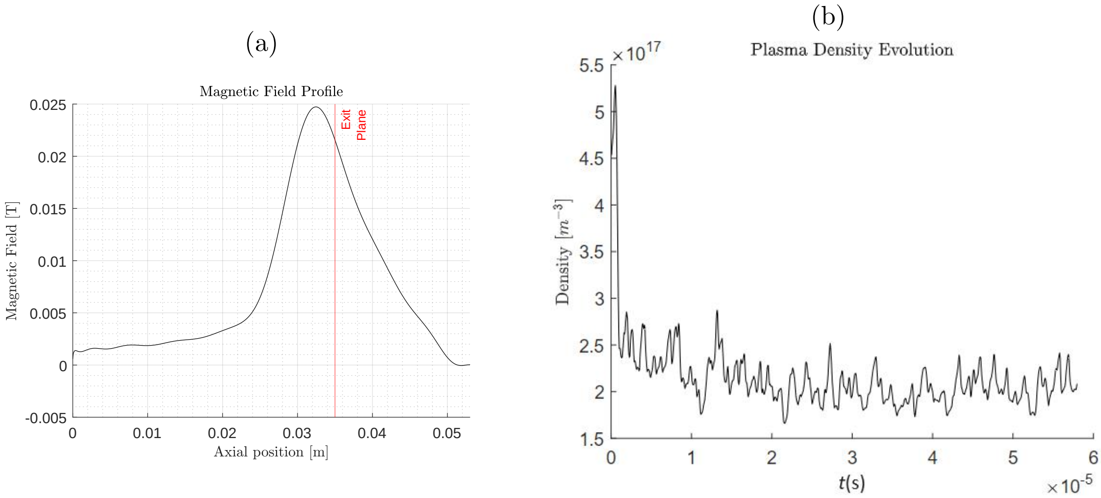

Figure 6.4: (a) Axial profile of the intensity of the magnetic field, B. (b) Spatially-averaged plasma density evolution with time

Simulation parameter	Units	Value
Time step (approx)	s	5×10^{-12}
Number of axial cells	-	4000
Number of radial cells	-	4000
Initial number of particles per axial/radial cell	-	30

Table 6.5: Numerical parameters of the simulation

6.3.2 Simulation results

Fig. 6.4(b) shows the time evolution of the plasma density averaged over the simulation domain. The elapsed real time of the run is relatively small, of around 4-5 days with only 10 cores in an Intel Xeon Gold (@2.10 GHz), considering that neutral dynamics are self-consistently solved [295,319]. This is achieved thanks to the computational cost reduction associated to the quasi-2D formulation [320]. After an initial density bump, the spatially-averaged plasma density seems to reach a steady condition, which is slowly evolving due to changes in the density of neutrals. Hereafter, all the time-averaged profiles and contours are computed over the last 10 μs.

Fig. 6.5 shows the time-averaged (and radially-averaged) axial profiles of the electric potential, ϕ; and the electron temperature, T_e. In Fig. 6.5(a), the profile of ϕ exhibits a steep fall right upstream the thruster chamber exit. This is, therefore, the location of the maximum electric field, which coincides with the position of the B peak, as typically occurs in a HET. The fact that a large portion of the potential fall takes place within the thruster chamber is characteristic of conventional US HETs, due to the upstream

(a) (b)

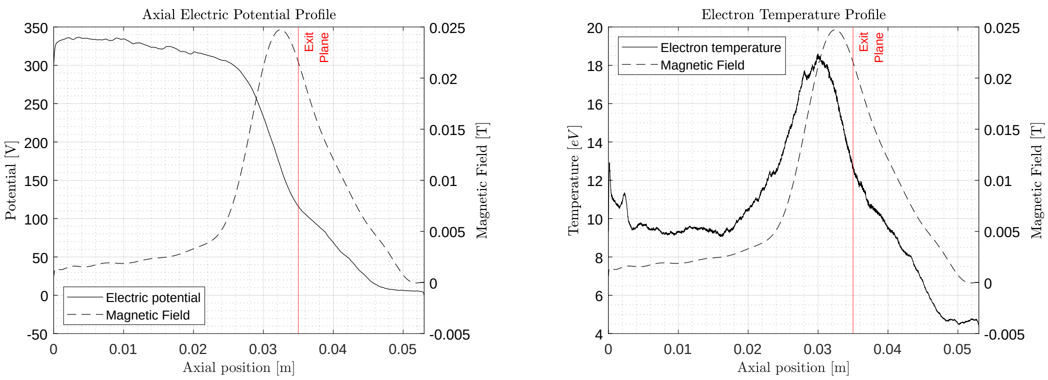

Figure 6.5: Time-averaged 1D axial profiles (radially-averaged) of the WET-HET discharge, with O_2 as propellant. (a) Electric potential ϕ, (b) electron temperature T_e

(a) (b)

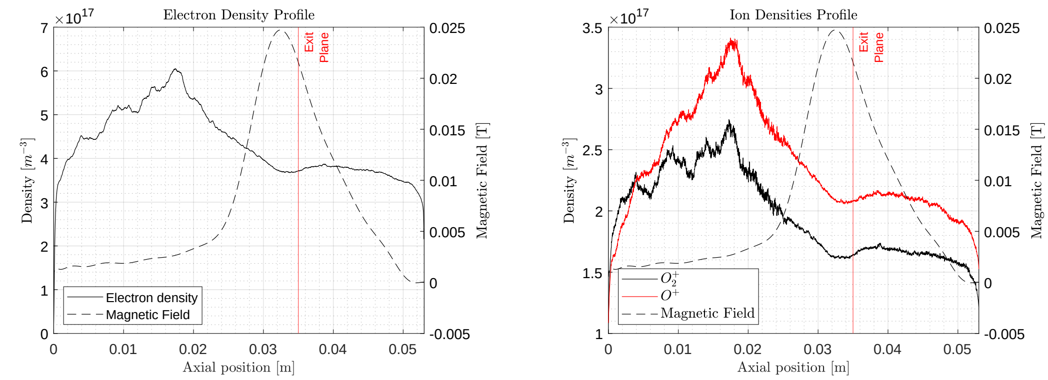

(c)

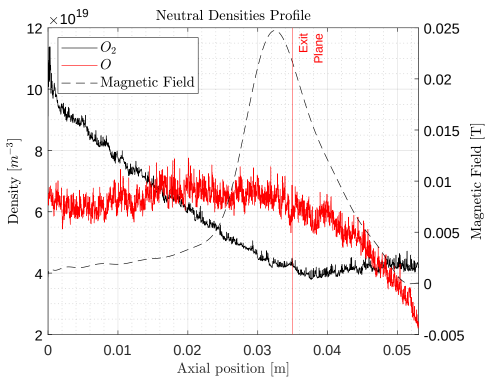

Figure 6.6: Time-averaged 1D axial profiles (radially-averaged) of the WET-HET discharge, with O_2 as propellant. (a) Electron density n_e, (b) ion species densities, n_{i,O_2^+} and n_{i,O^+} (c) neutral species densities, n_{n,O_2} and $n_{n,O}$.

location (with respect to MS HETs) of the B peak. The comparison of these results with those for the MS HT5k, in Fig. 3.4(a), evidences the difference between US and MS

HETs in terms of the axial position of the acceleration region. Back to Fig. 6.5(a), a sheath is observed in front of the anode with a ϕ drop of around 20-30 V, approximately 3 times the local T_e, as seen in Fig. 6.5(b). The relatively small decay of T_e from its maximum value towards the anode can be related to the low cross-section of electron-O_2 ionization collisions, as compared with the ones of typical HET propellants [295]. This same argument is used to explain why experimentally-observed T_e profiles are wider in Kr discharges than in Xe ones [260]. The downstream-most value of the velocity of O_2^+ ions is approximately 35 km/s, while the one of O^+ ions is 50 km/s. The ratio of both terms at the downstream boundary is $[u_{i,O^+}/u_{i,O_2^+}]_{x=5.3\mathrm{cm}} \approx 1.43$, which is approximately the inverse of the ratio of molecular masses, $\sqrt{2} \approx 1.41$. This means that both species experience, in average, the same effective acceleration voltage, V_{eff}. This, in turn, implies that, from energy conservation, one can state that both species ions are generated around the same axial position inside the thruster chamber.

Fig. 6.6 shows the time-averaged (and radially-averaged) axial profiles of the electron (plasma) density, n_e; the ion species densities n_{i,O_2^+} and n_{i,O^+}; and the neutral species densities n_{n,O_2} and $n_{n,O}$. In Fig. 6.6(a), the order of magnitude of n_e is similar to the one in the standard operation of a SPT-100 thruster with Xe [3]. The position of the n_e peak is also found in the usual location, upstream the exit plane and the acceleration region, with a profile similar to the one in the HT5k and HT20k discharges (see Figs. 3.4(d) and 5.4(b)). Regarding the ion density, in Fig. 6.6(b), both n_{i,O_2^+} and n_{i,O^+} exhibit similar magnitudes. The ratio of plasma densities averaged over the whole simulation domain $\tilde{n}_{i,O_2^+}/\tilde{n}_{i,O^+}$ is close to 0.8. Taccogna et al. [295] report a ratio even lower ($= 0.33$) under different operative conditions. Both results evidence the significance of dissociation energy losses in O_2 discharges. Fig. 6.6(c) further supports this conclusion, where the spatially-averaged values of n_{n,O_2} and $n_{n,O}$ are again similar to each other. The maximum of n_{n,O_2} is found close to the center (axial-wise) of the thruster chamber, in line with Ref. [295].

Performance metrics can be estimated from the time and space averaged values of the macroscopic plasma properties at the downstream-cathode boundary. The propellant utilization efficiency, η_u, is approximately 17%, which is consistent with a thrust efficiency of a 3% reported from experimental measurements of a similar WET-HET operation point (with $V_s = 305$ V, $\dot{m}_A = 1$ mg/s and $B_{\mathrm{peak}} = 0.024$ T) [321]. A stronger magnetic field and higher power operation can improve significantly the poor value of η_u, beyond a 40% [321]. The time-averaged thrust estimation from simulations yields an approximate value of 7.5 mN, very close to the reported F (≈ 8 mN) by Tejeda et al. [321] for a similar operation point.

Fig. 6.7 displays the repartition of power losses from inelastic collisions in the discharge. Ideally, all the power losses would be associated to O2-ionization, for the generation of ions and their subsequent acceleration for thrust generation. However, a significant amount of power is spent in other collision types, which implies an inefficient operation. In fact, ionization losses are not dominated by O2-ionization, but by O-ionization, in agreement with Ref. [295]. The oxygen atoms that are ionized come from dissociation reactions, whose power losses amount to more than a 10% of the total, in Fig. 6.7. This energy sink is one of the main drawbacks of the usage of molecular propellants [322], and

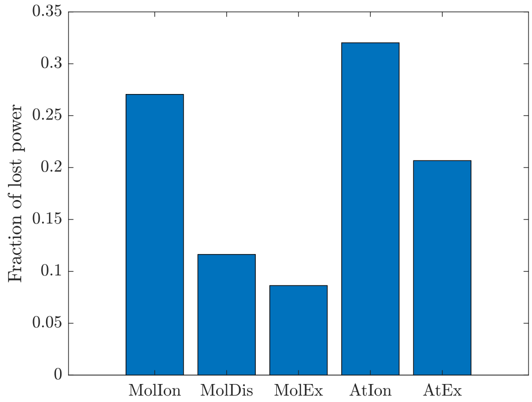

Figure 6.7: Fraction of power losses from inelastic collisions. The bars correspond to: O2-ionization, MolIon; O2-dissociation, MolDis; O2-excitation, MolEx; O-ionization, AtIon; and O-excitation, AtEx.

it is inherent to them because the bond energy of the molecule constituents is smaller than the first ionization potential (see Tab. 6.2). Excitation losses are very relevant, especially the ones from atomic excitation, as observed in Ref. [295]. The combined cost of molecular and atomic excitation amounts to a 30% of the total energy losses from collisions.

6.4 Conclusions

The axial-radial version of the quasi-2D full-PIC code PlasmaSim, developed at the Imperial Plasma Propulsion Laboratory, has been presented. The most relevant subroutines and algorithms of the numerical tool, which are mainly written in `C++` and `Unreal Engine`, have been briefly described. The Poisson Solver and Electric Field subroutine contains the implementation of the "quasi-2D" formulation, which is the main feature of PlasmaSim. This method consists on splitting the electric potential into the sum of two functions which depend, each of them, in just one single coordinate of the problem (e.g. one axial and one radial "potential" function). This allows to reduce the effective dimensionality of the problem, from a computational perspective, from two to one, while still accounting for 2D effects in an approximated way.

The upgrades of PlasmaSim carried out during the research stay have aimed at enabling faithful simulations of the WET-HET thruster, operated with water-electrolysis products or water vapour. Only the most relevant contributions have been presented in this section. In first place, the parallelization of most of the subroutines of the code. Two strategies have been followed, the latter one with OpenMP requiring the translation of the whole `Unreal Engine` interface into `C++` code. In second place, boundary conditions have been improved with: (*i*) a quasineutrality condition for the cathode boundary and, (*ii*) a constant and a linear model for SEE at the dielectric walls. In third place, an updated and improved version of the quasi-2D formulation has been implemented for the solution of Poisson's equation. In fourth place, the introduction of an anomalous collisionality, and the new chemical species O_2 and H_2O with their corresponding interactions with electrons and the thruster walls. In this regard, a set of new input files, for the sake of a further control over the simulations inputs, have been created, as well as the adequate input-output interface.

Some preliminary simulation results have been shown for a O_2-fuelled discharge of the WET-HET thruster. The implementation of the quasi-2D formulation allows a significant reduction in the computational cost as compared with standard state-of-the-art 2D simulation codes. This has permitted simulating, in a time-resolved manner, discharge times larger than the period of low-frequency oscillations, in 4-5 days wall-clock times with standard computer resources. The plasma profiles obtained from the numerical simulations are in line with previous experimental and numerical results in the literature. The importance of dissociation energy losses, as well as of monoatomic oxygen excitation collisions, has been shown.

Chapter 7

Conclusions

This chapter summarizes the main contributions of the Thesis and proposes some future lines of work.

7.1 Main contributions of the Thesis

The most relevant contributions of this Thesis can be divided into three groups, according to the three general tasks or objectives described in Sec. 1.3. These comprise the numerical studies and the associated code developments of: (*i*) the ion extraction and beam focusing in ion optics of GIT thrusters, with EP2PLUS; (*ii*) the plasma discharge in advanced real HET thrusters with magnetic-shielding topologies and centrally-mounted cathodes, with the HYPHEN code; and (*iii*) the plasma discharge of a HET operated with water electrolysis products or water vapour, with PlasmaSim.

Regarding the first task, the EP2PLUS simulations of the ion extraction and beam focusing and neutralization in the ion optics of a GIT, the major contributions are:

- The adaptation of EP2PLUS for the modeling of the ion optics scenario. This includes: (*i*) the capability of considering more than one electron population, (*ii*) an algorithm for the active control of the separation between electron populations in an ion optics scenario, based on the electric potential profile, (*iii*) a new surface type for the specular reflection of macroparticles to simulate the symmetric interaction of beamlets from different grid apertures, and (*iv*) the addition of electron inertia to the momentum equation. Besides this, dedicated set-up algorithms have been coded for the generation of the grid assembly geometry.

- The successful application of two different setups to the simulation of ion optics scenarios with EP2PLUS. The first setup, the infinite-apertures one, with a periodic array of holes, can be used for the estimation of the optimal perveance (in terms of divergence angle) of the grid assembly, with a small computational cost. The second setup, the finite-apertures one, with a complete grid assembly of 19 apertures but a significantly larger computational cost, allows characterizing the coalescence process of the beamlets into one single beam, and the electric current neutralization process and its dependence on the position of the external cathode. Both setups have been partially validated against experimental results and an original 1D semi-analytical model for the plume expansion.

- The conclusions concerning the charge and current neutralization process. It has been observed that current neutralization of the ion beamlets is strongly affected by the position of the neutralizer cathode; while the charge neutralization process and, therefore, the expansion and coalescence of the ion beamlets, is independent of the cathode location, provided that the latter is far enough from the grids to avoid perturbing the extraction.

Regarding the second task, the modeling with HYPHEN of advanced HET prototypes, the major contributions are:

- The upgrade of HYPHEN to enable the modeling of magnetically-shielded HETs with centrally-mounted cathodes. The main code developments have been the following. (*i*) The improvement in the boundary conditions to include metallic boundary surfaces for electron current injection, i.e. surface cathodes. Both neutrals and ion macroparticles can be injected from this new surface type, which permits a more faithful modeling of central cathodes. The injection of neutrals from the cathode boundary has been found to reduce the local numerical noise in the solution of the electron fluid equations. (*ii*) The generation of non-structured MFAM meshes for MS topologies with singular points inside the thruster chamber. (*iii*) The capability to define time-varying control inputs, i.e. the discharge voltage and the anodic mass flow rate. This new feature allows the simulation of direct-drive scenarios and modulation studies. The capability to consider a RLC filter between the cathode and the anode has also been included.

- The successful application of a experimentally-informed phenomenological model of the anomalous electron transport to the simulation of the discharges of the HT5k and HT20k thrusters. The model, which depends only on two unknown parameters α_{t1} and α_{t2}, has been tuned to match the experimental data of I_{d} and F of each operation point. Despite not being a target of the tuning process, the output low frequency oscillations of the discharge current agree well with the experimental ones.

- The complete 2D time-averaged numerical characterization of the plasma discharges of the HT5k and HT20k, with xenon as propellant. From this, the effectiveness of magnetic shielding in these thrusters have been proven. The magnetic shielding topology have been observed to shift the acceleration region outwards, with respect to conventional thrusters, keeping a relative high-density, low-temperature plasma inside the chamber. Low plasma temperature around the chamber walls leads to small energy deposition and small ion impact energies, under the sputtering threshold. This combination of high plasma density and low electron temperature has been observed to result in relative plasma currents to the walls similar to those in conventional HETs.

- The 2D time-averaged numerical characterization of the plasma discharge of the HT20k, with krypton as propellant; and the comparison with the xenon discharge, in terms of performance and local plasma properties. Although worsened with respect to Xe operation, magnetic shielding has been proved to remain effective with Kr. The HT20k thruster exhibits a relatively small overall efficiency gap between Xe and Kr operations. This is, in part, explained by the high propellant utilization efficiency of Kr (although still smaller than Xe) in the HT20k, reported from the simulations. It has been shown that the ionization and acceleration regions are wider towards the plume in the Kr operation points, as compared to the Xe ones. Thus, Kr cases feature higher divergence and species-wise velocity dispersion in the plume. Voltage utilization has been found lower with Kr, mainly due to a worse cathode-plume coupling. Current efficiency, in agreement with experimental data, is found higher for Kr. The same occurs with charge utilization. Although most of the previous observations are in line with past results from other thrusters, some disagreements have been found, proving the sensitivity of the analysis to the thruster design and configuration.

- The time-resolved characterization of the dynamic response of the HT5k thruster under sinusoidal modulation of the discharge voltage. The modulated or driven low-frequency mode of the discharge has been found to oscillate with the frequency of modulation, provided this is sufficiently close to the natural breathing mode one. At relatively large modulation frequencies, the natural breathing mode of the thruster has reappeared in the simulations, proving the partial loss of control of the voltage modulation over the discharge. The close qualitative agreement of the simulation results with previous modulation studies of different ExB thruster types has led to the conclusion that the same fundamental phenomena determines the modulated response across different designs: the natural breathing mode controlled by means of electron temperature oscillations, which are in turn controlled by the discharge voltage.

- The conclusion that efficiency gains from voltage modulation are limited in the HT5k thruster. This is a consequence of the coupling between plasma production and acceleration processes inherent to the operation of Hall effect thrusters. Nevertheless, the effective control that voltage modulation exerts over low-frequency discharge oscillations can be useful for EMI mitigation and plasma diagnostics.

- The application of the data-driven technique HODMD to the analysis of the complex spatio-temporal structure of the modulated plasma discharge of the HT5k. This has confirmed the breathing mode-like nature of the modulated modes and has allowed to identify the standing or travelling nature of the waves of the different plasma properties . It has been observed that ion recombination at the walls gives rise to an apparent 1D axial neutral density wave with phase velocity 5-6 times larger than the fluid velocity of neutrals.

Regarding the third task, the modeling of a water-fuelled HET, the major contributions are:

- The upgrade of the axial-radial version of PlasmaSim for the simulation of the water-fuelled WET-HET thruster. This includes: (*i*) the parallelization of most of the subroutines of the code, (*ii*) the improvement of the quasineutrality condition at the cathode surface and the addition of two secondary electron emission models for the dielectric walls (*iii*) the implementation of the updated version of the quasi-2D formulation for the solution of Poisson's equation and (*iv*) the addition to PlasmaSim of the new propellants O_2 and H_2O and their respective reactions and collisions with other species and wall interactions.

- The successful realization of a preliminary simulation of a O_2-fuelled discharge of the WET-HET thruster. The quasi-2D formulation of PlasmaSim has allowed obtaining two dimensional time-resolved results of a HET discharge with a significantly reduced computational effort as compared to state-of-the-art 2D simulation codes. The plasma profiles obtained have been found in line with experimental and numerical results in the literature, and it has been shown the relevance of dissociation and O-excitation energy losses in O_2-fuelled HET discharges.

7.2 Future work

In order to describe the future lines of research related to the work of this Thesis, it is convenient to present them organized into research objectives or tasks. The first group of future research lines, corresponding to the numerical analysis of the gridded ion thruster plasma discharge with EP2PLUS, includes:

- The further upgrade of the EP2PLUS code. Some possible future developments are: (*i*) enabling the coupling between discharge chamber and ion optics simulations and (*ii*) the implementation of a cylindrical coordinate system that facilitates the modeling of circular holes and radially-symmetric aperture patterns in the grids.

- The simulation of ion optics coupled with discharge chamber simulations. In the discharge chamber scenario, the grid assembly would be modeled as an infinitely thin surface with a given neutral and ion transparency. The continuous feedback between both types of scenarios would be as follows: on the one hand, ion optics simulations would provide the updated real transparency of the grid optics to the discharge chamber scenario; on the other hand, the discharge chamber simulation would inform the ion optics scenario about the updated ion fluxes distribution towards the grid optics.

- The numerical study of the real limit in current extraction capability of ion optics systems [323], and its comparison to the theoretical limit of space-charge-limited current from Child's law [3].

The second group of future research lines, corresponding to the modeling of advanced HETs with HYPHEN, includes:

- The further upgrade of the HYPHEN code. Some of the possible future developments are: (*i*) the implementation of a Poisson's solver, for the improved modeling of the low plasma density regions of the discharge where non-neutrality may arise, (*ii*) the translation of all the MFAM-wise electron module algorithms into rectangular mesh-wise, giving the user the possibility of choosing between both types of meshes and (*iii*) enabling the use of metallic materials for the lateral walls of the thruster chamber.

- The application of more complex spatial profiles to the function of the anomalous transport parameter, $\alpha(z, r)$, with experimentally-measured local plasma properties as targets of the turbulent transport tuning process [77].

- The numerical analysis of magnetically-shielded HETs with metallic/conducting walls [162] and the comparison to those with dielectric walls, in terms of performance, local plasma properties and power deposition to walls [163]. Since magnetic shielding significantly reduces plasma-wall interaction, the possibility of switching from dielectric to metallic walls in a HET is enabled, with an associated improvement in the mechanical and thermal properties of the thruster.

- The numerical study of the effect on the HET efficiency of different alternative configurations for propellant injection, such as reversed neutral gas feed or the rotating supply [324–326]. The need to increase propellant utilization efficiency in HET operation with alternative propellants justify the realization of this study.

The third group of future research lines, corresponding to the numerical analysis of the WET-HET thruster operated with water as propellant, includes:

- The further upgrade of the the axial-radial version of the PlasmaSim code. Some of the possible future developments are: (*i*) the implementation of a cylindrical coordinate system that correctly models the curvature of the HET annular geometry and (*ii*) the coupling of the axial and radial directions with the azimuthal one for the self-consistent resolution of the azimuthally-based anomalous transport [116].

- The full 2D time-averaged characterization of the WET-HET plasma discharge with water electrolysis products and water vapour. This includes the analysis of the main sources of inefficiencies, the comparison of local plasma properties with those in Xe discharges, the suggestion of ways for an improved operation of water (i.e. geometrical or operational modifications), and the comparison with experimental results [321].

- The time-resolved characterization of the WET-HET plasma operation with water as propellant. The analysis would focus on the low frequency oscillations of the discharge, the dynamics of the different species and how the breathing mode behaves in the discharge of molecular propellants.

Conclusiones

Este capítulo presenta las principales contribuciones de la Tesis y propone algunas futuras líneas de trabajo.

7.1 Principales contribuciones de la Tesis

Las contribuciones más relevantes de esta Tesis pueden dividirse en tres grupos, que corresponden a las tres tareas u objetivos generales descritos en la Sec. 1.3. Estos comprenden los estudios numéricos y los desarrollos de código relacionados con: (*i*) la extracción y focalización de haces de iones a través de las rejillas de un motor GIT, con EP2PLUS; (*ii*) la descarga de plasma en propulsores HET avanzados con topologías de apantallamiento magnético y cátodos centrales, con el código HYPHEN; y (*iii*) la descarga de plasma de un HET operado con productos de la electrólisis de agua o con vapor de agua, con PlasmaSim.

En cuanto a la primera tarea, las simulaciones con EP2PLUS del proceso de extracción, focalización y neutralización del haz de iones a través de las rejillas de un motor iónico, las principales contribuciones son:

- La adaptación de EP2PLUS para el modelado del escenario de la óptica de iones. Esto incluye: (*i*) la capacidad de considerar más de una población de electrones, (*ii*) un algoritmo para el control activo de la separación entre poblaciones de electrones en un escenario de óptica de iones, basado en el perfil de potencial eléctrico, (*iii*) un nuevo tipo de superficie para la reflexión especular de macropartículas para simular la interacción simétrica de sub-haces de iones provienents de las diferentes aperturas de la rejilla, y (*iv*) la consideración de la inercia en el ecuación del momento de electrones. Además, se han desarrollado algoritmos específicos para la generación de la geometría de las rejilla de un motor iónico.

- La aplicación con éxito de dos configuraciones diferentes a la simulación de escenarios de óptica de iones con EP2PLUS. La primera configuración, la de aperturas infinitas, con un conjunto periódico de agujeros, se puede utilizar para la estimación de la perveancia óptima (en términos de ángulo de divergencia) de la rejilla, con un pequeño coste computacional. La segunda configuración, la de un número finito de aperturas, con una rejilla completa de 19 agujeros pero con un coste computacional significativamente mayor, permite caracterizar el proceso de coalescencia de los sub-haces en un único haz, así como el proceso de neutralización de la corriente eléctrica y su dependencia con respecto a la posición del cátodo externo. Ambas configuraciones han sido parcialmente validadas frente a resultados experimentales y un modelo original semi-analítico 1D para la expansión del chorro de plasma.

- Las conclusiones relativas al proceso de neutralización de carga y de corriente. Se ha observado que la neutralización de corriente de los sub-haces de iones se ve fuertemente afectada por la posición del cátodo neutralizador; mientras que el proceso de neutralización de carga y, por tanto, la expansión y coalescencia de los sub-haces de iones, es independiente de la ubicación del cátodo, siempre que éste se encuentre lo suficientemente alejado de las rejillas como para no perturbar la extracción.

En cuanto a la segunda tarea, el modelado con HYPHEN de prototipos avanzados de HET, las principales contribuciones son:

- La mejora de HYPHEN para permitir el modelado de HETs con apantallamiento magnético y cátodos centrales. Los principales desarrollos del código han sido los siguientes (*i*) La mejora de las condiciones de contorno para incluir superficies de contorno metálicas como fuente de corriente de electrones, es decir, cátodos de superficie. Tanto las macropartículas de neutros como las de iones pueden inyectarse desde este nuevo tipo de superficie, lo que permite un modelado más fiel de los cátodos centrales. Se ha comprobado que la inyección de neutros desde la superficie del cátodo reduce el ruido numérico local en la solución de las ecuaciones del fluido de electrones. (*ii*) La generación de mallas MFAM no estructuradas para topologías MS con puntos singulares dentro de la cámara del propulsor. (*iii*) La capacidad de definir *inputs* de control, i.e. la tensión de descarga y el gasto másico, que cambien con el tiempo de una forma dada. Esta nueva característica permite la simulación de escenarios de *direct drive* y estudios de modulación. También se ha incluido la capacidad de considerar un filtro RLC entre el cátodo y el ánodo.

- La aplicación con éxito de un modelo fenomenológico del transporte anómalo de electrones, alimentado con datos experimentales, a la simulación de las descargas de los propulsores HT5k y HT20k. El modelo, que depende sólo de dos parámetros desconocidos α_{t1} y α_{t2}, se ha ajustado para que coincida con los datos experimentales de I_d y F para cada punto de operación. A pesar de no ser un objetivo del proceso de ajuste del modelo de transporte anómalo, las oscilaciones de baja frecuencia obtenidas para la corriente de descarga concuerdan bien con los datos experimentales.

- La caracterización numérica completa 2D promediada en el tiempo de las descargas de plasma del HT5k y HT20k, con xenón como propulsante. Se ha demostrado la efectividad del apantallamiento magnético en estos propulsores. Además, se ha observado que la topología de apantallamiento magnético desplaza la región de aceleración hacia el exterior, con respecto a una topología convencional, manteniendo un plasma de relativa alta densidad y baja temperatura en el interior de la cámara del motor. La baja temperatura del plasma alrededor de las paredes de la cámara consigue una reducida deposición de energía del plasma y pequeñas energías de impacto de iones, por debajo del umbral de *sputtering*. Se ha observado que esta combinación de alta densidad de plasma y baja temperatura de electrones da lugar a corrientes de plasma hacia las paredes similares a las de los HET convencionales.

- La caracterización numérica 2D promediada en el tiempo de la descarga de plasma del HT20k, con kriptón como propulsante; y la comparación con la descarga de xenón, en términos de rendimiento y propiedades locales del plasma. Aunque menos que con Xe, se ha demostrado que el blindaje magnético sigue siendo eficaz con Kr. El motor HT20k muestra una diferencia de eficiencia global relativamente pequeña entre las operaciones con Xe y Kr. Esto se explica, en parte, por la alta eficiencia de utilización de propulsante de Kr (aunque menor que la de Xe) en el HT20k, según se desprende de las simulaciones. Se ha demostrado que las regiones de ionización y aceleración se extienden más hacia afuera de la cámara en los puntos de operación con Kr, en comparación con los de Xe. Por lo tanto, los casos de Kr presentan una mayor divergencia y dispersión de la velocidad por especies en la pluma. La eficiencia de voltage ha sido hallada menor con Kr, debido principalmente a un peor acoplamiento eléctrico cátodo-pluma. La eficiencia de corriente, en línea con los datos experimentales, se ha observado más alta para Kr que para Xe. Lo mismo ocurre con la eficiencia de carga. Aunque la mayoría de las observaciones anteriores concuerdan con resultados previos en otros motores, se han detectado algunos diferencias, lo que demuestra la sensibilidad del análisis con respecto al diseño y configuración del propulsor.

- La caracterización con resolución temporal de la respuesta dinámica del propulsor HT5k sometido a una modulación sinusoidal del voltaje de descarga. Se ha comprobado que el modo modulado de baja frecuencia de la descarga oscila con la frecuencia de la modulación, siempre que ésta sea suficientemente próxima a la del modo natural o *breathing mode*. A frecuencias de modulación relativamente grandes, el modo natural de la descarga ha reaparecido en las simulaciones, demostrando la pérdida parcial del control sobre la descarga de la modulación. La similitud cualitativa de los resultados de la simulación con estudios previos de modulación de diferentes tipos de propulsores ExB ha llevado a la conclusión de que el mismo fenómeno fundamental determina la respuesta modulada en los diferentes diseños: el modo natural o *breathing mode* controlado mediante oscilaciones de la temperatura de los electrones, a su vez controlada por el voltage de descarga.

- La conclusión de que las ganancias de eficiencia conseguidas con la modulación del voltaje son limitadas en el propulsor HT5k. Esto es consecuencia del acoplamiento entre la producción de plasma y los procesos de aceleración inherente al funcionamiento de los propulsores de efecto Hall. Sin embargo, el control efectivo que la modulación de voltaje ejerce sobre las oscilaciones de descarga de baja frecuencia puede ser útil para la mitigación de EMI y el diagnóstico de descargas de plasmas.

- La aplicación de la técnica *data-driven* HODMD al análisis de la compleja estructura espacio-temporal de la descarga de plasma modulada del HT5k. Esto ha confirmado la naturaleza de tipo *breathing mode* de los modos modulados y ha permitido identificar la naturaleza estacionaria o viajera de las ondas de las diferentes propiedades del plasma. Se ha observado que la recombinación de iones en las paredes da lugar a una onda 1D aparente de densidad de neutros con velocidad de fase axial 5-6 veces mayor que la velocidad fluida de los neutros.

En cuanto a la tercera tarea, el modelado de un HET alimentado con agua, las principales contribuciones son:

- La actualización de la versión axial-radial de PlasmaSim para la simulación del propulsor WET-HET alimentado por agua. Esto incluye: (*i*) la paralelización de la mayoría de las subrutinas del código, (*ii*) la mejora de la condición de cuasineutralidad en la superficie del cátodo y la adición de dos modelos de emisión de electrones secundarios para las paredes dieléctricas (*iii*) la implementación de la versión actualizada de la formulación cuasi-2D para la solución de la ecuación de Poisson y (*iv*) la adición a PlasmaSim de las nuevas especies O_2 y H_2O y sus respectivas interacciones con otras especies y con los contornos del dominio.

- La realización con éxito de una simulación preliminar de una descarga del motor WET-HET, alimentado con O_2. La formulación cuasi-2D de PlasmaSim ha permitido obtener resultados bidimensionales (axial-radial) con resolución temporal, que se extienden el tiempo característico de un *breathing mode* con un esfuerzo computacional significativamente reducido en comparación con los códigos de simulación 2D del estado del arte. Los perfiles de plasma obtenidos se han encontrado en línea con los resultados experimentales y numéricos de la literatura, evidenciando principalmente la importancia de las pérdidas de energía por disociación y excitación atómica en las descargas HET con O_2 como propulsante.

7.2 Trabajo futuro

Para describir las futuras líneas de investigación relacionadas con el trabajo de esta Tesis, es conveniente presentarlas organizadas en objetivos o tareas de investigación. El primer grupo de futuras líneas de trabajo, correspondiente al análisis numérico de la óptica de iones con EP2PLUS, incluye:

- Avances en el modelado y algoritmia del código EP2PLUS. Algunos de los posibles desarrollos futuros son: (*i*) la habilitación del acoplamiento entre las simulaciones de cámara de ionización y las de óptica de iones y (*ii*) la implementación de un sistema de coordenadas cilíndricas que facilite el modelado de agujeros circulares y patrones de apertura radialmente simétricos en las mallas.

- La simulación de la óptica de iones acoplada a simulaciones de cámaras de ionización. En el escenario de la cámara de ionización, la rejilla se modelaría como una superficie infinitamente delgada con una transparencia para neutros y para iones determinada. La retroalimentación continua entre ambos tipos de escenarios sería de la siguiente manera: por un lado, las simulaciones de óptica de iones proporcionarían la transparencia real actualizada de la rejilla al escenario de la cámara de ionización; por otro lado, la simulación de la cámara informaría al escenario de óptica de iones sobre la distribución actualizada de los flujos de iones hacia la rejilla.

- El estudio numérico del límite real en la capacidad de extracción de corriente de los sistemas ópticos de motores iónicos [323], y su comparación con el límite teórico de la corriente limitada por la carga espacial siguiendo la ley de Child [3].

El segundo grupo de futuras líneas de trabajo, correspondiente al modelado de HETs avanzados con HYPHEN, incluye:

- Avances en el modelado y algoritmia del código HYPHEN. Algunos de los posibles desarrollos futuros son: (i) la implementación de una subrutina para la resolución de la ecuación de Poisson, para una mayor fidelidad del modelado de las regiones de baja densidad de plasma de la descarga, donde puede existir no neutralidad, (ii) la adaptación de la algoritmia del módulo de electrones para su uso en mallas rectangulares, dando al usuario la posibilidad de elegir entre una malla alineada con el campo magnético y una rectangular y (iii) permitir el uso de materiales metálicos/conductores para las paredes laterales de la cámara del motor.

- La aplicación de perfiles espaciales más complejos a la función del parámetro de transporte anómalo, $\alpha(z, r)$, usando propiedades locales del plasma, medidas experimentalmente, como objetivos del proceso de ajuste del transporte turbulento [77].

- El análisis numérico de HETs apantallados magnéticamente con paredes conductoras [162] y la comparación con HETs con paredes dieléctricas, en términos de rendimiento, propiedades locales del plasma y deposición de energía en las paredes [163]. Dado que el apantallamiento magnético reduce significativamente la interacción plasma-pared, es posible cambiar paredes dieléctricas por metálicas en un HET, con una mejora asociada en las propiedades mecánicas y térmicas del motor.

- El estudio numérico sobre el impacto en el rendimiento del uso de diferentes configuraciones alternativas para la inyección de propulsante, tales como la “alimentación invertida” o la “alimentación rotativa” [324–326]. La necesidad de aumentar la eficiencia de utilización del propulsante en la operación de un HET con propulsantes alternativos justifica la realización de este estudio.

El tercer grupo de futuras líneas de trabajo, correspondiente al análisis numérico del propulsor WET-HET operado con agua como propulsante, incluye:

- La mejora de la versión axial-radial del código PlasmaSim. Algunos de los posibles desarrollos futuros son: (i) la implementación de un sistema de coordenadas cilíndricas que modele correctamente la curvatura de la geometría anular HET y (ii) el acoplamiento de las direcciones axial y radial con la azimutal para la resolución autoconsistente del transporte anómalo [116].

- La caracterización completa 2D promediada en el tiempo de la descarga de plasma del WET-HET con productos de electrólisis de agua y vapor de agua. Esto incluye el análisis de las principales fuentes de ineficiencias, la comparación de las propiedades locales del plasma con las de las descargas de Xe, la sugerencia de mejoras para una operación más eficiente con agua (es decir, modificaciones geométricas u operativas), y la comparación con resultados experimentales [321].

- La caracterización, con resolución temporal, de la operación del motor WET-HET con agua como propulsante. El análisis se centraría en las oscilaciones de baja frecuencia de la descarga, la dinámica de las diferentes especies y cómo se comporta el *breathing mode* en una descarga con propulsantes moleculares.

Bibliography

[1] M. Winzierl, "Space, the final economic frontier," *Journal of Economic Perspectives*, vol. 32, no. 2, pp. 173–192, 2018.

[2] M. Martínez-Sánchez and J. Pollard, "Spacecraft electric propulsion — an overview," *Journal of Propulsion and Power*, vol. 14, no. 5, pp. 688–699, Sep. 1998.

[3] D. Goebel and I. Katz, *Fundamentals of Electric Propulsion: Ion and Hall Thrusters*. Jet Propulsion Laboratory, Pasadena, CA, 2008.

[4] E. Ahedo, "Plasmas for space propulsion," *Plasma Physics and Controlled Fusion*, vol. 53, no. 12, p. 124037, 2011. [Online]. Available: http://stacks.iop.org/0741-3335/53/i=12/a=124037

[5] S. Mazouffre, "Electric propulsion for satellites and spacecraft: established technologies and novel approaches," *Plasma Sources Science and Technology*, vol. 25, no. 3, p. 033002, 2016.

[6] J. Szabo, "Explosive growth in electric propulsion," *Aerospace America*, vol. 57, no. 11, pp. 46–46, 2019.

[7] M. Ansede, "All-electric propulsion satellites," https://www.airbus.com/en/newsroom/news/2017-06-all-electric-propulsion-satellites/, [Online; accessed 13-February-2024].

[8] J. Autric, P. Escourrou, and I. Laine, "Telecom spacecraft mission design : Electric orbit raising for airbus communications satellites," in *2018 SpaceOps Conference*, ser. AIAA 2018-2601. Marseille, France, May 28-June 1: AIAA, 2018.

[9] S. Feuerborn, D. Neary, and J. Perkins, "Finding a way: Boeing's all electric propulsion satellite," in *49th Joint Propulsion Conference, San Jose, CA*, ser. AIAA 2013-4126, 2013.

[10] K. Holste, P. Dietz, S. Scharmann, K. Keil, T. Henning, D. Zschätzsch, M. Reitemeyer, B. Nauschütt, F. Kiefer, F. Kunze *et al.*, "Ion thrusters for electric propulsion: Scientific issues developing a niche technology into a game changer," *Review of Scientific Instruments*, vol. 91, no. 6, p. 061101, 2020.

[11] C. Koppel and D. Estublier, "The SMART-1 Hall effect thruster around the moon: In flight experience," in *29th International Electric Propulsion Conference*, 2005.

[12] H. Kuninaka, K. Nishiyama, I. Funaki, T. Yamada, Y. Shimizu, and J. Kawaguchi, "Powered flight of electron cyclotron resonance ion engines on hayabusa explorer," *Journal of Propulsion and Power*, vol. 23, no. 3, pp. 544–551, 2007.

[13] O. Sutherland, D. Stramaccioni, J. Benkhoff, N. Wallace, D. Feili, A. Rocchi, and R. Jehn, "BepiColombo: ESA's interplanetary electric propulsion mission to Mercury," in *36th International Electric Propulsion Conference, Vienna, Austria*, 2019, pp. IEPC–2019–274.

[14] J. Cassady, B. Boyce, B. Kearney, D. Herman, and P. Peterson, "Development of 12 kW Hall thrusters for NASA lunar gateway power and propulsion element," in *8th Space Propulsion Conference, Estoril, Portugal*, ser. SP2022-438, 2022.

[15] A. Sasoh and Y. Arakawa, "Electromagnetic effects in an applied-field magnetoplasmadynamic thruster," *Journal of Propulsion and Power*, vol. 8, no. 1, pp. 98–102, 1992.

[16] R. Myers, "Geometric scaling of applied-field magnetoplasmadynamic thrusters," *Journal of Propulsion and Power*, vol. 11, no. 2, 1995.

[17] P. G. Mikellides and P. J. Turchi, "A theoretical model for the thrust and voltage of applied-field MPD thrusters," in *31st AIAA/ASME/SAE/ASEE Joint Propulsion Conference and Exhibit*, 1995, pp. AlAA 95–2676.

[18] H. Kaufman, "An ion rocket with an electron-bombardment ion source," National Aeronautics and Space Administration. Lewis Research Center, Cleveland, Tech. Rep., 1961.

[19] H. Bassner, R. Killinger, H. Leiter, and J. Müller, "Development steps of the RF-ion thrusters RIT," in *27th International Electric Propulsion Conference*, ser. paper 2001-105. Pasadena, California, October 15-19: Electric Rocket Propulsion Society, Fairview Park, OH, 2001.

[20] J. Brophy and P. Wilbur, "Simple performance model for ring and line cusp ion thrusters," *AIAA journal*, vol. 23, no. 11, pp. 1731–1736, 1985.

[21] D. Fearn, "The application of gridded ion thrusters to high thrust, high specific impulse nuclear-electric missions," *Journal of the British Interplanetary Society*, vol. 58, pp. 257–267, 2005.

[22] A. Morozov and V. Savelyev, "Fundamentals of stationary plasma thruster theory," in *Reviews of Plasma Physics, Vol. 21.* New York: Kluwer Academic, 2000.

[23] J. Sankovic, T. Haag, and D. Manzella, "Operating characteristics of the russian D-55 thruster with anode layer," in *30th Joint Propulsion Conference, Indianapolis, IN*, ser. AIAA 94-3011, 1994.

[24] H. Kaufman, "Technology of closed-drift thrusters," *AIAA Journal*, vol. 23, pp. 78–87, 1985.

[25] V. Kim, "Main physical features and processes determining the performance of stationary plasma thrusters," *J. Propulsion Power*, vol. 14, no. 5, pp. 736–743, 1998.

[26] R. Jahn, *Physics of Electric Propulsion.* Dover, 2006.

[27] M. Auweter-Kurtz, T. Gölz, H. Habiger, F. Hammer, H. Kurtz, M. Riehle, and C. Sleziona, "High-power hydrogen arcjet thrusters," *Journal of Propulsion and Power*, vol. 14, no. 5, pp. 764–773, 1998.

[28] F. Chen, "Plasma ionization by helicon waves," *Plasma Physics and Controlled Fusion*, vol. 33, no. 4, p. 339, 1991.

[29] R. Boswell and F. Chen, "Helicons-the early years," *IEEE Transactions on Plasma Science*, vol. 25, pp. 1229–1244, 1997.

[30] K. Takahashi, C. Charles, R. Boswell, W. Cox, and R. Hatakeyama, "Transport of energetic electrons in a magnetically expanding helicon double layer plasma," *Applied Physics Letters*, vol. 94, no. 19, p. 191503, 2009.

[31] E. Ahedo and J. Navarro-Cavallé, "Helicon thruster plasma modeling: Two-dimensional fluid-dynamics and propulsive performances," *Physics of Plasmas*, vol. 20, no. 4, p. 043512, 2013.

[32] T. Lafleur and A. Aanesland, "Ambipolar and non-ambipolar diffusion in an RF plasma source containing a magnetic filter," *Physics of Plasmas*, vol. 21, no. 6, p. 063510, 2014.

[33] J. Navarro-Cavallé, M. Wijnen, P. Fajardo, and E. Ahedo, "Experimental characterization of a 1 kw helicon plasma thruster," *Vacuum*, vol. 149, pp. 69–73, 2018.

[34] G. Bethke and D. Miller, "Cyclotron resonance thruster design techniques." *AIAA Journal*, vol. 4, no. 5, pp. 835–840, 1966.

[35] M. Lampe, G. Joyce, W. Manheimer, and S. Slinker, "Quasi-neutral particle simulation of magnetized plasma discharges: General formalism and application to ecr discharges," *IEEE Transactions on Plasma Science*, vol. 26, pp. 1592–1609, 1998.

[36] H. Kuninaka and S. Satori, "Development and demonstration of a cathodeless electron cyclotron resonance ion thruster," *Journal of Propulsion and Power*, vol. 14, no. 6, pp. 1022–1026, 1998.

[37] M. Gamero-Castaño and V. Hruby, "Electrospray as a source of nanoparticles for efficient colloid thrusters," *Journal of Propulsion and Power*, vol. 17, no. 5, pp. 977–987, 2001.

[38] J. Carretero and M. Martínez-Sánchez, "Numerical simulation of a colloidal thruster in the droplet regime," *Computer physics communications*, vol. 164, no. 1, pp. 202–208, 2004.

[39] P. Lozano, M. Martínez-Sánchez, and J. Lopez-Urdiales, "Electrospray emission from nonwetting flat dielectric surfaces," *Journal of colloid and interface science*, vol. 276, no. 2, pp. 392–399, 2004.

[40] J. Mitterauer, "Field emission electric propulsion: Emission site distribution of slit emitters," *Plasma Science, IEEE Transactions on*, vol. 15, no. 5, pp. 593–598, 1987.

[41] S. Marcuccio, A. Genovese, and M. Andrenucci, "Experimental performance of fiels emission microthrusters," *J. Propulsion and Power*, vol. 14, pp. 774–781, 1998.

[42] A. Solbes, K. Thomassen, and R. Vondra, "Analysis of solid teflon pulsed plasma thruster," *Journal of Spacecraft and Rockets*, vol. 7, no. 12, pp. 1402–1406, 1970.

[43] N. A. Gatsonis, R. Eckman, X. Yin, E. J. Pencil, and R. M. Myers, "Experimental investigations and numerical modeling of pulsed plasma thruster plumes," *Journal of Spacecraft and Rockets*, vol. 38, no. 3, pp. 454–464, 2001.

[44] H. Koizumi, R. Noji, K. Komurasaki, and Y. Arakawa, "Plasma acceleration processes in an ablative pulsed plasma thruster," *Physics of Plasmas*, vol. 14, no. 3, 2007.

[45] S. Barquero, M. Merino, and J. Navarro-Cavallé, "Experimental plume characterization of a low-power ablative pulsed plasma thruster (APPT)," in 37^{th} *International Electric Propulsion Conference*, no. IEPC-2022-556. Boston, MA, June 19-23: Electric Rocket Propulsion Society, 2022.

[46] J. Sovey, V. Rawling, and M. Patterson, "Ion propulsion development projects in U.S.: Space electric rocket test I to Deep Space 1," *Journal of propulsion and power*, vol. 17, p. 517–526, 2001.

[47] V. Kim, G. Popov, B. Arkhipov, V. Murashko, O. Gorshkov, A. Koroteyev, V. Garkusha, A. Semenkin, and S. Tverdokhlebov, "Electric propulsion activity in russia," in *27th International Electric Propulsion Conference, Pasadena, CA, USA*, ser. IEPC 01-05, 2001.

[48] I. Levchenko, K. Bazaka, Y. Ding, Y. Raitses, S. Mazouffre, T. Henning, P. J. Klar, S. Shinohara, J. Schein, L. Garrigues, M. Kim, D. Lev, F. Taccogna, R. W. Boswell, C. Charles, H. Koizumi, Y. Shen, C. Scharlemann, M. Keidar, and S. Xu, "Space micropropulsion systems for Cubesats and small satellites: From proximate targets to furthermost frontiers," *Applied Physics Reviews*, vol. 5, no. 1, p. 011104, 02 2018. [Online]. Available: https://doi.org/10.1063/1.5007734

[49] M. Armano and et al., "The LISA Pathfinder mission," *Journal of Physics: Conference Series*, vol. 610, p. 012005, 2015.

[50] S. Bathgate, M. Bilek, and D. Mckenzie, "Electrodeless plasma thrusters for spacecraft: a review," *Plasma Science and Technology*, vol. 19, no. 8, p. 083001, 2017.

[51] M. Patterson, S. Grisnik, and G. Soulas, “Scaling of ion thrusters to low power,” in *25th International Electric Propulsion Conference, Cleveland, OH*, ser. IEPC 97-098, 1997.

[52] A. Smirnov, Y. Raitses, and N. Fisch, “Experimental and theoretical studies of cylindrical Hall thrusters,” *Physics of Plasmas*, vol. 14, no. 5, p. 057106, 2007.

[53] K. Dannenmayer and S. Mazouffre, “Elementary scaling relations for Hall effect thrusters,” *Journal of Propulsion and Power*, vol. 27, no. 1, 2011.

[54] G. Giammarinaro, F. Marconcini, G. Becatti, M. Saravia, M. Andrenucci, and F. Paganucci, “A scaling methodology for high-power magnetically shielded Hall thrusters,” *Journal of Electric Propulsion*, vol. 2, 2023.

[55] J. Hamley, “Direct drive options for electric propulsion systems,” *IEEE Aerospace and Electronic Systems Magazine*, vol. 11, no. 2, pp. 20–24, 1996.

[56] M. Reza, F. Faraji, and T. Andreussi, “Characterization of a high-power hall thruster operation in direct-drive,” *Acta Astronautica*, vol. 178, pp. 392–405, 2021.

[57] R. Wirz, J. Anderson, D. M. Goebel, and I. J. Katz, “Decel grid effects on ion thruster grid erosion,” *IEEE Transactions on Plasma Science*, vol. 36, no. 5, pp. 2122–2129, 2008.

[58] S. Mazouffre, F. Dubois, L. Albarede, D. Pagnon, M. Touzeau, and M. Dudeck, “Plasma induced erosion phenomena in a Hall thruster,” in *Recent Advances in Space Technologies, 2003. RAST’03. International Conference on. Proceedings of*, IEEE, Ed., 2003, pp. 69–74.

[59] I. Mikellides, I. Katz, R. Hofer, D. Goebel, K. de Grys, and A. Mathers, “Magnetic shielding of the channel walls in a Hall plasma accelerator,” *Physics of Plasmas*, vol. 18, p. 033501, 2011.

[60] D. Rafalskyi, J. Martínez-Martínez, L. Habl, E. Zorzoli-Rossi, P. Proynov, A. Boré, T. Baret, A. Poyet, T. Lafleur, S. Dudin, and A. Aanesland, “In-orbit demonstration of an iodine electric propulsion system,” *Nature*, vol. 599, pp. 411–415, 2021.

[61] J. Yamasaki, S. Yokota and K. Shimamura, “Performance enhancement of an argon-based propellant in a hall thruster,” *Vacuum*, vol. 167, pp. 520–523, 2019.

[62] M.A. Hopkins and L.B. King, “Performance comparison between a magnesium-and xenon-fueled 2 kilowatt hall thruster,” *Journal of Propulsion and Power*, vol. 32, no. 4, pp. 1015–1021, 2016.

[63] J.M. Makela, R.L. Washeleski, D.R. Massey, L.B. King, and M.A. Hopkins, “Development of a magnesium and zinc Hall-effect thruster,” *Journal of Propulsion and Power*, vol. 26, no. 5, pp. 1029–1035, 2010.

[64] M.A. Bretti, "Progress and developments of ultra-compact 10 watt class adamantane fueled hall thrusters for picosatellites," in *37th International Electric Propulsion Conference, IEPC-2022-349, Massachusetts Institute of Technology, Cambridge, MA, USA*, 2022.

[65] J. Szabo, M. Robin and V. Hruby, "Bismuth vapor hall effect thruster performance and plume experiments," in *35th International Electric Propulsion Conference, IEPC-2017-25, Georgia Institute of Technology, Georgia, USA*, 2019.

[66] A.C. Scharlemann, "Theoretical and experimental investigation of C60-propellant for ion propulsion," *Acta Astronautica*, vol. 51, no. 12, pp. 865–872, 2002.

[67] J. Tejeda, M. Reza, F. Faraji, and A. Knoll, "Performance enhancement of hall effect thruster using radiofrequency excitation," *Acta Astronautica*, vol. 194, pp. 145–161, 2022.

[68] T. Kokan and C. Russell Joyner, "Mission comparison of Hall effect and gridded ion thruster utilizing various propellant options," in *AIAA SPACE Conference and Exposition, Pasadena, CA*, ser. AIAA 2012-5237, 2012.

[69] R. Hofer and S. Arestie, "Performance of a conducting wall, magnetically shielded hall thruster at 3000s specific impulse," in *37th International Electric Propulsion Conference*, ser. IEPC-2022-401, 2022.

[70] K. Hara, "An overview of discharge plasma modeling for Hall effect thrusters," *Plasma Sources Science and Technology*, vol. 28, no. 4, p. 044001, 2019.

[71] F. Taccogna and L. Garrigues, "Latest progress in Hall thrusters plasma modelling," *Reviews of Modern Plasma Physics*, vol. 3, no. 1, p. 12, 2019.

[72] F. Taccogna, F. Cichocki, D. Eremin, G. Fubiani, and L. Garrigues, "Plasma propulsion modeling with particle-based algorithms," *Journal of Applied Physics*, vol. 134, no. 15, p. 150901, 10 2023. [Online]. Available: https://doi.org/10.1063/5.0153862

[73] M. Merino, F. Cichocki, and E. Ahedo, "A collisionless plasma thruster plume expansion model," *Plasma Sources Science and Technology*, vol. 24, no. 3, p. 035006, 2015.

[74] I. Mikellides and I. Katz, "Numerical simulations of Hall-effect plasma accelerators on a magnetic-field-aligned mesh," *Physical Review E*, vol. 86, no. 4, p. 046703, 2012.

[75] I. G. Mikellides, B. Jorns, I. Katz, and A. Lopez Ortega, "Hall2De simulations with a first-principles electron transport model based on the electron cyclotron drift instability," in *52nd AIAA/SAE/ASEE Joint Propulsion Conference*, 2016, p. 4618.

[76] A. Ortega, I. Katz, I. Mikellides, and D. Goebel, "Self-consistent model of a high-power Hall thruster plume," *IEEE Transactions on Plasma Science*, vol. 43, no. 9, pp. 2875–2886, 2015.

[77] I. G. Mikellides and A. Lopez Ortega, "Challenges in the development and verification of first-principles models in Hall-effect thruster simulations that are based on anomalous resistivity and generalized Ohm's law," *Plasma Sources Science and Technology*, vol. 28, p. 014003, 2019.

[78] E. Ahedo, "Using electron fluid models to analyze plasma thruster discharges," *Journal of Electric Propulsion*, vol. 2, no. 1, p. 2, 2023.

[79] T. Andreussi, V. Giannetti, A. Leporini, M. M. Saravia, and M. Andrenucci, "Influence of the magnetic field configuration on the plasma flow in Hall thrusters," *Plasma Phys. Control. Fusion*, vol. 60, no. 1, 2018.

[80] R. Hockney and J. Eastwood, *Computer simulation using particles.* CRC Press, Boca Ratón, FL, 1988.

[81] C. Birdsall and A. Langdon, *Plasma Physics via Computer Simulation.* Bristol: Institute of Physics Publishing, 1991.

[82] D. Sydorenko, A. Smolyakov, I. Kaganovich, and Y. Raitses, "Modification of electron velocity distribution in bounded plasmas by secondary electron emission," *Plasma Science, IEEE Transactions on*, vol. 34, no. 3, pp. 815–824, 2006.

[83] I. Kaganovich, Y. Raitses, D. Sydorenko, and A. Smolyakov, "Kinetic effects in a Hall thruster discharge," *Physics of Plasmas*, vol. 14, p. 057104, 2007.

[84] F. Taccogna, S. Longo, M. Capitelli, and R. Schneider, "Particle-in-cell simulation of stationary plasma thruster," *Contributions to Plasma Physics*, vol. 47, no. 8-9, pp. 635–656, 2007.

[85] D. Tskhakaya, K. Matyash, R. Schneider, and F. Taccogna, "The particle-in-cell method," *Contributions to Plasma Physics*, vol. 47, no. 8-9, pp. 563–594, 2007.

[86] V. Croes, "Modélisation de la décharge plasma d'un propulseur à effet Hall," PhD Thesis, Université Paris-Saclay, École Polytechnique, 2017.

[87] A. Domínguez-Vázquez, F. Taccogna, and E. Ahedo, "Particle modeling of radial electron dynamics in a controlled discharge of a Hall thruster," *Plasma Sources Science and Technology*, vol. 27, no. 6, p. 064006, 2018.

[88] J. Szabo, "Fully kinetic numerical modeling of a plama thruster," Ph.D. dissertation, Massachusetts Institute of Technology, 2001.

[89] P. Coche and L. Garrigues, "A two-dimensional (azimuthal-axial) particle-in-cell model of a hall thruster," *Physics of Plasmas*, vol. 21, p. 023503, 2014.

[90] V. Kolobov and R. Arslanbekov, "Towards adaptive kinetic-fluid simulations of weakly ionized plasmas," *Journal of Computational Physics*, vol. 231, no. 3, pp. 839–869, 2012.

[91] K. Hara, I. D. Boyd, and V. I. Kolobov, "One-dimensional hybrid-direct kinetic simulation of the discharge plasma in a Hall thruster," *Physics of Plasmas*, vol. 19, no. 11, p. 113508, 2012.

[92] C. Cui and J. Wang, "Grid-based Vlasov simulation of collisionless plasma expansion," *Physics of Plasmas*, vol. 9, no. 28, p. 093510, 2021.

[93] J. M. Fife, "Hybrid-PIC modeling and electrostatic probe survey of Hall thrusters," Ph.D. dissertation, Massachusetts Institute of Technology, 1998.

[94] G. Hagelaar, J. Bareilles, L. Garrigues, and J. Boeuf, "Two-dimensional model of a stationary plasma thruster," *Journal of Applied Physics*, vol. 91, no. 9, pp. 5592–5598, 2002.

[95] M. Santi, "Hall thruster plume simulation using a hybrid-PIC algorithm," Ph.D. dissertation, Massachusetts Institute of Technology, Boston, MA, 2003.

[96] F. I. Parra, E. Ahedo, J. M. Fife, and M. Martínez-Sánchez, "A two-dimensional hybrid model of the Hall thruster discharge," *Journal of Applied Physics*, vol. 100, no. 2, p. 023304, 2006.

[97] D. Escobar and E. Ahedo, "Two-dimensional electron model for a hybrid code of a two-stage Hall thruster," *IEEE Transactions on Plasma Science*, vol. 36, pp. 2043–2057, 2008.

[98] F. Cichocki, "Analysis of the expansion of a plasma thruster plume into vacuum," Ph.D. dissertation, Universidad Carlos III de Madrid, Leganés, Spain, 2017.

[99] A. Domínguez-Vázquez, "Axisymmetric simulation codes for hall effect thrusters and plasma plumes," Ph.D. dissertation, Universidad Carlos III de Madrid, Leganés, Spain, 2019.

[100] F. Cichocki, A. Domínguez-Vázquez, M. Merino, and E. Ahedo, "Hybrid 3D model for the interaction of plasma thruster plumes with nearby objects," *Plasma Sources Science and Technology*, vol. 26, no. 12, p. 125008, 2017.

[101] F. Cichocki, M. Merino, and E. Ahedo, "Spacecraft-plasma-debris interaction in an ion beam shepherd mission," *Acta Astronautica*, vol. 146, pp. 216–227, 2018.

[102] A. Modesti, F. Cichocki, J. Zhou, and E. Ahedo, "A 3D electron fluid model with energy balance for plasma plumes," in *IEPC 2022*, Boston, Massachusetts, United States, June 19-23, 2022.

[103] F. Cichocki, M. Merino, and E. Ahedo, "Three-dimensional geomagnetic field effects on a plasma thruster plume expansion," *Acta Astronautica*, vol. 175, pp. 190 – 203, 2020.

[104] F. Cichocki, A. Domínguez-Vázquez, M. Merino, P. Fajardo, and E. Ahedo, "Three-dimensional neutralizer effects on a Hall-effect thruster near plume," *Acta Astronautica*, vol. 187, pp. 498–510, 2021.

[105] A. Domínguez-Vázquez, J. Zhou, P. Fajardo, and E. Ahedo, "Analysis of the plasma discharge in a Hall thruster via a hybrid 2D code," in 36^{th} *International Electric Propulsion Conference*, no. IEPC-2019-579. Vienna, Austria: Electric Rocket Propulsion Society, 2019.

[106] D. Pérez-Grande, "Fluid modeling and simulation of the electron population in hall effect thrusters with complex magnetic topologies," Ph.D. dissertation, Universidad Carlos III de Madrid, Leganés, Spain, 2018.

[107] J. Zhou, "Modeling and simulation of the plasma discharge in a radiofrequency thruster," Ph.D. dissertation, Universidad Carlos III de Madrid, Leganés, Spain, 2021.

[108] D. Pérez-Grande, O. González-Martínez, P. Fajardo, and E. Ahedo, "Analysis of the numerical diffusion in anisotropic mediums: benchmarks for magnetic field aligned meshes in space propulsion simulations," *Applied Sciences*, vol. 6, no. 11, p. 354, 2016.

[109] A. Sánchez-Villar, J. Zhou, M. Merino, and E. Ahedo, "Coupled plasma transport and electromagnetic wave simulation of an ECR thruster," *Plasma Sources Science and Technology*, vol. 30, no. 4, p. 045005, 2021.

[110] J. Zhou, A. Domínguez-Vázquez, P. Fajardo, and E. Ahedo, "Magnetized fluid electron model within a two-dimensional hybrid simulation code for electrodeless plasma thrusters," *Plasma Sources Science and Technology*, vol. 31, no. 4, p. 045021, 2022.

[111] P. Jiménez, M. Merino, and E. Ahedo, "Wave propagation and absorption in a helicon plasma thruster source and its plume," *Plasma Sources Science and Technology*, vol. 31, no. 4, p. 045009, 2022.

[112] A. Sánchez-Villar, F. Boni, V. Désangles, J. Jarrige, D. Packan, E. Ahedo, and M. Merino, "Comparison of a hybrid model and experimental measurements for a dielectric-coated coaxial ECR thruster," *Plasma Sources Science and Technology*, vol. 32, no. 1, p. 014002, 2023.

[113] A. Domínguez-Vázquez, D. Pérez-Grande, P. Fajardo, and E. Ahedo, "Nomads: Development of a versatile plasma discharge simulation platform for electric propulsion," in *Space Propulsion Conference 2016*, no. paper 2016-3124869. Rome, Italy, May 2-6: Association Aéronautique et Astronautique de France, 2016.

[114] A. Domínguez-Vázquez, F. Cichocki, M. Merino, P. Fajardo, and E. Ahedo, "2D and 3D hybrid PIC/fluid modelling of electric thruster plumes," in 35^{th} *International Electric Propulsion Conference*, no. IEPC-2017-209. Atlanta, GA: Electric Rocket Propulsion Society, 2017.

[115] ——, "Axisymmetric plasma plume characterization with 2D and 3D particle codes," *Plasma Sources Science and Technology*, vol. 27, no. 10, p. 104009, 2018.

[116] F. Faraji, M. Reza, and A. Knoll, "Enhancing one-dimensional particle-in-cell simulations to self-consistently resolve instability-induced electron transport in Hall thrusters," *Journal of Applied Physics*, vol. 131, p. 193302, 2022.

[117] M. Reza, F. Faraji, and A. Knoll, "Influence of the magnetic field's curvature on the radial-azimuthal dynamics of a hall thruster plasma discharge with different propellants," *arXiv preprint arXiv:2309.00565*, 2023.

[118] ——, "Concept of the generalized reduced-order particle-in-cell scheme and verification in an axial-azimuthal Hall thruster configuration," *Journal of Physics D: Applied Physics*, vol. 56, no. 17, p. 18, 2023.

[119] F. Faraji, M. Reza, A. Knoll, and J. Kutz, "Dynamic mode decomposition fordata-driven analysis and reduced-ordermodeling of E x B plasmas: II. Dynamics forecasting," *Journal of Physics D: Applied Physics*, vol. 57, no. 6, 2023.

[120] Epic Games, "Unreal engine," https://www.unrealengine.com/, [Online; accessed 20-July-2021].

[121] J. Perales-Díaz, F. Cichocki, M. Merino, and E. Ahedo, "Formation and neutralization of electric charge and current of an ion thruster plume," *Plasma Sources Science and Technology*, vol. 30, no. 10, p. 105023, 2021.

[122] J. Perales-Díaz, A. Domínguez-Vázquez, P. Fajardo, E. Ahedo, F. Faraji, M. Reza, and T. Andreussi, "Hybrid plasma simulations of a magnetically shielded Hall thruster," *Journal of Applied Physics*, vol. 131, no. 10, p. 103302, 2022.

[123] J. Perales-Díaz, A. Domínguez-Vázquez, P. Fajardo, and E. Ahedo, "Simulations of driven breathing modes of a magnetically shielded Hall thruster," *Plasma Sources Science and Technology*, vol. 32, no. 7, p. 075011, 2023.

[124] D. M. Goebel and I. Katz, *Fundamentals of Electric Propulsion: Ion and Hall Thrusters*. JPL, 2008.

[125] R. Kafafy, "Immersed finite element particle-in-cell simulations of ion propulsion," Ph.D. dissertation, Virginia Polytechnic Instititute and State University, Blacksburg, VA, 2005.

[126] C. Farnell, J. Williams, and P. Wilbur, "Numerical simulation of an ion thruster optics," in *28th International Electric Propulsion Conference*, 2003.

[127] J. Anderson, I. Katz, and D. Goebel, "Numerical simulation of two-grid ion optics using a 3d code," in *40th AIAA/ASME/SAE/ASEE Joint Propulsion Conference and Exhibit*, ser. AIAA-2006-4834, 2004.

[128] T. Binder, M. Pfeiffer, s. Fasoulas, and H. Leiter, "High-fidelity particle-in-cell simulations of ion thruster optics," in *35th International Electric Propulsion Conference, Atlanta GA, USA*, ser. IEPC-2017-451, 2017.

[129] A. Lovtsov and D. Kravchenko, "Kinetic simulation of plasma in ion thruster discharge chamber. comparison with experimental data," in *6th Russian-German Conference on Electric Propulsion and Their Application*, 2016.

[130] M. Nakano, K. Nakamura, Y. Nakagawa, T. D., Y. Takao, and H. Koizumi, "Numerical simulation of full-aperture-pair ion optics in a miniature ion thruster," *Physics of Plasma*, vol. 25, no. 1, 2018.

[131] I. Katz, I. Mikellides, R. Wirz, J. Anderson, and D. Goebel, "Ion thruster life models," in *41st AIAA/ASME/SAE/ASEE Joint Propulsion Conference and Exhibit*, ser. AIAA 2005-4256, 2005.

[132] C. Farnell, J. Williams, and P. Wilbur, "Next ion optics simulations via ffx," in *39th Joint Propulsion Conference*, 2003.

[133] B. Korkut, Z. Li, and D. Levin, "3-D simulation of ion thruster plumes using octree adaptive mesh refinement," *IEEE Transactions on Plasma Science*, vol. 43, no. 5, pp. 1706–1721, 2015.

[134] Z. Lingwei, L. Yu, L. Juan, G. Zuo, J. Haocheng, W. Haixing, and T. Haibing, "Numerical simulation of characteristics of cex ions in ion thruster optical system," *Chinese Journal of Aeronautics*, vol. 23, pp. 15–21, 2010.

[135] I. Katz and I. Mikelides, "Neutral gas free molecular flow algorithm including ionization and walls for use in plasma simulations," *Journal of Computational Physics*, vol. 230, no. 4, pp. 1454–1464, 2010.

[136] R. Pan, Z. Li, S. Cao, J. Ren, and H. Tang, "Parallel codes using particles decomposition and view factor model methods for the particle in cell-Monte Carlo collision (PIC-MCC) simulation on cylinder hall thruster," in *36th International Electric Propulsion Conference*, 2019.

[137] M. Nakano, K. Nakamura, and I. Funaki, "Jiedi tool: Numerical life qualification tool for ion engine optics," *Trans. JSASS Aerospace Tech. Japan*, vol. 10, no. 28, pp. 85–90, 2012.

[138] F. L. Pedrotti, L. Pedrotti, and L. Pedrotti, *Introduction to optics.* Cambridge University Press, 2017.

[139] G. Aston, H. Kaufman, and P. Wilbur, "Ion beam divergence characteristics of two-grid accelerator systems," *AIAA Journal*, vol. 16, pp. 516–524, 1978. [Online]. Available: http://adsabs.harvard.edu/abs/1978AIAAJ..16..516A

[140] V. J. Noord and N. Center, *NEXT Ion Thruster Thermal Model*. National Aeronautics and Space Administration, Glenn Research Center, 2010.

[141] J. Foster, G. Williams, and M. Patterson, "Characterization of an ion thruster neutralizer," *Journal of Propulsion and Power*, vol. 23, no. 4, pp. 828–835, 2007.

[142] F. Filleul, O. Sutherland, F. Cipriani, and C. Charles, "Bepicolombo: A platform for improving modeling of electric propulsion-spacecraft interactions," *Frontiers in Space Technologies*, vol. 2, p. 1, 2021. [Online]. Available: https://www.frontiersin.org/article/10.3389/frspt.2021.639819

[143] J. Foster, G. Soulas, and M. Patterson, "Plume and discharge plasma measurements of an NSTAR-type ion thruster," in *36th Joint Propulsion Conference and Exhibit*, ser. paper 2000-3812. Huntsville, Alabama, July 16-19: American Institute of Aeronautics and Astronautics, Reston, VA, 2000.

[144] K. de Grys, A. Mathers, B. Welander, and V. Khayms, "Demonstration of 10,400 hours of operation on a 4.5 kW qualification model Hall thruster," in *Joint Propulsion Conference, AIAA-10*, vol. 6698, 2010.

[145] J. Zubair, "Development of a 12.5 kW Hall thruster for the advanced electric propulsion system," in *AIAA Propulsion and Energy 2020 Forum*, ser. AIAA 2020-3628, 2020.

[146] R. Hofer, D. Goebel, I. Mikellides, and I. Katz, "Magnetic shielding of a laboratory Hall thruster. II. experiments," *Journal of Applied Physics*, vol. 115, no. 4, p. 2008, 2014.

[147] S. B. Cusson, B. A. Jorns, and A. D. Gallimore, "Non-invasive in situ measurement of the near-wall ion kinetic energy in a magnetically shielded Hall thruster," *Plasma Sources Science and Technology*, vol. 28, no. 10, 2019.

[148] H. Kamhawi, W. Huang, T. Haag, J. Yim, L. Chang, L. Clayman, D. A. Herman, R. Shastry, R. Thomas, C. Griffith *et al.*, "Overview of the development of the solar electric propulsion technology demonstration mission 12.5-kW Hall thruster," in *50th AIAA/ASME/SAE/ASEE Joint Propulsion Conference*, ser. AIAA-2014-3898, 2014.

[149] V. Gianetti, E. Ferrato, A. Piragino, M. Reza, F. Faraji, M. Andrenucci, and T. Andreussi, "HT5k thruster unit development history, status and way forward," in *Proc. 36th International Electric Propulsion Conference*, ser. IEPC-2019-878, Vienna, Austria, 2019.

[150] T. Andreussi, A. Piragino, M. Reza, V. Gianetti, F. Faraji, E. Ferrato, D. Pedrini, A. Kitaeva, A. Rossodivita, and M. Andrenucci, "Development status and way forward of SITAEL's 20kW class Hall thruster, the HT20k," in 36^{th} *International Electric Propulsion Conference, Vienna, Austria*, no. IEPC-2019-8251, 2019.

[151] R. W. Conversano, D. M. Goebel, R. R. Hofer, I. G. Mikellides, and R. E. Wirz, "Performance analysis of a low-power magnetically shielded Hall thruster: Experiments," *Journal of Propulsion and Power*, vol. 33, no. 4, pp. 975–983, 2017.

[152] L. Grimaud and S. Mazouffre, "Ion behavior in low-power magnetically shielded and unshielded Hall thrusters," *Plasma Sources Science and Technology*, vol. 26, no. 5, p. 055020, 2017.

[153] I. G. Mikellides, I. Katz, R. R. Hofer, and D. M. Goebel, "Magnetic shielding of a laboratory Hall thruster. I. theory and validation," *Journal of Applied Physics*, vol. 115, no. 4, p. 043303, 2014.

[154] I. G. Mikellides, R. R. Hofer, I. Katz, and D. M. Goebel, "Magnetic shielding of Hall thrusters at high discharge voltages," *Journal of Applied Physics*, vol. 116, p. 053302, 2014.

[155] A. L. Ortega, I. G. Mikellides, and V. H. Chaplin, "Numerical simulations for the assessment of erosion in the 12.5-kW Hall effect rocket with magnetic shielding (HERMeS)," in *35th International Electric Propulsion Conference, Atlanta, GA, IEPC-2017-154*, 2017.

[156] T. A. Marks, A. Lopez Ortega, I. G. Mikellides, and B. Jorns, "Self-consistent implementation of a zero-equation transport model into a predictive model for a Hall effect thruster," in *AIAA Propulsion and Energy 2021 Forum*, ser. AIAA 2021-3424, 2021.

[157] R. W. Conversano, D. M. Goebel, I. G. Mikellides, R. R. Hofer, and R. E. Wirz, "Performance analysis of a low-power magnetically shielded Hall thruster: computational modeling," *Journal of Propulsion and Power*, vol. 33, no. 4, pp. 992–1001, 2017.

[158] L. Ghislanzoni, L. Benetti, M. Tommaso, G. Cesaretti, and F. L., "Hall effect thruster direct drive PPU's, experimental investigation of the cathode potential grounding problem," in *E3S Web of Conferences 16 (2017) 15002*, 2017.

[159] L. Garrigues, S. Santhosh, L. Grimaud, and S. Mazouffre, "Operation of a low-power Hall thruster: comparison between magnetically unshielded and shielded configuration," *Plasma Sources Science and Technology*, vol. 28, no. 3, 2019.

[160] A. Domínguez-Vázquez, F. Taccogna, P. Fajardo, and E. Ahedo, "Parametric study of the radial plasma-wall interaction in a Hall thruster," *Journal of Physics D: Applied Physics*, vol. 52, no. 47, p. 474003, 2019. [Online]. Available: https://doi.org/10.1088%2F1361-6463%2Fab3c7b

[161] A. Marín-Cebrián, A. Domínguez-Vázquez, P. Fajardo, and E. Ahedo, "Macroscopic plasma analysis from 1D-radial kinetic results of a Hall thruster discharge," *Plasma Sources Science and Technology*, vol. 30, no. 11, p. 115011, November 2021. [Online]. Available: https://doi.org/10.1088/1361-6595/ac325e

[162] D. M. Goebel, R. R. Hofer, I. G. Mikellides, I. Katz, J. E. Polk, and B. N. Dotson, "Conducting wall Hall thrusters," *IEEE Transactions on Plasma Science*, vol. 43, no. 1, pp. 118–126, 2015.

[163] L. Grimaud and S. Mazouffre, "Conducting wall Hall thrusters in magnetic shielding and standard configurations," *Journal of Applied Physics*, vol. 122, no. 3, 2017.

[164] G. Janes and R. Lowder, "Anomalous electron diffusion and ion acceleration in a low-density plasma," *Physics of Fluids*, vol. 9, no. 6, pp. 1115–1123, 1966.

[165] A. Morozov, Y. Esipchuk, A. Kapulkin, V. Nevrovskii, and V. Smirnov, "Effect of the magnetic field on a closed-electron-drift accelerator," *Sov. Phys.-Tech. Phys.(Engl. Transl.) 17: No. 3, 482-7 (Sep 1972).*, 1972.

[166] E. Choueiri, "Plasma oscillations in Hall thrusters," *Physics of Plasmas*, vol. 8, no. 4, pp. 1411–1426, 2001.

[167] K. Hara and S. Tsikata, "Cross-field electron diffusion due to the coupling of drift-driven microinstabilities," *Phys. Rev. E*, vol. 102, no. 2, p. 023202, 2020.

[168] T. Charoy, J. P. Boeuf, A. Bourdon, J. A. Carlsson, P. Chabert, B. Cuenot, D. Eremin, L. Garrigues, K. Hara, I. D. Kaganovich, A. T. Powis, A. Smolyakov, D. Sydorenko, A. Tavant, O. Vermorel, and W. Villafana, "2d axial-azimuthal particle-in-cell benchmark for low-temperature partially magnetized plasmas," *Plasma Sources Science and Technology*, vol. 28, no. 10, p. 105010, 2019.

[169] E. Ahedo, J. Gallardo, and M. Martínez-Sánchez, "Effects of the radial-plasma wall interaction on the axial Hall thruster discharge," *Physics of Plasmas*, vol. 10, no. 8, pp. 3397–3409, 2003.

[170] J. Koo and I. Boyd, "Modeling of anomalous electron mobility in Hall thrusters," *Physics of Plasmas*, vol. 13, p. 033501, 2006.

[171] B. Jorns, "Predictive, data-driven model for the anomalous electron collision frequency in a Hall effect thruster," *Plasma Sources Science and Technology*, vol. 27, no. 10, p. 104007, 2018.

[172] T. Andreussi, V. Giannetti, A. Kitaeva, M. Reza, E. Ferrato, L. Onida, A. Leporini, C. A. Paissoni, D. Pedrini, F. Nania, S. Gregucci, and E. Casali, "Development status of the xenon propulsion subsystem for the Ital-GovSatCom platform," in *In Proc. 71st International Astronautical Congress, IAC-20,C4,5,5,x59830.*, 2020.

[173] A. Piragino, E. Ferrato, F. Faraji, M. Reza, T. Andreussi, A. Rossodivita, and M. Andrenucci, "Experimental characterization of a 5 kW magnetically-shielded Hall thruster," in *Space Propulsion Conference 2018*, ser. SP-2019-427, 2018.

[174] A. Domínguez-Vázquez, F. Cichocki, M. Merino, P. Fajardo, and E. Ahedo, "On heavy particle-wall interaction in axisymmetric plasma discharges," *Plasma Sources Science and Technology*, vol. 30, no. 8, p. 085004, aug 2021.

[175] J. Bittencourt, *Fundamentals of plasma physics.* Springer, Berlin, Germany, 2004.

[176] J. Boeuf and L. Garrigues, "Low frequency oscillations in a stationary plasma thruster," *J. Applied Physics*, vol. 84, no. 7, pp. 3541–3554, 1998.

[177] J. Zhou, D. Pérez-Grande, P. Fajardo, and E. Ahedo, "Numerical treatment of a magnetized electron fluid within an electromagnetic plasma thruster code," *Plasma Sources Science and Technology*, vol. 28, no. 11, p. 115004, 2019.

[178] C. G. Petra, O. Schenk, M. Lubin, and K. Gartner, "An augmented incomplete factorization approach for computing the schur complement in stochastic optimization," *SIAM Journal on Scientific Computing*, vol. 36(2), pp. C139–C162, 2014.

[179] C. G. Petra, O. Schenk, and M. Anitescu, "Real-time stochastic optimization of complex energy systems on high-performance computers," *Computing in Science and Engineering*, vol. 16(5), pp. 32–34, 2014.

[180] I. Mikellides, I. Katz, D. M. Goebel, K. K. Jameson, and J. E. Polk, "Wear mechanisms in electron sources for ion propulsion, 2: Discharge hollow cathode," *Journal of Propulsion and Power*, vol. 24, no. 4, pp. 866–879, 2008.

[181] Stephen Francis Biagi, "Cross sections extracted from PROGRAM MAGBOLTZ, version 7.1 june 2004," June 2004, [Online; accessed 5-July-2021]. [Online]. Available: www.lxcat.net/Biagi-v7.1

[182] M. Mitchner and C. Kruger Jr., *Partially ionized gases.* John Wiley and Sons, Hoboken, NJ, 1973.

[183] V. Murray, M. Pilinski, E. Smoll Jr, M. Qian, T. Minton, S. Madzunkov, and M. Darrach, "Gas–surface scattering dynamics applied to concentration of gases for mass spectrometry in tenuous atmospheres," *The Journal of Physical Chemistry C*, vol. 121, no. 14, pp. 7903–7922, 2017.

[184] R. Santos, "Código híbrido avanzado de motores de plasma de efecto Hall," Ph.D. dissertation, Universidad Politécnica de Madrid (UPM), Madrid, Spain, 2012.

[185] S. Mazouffre, P. Echegut, and M. Dudeck, "A calibrated infrared imaging study on the steady state thermal behaviour of Hall effect thrusters," *Plasma Sources Science and Technology*, vol. 16, no. 1, p. 13, 2006.

[186] S. Araki and R. Wirz, "Magnetic field aligned mesh for ring-cusp discharge chambers," in *50th AIAA/ASME/SAE/ASEE Joint Propulsion Conference & Exhibit*, no. AIAA 2014-3830, Cleveland, Ohio, US, 2014.

[187] G. Hagelaar, J. Bareilles, L. Garrigues, and J. Boeuf, "Role of anomalous electron transport in a stationary plasma thruster simulation," *Journal of Applied Physics*, vol. 93, no. 1, pp. 67–75, 2003.

[188] J. Bareilles, G. Hagelaar, L. Garrigues, C. Boniface, J. Boeuf, and N. Gascon, "Critical assessment of a two-dimensional hybrid hall thruster model: Comparisons with experiments," *Physics of Plasmas*, vol. 11, no. 6, pp. 3035–3046, 2004.

[189] J. Fife, M. Martínez-Sánchez, and J. Szabo, "A numerical study of low-frequency discharge oscillations in Hall thrusters," in *33rd Joint Propulsion Conference, Seattle, WA*, ser. AIAA 97-3052, 1997.

[190] S. Barral and E. Ahedo, "Low-frequency model of breathing oscillations in Hall discharges," *Physical Review E*, vol. 79, p. 046401, 2009.

[191] M. M. Saravia, A. Giacobbe, and T. Andreussi, "Bayesian analysis of triple langmuir probe measurements for the characterization of hall thruster plasmas," *Review of Scientific Instruments*, vol. 90, p. 023502, 2019.

[192] V. H. Chaplin, B. A. Jorns, A. Lopez Ortega, I. G. Mikellides, R. W. Conversano, R. B. Lobbia, and R. R. Hofer, "Laser-induced fluorescence measurements of acceleration zone scaling in the 12.5 kW HERMeS Hall thruster," *Journal of Applied Physics*, vol. 124, no. 18, 2018.

[193] R. W. Conversano, "Low-power magnetically shielded Hall thrusters," PhD Thesis, University of California, Los Angeles, 2015.

[194] M. Cappelli, N. Meezan, and N. Gascon, "Transport physics in Hall plasma thrusters," in *38th Joint Propulsion Conference, Indianapolis, IN*, ser. AIAA 2002-0485, 2002.

[195] J. Fox, A. Batishcheva, O. Batishchev, and M.Martinez-Sanchez, "Adaptively meshed fully-kinetic PIC-Vlasov model for near vacuum Hall thrusters," in *42th Joint Propulsion Conference, Sacramento, CA*, ser. AIAA 2006-4324, 2006.

[196] I. Maqueda, D. Escobar, and E. Ahedo, "Advances on a Hall thruster hybrid code," in *30th International Electric Propulsion Conference, Florence, Italy*, ser. IEPC 2007-066, 2007.

[197] E. Ahedo and M. Merino, "Two-dimensional supersonic plasma acceleration in a magnetic nozzle," *Physics of Plasmas*, vol. 17, no. 7, p. 073501, 2010.

[198] N. P. Brown and M. L. R. Walker, "Review of plasma-induced hall thruster erosion review of plasma-induced hall thruster erosion," *Applied Sciences*, vol. 10, no. 11, p. 3775, 2020.

[199] E. Ahedo and V. Pablo, "Combined effects of electron partial thermalization and secondary emission in Hall thruster discharges," *Physics of Plasmas*, vol. 14, p. 083501, 2007.

[200] G. Hobbs and J. Wesson, "Heat flow through a langmuir sheath in the presence of electron emission," *Plasma Physics*, vol. 9, p. 85, 1967.

[201] E. Ahedo, "Presheath/sheath model of a plasma with secondary emission from two parallel walls," *Physics of Plasmas*, vol. 9, no. 10, pp. 4340–4347, 2002.

[202] S. Barral, K. Makowski, Z. Peradzynski, N. Gascon, and M. Dudeck, "Wall material effects in stationary plasma thrusters. II. Near-wall and in-wall conductivity," *Phys. Plasmas*, vol. 10, no. 10, pp. 4137–4152, 2003.

[203] F. Taccogna, S. Longo, and M. Capitelli, "Plasma sheaths in Hall discharge," *Physics of Plasmas*, vol. 12, no. 9, p. 093506, 2005.

[204] R. Santos and E. Ahedo, "Implementation of the kinetic Bohm condition in a Hall thruster hybrid code," in *45th Joint Propulsion Conference*, ser. AIAA 2009-4913. Denver, Colorado, August 2-5: AIAA, Reston, VA, 2009.

[205] E. Ahedo, R. Santos, and F. Parra, "Fulfillment of the kinetic Bohm criterion in a quasineutral particle-in-cell model," *Physics of Plasmas*, vol. 17, no. 7, p. 073507, 2010.

[206] E. Choueiri, "Fundamental difference between the two Hall thruster variants," *Physics of Plasmas*, vol. 8, no. 11, pp. 5025–5033, 2001.

[207] G. Tilinin, "High-frequency plasma waves in a Hall accelerator with an extended acceleration zone," *Sov. Phys.-Tech. Phys.(Engl. Transl.);(United States)*, vol. 22, no. 8, 1977.

[208] K. Hara, M. J. Sekerak, I. D. Boyd, and A. D. Gallimore, "Perturbation analysis of ionization oscillations in hall effect thrusters," *Physics of Plasmas*, vol. 21, no. 12, p. 122103, 2014.

[209] E. T. Dale and B. A. Jorns, "Two-zone hall thruster breathing mode mechanism, part i: Theory," in *36th International Electric Propulsion Conference*, ser. IEPC 2019-354, Vienna, Austria, 1019.

[210] T. Lafleur, P. Chabert, and A. Bourdon, "The origin of the breathing mode in Hall thrusters and its stabilisation," *Journal of Applied Physics*, vol. 130, no. 5, p. 053305, 2021.

[211] E. T. Dale and B. A. Jorns, "Experimental characterization of Hall thruster breathing mode dynamics," *Journal of Applied Physics*, vol. 130, no. 13, p. 133302, 2021.

[212] O. Chapurin, A. Smolyakov, G. Hagelaar, and Y. Raitses, "On the mechanism of ionization oscillations in hall thrusters," *Journal of Applied Physics*, vol. 129, no. 23, p. 233307, 2021.

[213] L. Wei, W. Chunsheng, H. Ke, and D. Yu, "Effect of ionization distribution on the low frequency oscillations mode in Hall thrusters," *Physics of Plasmas*, vol. 19, no. 1, p. 075502, 2012.

[214] T. Tamida, T. Nakagawa, I. Suga, H. Osuga, T. Ozaki, and K. Matsui, "Determining parameter sets for low-frequency-oscillation-free operation of Hall thruster," *Journal of Applied Physics*, vol. 102, no. 4, p. 043304, 2007.

[215] L. Sekerak, B. Longmier, A. Gallimore, R. Hofer, and J. Polk, "Mode transitions in hall effect thrusters," in *49th AIAA/ASME/SAE/ASEE Joint Propulsion Conference*, 2013, San Jose, CA.

[216] K. Hara, M. J. Sekerak, I. D. Boyd, and A. D. Gallimore, "Mode transition of a Hall thruster discharge plasma," *Journal of Applied Physics*, vol. 115, no. 20, p. 203304, 2014.

[217] L. Sekerak, B. Longmier, A. Gallimore, W. Huang, H. Kamhawi, R. Hofer, B. Jorns, and J. Polk, "Mode transitions in magnetically shielded Hall effect thrusters," in *50th AIAA/ASME/SAE/ASEE Joint Propulsion Conference*, 2014, Cleveland, Ohio.

[218] L. Sekerak, A. Gallimore, D. Brown, R. Hofer, and J. Polk, "Mode transitions in Hall-effect thrusters induced by variable magnetic field strength," *Journal of Propulsion and Power*, vol. 32, no. 4, 2016.

[219] S. Barral and J. Miedzik, "Numerical investigation of closed-loop control for Hall accelerators," *Journal of Applied Physics*, vol. 109, no. 1, p. 013302, 2011.

[220] L. Wei, W. Li, Y. Ding, and D. Yu, "Effect of low-frequency oscillation on performance of Hall thrusters," *Plasma Sources Science and Technology*, vol. 20, no. 7, p. 075502, 2018.

[221] J. Vaudolon, L. Balika, and L. Mazouffre, "Photon counting technique applied to time-resolved laser-induced fluorescence measurements on a stabilized discharge," *Review of Scientific Instruments*, vol. 84, no. 7, p. 073512, 2013.

[222] S. Keller, Y. Raitses, and A. Diallo, "Driving low frequency breathing oscillations in a Hall thruster," in *50th AIAA/ASME/SAE/ASEE Joint Propulsion Conference*. Cleveland, OH: American Institute of Aeronautics and Astronautics, Reston, VA, 2014.

[223] A. Diallo, S. Keller, Y. Shi, Y. Raitses, and S. Mazouffre, "Time-resolved ion velocity distribution in a cylindrical Hall thruster: heterodyne-based experiment and modeling," *Review of scientific instruments*, vol. 86, no. 3, p. 033506, 2015.

[224] K. Hara, S. Keller, and Y. Raitses, "Measurements and theory of driven breathing oscillations in a Hall effect thruster," in *52nd AIAA/ASME/SAE/ASEE Joint Propulsion Conference and Exhibit*, Salt Lake City, Utah, July 25-27, 2016.

[225] I. Romadanov, Y. Raitses, A. Diallo, I. Kaganovich, K. Hara, and A. Smolyakov, "Time resolved measurements of modulated breathing oscillations in Cylindrical Hall Thruster," in 35^{th} *International Electric Propulsion Conference*, no. IEPC-2017-267. Atlanta, Georgia, USA: Electric Rocket Propulsion Society, Fairview Park, OH, 2017.

[226] I. Romadanov, Y. Raitses, A. Diallo, K. Hara, I. Kaganovich, and A. Smolyakov, "On limitations of laser-induced fluorescence diagnostics for xenon ion velocity distribution function measurements in hall thrusters," *Physics of Plasmas*, vol. 25, no. 3, p. 033501, 2018.

[227] N. Yamamoto, H. Takegahara, J. Aoyagi, K. Kuriki, T. Tamida, and H. Osuga, "Development of a novel power processing unit for hall thrusters," *IEEE Transactions on Plasma Science*, vol. 43, no. 1, pp. 158–164, 2015.

[228] K. Nagamine, H. Takegahara, A. Kamami, N. Yamamoto, and T. Tamida, "Application of a pulsating voltage drive to an Anode-Layer-Type Hall thruster," *Trans. JSASS Aerospace Tech. Japan*, vol. 19, no. 5, pp. 621–628, 2021.

[229] T. Tamida, H. Osuga, N. Yamamoto, H. Takegahara, J. Aoyagi, and K. Kuriki, "Performance improvement of Hall thrusters using a pulse-synchronous driver system," *Journal of Propulsion and Power*, vol. 31, no. 3, pp. 956–961, 2014.

[230] N. Yamamoto, T. Ito, H. Takegahara, H. Watanabe, T. Tamida, and H. Osuga, "Thrust performance in Hall thruster with pulsating operation," *Trans. JSASS Aerospace Tech. Japan*, vol. 14, pp. 173–176, 2016.

[231] I. Romadanov, Y. Raitses, and A. Smolyakov, "Hall thruster operation with externally driven breathing mode oscillations," *PSST*, vol. 27, 2018.

[232] ——, "Control of coherent structures via external drive of the breathing mode," *Plasma Physics Reports*, vol. 45, no. 2, pp. 134–146, 2019.

[233] J. Simmonds and Y. Raitses, "Theoretical analysis of performance parameters in oscillating plasma thrusters," *Journal of Propulsion and Power*, vol. 37, no. 10, 2021.

[234] J. Simmonds, Y. Raitses, A. Smolyakov, and O. Chapurin, "Application of hall thrusters with modulated oscillations," in *AIAA Propulsion and Energy 2020 Forum*, ser. AIAA 2020-3618, 2020.

[235] ——, "Studies of a modulated hall thruster," *Plasma Sources Science and Technology*, vol. 30, no. 5, 2021.

[236] A. Ortega, I. Mikellides, M. Sekerak, and B. Jorns, "Plasma simulations in 2-d (r-z) geometry for the assessment of pole erosion in a magnetically shielded Hall thruster," *Journal of Applied Physics*, vol. 125, no. 3, 2019.

[237] A. Ortega, I. Mikellides, V. Chaplin, J. Snyder, and G. Lenguito, "Facility pressure effects on a Hall thruster with an external cathode, i: numerical simulations," *Plasma Sources Science and Technology*, vol. 29, no. 3, 2020.

[238] E. T. Dale and B. A. Jorns, "Non-invasive time-resolved measurements of anomalous collision frequency in a Hall thruster," *Physics of Plasma*, vol. 26, no. 1, p. 013516, 2019.

[239] T. Marks and B. Jorns, "Challenges with the self-consistent implementation of closure models for anomalous electron transport in fluid simulations of Hall thrusters," *Plasma Sources Science and Technology*, vol. 32, no. 4, p. 045016, 2023.

[240] D. Maddaloni, A. Domínguez-Vázquez, F. Terragni, and M. Merino, "Data-driven analysis of oscillations in hall thruster simulations," *Plasma Sources Science and Technology*, vol. 31, no. 4, p. 045026, apr 2022.

[241] Y. Raitses, D. Staack, A. Smirnov, and N. Fisch, "Space charge saturated sheath regime and electron temperature saturation in Hall thrusters," *Physics of Plasmas*, vol. 12, p. 073507, 2005.

[242] S. Le Clainche and J. M. Vega, "Higher order dynamic mode decomposition," *SIAM J. Appl. Dyn. Syst.*, vol. 16, pp. 882–925, 2017.

[243] J. M. Vega and S. Le Clainche, *Higher order dynamic mode decomposition and its applications*. Academic Press, 2020.

[244] P. J. Schmid, "Dynamic mode decomposition of numerical and experimental data," *Journal of Fluid Mechanics*, vol. 656, pp. 5–28, 2010.

[245] S. Barral, K. Makowski, Z. Peradzynski, and M. Dudeck, "Transit-time instability in Hall thrusters," *Physics of Plasmas*, vol. 12, p. 073504, 2005.

[246] J. Perales-Díaz, A. Domínguez-Vázquez, P. Fajardo, E. Ahedo, T. Andreussi, and A. Piragino, "Hybrid 2D plasma simulations of a 20kW-class magnetically shielded Hall effect thruster," in 37^{th} *International Electric Propulsion Conference*, no. IEPC-2022-322. Boston, MA, June 19-23: Electric Rocket Propulsion Society, 2022.

[247] D. Pedrini, T. Misuri, F. Paganucci, and M. Andrenucci, "Development of hollow cathodes for space electric propulsion at Sitael," *Aerospace*, vol. 4, 2017.

[248] S. Zurbach and N. Cornu, "Performance evaluation of a 20 kw Hall effect thruster," in *32th International Electric Propulsion Conference, Wiesbaden, Germany*, ser. IEPC-2011-020, 2011.

[249] A. Piragino, E. Ferrato, F. Faraji, M. Reza, V. Giannetti, A. Kitaeva, D. Pedrini, M. Andrenucci, and T. Andreussi, "SITAEL's magnetically shielded 20 kW Hall thruster tests," in 36^{th} *International Space Propulsion Conference 2019, Vienna, Austria*, ser. IEPC-2019-879, 2019.

[250] A. Domínguez-Vázquez, J. Zhou, A. Sevillano-González, P. Fajardo, and E. Ahedo, "Analysis of the electron downstream boundary conditions in a 2D hybrid code for Hall thrusters," in 37^{th} *International Electric Propulsion Conference*, no. IEPC-2022-338. Boston, MA, June 19-23: Electric Rocket Propulsion Society, 2022.

[251] Y. Raitses, J. Ashkenazy, and M. Guelman, "Propellant utilization in Hall thrusters," *J. Propulsion Power*, vol. 14, no. 2, pp. 247–253, 1998.

[252] B. M. Reid, "The influence of neutral flow rate in the operation of Hall thrusters," Ph.D. dissertation, Department of Aerospace Engineering, The University of Michigan, Ann Arbor, MI, 2009.

[253] J. Linnell and A. Gallimore, "Efficiency analysis of a Hall thruster operating with krypton and xenon," *Journal of Propulsion and Power*, vol. 22, no. 6, pp. 1402–1412, 2006.

[254] R. Hofer and A. Gallimore, "High-specific impulse Hall thrusters, part 2: Efficiency analysis," *Journal of Propulsion and Power*, vol. 22, no. 4, pp. 732–740, 2006.

[255] D. L. Brown, C. W. Larson, B. E. Bealand, and A. D. Gallimore, "Methodology and historical perspective of a Hall thruster efficiency analysis," *Jounal of propulsion and power*, vol. 25, no. 6, 2009.

[256] L. Su, , and J. B.A., "Performance comparison of a 9-kw magnetically shielded Hall thruster operating on xenon and krypton," *Journal of Applied Physics*, vol. 130, no. 16, p. 163306, 2021.

[257] K. K. Jameson, D. M. Goebel, R. R. Hofer, and R. M. Watkins, "Cathode coupling in Hall thrusters," in *30th International Electric Propulsion Conference*, ser. IEPC-2007-278, Florence, Italy, 2007.

[258] R. Hofer, L. Johnson, D. Goebel, and R. Wirz, "Effects of internally mounted cathodes on Hall thruster plume properties," *IEEE Transactions on Plasma Science*, vol. 36, no. 5, pp. 2004–2014, 2008.

[259] P. Peterson, D. T. Jacobson, D. Manzella, and J. John, "The performance and wear characterization of a high-power high-Isp NASA Hall thruster," in *41st AIAA/ASME/SAE/ASEE Joint Propulsion Conference and Exhibit*, ser. AIAA 2005-4243, Tucson, Arizona, 2005.

[260] T. Andreussi, M. M. Saravia, and M. Andrenucci, "Plasma characterization in Hall thrusters by Langmuir probes," *Journal of Instrumentation*, vol. 14, p. C05011, 2019.

[261] R. Hofer, "Development and characterization of high-efficiency, high-specific impulse xenon hall thrusters," Ph.D. dissertation, Department of Aerospace Engineering, Univ. of Michigan, Ann Arbor, MI, 2004.

[262] R. Hofer and A. Gallimore, "The role of magnetic field topography in improving the performance of high-voltage Hall thrusters," in *38th Joint Propulsion Conference*, ser. AIAA 2002-4111, Indianapolis, IN, 2002.

[263] D. Jacobson and D. Manzella, "50 kW class krypton Hall thruster performance," in *39th AIAA/ASME/SAE/ASEE Joint Propulsion Conference and Exhibit*, ser. AIAA Paper 2003-4550, Huntsville, Alabama, 2003.

[264] M. Nakles, W. A. Hargus, J. Delgado, and R. Corey, "A performance comparison of xenon and krypton propellant on an SPT-100 Hall thruster," in *32nd International Electric Propulsion Conference*, ser. IEPC 2011-003, Weisbaden, Germany, 2011.

[265] S. E. Cusson, B. A. Jorns, and A. D. Gallimore, "Simple model for cahode coupling voltage versus background pressure in a Hall thruster," in *53rd AIAA/SAE/ASEE Joint Propulsion Conference, Atlanta, GA*, ser. AIAA 2017-4889, 2017.

[266] J. Linnell and A. Gallimore, "Internal plasma potential measurements of a Hall thruster using xenon and krypton propellant," *Physics of Plasmas*, vol. 13, no. 9, p. 093502, 2006.

[267] J. Samson and R. Cairns, "Ionization potential of molecular xenon and krypton," *J. Opt. Soc. Am.*, vol. 56, pp. 1140–1141, 1966.

[268] V. Kim, G. Popov, V. Kozlov, A. Skrylnikov, and D. Grdlichko, "Investigation of the SPT performance and particularities of its operation with Kr and Kr/Xe mixtures," in *27th International Electric Propulsion Conference, Pasadena, CA, USA*, ser. IEPC 01-065, 2001.

[269] M. Nakles, W. A. Hargus, J. Delgado, and R. Corey, "A performance and plume comparison of xenon and krypton propellant on the SPT-100," in *48th AIAA/ASME/SAE/ASEE Joint Propulsion Conference & Exhibit*, ser. AIAA 2012-4116, Atlanta, Georgia, 2012.

[270] K. Dannenmayer, "Scaling laws and electron properties in Hall effect thrusters," PhD Thesis, Université d'Orléans, 2012.

[271] S. Mazouffre, G. Bourgeois, K. Dannenmayer, and A. Lejeune, "Ionization and acceleration processes in a small, variable channel width, permanent-magnet Hall thruster," *J. Phys. D: Appl. Phys.*, vol. 45, p. 185203, 2012.

[272] W. Hargus, G. Azarnia, and M. Nakles, "A comparison of ion acceleration characteristics for krypton and xenon propellants within a 600 w hall effect thruster," in *48th AIAA/ASME/SAE/ASEE Joint Propulsion Conference & Exhibit, Atlanta, Georgia*, ser. AIAA 2012-3871, 2012.

[273] A. Modesti, J. Zhou, F. Cichocki, A. Domínguez-Vázquez, and E. Ahedo, "Simulation of the expansion within a vacuum chamber of the plume of a hall thruster with a centrally mounted cathode," in *Space Propulsion Conference 2022*, no. 00155. May 9-13: Association Aéronautique et Astronautique de France, 2022.

[274] J. Ekholm, W. Hargus, C. Larson, M. Nakles, G. Reed, and C. Niemela, "Plume characteristics of the Busek 600 W Hall thruster," in *42nd AIAA/ASME/SAE/ASEE Joint Propulsion Conference & Exhibit, Sacramento, California*, ser. AIAA-2016-4659, 2006.

[275] A. Bugrova and A. Morozov, "Influence of vacuum conditions on the SPT operation," in *24th International Electric Propulsion Conference, Moscow, Russia*, ser. IEPC-1995-046, 1995.

[276] R. Hofer, P. Peterson, and A. Gallimore, "Characterizing vacuum facility backpressure effects on the performance of a Hall thruster," *IEPC Paper*, no. 01-045, 2001.

[277] K. Diamant, R. Liang, and R. Corey, "The effect of background pressure on SPT-100 Hall thruster performance," in *50th AIAA/ASME/SAE/ASEE Joint Propulsion Conference, Cleveland, OH*, ser. AIAA 2014-3710, 2014.

[278] T. Randolph, V. Kim, H. Kaufman, K. Kozubsky, V. Zhurin, and M. Day, "Facility effects on stationary plasma thruster testing," in *23rd International Electric Propulsion Conference*, no. 844. The Electric Rocket Propulsion Society Worthington, OH, 1993, pp. 13–16.

[279] M. Walker and A. Gallimore, "Performance characteristics of a cluster of 5-kW laboratory Hall thrusters," *Journal of Propulsion and Power*, vol. 23, no. 1, pp. 35–43, 2007.

[280] A. Piragino, F. Faraji, M. Reza, E. Ferrato, A. Piraino, and T. Andreussi, "Background pressure effects on the performance of a 20 kw magnetically shielded hall thruster operating in various configurations," *Aerospace*, vol. 8, no. 3, p. 69, 2021.

[281] R. Spektor, W. Tighe, P. Stoltz, and K. Beckwith, "Facility effects on hall thruster performance through cathode coupling," in *34th International Electric Propulsion Conference*, ser. IEPC-2015-309. Kobe, Japan, 4–10 July: Electric Rocket Propulsion Society, 2015.

[282] I. G. Mikellides, A. L. Ortega, V. H. Chaplin, and S. J. S., "Facility pressure effects on a Hall thruster with an external cathode, ii: theoretical model of the thrust and the significance of azimuthal asymmetries in the cathode plasma," *Plasma Sources Science and Technology*, vol. 29, no. 3, 2020.

[283] B. A. Jorns and M. P. Byrne, "Model for the dependence of cathode voltage in a hall thruster on facility pressure," *Plasma Sources Science and Technology*, vol. 30, no. 1, p. 18, 2021.

[284] M. Nakles and W. A. Hargus, “Background pressure effects on ion velocity distribution within a medium-power Hall thruster,” *Journal of Propulsion and Power*, vol. 27, no. 4, 2011.

[285] A. Piragino, “Characterization of the background pressure effects on high power Hall thrusters,” Ph.D. dissertation, Università di Pisa, 2021.

[286] K. Diamant, T. Curtiss, R. Spektor, E. Beiting, V. Hruby, B. Pote, J. Kolencik, and S. Paintal, “Performance and plume characterization of the BHT-1500 Hall thruster,” in *34th International Electric Propulsion Conference*, ser. IEPC 2015-069, 2015.

[287] N. MacDonald-Tenenbaum, Q. Pratt, M. Nakles, N. Pilgram, M. Holmes, and W. Hargus, “Background pressure effects on ion velocity distributions in an SPT-100 Hall thruster,” *Journal of Propulsion and Power*, vol. 35, no. 2, pp. 403–412, 2019.

[288] I. Mikellides and A. Lopez-Ortega, “Assessment of pole erosion in a magnetically shielded Hall thruster,” in *50th AIAA/ASME/SAE/ASEE Joint Propulsion Conference*, ser. AIAA 2014-3897, Cleveland, OH, 2014.

[289] J. P. Boris *et al.*, “Relativistic plasma simulation-optimization of a hybrid code,” in *Proc. Fourth Conf. Num. Sim. Plasmas*, 1970, pp. 3–67.

[290] S. Mattei, K. Nishida, M. Onai, J. Lettry, M. Tran, and A. Hatayama, “A fully-implicit particle-in-cell Monte Carlo collision code for the simulation of inductively coupled plasmas,” *Journal of Computational Physics*, vol. 350, pp. 891–906, 2017.

[291] E. Anderson, Z. Bai, C. Bischof, S. Blackford, J. Demmel, J. Dongarra, J. Du Croz, A. Greenbaum, S. Hammarling, A. McKenney, and D. Sorensen, *LAPACK Users' Guide*, 3rd ed. Philadelphia, PA: Society for Industrial and Applied Mathematics, 1999.

[292] R. Chandra, L. Dagum, D. Kohr, R. Menon, D. Maydan, and J. McDonald, *Parallel programming in OpenMP*. Morgan kaufmann, 2001.

[293] A. Smirnov, Y. Raitses, and N. Fisch, “Electron cross-field transport in a low power cylindrical Hall thruster,” *Physics of Plasmas*, vol. 11, p. 4922, 2004.

[294] P. Dawson, “Secondary electron emission yields of some ceramics,” *Journal of Applied Physics*, vol. 37, 1966.

[295] F. Taccogna, F. Cichocki, and P. Minelli, “Coupling plasma physics and chemistry in pic model of electric propulsion: application to an air-breathing low power hall thruster,” *Frontiers*, vol. 10, p. 1006994, 2022.

[296] G. Guennebaud, B. Jacob *et al.*, “Eigen v3,” http://eigen.tuxfamily.org, 2010.

[297] Y. Itikawa, “Cross sections for electron collisions with oxygen molecules,” *Journal of Physical and Chemical Reference Data*, vol. 38, pp. 1–20, 2009.

[298] Y. Itikawa and A. Ichimura, “Cross sections for collisions of electrons and photons with atomic oxygen,” *Journal of Physical and Chemical Reference Data*, vol. 19, pp. 637–651, 1990.

[299] R. Laher and F. Gilmore, “Updated excitation and ionization cross sections for electron impact on atomic oxygen,” *Journal of Physical and Chemical Reference Data*, vol. 19, pp. 277–305, 1990.

[300] Y. Itikawa and N. Mason, “Cross sections for electron collisions with water molecules,” *Journal of Physical and Chemical Reference Data*, vol. 34, no. 1, 2005.

[301] K. Chakrabarti, V. Laporta, and J. Tennyson, “Calculated cross sections for low energy electron collision with OH,” *Plasma Sources Science and Technology*, vol. 28, p. 085013, 2019.

[302] J. Yoon, M. Song, J. Han, S. Hwang, W. Chang, B. Lee, and Y. Itikawa, “Cross sections for electron collisions with hydrogen molecules,” *Journal of Physical and Chemical Reference Data*, vol. 37, no. 2, 2008.

[303] R. Janev and J. Smith, “Cross sections for collision processes of hydrogen atoms with electrons, protons and multiply charged ions,” International Atomic Energy Agency, Vienna (Austria), Tech. Rep., 1993.

[304] K. Ralphs, G. Serna, L. Hargreaves, M. Khakoo, C. Winstea, and V. McKoy, “Excitation of the six lowest electronic transitions in water by 9–20 eV electrons,” *J. Phys. B: At. Mol. Opt. Phys.*, vol. 46, no. 12, 2013.

[305] M. Song, H. Cho, G. Karwasz, V. Kokoouline, Y. Nakamura, J. Tennyson, A. Faure, N. Mason, and Y. Itikawa, “Cross sections for electron collisions with H2O,” *J. Phys. Chem. Ref. Data*, vol. 50, no. 2, p. 023103, 2021.

[306] B. Darwent and National Standard Reference Data System, *Bond dissociation energies in simple molecules.* U.S. Dept. of Commerce National Bureau of Standards, 1970.

[307] National Institute of Standards and Technology (NIST), “69 chemistry web book,” https://www.nist.gov//, 2023.

[308] “Biagi database,” https://nl.lxcat.net, accessed: 2019-10-23.

[309] F. Lang and C. Smith, “Ionization energies of atoms and atomic ions,” *Journal of Chemical Education*, vol. 80, no. 8, 2003.

[310] M. Petro and R. Sedwick, “Effects of water-vapor propellant on electrodeless thruster performance,” *Journal of Propulsion and Power*, vol. 33, no. 6, pp. 1410–1417, 2017.

[311] W. Yang, “A tutorial overview on the angular scattering models of electron-neutral, ion-neutral, neutral-neutral, and Coulomb collisions in Monte Carlo colliions modeling on low temperature plasma,” *Arxiv preprint arXiv:2308.06012*, 2023.

[312] S. Yoshida, A. Phelps, and L. Pitchford, “Effect of electrons produced by ionization on calculated electron-energy distributions,” *Phys. Rev. A*, vol. 27, p. 2858, 1983.

[313] H. Nguyen, J. Mankowski, J. Dickens, A. A. Neuber, and R. Joshi, “Monte Carlo analysis of field-dependent electron avalanche coefficients in nitrogen at atmospheric pressure,” *Physics of Plasma*, vol. 24, no. 12, p. 124501, 2017.

[314] C. Opal, W. Peterson, and E. Beaty, “Measurements of secondary electron spectra produced by electron impact ionization of a number of simple gases,” *J. Chem. Phys*, vol. 55, pp. 4100–4106, 1971.

[315] G. Marsaglia, “Choosing a point from the surface of a sphere,” *The Annals of mathematical statistics*, vol. 43, no. 2, pp. 645–646, 1972.

[316] J. Boeuf and E. Marode, “A Monte Carlo analysis of an electron swarm in a non-uniform field: the cathode region of a glow discharge in helium,” *J. Phys. D: Appl. Phys*, vol. 15, p. 2196, 1982.

[317] J. Chew, P. Gibbon, and D. Brommel, “Three-dimensional first principles simulation of a hydrogen discharge,” *Plasma Phys. Control. Fusion*, vol. 63, p. 045012, 2021.

[318] D. Sydorenko, “Particle-in-cell simulations of electron dynamics in low pressure discharges with magnetic fields,” PhD Thesis, University of Saskatchewan, 2006.

[319] A. Marín-Cebrián, E. Bello-Benítez, A. Domínguez-Vázquez, and E. Ahedo, “Non-maxwellian electron effects on the macroscopic response of a hall thruster discharge from an axial–radial kinetic model,” *Plasma Sources Science and Technology*, vol. 33, no. 2, p. 025008, feb 2024. [Online]. Available: https://dx.doi.org/10.1088/1361-6595/ad227c

[320] F. Faraji, M. Reza, and A. Knoll, “Verification of the generalized reduced-order particle-in-cell scheme in a radial-azimuthal exb plasma configuration,” *AIP Advances*, vol. 13, no. 2, 2023.

[321] JM. Tejeda and A. Knoll, “A water vapour fuelled Hall effect thruster: characterization and comparison with oxygen,” *Acta Astronautica*, vol. 211, pp. 702–715, 2023.

[322] V.-G. Tirila, A. Demairé, and C. N. Ryan, “Review of alternative propellants in hall thrusters,” *Acta Astronautica*, 2023.

[323] H. Li, L. Zhang, S. Zhang, Y. J., and A. Sun, “On the space-charge effects in the beam extraction process of ion thrusters: the roles of compensating electrons and changing beam radius,” *Plasma Sources Science Technology*, vol. 32, no. 4, p. 044002, 2023.

[324] L. Garrigues, G. Hagelaar, C. Boniface, and J. Boeuf, "Optimized atom injection in a Hall effect thruster," *Applied Physics Letters*, vol. 85, no. 22, 2004.

[325] G. Xia, H. Li, X. Zhu, Z. Ning, S. Chen, D. Yu, and C. Zhou, "Effects of rotating supply mode on the ionization parameters of a krypton Hall thruster," *Vacuum*, vol. 181, p. 109664, 2020.

[326] S. Boccelli, T. Magin, and A. Frezzotti, "Numerical investigation of reversed gas-feed configurations for Hall thrusters," *Journal of Propulsion and Power*, vol. 37, no. 12, pp. 1–9, 2021.